Light manipulation for enhanced photodetection performance and novel functionalities in colloidal nanocrystal-based infrared sensing devices

Tung Huu Dang

Université Paris-Cité

ED564: Physique en Île-de-France

Laboratoire de Physique de l'École Normale Supérieure

Light manipulation for enhanced photodetection performance and novel functionalities in colloidal nanocrystal-based infrared sensing devices

par

Tung Huu DANG

Thèse de doctorat de physique

Dirigée par Angela VASANELLI

Thèse présentée et soutenue publiquement le 27/09/2023

Devant un jury composé de :

M. Jean-Pierre HERMIER (Professeur - GEMaC, UVSQ)	Rapporteur
M. Riad HAIDAR (HDR – ONERA, École Polytechnique)	Rapporteur
Mme. Agnès MAÎTRE (Professeure – INSP, Sorbonne Université)	Examinatrice
M. Roman KRAHNE (Scientist - Italian Institute of Technology)	Examinateur
M. Jean-Christophe LACROIX (Professeur - Université Paris Cité)	Examinateur
Mme. Angela VASANELLI (Professeure – Université Paris Cité)	Directrice de thèse
M. Emmanuel LHUILLIER (CR – INSP, Sorbonne Université)	Invité

Résumé

Cette thèse porte sur la réalisation de photodetecteurs infrarouges combinant des nanocristaux colloïdaux de HgTe et des résonateurs plasmoniques. Dans le cas des photodétecteurs à base de nanocristaux, l'utilisation de résonateurs est particulièrement bénéfique en raison du transport à courte distance résultant du caractère polycristallin du film. En effet, dans un réseau de nanocristaux de HgTe, le mécanisme de « hopping » limite la longueur de diffusion des porteurs à quelques dizaines de nanomètres, une longueur significativement plus courte que la profondeur d'absorption du matériau. Cette décorrélation entre les longueurs caractéristiques de l'absorption et du transport conduit à un compromis entre l'absorption optique et l'efficacité de la collecte de charges. Les résonateurs plasmoniques permettent la manipulation de la lumière à des échelles inférieures à la longueur d'onde. Ils peuvent ainsi être exploités pour focaliser la lumière sur des films de nanocristaux ultrafins compatibles avec le transport de charges. Dans ce travail de thèse, nous démontrons une amélioration des performances des détecteurs grâce à l'utilisation de résonateurs. De plus, nous montrons que des fonctionnalités avancées, comme la modulation électrique de la photoréponse des dispositifs, peuvent être obtenues en couplant les nanocristaux avec des structures plasmoniques. Le transport par hopping, souvent considéré comme une limitation pour les dispositifs optoélectroniques, est dans ce cas un ingrédient bénéfique. Enfin, une photodiode avec une architecture basée sur des résonateurs plasmoniques sera présentée. Le dispositif obtenu est parmi les photodétecteurs à nanocristaux les plus sensibles et les plus rapides rapportés jusqu'à présent dans le moyen infrarouge à température cryogénique. De plus, nous démontrons que l'architecture plasmonique utilisée permet d'obtenir une réponse multi-longueur d'onde, reconfigurable avec la tension. De nouvelles fonctionnalités peuvent aussi être démontrées avec ce dispositif, telles que la réjection de bande et la bidirectionnalité du courant.

Mots clés : infrarouge, nanocristaux colloïdaux, HgTe, structures photoniques, photonique active, réponse reconfigurable.

Abstract

This thesis focuses on the use of optical nanostructures in nanocrystal-based infrared photodetectors. Integrating optical structures into photodetectors has been demonstrated to improve the devices' speed and sensitivity. In the case of nanocrystal-based photodetectors, using optical resonators is particularly beneficial. Indeed, because of the hopping mechanism, carrier diffusion lengths in a nanocrystal array are several times shorter than the material's absorption depth. This limited transport leads to a trade-off for the thickness of nanocrystal films between optical absorption and charge collection efficiency in photodetectors. Optical nanostructures enable the manipulation of light at subwavelength scales. They can thus be exploited to focus light on ultrathin nanocrystal films compatible with carrier transport. In addition to the enhanced performance of the sensing devices, we also show that advanced functionalities can be generated by coupling nanocrystals with optical structures. Such functionalities result from the bias-reconfigurable photoresponse of the devices. We show that hopping transport, often seen as a limitation for optoelectronic devices, is a crucial ingredient for bias reconfigurability and the design of active photoconductive nanocrystal devices. Lastly, a combination of a photodiode structure and plasmonic resonators will be presented. The obtained device is among the most sensitive and fastest mid-wave infrared photodetectors reported so far based on colloidal nanocrystals operating at cryogenic temperature. Furthermore, we demonstrate that combining our plasmonic structures with a single diode stack can generate a multicolor bias reconfigurable response and introduce new functionalities such as band rejection and current bi-directionality.

Keywords: infrared, colloidal nanocrystals, HgTe, photonic structures, active photonics, reconfigurable response.

Acknowledgements

First of all, I would like to thank Jean-Pierre Hermier, Riad Haidar, Agnès Maître, Roman Krahne, and Jean-Christophe Lacroix for accepting to be members of my jury and for their interest in my work.

I am grateful to my PhD advisors, Angela and Emmanuel, for giving me the opportunity to work on this fascinating project and for their supervision and countless support over the last three years. My PhD journey would not have been so enjoyable without their confidence and encouragement for my work.

I am thankful to Carlo for always being friendly and supportive. I am always impressed with his deep knowledge of device physics and enthusiasm for scientific discussions. I would like to thank Yanko for many helpful and joyful conversations. I thank Djamal for always being willing to help and the instruction for many experiments.

I am lucky enough to work with many great collaborators. I want to thank Grégory Vincent and Baptiste Fix from the ONERA for many interesting scientific discussions and for their efforts with SNOM measurements. I wish to acknowledge Christophe Delerue from IEMN, Lille, for the tight-binding simulation that helped us understand the Stark effect in HgTe quantum dots. Thanks to Alexei Baranov from IES, Montpellier, for providing the 2.5 μm laser diode for response time measurements of the broadband detectors. Thanks to Armel Descamps-Mandine from Centre de MicroCaractérisation Raimond Castaing, Toulouse, for the magnificent cross-sectional image and EDX mapping. Last but not least, thanks to Yoann Prado, who provided excellent nanocrystals that are a central part of this work.

I am also grateful to all the cleanroom technical teams I worked with during this PhD. Thanks to Erwan and Loïc from INSP for keeping the cleanroom running and providing a pleasant working environment. At ENS, thanks to Michael for teaching me ebeam lithography and for helping me become familiar with other equipment; thanks to José for his help with RIE and for always being supportive.

I would like to acknowledge as well all the members of the QUAD team at LPENS and the OCN team at INSP for making my PhD experience very enjoyable. Andy, for introducing me to the COMSOL Blog, where I am still learning more about electromagnetic simulation. Thomas, for teaching me the very first measurements with FTIR and infrared alignment. Audrey, for many tips and tricks with lithography and much knowledge about device characterization, you showed me how to carry out my PhD! Charlie, for the ink recipe that I (and everyone in the OCN team) still follow today, for many interesting discussions on measurements, for Blender ideas, for the football game tickets, for your delicious cakes, and so on. Adrien, for showing me how to build a diode and always being in a positive mood. Corentin, for the unlimited jokes and interesting stories. Mariarosa, for sharing (and suffering in) the same office, for the inspiration in fine arts, for the food experiences, and for being Italian. Huichen, for introducing me to the best spicy (and affordable) foods in Paris. Erwan, for being so pleasant to work with. Claire, for always being friendly. Rodolphe, for the football jokes and discussions. Nicolas, for many interesting conversations and for your food passion. Debora, for always being so kind and easy

to talk to. Further thanks to other past and current members from both teams, in random orders: Junling, Sang Soo, Prachi, Stefano, and Eva from the OCN team; Mohsen, Mohammadreza, Jihye, Marta, Usama, Livia, Hamza, Azzurra, (young) Thomas, Étienne, Grégoire, Joel, Jiawen, and Francesco from the QUAD team. It has been a great pleasure and privilege to work with these wonderful people.

These three years would not be possible without the support of my friends and family, who helped me keep a balance between work and personal life. I am thankful to Phương, my girlfriend, for always being the nicest, most supportive, and most optimistic person I can share everything with. Many thanks to Christian for showing me around in Münster, for the fantastic Dortmund game, for being so open-minded with food, and for many other unforgettable memories. Thanks to Juliana for letting me take care of the birds (and Christian) from time to time, for many great chats and stories, and for always making me feel so welcome. Thanks to Joaquin for being so fun, for helping me with the mice traps, and for having great lunchtimes together. Thanks to Zixin for many great conversations about life and physics and for teaching us how to make dumplings. Thanks to Linh for nearly 10 years of friendship, for hosting me in Cologne, and for many deep and shallow conversations. Thanks to Thành, Đức Anh, Thái, anh Huy for the long walks around Paris talking about various important topics that I can(not) remember. Thanks to many other Vietnamese friends in France for many great moments together and for making me feel at home from the time I began my master's here until today: Tú, Mít (Duyên), Quý, Trúc, Minh, Vân Anh, 2 Yến, Hoàn, anh Đức, chị Ngà, Phong, and Mai. From more than 10,000 km away, I am grateful to my dear friends in Viet Nam: Quảng, Huyền, Hoa, Đức Anh, for many discussions about life and carrier, for their presence at the right moments, and for reminding me about where I come from.

Finally, I want to especially thank my parents, who have always been there for me. Con cảm ơn bố mẹ vì luôn ủng hộ con trên con đường mà con đã chọn! Con mong rằng những nỗ lực này sẽ làm bố mẹ tự hào và hi vọng rằng bố mẹ sẽ tiếp tục ủng hộ con trên những chặng đường sắp tới!

Contents

List of abbreviations

Abbreviation	Meaning
NC, NCs	Nanocrystal, nanocrystals
IR	Infrared
NIR	Near-infrared
SWIR	Short-wave infrared
MWIR	Mid-wave infrared
LWIR	Long-wave infrared
FIR	Far infrared
TGS	Triglycine sulfate
DTGS	Deuterated triglycine sulfate
MCT	Mercury cadmium telluride
QWIP	Quantum well infrared photodetectors
QCD	Quantum cascade detector
CSIP	Charge sensitive infrared photodetectors
FPA	Focal plane array
EQE	External quantum efficiency
IQE	Internal quantum efficiency
NEP	Noise equivalent power
BLIP	Background-limited performance
HOT	High operating temperature
NETD	Noise equivalent temperature difference
VB, CB	Valence band, conduction band
MBE	Molecular beam epitaxy
MOCVD	Metal-organic chemical vapor deposition
TOP	Trioctylphosphine
TOPO	Trioctylphosphine oxide
TEM/SEM	Transmission/scanning electron microscope
HH/LH	Heavy hole/ light hole
PL	Photoluminescence
EDT	Ethanedithiol
DDT	Dodecanethiol
MPOH	2-mercaptoethanol
DMF	N,N dimethylformamide
LED	Light emitting diode
FET	Field-effect transistor
ITO/ FTO	Indium Tin Oxide/ Fluorine-doped Tin Oxide
PMMA	Poly(methyl methacrylate)
UV	Ultraviolet
ROIC	Readout integrated circuit
VGA	Video graphics array
CMOS	Complementary metal-oxide-semiconductor

GMR	Guided-mode resonator
MDM	Metal-dielectric-metal
TE/TM	Transverse electric/ transverse magnetic
SPP	Surface plasmon polariton
AFM	Atomic force microscopy
EDX	Energy dispersive X-ray
FIB	Focused ion beam
MEMS	Micro-electromechanical systems
ALD	Atomic layer deposition
SNOM	Scanning near-field optical microscopy
TCO	Transparent conductive oxide
ACN	Acetonitrile

Preface

Discovered more than 200 years ago, infrared radiation has become one of the most essential and applicable parts of the electromagnetic spectrum. Initially motivated by the strategic military advantages on the battlefield, infrared detection now can be found in numerous civilian applications, including industrial, scientific, commercial, and medical purposes. However, high-performance infrared detection primarily relies on epitaxial III-V and II-VI semiconductors, which require expensive equipment and highly complicated processing. These factors contribute to the extensive price of current infrared sensing devices. As a result, infrared detection is generally regarded as an expensive technology.

Recent years have seen the emergence of colloidal nanoparticles in infrared optoelectronics. These nanocrystals are prepared with chemical methods, thus enabling mass production of the materials and solution-processability for device fabrication. Initial demonstrations of infrared sensors based on colloidal materials have already shown great potential for fast and sensitive detection. Thus, colloidal nanocrystals are a highly promising platform for the development *of cost-effective and high-performing* infrared sensing devices.

Thanks to recent progress in material development, colloidal materials are now ready to be integrated into advanced device architectures. This thesis focuses on the use of photonic structures for light manipulation in nanocrystal-based infrared sensors. The main objectives of this work include: (i) *improving the device's detection performance*, and (ii) *obtaining active spectral response shaping through light-nanocrystal coupling*. While the first goal is the ultimate challenge for detecting systems, the second objective is a domain mostly unexplored in nanocrystal-based infrared sensors. The ability to actively control the device's optical response is of great interest for infrared sensing applications since imaging contrast could be substantially improved by tuning the device's spectral response.

During this project, several photonic structures have been explored. A significant part of my work involves designing and optimizing optical structures, fabricating the detectors with material and device processing, and infrared optoelectronic characterizations.

This manuscript is divided into four main chapters. The organization and main topic of each chapter are presented as follows.

Chapter 1 will review the historical progression of infrared detection technology and the current status of the field. Specifically, the underlying physics and working principles of quantum infrared photodetectors will be described. In addition, key figures of merit for evaluating and comparing the performance of different infrared detection technologies will be introduced.

Chapter 2 provides an overview of the current status of photonic structures for nanocrystal-based infrared photodetectors. Subsequently, we introduce our optical structure for achieving broadband infrared photodetection based on colloidal HgTe nanocrystals and metal-dielectric-metal cavities.

Chapter 3 focuses on bias reconfigurability and presents our strategy to achieve this functionality in nanocrystal-based infrared sensors. The field-dependent hopping transport mechanism is a key property, which will be exploited in combination with optical resonances generated by our photonic designs to generate actively reconfigurable photoresponse. This approach offers a pathway toward active photonics based on colloidal nanocrystals.

Lastly, in **Chapter 4**, we show our strategy to optimize the optical design of a photodiode structure. Compared to the commonly used design in which transparent conductive oxides (ITO, FTO…) are used as electrodes, our optimized structure allows for significant nanocrystal absorption enhancement, leading to a state-of-the-art detection performance in the mid-wave infrared for a nanocrystal-based photodetector. Furthermore, by multiplexing an array of plasmonic resonators on the same substrate, we show that the multicolor bias-selectable photoresponse on a single diode stack can be obtained.

Chapter 1: Nanocrystal–based infrared photodetectors

Contents

Related publications:

- Lhuillier, E.; Dang, T. H.; Cavallo, M.; Abadie, C.; Khalili, A.; Peterson, J. C.; Gréboval, C. Infrared Sensing Using Mercury Chalcogenide Nanocrystals. In *Handbook of II-VI Semiconductor-Based Sensors and Radiation Detectors: Volume 2, Photodetectors*; Springer International Publishing: Cham, 2023; pp 155–181.
- Lhuillier, E.; Dang, T. H.; Cavallo, M.; Abadie, C.; Khalili, A.; Gréboval, C. Electronic Structure of Mercury Chalcogenides Nanocrystals. In *Handbook of II-VI Semiconductor-Based Sensors and Radiation Detectors: Volume 1, Materials and Technology*; Springer International Publishing: Cham, 2023; pp 133–156.

1.1. Infrared photodetection

The infrared is generally defined as the spectral range with wavelengths longer than the visible, as shown in Figure 1.1. Thus, infrared radiation is not detectable by human eyes. For this reason, the development of infrared technology has been closely associated with military applications, in which "see without being seen" brings significant advantages on the battlefield. However, several civilian applications also benefit from infrared. Non-military uses of the infrared involve telecommunications, spectroscopy, facility inspections, biological analysis, and environmental monitoring. Therefore, there is a great interest in making these technologies cost-effective and accessible beyond specific military uses.

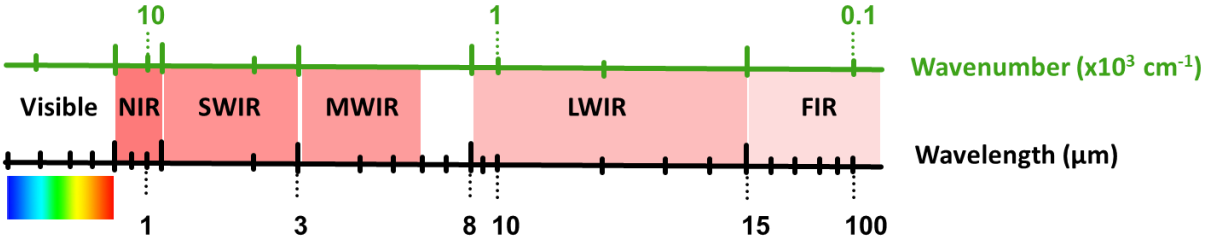

Figure 1.1: The infrared range in the electromagnetic spectrum. *Subdivisions of the infrared are also presented. The top axis provides relevant values in the unit of wavenumber (cm^{-1}).*

As the infrared covers a broad spectrum of wavelengths, it is typically subdivided into smaller bands with specific bandwidths. A typical subdivision scheme includes:

- The near-infrared (NIR) covers the wavelength range from 0.7 to 1.4 µm. Applications of NIR detection involve astronomical spectroscopy, remote sensing for Earth monitoring, food inspection, and telecommunication.
- The short-wave infrared (SWIR) is typically defined from 1.4 to 3 µm. SWIR is important in fiber optics communication (the wavelength range 1530 – 1550 nm) and active imaging. Furthermore, some objects are transparent in the SWIR but not in the visible, such as silicon. Therefore, SWIR is also used in wafer inspection in semiconductor industry.
- The mid-wave infrared (MWIR) expands from 3 to 5 µm. The main interest in this spectral range comes from the atmospheric transparency window, which allows thermal imaging without significant loss caused by the ambiance.
- The long-wave infrared (LWIR) deals with wavelength range from 8 to 15 µm where complete passive imaging of objects with temperatures higher than room temperature, such as the human body, can be implemented.
- The far infrared (FIR) covers the wavelength range above 15 µm. This range is also useful for passive thermal imaging. In addition, FIR spectroscopy is used in astronomy to study galaxies and large energy sources.

The significance of the infrared for applications has led to the development of various detection technologies. This section will briefly review the historical progression of infrared detection and the current status of the field. Specifically, the underlying physics and working principles of quantum infrared photodetectors will be described. Finally, key figures of merit for evaluating and comparing the performance of different infrared detection technologies will be introduced.

1.1.1. Historical background

The first experiment of infrared detection can be traced back to 1800 when William Herschel used a prism to refract and detect light beyond the red part of the visible spectrum. In this experiment, infrared radiation has been measured through temperature increase in a thermometer. Although most detectors used for infrared detection in the XIX century were based on thermal effect, as early as 1850, Antoine Becquerel observed that some materials respond to light by generating an electrical current [1]. This observation can be seen as the first experimental demonstration of semiconductor detectors. However, it took almost one century to physicists to develop the quantum theory of condensed matter, which could explain Becquerel's observation satisfactorily.

Figure 1.2: Infrared photodetectors developed in the 20th century. *From reference [2].*

Nowadays, although various technologies for infrared photodetection have been developed, the classification of detectors based on their working principles remains. Photodetectors are commonly divided into two main categories:

- Thermal detectors, which are based on a temperature change of the active material under infrared illumination. This change in temperature leads to changes in physical properties, which can be evaluated electrically. Typical thermal detectors include:
  - Thermopiles, whose working principle is based on the thermoelectric effect [3]. A thermopile is usually an array of thermocouples connected in series. Voltage is generated in response to temperature difference, which is caused by infrared thermal radiation (*i.e.*, black-body radiation).
  - Pyroelectric detectors (e.g., TGS and DTGS crystals), which are based on the pyroelectric effect [4].
  - Bolometers, whose electrical resistance depends on the temperature [5]. The active material of a bolometer is typically a resistor with a large temperature coefficient of resistance. As a result, incident infrared radiation could heat the detector and causes a significant change in the resistance.
- Photoconductive and photovoltaic semiconductor detectors, or photon detectors, in which optical transitions between quantum states cause variations in the material's electrical conductivity. This group can be further subdivided into:
  - Interband detectors, which operate based on optical transitions between the conduction and valence bands, thus involving two kinds of carriers, electrons and holes: HgCdTe (MCT) [6], III-V-based photodiodes (InSb, InGaAs) [7], [8].
  - Intraband detectors, which rely on transitions between subbands within the same band (*i.e.*, either conduction or valence band), thus are influenced by only one type of carriers: quantum well infrared photodetectors (QWIP) [9], quantum cascade detectors (QCD) [10], charge sensitive infrared photodetectors (CSIP) [11].

The development of infrared detectors began first with thermal detectors. Thomas Seebeck discovered the thermoelectric effect around the 1820s and demonstrated the first thermocouple soon after. Around 1829, Nobili built the first thermopile consisting of various thermocouples in series. Themopiles became the most popular infrared detectors until the

introduction of Langley's bolometers around the 1880s. The newly developed bolometers were more compact, more sensitive, and faster than all other infrared devices known at the time.

The development of semiconductor photodetectors only began in the XX century with the invention of quantum physics and progress in materials science, specifically in semiconductor manufacturing. The first infrared photoconductors, based on a compound of Thallium and Sulphur (Tl_2S), were developed by Theodore Case around the 1920s [12]. However, these detectors present a high level of instability with high noise, low saturation threshold, and ultimately lack of reproducibility [13]. The 1950s saw the introduction of lead salt polycrystalline photodetectors for the SWIR from 1.3 to 3 µm. The materials were produced with vacuum evaporation and chemical processes [14], followed by a sensitization step. Indium antimonide-based detectors (InSb), which work in the MWIR from 3 to 5 µm, were developed a few years after.

The rapid progress in semiconductor alloys at the beginning of the 1960s led to the introduction of various narrow-gap materials, including InAsSb, PbSnTe, and in particular, HgCdTe (MCT). The first detectors based on MCT alloys present a strongly tunable bandgap, enabling infrared photodetection up to 12 µm [15]. Until now, MCT remains *the most widely used material* for infrared photodetection.

Intraband photodetectors appeared in the 1980s thanks to the advancements in growth processes, which enabled the development of heterostructure semiconductors with unprecedented levels of purity. The QWIP based on GaAs/AlGaAs was first demonstrated during this period [9]. With respect to MCT, GaAs/AlGaAs quantum wells present numerous advantages, including the use of mature processing technologies, well-controlled growth process for large wafers, thus higher fabrication yield and lower cost, and more thermal stability. Fundamentally, QWIPs possess very fast response. However, due to the nature of intraband transitions, QWIP generally have low quantum efficiencies (see section 1.1.3) and narrow spectral response band.

It should be noted that progress in photodetectors was not only made from the material side but also from device architecture development. Particularly, a lot of attention has been paid to integrating infrared materials onto focal plane arrays (FPA) for infrared imaging. Figure 1.2 summarizes the main achievements in infrared sensing technologies of the last century.

1.1.2. Photoconductors and photodiodes

As mentioned in the previous section, the most widely used infrared photodetectors are currently based on interband transitions. According to their charge separation mechanisms, these devices are further separated into two classes: photoconductors and photodiodes. This section recalls the physical phenomena behind the working principle of these device operation.

Photoconductors

In photoconductors, incoming photons with energies higher than the material's bandgap cause the generation of electron-hole pairs. This results in an increase in the conductivity of the material, which is called photoconductivity. The generated charges contribute to the flowing current in the circuit, which increases as a function of the photon flux (*i.e.*, light intensity).

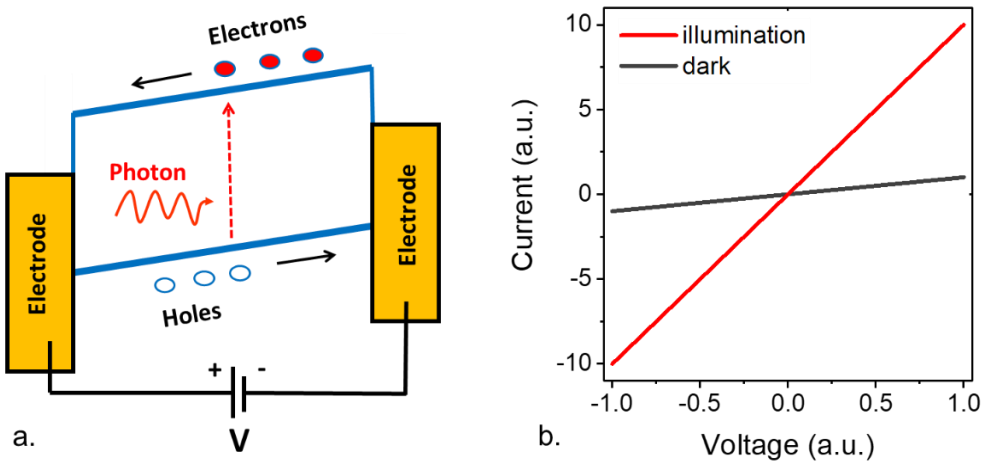

Figure 1.3: Photoconductive devices. *a. Simplified band diagram of a photoconductive detector under applied bias. Upon light absorption, the charge carriers are generated. Electron and hole extractions occur thanks to the applied bias. b. Typical current-voltage (I-V) characteristics of a photoconductor under the dark and illumination conditions. The I-V curve shows a typical Ohmic behavior.*

A typical energy scheme for photoconductors is illustrated in Figure 1.3a. Upon light absorption, the photon's energy is transferred to an electron-hole pair in the photoconductor, which will be extracted by the applied bias. In the absence of Schottky barriers, the typical current-voltage characteristic of a photoconductor is linear (*i.e.*, Ohmic behavior), as presented in Figure 1.3b. In the absence of the incoming light, the I-V curve features the device's *dark current*, which is also present in the device's total current (*i.e.*, dark current + photocurrent) when being illuminated. *Dark current* is the main noise source that leads to the limited sensitivity of detecting devices.

It is possible to establish the relationship between the material's physical properties and the photogenerated current in a photoconductive device [1]. Consider a thin slab of photoconductor with dimension w × l × d, as indicated in Figure 1.4.

The irradiance at depth z into the semiconductor can be written as

$$\varphi(z) = \varphi_0 \exp(-\alpha z) \tag{1.1}$$

where φ_0 is the flux of incident photons and α is the absorption coefficient of the semiconductor. The generation rate (in cm^{-3} s^{-1}) of electron-hole pairs under illumination is given by [1]

$$G_{op}(z) = \alpha\varphi_0 \exp(-\alpha z) \tag{1.2}$$

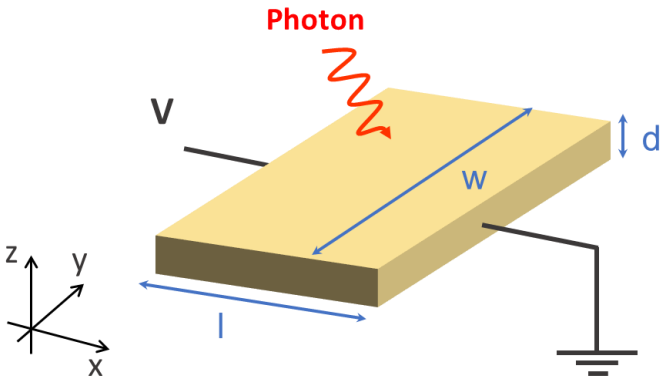

Figure 1.4: A photoconductive detector under illumination.

Assuming the material under consideration is a p-type semiconductor, the population of electrons governs the photoconductor operation. The generated carriers, with volume density Δn, face two possibilities: they recombine or will be extracted by the applied electric field. The equation that describes this mechanism is written as

$$\frac{\Delta n}{\tau} - D\frac{d^2}{dz^2}\Delta n = G_{op}(z) = \alpha\varphi_0 \exp(-\alpha z) \tag{1.3}$$

where τ is the electron lifetime, and D is the diffusion coefficient.

Solving equation 1.3, the total generated carrier over the semiconductor volume can be obtained. Assuming the current only flows in the direction of the applied bias, z, the number of *generated carriers per unit surface* is given by

$$\Delta n_{tot} = \int_0^d \Delta n(z)dz = \tau\varphi_0 \exp(-\alpha d) \tag{1.4}$$

If we neglect the carrier inhomogeneity in the z direction, the photocurrent density is expressed as

$$j_{photo} = \Delta n_{tot} e\mu_e E/d = \tau\varphi_0 e\mu_e E \exp(-\alpha d)/d \tag{1.5}$$

where $E = V/l$ is the transverse electrostatic field, e is the elementary charge, and μ_e is the electron mobility. The total photocurrent flowing in the device is obtained as:

$$I_{photo} = j_{photo} \times w \times d = e\varphi_0 \exp(-\alpha d) \times w \times (\tau\mu_e E) \tag{1.6}$$

The term $\mu_e E$ is the electron drift velocity. The transit time $\tau_{transit} = l/(\mu_e E)$ is the time taken for electrons to travel across the photoconductor. Thus, it is convenient to define the photoconductive gain

$$g = \frac{\tau\mu_e E}{l} = \frac{\tau}{\tau_{transit}} \tag{1.7}$$

If the electron lifetime is longer than the transit time, the photoconductive gain can be greater than unity. However, high gain also leads to a long lifetime of photogenerated carriers, which limits the speed of the photodetector. This is the gain/bandwidth trade-off in photoconductors.

Photodiodes

Photodiodes are based on heterojunctions or homojunctions of semiconductors. When a p-n junction is formed, the built-in potential is responsible for charge circulation. The generated charges in the depletion region are swept to the electrodes due to the high internal electric field, as described in Figure 1.5a. Thus, an applied bias is not required for photodetection with a diode.

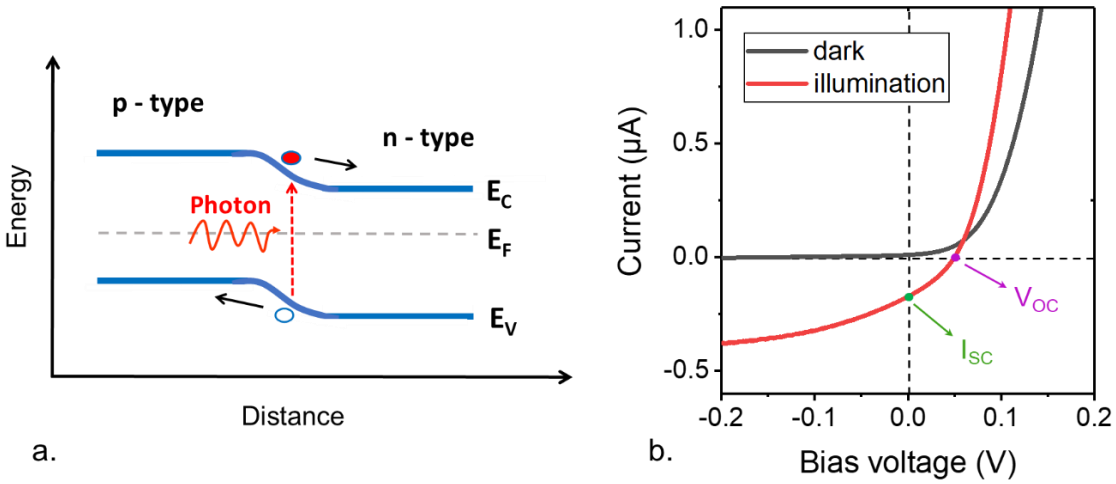

Figure 1.5: Photodiodes. *a. Simplified band diagram of a p-n junction at equilibrium. Upon light absorption, the charge carriers are generated in the depletion region. Electron and hole extractions occur thanks to the built-in potential. b. Current-voltage (I-V) characteristics of a photodiode under the dark and illumination conditions. The I-V curve shows rectifying behavior. For the curve describing operation under illumination, short-circuit current (I_{SC}) and open-circuit voltage (V_{OC}) are highlighted.*

In the dark, no open-circuit voltage is present. The dark current in a photodiode is given by

$$I_{dark} = I_s(e^{\frac{eV}{kT}} - 1) \tag{1.8}$$

where I_s is the saturation current of the photodiode, V is the applied bias voltage. Under illumination, the generated photocurrent contributes to the total current of the device. The current flowing in the device is written as

$$I_{total} = I_{dark} + I_{photo} = I_s\left(e^{\frac{eV}{kT}} - 1\right) + I_{photo} \tag{1.9}$$

There are two important quantities for the photodiode operation. The short-circuit current I_{SC} is identified in zero-bias operation ($V = 0$) and is simply equal to the photocurrent $I_{SC} = I_{photo}$. The open-circuit bias is identified in zero-current operation ($I_{total} = 0$) and is expressed by

$$V_{OC} = \frac{kT}{e}\ln(1 + \frac{I_{photo}}{I_s}) \tag{1.10}$$

Both quantities are connected to the intensity of incident light.

Photodiodes can operate in two detection modes:

- In *photovoltaic mode*, no external bias is required. Under illumination, the generated open-circuit voltage is measurable directly without a load resistor.

- In *photoconductive mode*, a reverse bias is applied across the p-n junction. Thus, the I-V characteristic of the diode follows equation 1.9. The advantage of the photoconductive mode is the fast detection response. However, applying an external bias introduces noise, which limits the sensitivity of the device.

1.1.3. Figures of merit

The performance of photodetectors is characterized by a number of parameters. This section introduces the most commonly used *figures of merit* for infrared sensors.

Responsivity

Responsivity is the ability of a photodetector to transfer photon energy into electrical output. Typically, the unit of responsivity is A/W. The *spectral responsivity* is defined as

$$R(\lambda) = \frac{I_{photo}}{\Phi(\lambda)} \tag{1.11}$$

where I_{photo} is the photocurrent signal, and $\Phi(\lambda)$ is the spectral radiant flux. The spectral responsivity is typically measured with monochromatic light sources.

Apart from the wavelength-dependent responsivity defined above, *blackbody responsivity* is also commonly used. Blackbody radiation is a standard means to calibrate the detection performance of infrared devices. The blackbody responsivity is given by

$$R_{BB} = \frac{I_{photo}}{\int \Phi(\lambda).d\lambda} = \frac{I_{photo}}{P_{BB}} \tag{1.12}$$

Here, the incident power P_{BB} is the integral of the spectral density of power from a blackbody over the spectral detection range of the photodetector.

According to Planck's law, the power irradiated per unit wavelength by a blackbody source at temperature T is expressed as

$$\frac{d\Phi}{d\lambda} = \frac{2hc^2}{\lambda^5} \frac{1}{\exp\left(\frac{hc}{\lambda kT}\right)-1} \tag{1.13}$$

where h is the Planck's constant, c is the speed of light, and k is Boltzmann constant.

Figure 1.6a provides the radiance spectrum of a blackbody with different temperatures from equation 1.13. As the blackbody's temperature increases, the emission peak shifts towards shorter wavelengths (*i.e.*, higher energies), and the overall emission power increases.

Considering a detector with area A_{det} absorbing incident light from the blackbody with a field of view θ, as described in Figure 1.6b, the incoming power to the detector (the denominator in equation 1.12) is calculated as:

$$P_{BB} = \pi A_{det} \cdot \sin^2\left(\frac{\theta}{2}\right) \cdot \int \frac{2hc^2}{\lambda^5} \frac{1}{\exp\left(\frac{hc}{\lambda kT}\right)-1} d\lambda \tag{1.14}$$

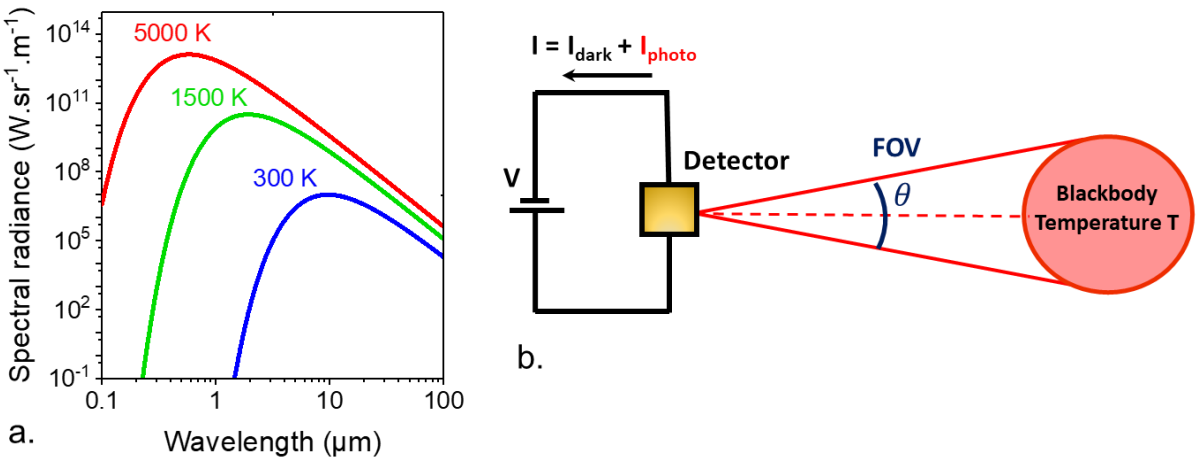

Figure 1.6: Blackbody radiation. *a. Spectral radiance of a blackbody with different temperatures. The radiance peak shifts towards shorter wavelengths as the blackbody's temperature increases. b. Simplified scheme of responsivity measurement with a blackbody. Blackbody responsivity can be determined from the photocurrent and the incoming power the detector receives.*

The blackbody responsivity R_{BB} can be obtained experimentally by measuring the photocurrent and the incident power onto the detector. Responsivity allows predicting how much output signal one could expect for a specific application. Although responsivity is a good indicator of high performance, it does not provide information about the intrinsic noise of the device, and thus cannot reflect the level of sensitivity of the photodetectors. Other figures of merit are needed for the comparative evaluation of different infrared detection systems.

Quantum efficiency

Quantum efficiency is the probability for a single photon to generate a carrier pair contributing to the photocurrent. *External quantum efficiency* (EQE) is expressed in percentage and is given by

$$\eta(\lambda) = \frac{N_e}{N_\lambda} \tag{1.15}$$

where N_e is the number of carrier pairs produced, N_λ is the number of incident photons. It is important to differentiate EQE from the *internal quantum efficiency* (IQE), which is connected to the number of photons absorbed by the device.

Both EQE and spectral responsivity are functions of wavelength. They are related by

$$\eta(\lambda) = \frac{R(\lambda)}{\lambda} \times \frac{hc}{e} \tag{1.16}$$

Noise current source and noise equivalent power

The current flowing in a photodetector has temporal fluctuations that cause electrical noise in photodetectors. The current noise is thus directly connected to the magnitude of the dark current. There are different mechanisms that generate current noise in a photodetector:

- Thermal noise $S_R = \frac{4kT}{R_0}$, which is generated due to random thermal fluctuation of charge carriers inside the photodetector [16]. Thermal noise depends on the temperature and the photodetector resistance R_0.
- Generation – recombination noise $S_{G-R} = 4egI_{dark}$, which originates from the fluctuations of generation and recombination rates of the charge carriers in photoconductive detectors [1]. Under illumination, shot noise due to photogenerated current needs to be considered. Note that for photodiodes, $S_{G-R} = 2egI_{dark}$, with g smaller than unity. The factor of 2 difference is attributed to the fact that recombination and generation processes are uncorrelated in photoconductors, which leads to higher detector noise [2].
- 1/f noise $S_{1/f}$, or pink noise, generally occurs in electrical circuits with noise density depending on the frequency. The 1/f noise density is inversely proportional to the modulation frequency. The origin of 1/f noise is still under debate and is explicitly analyzed for specific systems. For instance, 1/f noise in solid film of quantum dots has been shown to be dependent on the intercoupling between the particles rather than the quantum dot material [17].

When characterizing a photodetector over a frequency integration bandwidth $\Delta f = 1/2t_{int}$, where t_{int} is the integration time, noise current density can be evaluated. The noise current at frequency ω is the sum of all noise contributions:

$$i_N = \sqrt{\Delta f \cdot \sum_j S_j^i(\omega)} = \tilde{\imath}_N(\omega)\sqrt{\Delta f} \tag{1.17}$$

The signal-to-noise ratio can be calculated from the photocurrent and the noise current

$$S/N = \frac{I_{photo}}{i_n} = \frac{I_{photo}}{\tilde{\imath}_N(\omega)\sqrt{\Delta f}} \tag{1.18}$$

The *noise equivalent power* (NEP) is the incident power that induces a signal-to-noise ratio equal to unity. In other words, the NEP is the lowest detectable optical power for a photodetector. Replacing equations (1.11) to (1.19), we obtain

$$NEP = \frac{\tilde{\imath}_N(\omega)\sqrt{\Delta f}}{R} \tag{1.19}$$

Thus, NEP can be calculated from the responsivity of the device. Since the noise depends on the measured bandwidth, the NEP is determined over a fixed frequency band, typically with the bandwidth of 1 Hz.

Detectivity and BLIP operation

Although NEP is convenient for evaluating a photodetector's performance, it does not allow comparing sensitivities between different technologies. As current noise scales with the detector area, the universal figure of merit for a photodetector's performance is *specific detectivity*, which is given by

$$D^* = \frac{\sqrt{A_{det}}}{NEP} = \frac{R\sqrt{A_{det}}}{\tilde{\imath}_N(\omega)\sqrt{\Delta f}} \tag{1.20}$$

where A_{det} is the photodetector optical area. The unit of detectivity is $cm \cdot Hz^{1/2} \cdot W^{-1}$, or Jones. Similar to NEP, detectivity is normally measured with modulated optical excitation at a given frequency and determined over a bandwidth Δf. It is thus important to specify these quantities for a measured value of D^*.

Obtaining higher detectivity is the ultimate objective when developing detecting devices. However, there are practical limits that must be considered in device's operation. While thermal noise and dark current can be strongly suppressed by lowering the detector's temperature, the background photon flux sets the limit to the detectivity, called background-limited detectivity D^*_{BLIP}. Background photocurrent can be determined as:

$$I_{bg} = R \cdot \phi_{bg}(T_{bg}) \cdot A_{det} \tag{1.21}$$

where $\phi_{bg}(T_{bg})$ is the background photon incident power. Note that the background flux depends on the background temperature T_{bg}, which differs from the detector's temperature. D^*_{BLIP} is reached when the shot noise, due to the absorption of background photons, dominates all other noise sources. For a photoconductor, D^*_{BLIP} is given by

$$D^*_{BLIP} = \frac{R\sqrt{A_{det}}}{\sqrt{4egI_{bg}}} = \frac{R\sqrt{A_{det}}}{\sqrt{4eg \cdot R \cdot \phi_{bg} \cdot A_{det}}} \tag{1.22}$$

where I_{bg} is the photocurrent generated by the background photons.

For the device operation, the BLIP temperature T_{BLIP} is an important figure of merit. At this temperature, the background photocurrent is equal to the dark current of the device. The detectivity at T_{BLIP} is expressed by

$$D^*(T_{BLIP}) = \frac{R\sqrt{A_{det}}}{\sqrt{4eg(I_{bg}+I_{dark})}} = \frac{R\sqrt{A_{det}}}{\sqrt{2 \cdot 4egI_{bg}}} = \frac{D^*_{BLIP}}{\sqrt{2}} \tag{1.23}$$

In order to enhance the detector's performance, cryogenic techniques are typically employed to lower the detector's temperature. However, the cooling process requires bulky and costly equipment, which is the main obstacle for MWIR and LWIR sensors. Therefore, it is necessary to develop detectors with increased working temperature while maintaining high performance. These devices are known as high-operating-temperature (HOT) infrared detectors, which currently gain much interest from the infrared community.

Time response

Another essential characteristic of a photodetector is how fast the detector responds to a change in the input signal. When light is shone on the detector, it takes a finite time for the photocurrent to appear and reach a steady value. Similarly, the current needs a finite period to decay when the light is turned off. *Rise time* and *fall time* are typically used to describe those processes. Rise time is the time difference for the signal to increase from the value of its 10% peak response to 90% peak response. Fall time, on the other hand, is defined as the time between 90% peak response and 10% peak response when the signal decreases. It is noted that rise time and fall time of a photodetector are usually different.

The response time of a photoconductive detector is determined by two factors: the lifetime of the carriers and the RC time constant of the electrical circuit. In a photodiode, as gain is limited to unity, the detector's speed is ultimately set by the transit time of photogenerated carriers

across the active layer, which depends on the width of the depletion region and the carrier mobility. Regarding the RC time constant, it is important to minimize the capacitance in the circuit to increase the detector's speed. Inherent capacitance and resistance associated with the device thus must be taken into consideration.

Noise equivalent temperature difference

Imaging in the MWIR and LWIR provides information about objects' temperature, called thermal imaging. The noise equivalent temperature difference (NETD) characterizes the performance of the thermal imaging system. NETD is the minimal temperature difference measurable by an infrared detector. Therefore, smaller values of NETD correspond to better sensitivities. NETD can be determined experimentally from

$$NETD = i_N \frac{\Delta T}{\Delta I_S} \tag{1.24}$$

where i_N is the rms current noise, ΔI_S is the signal difference induced by temperature difference ΔT. It is noted that NETD is strongly affected by the background signal, and thus, is limited by the background fluctuation noise. NETD is applicable for single element detectors. However, it is more commonly used for focal plane arrays. Depending on the materials, NETD of commercial semiconductor detectors are typically around 10 to 30 mK. For bolometer arrays, NETD is typically from 30 to 75 mK.

1.2. Infrared photodetection with colloidal nanocrystals

Beyond the conventional infrared materials presented in the previous chapter, the last decade observed the emergence of new classes of materials with great potential for infrared applications, such as two-dimensional materials (*e.g.*, black phosphorus [18], [19] and transition metal dichalcogenides, notably PtS_2, $PtSe_2$, $PdSe_2$ [20], [21]) and colloidal nanocrystals (NCs) [22]–[25]. While the former group appears limited for device scalability, the latter is very promising for practical applications. Colloidal NCs are prepared with chemical methods; thus, mass production can be conveniently achieved. Additionally, device integration has now become straightforward with NCs thanks to solution processability that eases all the lattice-match constraints imposed in conventional semiconductors.

This sub-chapter will review the basic background of NCs synthesized via colloidal synthesis and their emergence into infrared optoelectronics. Specifically, we will focus on narrow-bandgap colloidal mercury telluride (HgTe) NCs and the integration of this material into infrared-sensing devices. A significant part of the chapter will be dedicated to presenting the critical properties that make HgTe NCs a promising material for infrared applications, as well as state-of-the-art of actual NC-based infrared photodetectors.

The next sections will be organized as follows. Sections 1.2.1 and 1.2.2 will provide the important features of colloidal nanocrystals and the general methods to synthesize this interesting class of materials. Section 1.2.3 presents colloidal HgTe NCs with a focus on their critical physical properties and potential as infrared active materials. Finally, in section 1.2.4, the current status of sensing devices based on HgTe NCs will be exhibited.

1.2.1. Quantum confinement in nanocrystals

Colloidal nanocrystals, or colloidal quantum dots, are solution-processed semiconductor particles with dimensions on the nanometer scale. In a bulk semiconductor (Figure 1.7a), the valence and conduction bands are separated by a fixed energy gap, which determines the material optical and electronic properties. The situation for NCs is different since the particle's sizes are so small, comparable to the de Broglie wavelengths of the electrons and holes, allowing for the observation of quantum confinement effect. This effect can be described by the "particle in a box" model.

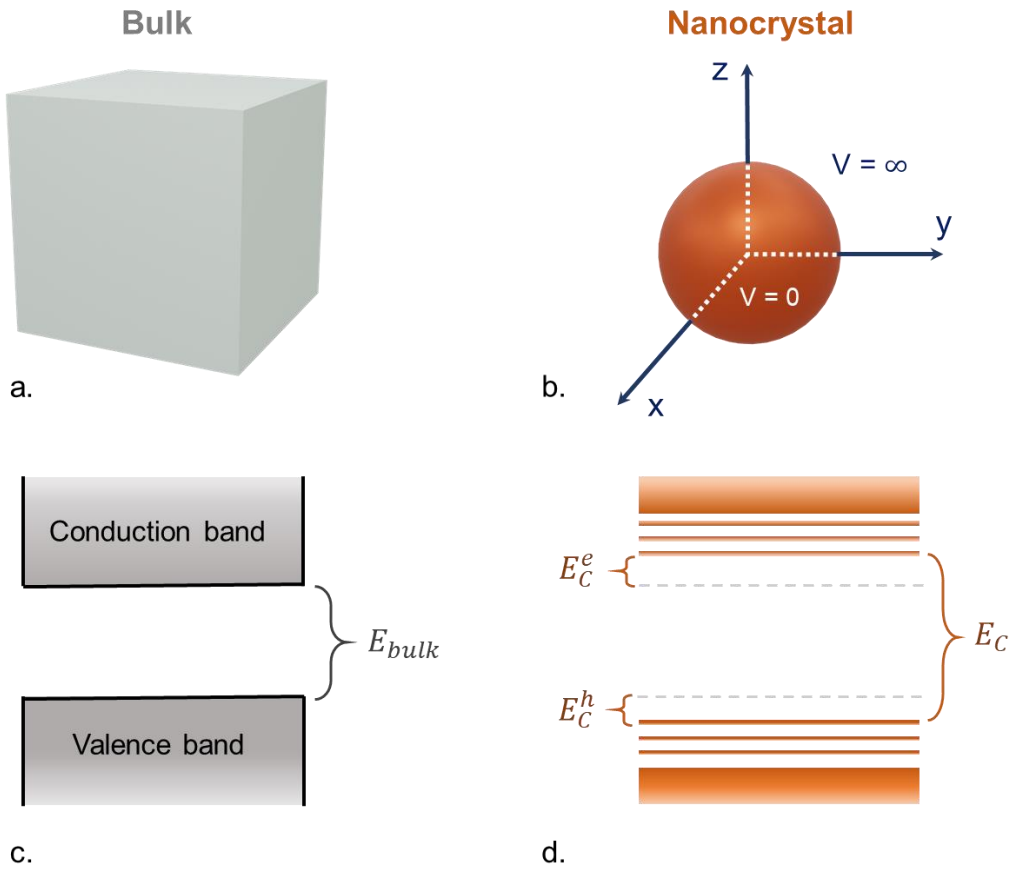

Figure 1.7: Illustration on the effect of quantum confinement on small sized particles. *a. Bulk form with a fixed band gap that governs a material's optical and electronic properties. b. A nanosized particle from the same material presents size confinement. c-d. The band gap of the nanoparticle increases due to quantum confinement.*

Let us consider a particle of mass *m* confined in a spherical box (3D) with radius *a*, as illustrated in Figure 1.7b. The eigenenergies can be written as

$$E_{nl} = \frac{\hbar^2}{2ma^2}\beta_{nl}^2 \tag{1.25}$$

where β_{nl} is the n^{th} zero of the l^{th} spherical Bessel function. Note that the corresponding states are degenerate with respect to the magnetic quantum number. Here, n and l are, respectively, the principal and azimuthal quantum numbers that determine the radial wavefunction. These two quantum numbers are conventionally labeled by spectroscopists with $n = \{1,2,\dots\}$ and $l = \{s,p,d,f,\dots\}$. Some values of β_{nl} are listed below.

Table 1.1: *The first few zeros of the spherical Bessel function* β_{nl}

	$n = 1$	$n = 2$	$n = 3$	$n = 4$
s	3.14	6.28	9.43	12.57
p	4.49	7.73	10.90	14.07
d	5.76	9.10	12.32	15.52
f	6.99	10.42	13.70	16.92

A spherical shape NC has an increase in the energy gap with respect to its bulk counterpart from the same material due to the effect of quantum confinement. The NC effective band gap is expressed by

$$E_G = E_{bulk} + \frac{\hbar^2}{2m_e^* a^2}\beta_{1s}^2 + \frac{\hbar^2}{2m_h^* a^2}\beta_{1s}^2 \tag{1.26}$$

where m_e^* and m_h^* are electron and hole effective masses. m_e^* and m_h^* are not directly connected to the real electron mass and are typically smaller. The last two terms in equation 1.26 represent the electron and hole confinement energies. The total confinement energy E_C of the system is the sum of electron and hole confinement energies:

$$E_C = \frac{\hbar^2}{2m_e^* a^2}\beta_{1s}^2 + \frac{\hbar^2}{2m_h^* a^2}\beta_{1s}^2 = \frac{\hbar^2}{2m_{eh}^* a^2}\beta_{1s}^2 \tag{1.27}$$

where m_{eh}^* is the reduced effective mass: $(m_{eh}^*)^{-1} = (m_e^*)^{-1} + (m_h^*)^{-1}$.

When a semiconductor material is illuminated, the photon absorption process creates electron-hole pairs bounded by the Coulomb interaction. This bounded state is called an exciton. The separation distance between the electron and hole is called exciton Bohr radius and is given by

$$a_0 = \frac{4\pi\varepsilon_0\varepsilon_r\hbar^2}{m_{eh}^* e^2} \tag{1.28}$$

where ε_r is the semiconductor relative permittivity and e is the elementary charge. It is thus necessary to consider electron-hole interaction for the eigenenergies of the system. According to Brus [26], the optical band gap of the nanocrystals is renormalized by adding the electrostatic interaction of the electron-hole pair:

$$E_G^* \simeq E_{bulk} + E_C + E_{Coulomb} = E_{bulk} + \frac{\hbar^2}{2m_{eh}^* a^2}\beta_{1s}^2 - \frac{1.8e^2}{\varepsilon_r a} \tag{1.29}$$

The Coulomb term depends on the NC size as $1/a$, while the confinement term is proportional to $1/a^2$. Therefore, the band gap always increases for a small enough a, which has been observed experimentally in various materials [27]–[30]. Note that equation 1.29 concerns only the first excited electronic state. The absorption of NCs includes optical transitions from all values of k vector in the Brillouin zone. Thus, optical absorption at energies above the band gap is less sensitive to the particle size [26].

In practice, there are several ways to realize nanocrystals. Typical methods include *epitaxial growth*, such as molecular beam epitaxy (MBE) and metal-organic chemical vapor deposition (MOCVD), as well as *colloidal synthesis*. While MBE and MOCVD permit the growth of nanocrystals with relatively precise size and location, they also share the disadvantages of

being expensive and time-consuming. Furthermore, the density of nanocrystals practically obtained from these techniques is limited for many optoelectronic applications.

On the other hand, large batches of nanocrystals with size dispersion as narrow as 5% can be synthesized with colloidal synthesis. This method offers scalability as a significant advantage, making it highly promising for commercial applications. In the following section, we provide an overview on colloidal synthesis for nanocrystals.

1.2.2. Colloidal synthesis of nanocrystals

The first efforts to develop semiconductor particles in liquid colloids [31]–[36] began in the 1970s, initially for the fundamental interest in spectroscopy as well as potential solar applications. Understanding the growth process and reducing the size dispersion of the particles were the main challenges in the early days.

Figure 1.8: Colloidal synthesis of nanocrystals. *a. Photo of a typical setup for colloidal synthesis. b. Absorbance spectra of CdSe NCs with different sizes. From reference [37]. c. Emission from CdSe colloidal NCs of different sizes in solution when illuminated with UV light (©Nexdot). d. Transmission electron microscope (TEM) images of CdSe CQD. The inset presents a high-resolution TEM image of a single CdSe dot with an observable crystalline structure. From reference [38].*

In 1993, a major achievement was made by the Bawendi group at the Massachusetts Institute of Technology with the introduction of monodisperse syntheses of colloidal NCs through the *hot injection method* [37]. They demonstrated the growth of high-quality CdE (E = Se, Te, and S) semiconductor NCs. Cadmium and chalcogenide precursors were rapidly injected into hot, near 300ºC TOP/TOPO solvent under an inert atmosphere, resulting in a nucleation burst. The subsequent growth of the nanocrystallites can be controlled through the reaction temperature and duration, and the presence of *ligands*. This method allows obtaining size-selective NC solutions after precipitation steps. The monodispersity results in observable absorption features and narrow band-edge emission that are size-tunable. A typical chemical synthesis setup is shown in Figure 1.8a. Figure 1.8b-c show the size-dependent absorption and emission properties of CdSe NCs. High-quality NCs with a narrow size distribution of less than 5% in diameter can be routinely obtained through this synthetic route.

A variety of materials can now be obtained under the colloidal form. Some examples of the semiconductor cores and surface ligands are given in Figure 1.9. These surface ligands,

typically containing headgroups and functional tails, play a critical role in the material synthesis and the electronic properties of the NCs, as will be discussed in the following sections.

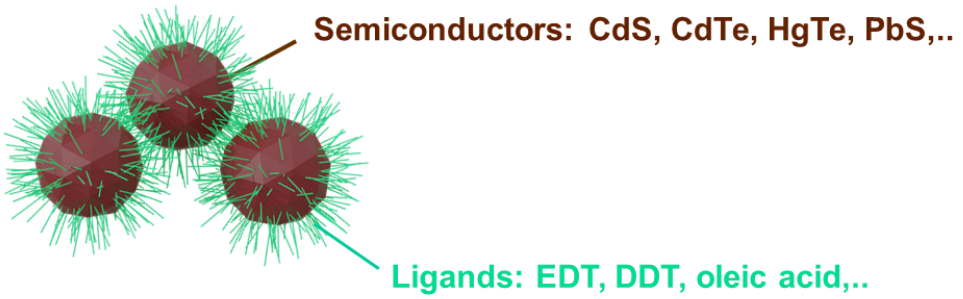

Figure 1.9: Colloidal nanocrystals. *Illustration that highlights the semiconducting cores and the surface ligands of colloidal nanocrystals.*

Some primary purposes for the use of different types of ligands are the followings:

- Surface ligands allow controlling the growth process during the NC synthesis, helping to regulate the size and shape of the synthesized NCs.
- The binding behavior of the functional tails governs the dispersibility in solution, preventing aggregation and ensuring colloidal stability.
- The headgroup determines the inorganic-organic interface, which is correlated to surface trap states in the NC energy gap. The surface ligands thus strongly impact the NCs' electronic and charge transport properties. As a result, carrier dynamic and radiative/nonradiative relaxation mechanisms can be engineered with the surface ligands.

Colloidal synthesis enables cost-effective, mass production of NCs compared to conventional epitaxial techniques, which generally demand expensive equipment. Nowadays, colloidal NCs have reached mass industrial-scale production, particularly for display applications. As the field becomes mature, other uses of NCs can be targeted. Among many possibilities, infrared photodetection is a field that can greatly benefit from all the advantages of colloidal materials. High-performing infrared photodetectors are currently based on epitaxially grown materials, which are not widely accessible for many applications due to the high manufacturing cost. Therefore, the quest to find alternative materials that enable *fast, sensitive, and affordable* infrared sensing is of utmost interest.

The next parts of this chapter will focus on HgTe NCs and their potential as a cost-effective platform for infrared sensing applications. We first present the fundamental aspects, such as the optical and transport properties of the materials, before reviewing the recent progress on the development of HgTe NC-based devices that have demonstrated a great potential for infrared sensing applications.

1.2.3. Colloidal HgTe nanocrystals

The synthesis of HgTe NCs was first demonstrated by Rogach *et al.* in the early 2000s [39] with the initial targeted application for optical amplification. Soon after, in the following years, initial attempts to develop photodetectors based on HgTe NCs were reported [40], [41]. The

original interest stems from the desire to extend the optical feature of NCs into the infrared range without being limited by the bulk energy gap. As bulk HgTe is a semimetal, the absorption of colloidal HgTe NCs can be tuned from 1.5 eV for the most confined colloidal form to virtually zero. This property is the first fundamental aspect to motivate the material development.

Electronic structure and optical properties

In conventional wide bandgap II-VI semiconductors, such as CdTe, a *normal band ordering* at Γ point will present a conduction band with Γ_6 symmetry above the valence bands with Γ_8 symmetry, as shown in Figure 1.10a. Strong spin-orbit coupling and significant Darwin term in HgTe cause a *reversed order* [42]. Essentially, the resulting band structure is flipped at the Γ point with Γ_8 states now above the Γ_6 one, see Figure 1.10b. Furthermore, the Fermi level in bulk HgTe lies between the two Γ_8 bands. HgTe thus presents a zero bandgap in the bulk form ($E_{bulk} = 0$). This lack of the bulk band gap has a profound impact on the optical properties of colloidal HgTe NCs.

Figure 1.10: *Bulk band structure of CdTe (a) and HgTe (b). The ordering of the conduction and valence bands near the band gap at the Γ point in HgTe is opposite to the one in CdTe. In HgTe, the hole state is above the electron state. From reference [43].*

Under the colloidal form, optical transitions in HgTe NCs (red arrow in Figure 1.10b) occur between the Γ_8 bands (denoted HH – heavy hole and LH – light hole). As a result of quantum confinement, colloidal HgTe NCs naturally possess narrow optical bandgaps, well-suited to address the infrared range. Indeed, colloidal materials based on HgTe have demonstrated optical features covering a wide spectral range from the NIR to the THz range [44], [45].

Synthesis of the materials

As mentioned, a water-based synthesis process to obtain HgTe NCs was first reported by Rogach *et al.* [39], [46], allowing for obtaining HgTe nanocrystals with tunable sizes from 3 to 6 nm. Later on, Kovalenko *et al.* [47] made an improvement with an additional Ostwald ripening step that extended size tunability to around 10 nm and PL signal to 3.7 µm. However, aqueous syntheses use H_2Te, which generally requires complex synthetic setups and careful handling.

In 2011, Keuleyan *et al.* [48] introduced a simple approach for synthesizing colloidal HgTe in organic solvents and demonstrated photoconduction up to 5 µm for the first time, see Figure 1.11. This synthesis results in larger particles up to 12 nm. Nevertheless, size dispersity remained a critical problem.

Figure 1.11: HgTe NCs obtained from Keuleyan's procedure. *a. TEM image of HgTe NCs having PL peak around 2500 cm^{-1}. The scale bar is 20 nm. b. Normalized absorbance spectra of HgTe NCs solutions. c. Photocurrent spectra of HgTe NC films with different NC sizes. From reference [48].*

The last decade observed several advancements in synthesis techniques, which led to improvements in the size and shape control of the nanocrystals [49]–[51]. Notable achievements include the demonstration of 2D HgTe structures (*i.e.*, so-called nanoplatelets) from cation exchange [44] and the development of core/shell heterostructures [52], [53]. These achievements enable, respectively, observation of narrow PL emission in the solution and enhanced thermal stability of NC films. In particular, highly monodisperse HgTe NCs with a size distribution of less than 10% can now be obtained [54], allowing the observation of narrow optical features [54], and facilitating better NC packing and improved carrier mobilities in solid films [55]. Thanks to the recent developments, optical properties now can be finely tuned through the synthesis process, and transport properties of the NC solids have been strongly improved. The latter is the second essential fundamental aspect to permit high-performing optoelectronic devices.

Transport properties

Besides the optical feature, a sufficiently good electrical conductivity is also a requirement for employing colloidal nanocrystals in optoelectronic applications, particularly for infrared photodetection. In solid films of NCs, the semiconductor cores serve as nanometer-scale building blocks to construct the solid form. The size, shape, and composition of the NCs govern the film packing, and thus, NC separation distances, which dictate the intercoupling of the semiconductor cores. Furthermore, due to the synthesis procedure, the transport properties of NC arrays are directly related to the NC's surface chemistry (*i.e.*, surface ligands). Early-developed HgTe NCs are limited in carrier mobilities, hindering many possibilities for practical devices. Therefore, it is important to discuss this fundamental aspect

and review the experimental approaches to overcome the limited transport from a material's point of view.

Hopping transport

Solid nanocrystal films are formed by depositing NC solution on a flat surface. In an ideal picture, the NCs are monodisperse (*i.e.*, the same size, shape, and composition) and have the same surrounding environment (*i.e.*, the same distribution of ligands). However, NCs are synthesized with size deviation. As mentioned, the best synthetic methods could provide samples with size dispersion varying from 5 to 10%. In addition, defects are usually formed on the NC surfaces, and ligands are thus not uniformly distributed. The deposition processes (*i.e.*, spin-coating, drop-casting) to transform NC solution into NC films can also cause pinholes and microbubbles, which act as energy barriers for the charge carriers. These non-idealities lead to an inhomogeneous energy landscape in the NC films where electron and hole states between semiconductor cores are weakly coupled. In order to reach the electrodes, these carriers need to travel across the NC film by hopping steps from one NC to the others, as illustrated in Figure 1.12a. This is referred to as *hopping transport*.

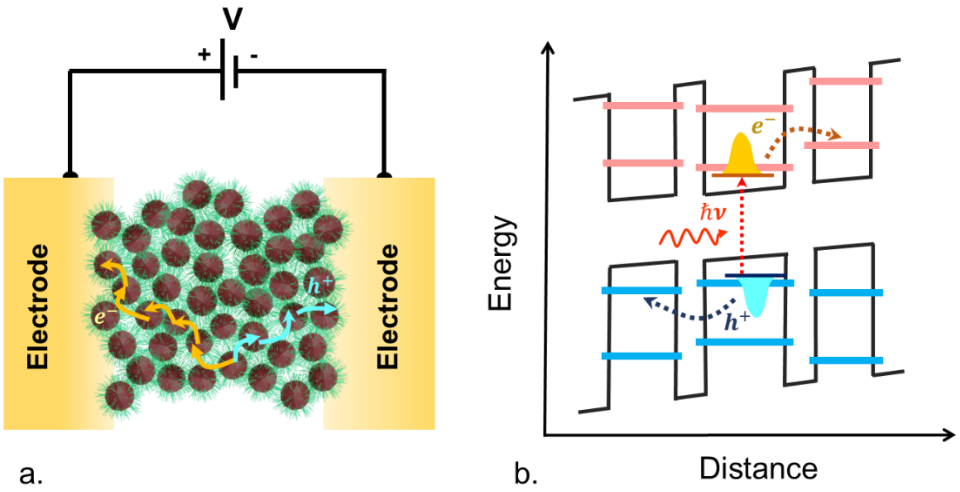

Figure 1.12: Hopping transport in a nanocrystal film. *a. Schematic of hopping transport in a nanocrystal film. The film is deposited on two electrodes that are biased with voltage V. The carriers transfer towards the electrodes by hopping. b. The schematized energy landscape in the film shows the localized wavefunctions of electrons and holes in the nanocrystal film.*

Hopping transport occurring between localized states, described in Figure 1.12b, is responsible for the low mobilities of the charge carriers in NC arrays. In this regime, hopping can only be supported by thermal activation energy or quantum tunneling through the barriers. The hopping mobility, which can be derived from the tunneling coefficient and Einstein's equation [56], is expressed by

$$\mu_{hop} = \frac{ea^2 E_a}{3hk_B T} exp\left(-\chi l - \frac{E_a}{k_B T}\right) \quad (1.30)$$

where e is the elementary charge unit, a is the center-to-center distance between NCs, E_a is the activation energy for carrier transport, χ is the extension of the carrier wavefunction in the barriers (typically 1 $Å^{-1}$), l is the barrier width, and h and k_B are Planck and Boltzmann

constants, respectively. It is noted that lateral field dependence can arise in the hopping transport mechanism as the applied electrostatic field lowers the transport barriers between localized states, as will be discussed further in Chapter 3.

Improving charge mobility in NC films is essential to enhance the performance of NC-based optoelectronic devices. However, it is equally important to preserve the quantum-confined electronic states within these films. Engineering interparticle coupling without disturbing optical transitions thus becomes crucial in NC processing. The following section focuses on ligand exchange as a very effective strategy to achieve this objective.

Ligand exchange

As it can be seen from equation (1.30), the transport properties of charge carriers in NC films strongly depend on the barrier width. In a solid NC film, these barriers mainly constitute the surface ligands. In particular, long organic ligands are typically used in synthesis to quench the growing process and maintain the NC solution's colloidal stability. The as-synthesized NCs thus normally form NC films with poor transport properties. With the necessity of high-mobility NC films for optoelectronic devices, surface chemistry engineering by *ligand exchange* processes has been one of the most investigated research topics in the NC field.

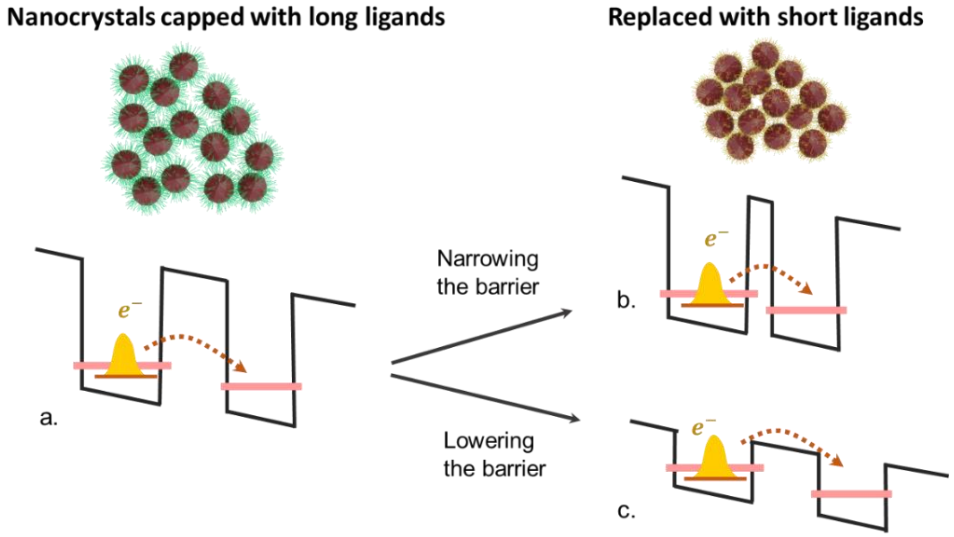

Figure 1.13: Effect of ligand exchange on interparticle coupling. *a. Schematic of nanocrystal arrays capped with long ligands (top) and the associated illustration of energy landscape (bottom). b. Illustration of energy landscape when shorter ligands replace the initial long ones. c. Illustration of the energy landscape when new ligands can lower energy barriers.*

The idea behind ligand exchange is described in Figure 1.13. Better coupling between the NCs inside a solid film can be achieved by replacing the long organic ligands with shorter ones. The new ligands offer narrower or lower tunnel channels, thus improving carrier transport. An efficient ligand exchange process typically leads to both reduced barrier height and shortened barrier length while maintaining efficient surface passivation. This technique can be conducted in two different manners: in the *solid-state phase* and the *liquid phase*.

Solid-state ligand exchange is typically conducted by exposing thin slabs of NCs capped with long ligands into a diluted solution of short ligands. The concentration of the short ligands must

be optimized: a low concentration could lead to inefficient ligand exchange processes, and concentrated short-ligand solutions could peel off the NC film from the substrate. As the long ligands are replaced with the short ones, the volume of the NC film tends to reduce, which causes the formation of cracks and voids inside the film, see illustration in Figure 1.14b. Repeating the deposition and exchange process several times could thus help "heal" the induced cracks while ensuring an efficient ligand replacement.

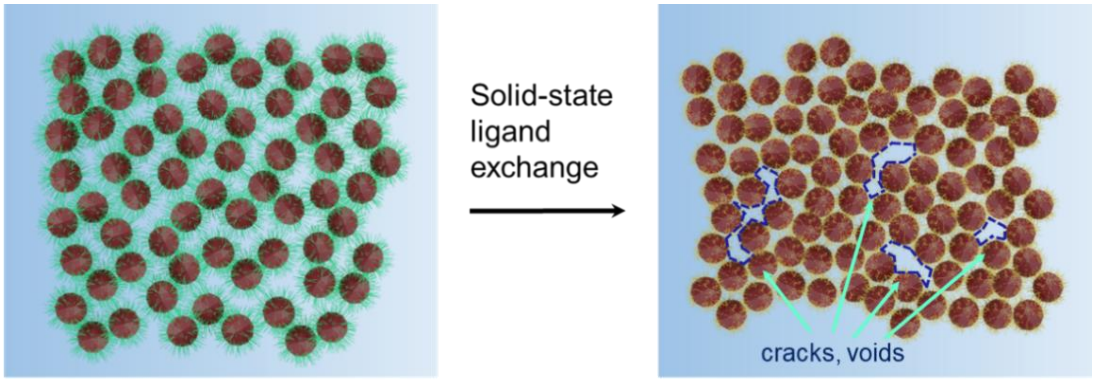

Figure 1.14: Solid-state ligand exchange is conducted with solid films of NCs. *Long ligands capping NCs (left schematic) are replaced by shorter ones (right schematic), allowing better coupling between NCs. The distances between the NCs are reduced. However, since the process is conducted with solid NC films, cracks and voids (highlighted by the dark dashed boundaries) can be formed during the exchange process due to volume contraction. Multilayer deposition is typically performed to achieve smooth NC films.*

The ligand exchange process for HgTe NCs was introduced to replace the sintering technique, the common approach to improve transport properties in the early days [57]–[59]. The solid-state ligand exchange step is typically performed with ethanedithiol (EDT) treatment to replace the initial long DDT ligands of the HgTe NCs [60]. The procedure has been inspired by previously developed ligand exchange techniques for more mature materials, such as CdSe [61], PbS [62], and PbSe [63]. Typically, the NC films are immersed in a solution of EDT in ethanol (typically 1% in mass). Multiple NC deposition and ligand exchange steps can be performed to obtain smooth, thick films up to 300 nm. However, building thicker films is generally challenging as it could lead to flaking and, consequently, delamination.

Another ligand exchange technique recently developed for NCs is *liquid phase ligand exchange* [64]–[68]. The original motivation for this technique is to overcome the problem of crack and void formations in solid-state ligand exchange since, in this case, the film could be achieved after one-step deposition. As described in Figure 1.15a, the ligand exchange is conducted when the NCs capped with long ligands in a nonpolar solvent are blended with a polar solvent containing short ionic ligands. After the exchange, the NCs become soluble and migrate to the polar phase. The nonpolar solvent can be discarded, and we obtain a concentrated NC ink for conductive film deposition. This technique allows thick films (*i.e.*, thicker than 500 nm) of NCs to be achieved.

The initial development of liquid phase ligand exchange was introduced by the Talapin group, who first demonstrated the exchange of long organic capping ligands for metal chalcogenide ligands [64] on several colloidal materials in 2009. Following this study, the same group developed the exchange process for metal-free inorganic ions, such as S^{2-}, HS^{-}, Se^{2-}, HSe^{-},

OH^-, and NH_2^- [65]. Subsequent works from the Sargent group, focusing on PbS films prepared with liquid phase ligand exchange, have shown clear improvements in the performances of photovoltaic devices [66], [68].

Figure 1.15: Liquid phase ligand exchange. *a. Long ligands capping NCs are replaced by shorter ones in the liquid phase. The NCs capped with long ligands in a nonpolar solvent are mixed with a polar solvent containing short ionic ligands. b. Infrared absorption spectra of as-synthesized HgTe NCs and the NC ink obtained from ligand exchange process. The NCs have a cut-off wavelength of around 2.5 µm. The initial solvent is toluene. Ligand exchange reduces the C-H absorption and gives rise to the O-H bond from the short ligands (MPOH). From reference [69].*

Motivated by these results, the ligand exchange processes in the liquid phase for HgTe NCs [55], [69] were introduced. Specifically, the DDT capped-NCs in toluene are blended with a mixture of MPOH and $HgCl_2$ in DMF (*i.e.*, the polar solvent). Phase exchange occurs when a few drops of hexane (*i.e.*, the nonpolar solvent) are added to the solution. At the end of the process, the NCs migrate to the polar phase, and DDT ligands are replaced with short ionic ones. The NCs are dispersed in DMF to form an ink solution, which can be directly used to deposit conductive solid films. In general, the absorption spectrum of HgTe NCs is mildly affected by the ligand exchange process. Notable changes in the ink absorption compared with the original NC solution are a broadening of the NC band edge and the suppression of the C-H band around 2900 cm^{-1} due to the removal of the long ligands, see Figure 1.15b. Interestingly, it has been shown that films prepared with liquid phase ligand exchange are more stable under air conditions, which is beneficial for device stability [55], [69].

The development of ligand exchange has enabled significant improvement in carrier mobilities of HgTe NC solids. With *solid-state ligand exchange*, mobilities in HgTe films are typically in the order of 10^{-3} – 10^{-1} $cm^2\,V^{-1}\,s^{-1}$. With *liquid phase ligand exchange*, record value of carrier mobility up to 18 $cm^2\,V^{-1}\,s^{-1}$ has been reported [70]. These advancements on the transport properties of the material are promising to push forward the device's performance.

Effect of ligand exchange on carrier density

It should be noted that NC surface chemistry impacts not only interparticle coupling but also the electronic states of the NCs. Surface ligands are associated with electric dipoles, which result in surface gating. This effect induces band bending, which is given by

$$\Delta E = -N\frac{\mu_D}{\varepsilon_0 \varepsilon} \tag{1.31}$$

where μ_D is the dipole moment, N is the surface density of the dipoles, and ε is the relative permittivity of the ligands. Note that ΔE is independent on the NC's bandgap. Thus, the gating

effect leads to a shift of the Fermi level with respect to the valence and conduction band, which can be significant for narrow-bandgap materials. Brown et al. investigated the effect of different ligand treatments on PbS NCs using ultraviolet photoelectron spectroscopy [71]. While the NCs possess an optical bandgap of 1.23 eV that remains relatively unchanged, the authors observed a maximum shift up of 0.9 eV of the valence band (and corresponding conduction band) upon different ligand treatments.

Figure 1.16: Impact of various ligands on electronic states in SWIR HgTe NCs. *Relative energies of the ground states of valence and conduction band, and Fermi energy in HgTe NCs with 1.7 µm cut-off wavelength with different capping ligands. From reference [72].*

Chu *et al.* investigated a ranges of ligands compatible with transport in SWIR HgTe NCs [72]. They showed that the ligand-induced shift can be sufficiently strong to alter the majority carriers, as depicted in Figure 1.16. Controlling carrier density is desirable for designing p-n junctions in optoelectronic devices, such as photodiode sensors and light-emitting diodes (LEDs). In this context, ligand engineering is attractive as doping can be introduced through a simple ligand exchange step.

Field-effect transistors

As soon as conductive NC films are obtained, experimental methods are required to probe the transport properties of the charge carriers in NC films. In solid-state physics, the two most commonly used techniques for transport measurements are Hall effect and field-effect transistors (FET). The former is generally complicated for low-mobility materials due to low signal and sign-change of the Hall coefficient [73]. As a result, FET is the most popular platform for investigating carrier transport of NC arrays.

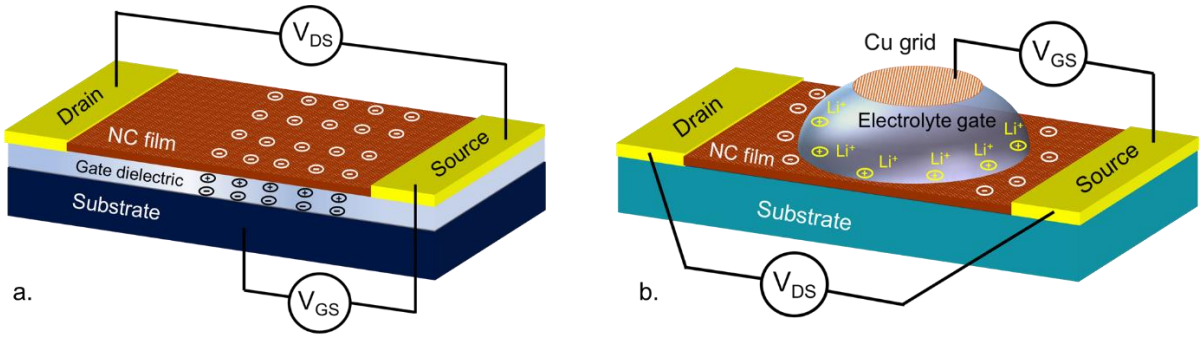

Figure 1.17: Field-effect transistor with NC film. *a. Field-effect transistor with back-gate configuration. Under applied gate bias, electrons are injected into the NC film to screen the positive charges in the gate dielectric. This injection leads to a shift in the Fermi level in the NCs. b. Field-effect transistor with an electrolyte top-gate. Under applied gate bias, Li^+ ions percolate within the NC array, resulting in electron injection in the NC film to screen the positive charges.*

In the FET, three terminals are drain, source, and gate electrodes. Bias voltages can be applied through drain-source (V_{DS}) channel and the dielectric gate (V_{GS}). Figure 1.17a describes a FET with a typical back-gate configuration, in which the drain-source channel is made of the material of interest (*i.e.*, a nanocrystal film in our case). The gate is a dielectric material (typically insulating oxides, such as SiO_2 or Al_2O_3), and the gate bias is used to modulate the material conductivity. Tuning V_{GS} electrostatically shifts the Fermi level and allows modulation of carrier concentration in the NC film.

When the applied gate bias is positive ($V_{GS} > 0$), positive charges accumulate in the gate dielectric close to the interface between the gate and the NCs. Electrons are thus injected into the NC film to screen the charge accumulation, see Figure 1.17a. Under a constant V_{DS}, the drain-source current I_{DS} is dependent on V_{GS} and called the FET *transfer curve*. The evolution of I_{DS} provides information on carrier transport under electron injection. If I_{DS} increases as V_{GS} increases, electrons are the majority carriers, and the material is an *n-type* semiconductor. Similarly, transport properties can be probed under hole injection with negative applied gate bias ($V_{GS} < 0$). If holes are the majority carriers, the material is *p-type*. The NC film is called *ambipolar* if the majority carriers change upon carrier injection.

A typical FET transfer curve measured on an ambipolar HgTe NC film is presented in Figure 1.18. The red curve is drain-source current I_{DS} through the NC channel, while the blue curve represents I_{GS}, the leakage current through the gate layer. It is necessary that I_{GS} stays well below I_{DS} in a reliable measurement. Here, the film conduction increases with the increasing magnitude of gate bias voltages in both positive and negative directions, implying the ambipolar nature of the material.

When V_{DS} is small compared to V_{GS}, carrier concentration can be assumed to be uniform in the drain-source channel. One can derive the relation between the drain-source current I_{DS} and the gate bias V_{GS}, which allows calculating carrier mobilities in NC films from the measured *transfer curves* [74]. The carrier mobilities are given by

$$\mu = \frac{L}{W.C_i.V_{DS}} \times \frac{\partial I_{DS}}{\partial V_{GS}} \tag{1.32}$$

where L is the channel length, W is the channel width, C_i is the gate insulator capacitance per unit area, and I_{DS} is the drain-source current.

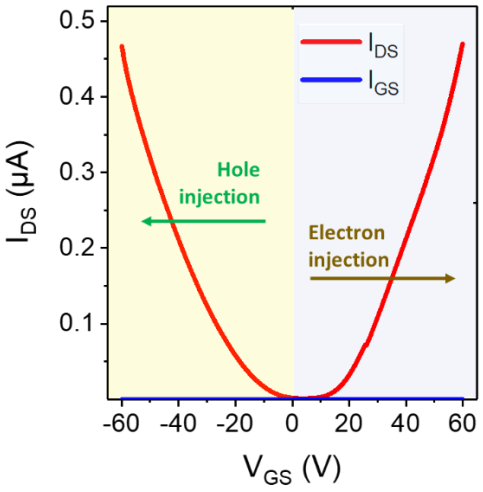

Figure 1.18: Transfer curve measured with a NC-based field-effect transistor. *FET transfer curve at 150 K of a HgTe NC film on Si/SiO_2 substrate. The NCs present a cut-off wavelength of around 2.5 µm. The film conduction increases for both positive and negative gate bias voltages, showing the ambipolar nature of the material.*

In practice, the carrier concentration modulation in back-gated FETs only occurs in a thin layer (around 50 to 100 nm) close to the gate/semiconductor interface, which might contain defects that affect carrier mobility. For example, it is well known that SiO_2 dielectric could introduce trap states on the surface, lowering the effective electron mobility. Therefore, it is important to consider the influence of the gate material on the investigated semiconductor.

Apart from the oxide gate dielectrics, ion-gel electrolytes [75]–[77] are commonly used as gate media in NC-based FET. In this case, the FETs operate with a top-gate configuration, as sketched in Figure 1.17b. For instance, $LiClO_4$ electrolyte can be employed as the gate material [76], [77]. A copper grid is usually placed on top of the electrolyte to induce a homogeneous electrostatic field inside the gate medium. Under applied bias, the Li^+ ions percolate within the NC array, resulting in electron injection in the NC film to screen the positive charges. Since this electrolyte gate typically has a large capacitance (around 1 µF.cm^{-2}) compared to the traditional SiO_2 dielectric (around 10 nF.cm^{-2}), strong modulation of carrier concentration with electrolyte gate can be obtained by applying relatively low gate voltages. However, electrolytes also face some limitations in terms of operating temperature, sweeping rate, and not well-defined gate capacitances. While the last problem could be overcome by adding a reference electrode, the other drawbacks inherently originate from the ionic nature of the gate material. The gating effect in electrolyte-based FETs is based on ion displacement, which is intrinsically slow and thus limits the gate bias sweep rate. Furthermore, it is necessary to operate the FETs above the electrolyte freezing point (above 200 K), which prohibits low-temperature measurements. In addition, the applied gate voltage is also limited by the electrochemical stability window of the electrolyte (typically less than 3 V). Despite these limitations, electrolyte-gated FET is commonly used as a first examination of NC transport properties due to its convenience and accessibility.

1.2.4. Emergence of nanocrystals for infrared photodetection

The broadly tunable optical features of colloidal HgTe NCs in the infrared have generated significant interest for potential applications in infrared sensing. In spite of this interest, only a limited number of photodetectors based on HgTe NCs were reported in the first 10 years following the introduction of colloidal HgTe [40], [41]. On the contrary, the last decade witnessed tremendous progress in sensing devices based on HgTe NCs, which can be attributed to the increased maturity of the materials. The availability of higher quality materials has enabled the realization of more robust and sensitive sensors, as well as the development of complex device architectures with novel functionalities. The following section of this introductory chapter will focus on the device perspective and progress in developing infrared photodetectors based on HgTe NCs.

Photoconductive detectors

The first HgTe-based infrared sensors were photoconductive thanks to their simplicity [41], [42]. In these devices, the NC solution was drop-casted on silicon substrates with predefined electrodes to form solid NC films. The authors demonstrated detection in the SWIR (up to 2 µm) with organic-capped and closed-packed HgTe NCs prepared with the Rogach's procedure [39], see Figure 1.19a-b. However, the response was relatively slow. The responsivity and detectivity of these initial detectors were not reported. Seong *et al.* exploited the same material in the following work and developed the first vertical device structure with HgTe NC film sandwiched between ITO and gold electrodes [78]. The schematic and I-V characteristics of this detector are shown in Figure 1.19c.

Figure 1.19: Early developed-photoconductive-detectors based on colloidal HgTe NCs. *a. The first reported detecting device using organic-capped HgTe NCs. b. I-V characteristics of the device in part under dark and illumination conditions. From reference [41]. c. Schematic and I-V characteristics of the first HgTe NC-based detector with vertical structure. From reference [78]. d. Top view of the interdigitated contacts with ink-jet printed stripes of colloidal HgTe NCs. e. Normalized photocurrent spectra of the device in part d with two different sizes of NCs. HgTePD2:4nm and HgTePD3: 6 nm. From reference [79].*

Around 2007, Wolfgang Heiss' group, taking advantage of their progress in material synthesis [47], demonstrated photoconductive HgTe detectors operating up to 3 µm [79], see Figure 1.19e. In particular, the devices were prepared using ink-jet printed HgTe NC film, as presented in Figure 1.19d. This paper reported a high responsivity of 4.4 $A \cdot W^{-1}$ under low

illumination power. The device's detectivity was 3.2×10^{11} Jones at the detection peak of 1.4 μm for room temperature operation.

It is worth noting that although SWIR HgTe NC-based devices showed promising performance, there had been great competition to address this spectral range from colloidal lead chalcogenides [24], [25], [80], [81]. However, due to their bulk energy gaps, extending the photoresponse of lead-based compounds to MWIR is challenging since large-size particles are required, which unfortunately show with poor colloidal stability. The advantage of HgTe NCs thus explicitly appears above 2 μm. The organic-based synthesis developed by Keuleyan *et al.* [48] was, therefore, an important achievement. Colloidal HgTe NCs prepared by this method and detectors based on these NCs present spectral responses up to 5 μm, as previously shown in Figure 1.11. Many device advancements later on were based on NCs synthesized through this procedure.

Figure 1.20: Interdigitated electrodes and HgTe films prepared with novel methods. *a. Optical microscope image of gold interdigitated electrodes fabricated on a Si substrate. b. False-color SEM image of patterned HgTe film made with PMMA-assisted transfer. From reference [82]. c. Cross-sectional SEM image of original/imprinted HgTe NC film. The scale bar is 100 nm. From reference [83]. d. Optical microscope image of NC patterns prepared with direct optical lithography. The scale bars are 100 μm. From reference [84].*

Since photoconductive devices comprise a solid film of NCs and electrodes, improving the devices' performance is directly related to optimizing the film preparation process and electrode patterning. Interdigitated electrodes, shown in Figure 1.20a, are the most commonly used geometry for NC-based photoconductive detectors. The pattern consists of an array of metallic stripes that act as current amplifiers for lateral carrier transport. Films can be deposited on top of the pre-patterned substrate using popular deposition techniques, such as drop casting [60], [85], spin coating [86], and spray coating [87]–[89]. In this direction, shrinking the electrode spacing to introduce gain and optical resonances for NC-based photoconductive devices has been proven an effective approach to enhance detection performance [90]–[92].

Regarding film preparation, other methods apart from the mentioned standard techniques have also been explored for HgTe NC film, including PMMA-assisted transfer [82], imprinting [83], and direct NC lithography [84]. Generally, they offer additional spatial control and complexity for the NC structures, see Figure 1.20b-d. However, these methods demand

specific preparation (*i.e.*, suitable material and substrate for the transfer and imprinting, ligand engineering for UV-sensitization) as well as a careful post-processing film quality evaluation.

Compared with the early devices, photoconductive detectors based on HgTe NCs now display a great level of maturity. Detectivities around 10^{11} Jones at room temperature can be consistently obtained for devices working in the wavelength range from 1.5 to 2.5 µm. Similar performances can be achieved with MWIR photoconductive detectors at cryogenic temperatures (around 80 K). Furthermore, fast photoresponse can be obtained with HgTe-based photoconductors. For MWIR sensors, a response time as short as 20 ns has been reported [93].

Photodiodes

Photodiodes offer the benefit of reduced current noise through photovoltaic operation when compared to photoconductive detectors. Multilayer deposition is required to construct diode stacks, and band alignment between different layers is the key to charge extraction.

Figure 1.21: HgTe NC-based photodiodes of first generations. *a. Schematic illustration of the solar cell-like device structure using NIR HgTe NC absorber. b. Band energy diagram for the device in part a. c. Absorption spectrum and TEM image (in the inset) of the NCs. From reference [94]. d. Schematic of the first MWIR diode. e. Photocurrent spectra of some diodes in part d. f. Current-voltage characteristic of a MWIR diode. The black curve is the dark I-V with the thermal shield closed. The blue curve is measured with the shield open, implying the detector reaches BLIP regime. The red curve is measured under blackbody illumination. From reference [95].*

Initial attempts on HgTe NC-based photodiodes [94], [96], [97] were inspired by dye-sensitized solar cells [98]. In these devices, the NC layers play the role of NIR absorbers, see Figure 1.21a-c. Carrier transport is facilitated by blending the NCs with hole-conducting polymers and electron conductors. However, this strategy presents limitations when extending to longer wavelengths due to the strong organic absorption.In order to solve this problem, Jagtap *et al.* proposed to replace the polymers with a layer of inorganic MoO_3, and thus were able to demonstrate SWIR photoresponse with NC-based diodes [86]. Nevertheless, their device based on FTO/TiO_2/HgTe/MoO_3/Au presents a limited responsivity, around a few $mA \cdot W^{-1}$. This

low signal was later attributed to the presence of the TiO_2 layer, which filters out not only dark current but also photocurrent due to large band alignment mismatch.

Figure 1.22: Recent advancements in MWIR and SWIR photodiodes. *a. Schematic of the first MWIR diode based on HgTe/Ag_2Te stack. b. Thermal imaging capture with a MWIR diode with structure in part a. From reference [99]. c. Schematic of SWIR with CdSe electron transport layer. d. SEM cross-sectional image of the stack. d. Detectivity as a function of temperature for the diode in parts c and d. From reference [100].*

The first MWIR NC-based photodiodes were introduced by Phillippe Guyot-Sionnest's group in 2015 [95]. The diode stack was formed by connecting MWIR HgTe NCs with NiCr and Ag contact, see Figure 1.21d. Interestingly, the silver contact was made by depositing silver paint on top of the NC film. Although having a simple structure, the device presents very good detection performance when cooled down. MWIR response was obtained, as shown in Figure 1.21e, and the authors reported background-limited operation at 90 K, achieved for the first time with a NC-based photodetector, see Figure 1.21f. Despite being a big success, using silver paint is suboptimal. In terms of fabrication, defining the device area with silver paint is complicated. Furthermore, the deposition process could easily lead to electrical shorts between the top and bottom electrodes if the wettability is not well-controlled. In fact, the use of silver was intended to introduce a hole-extracting Ag_2Te layer at the Ag/HgTe interface through the diffusion of Ag ions. However, the formation of this layer is hard to regulate using silver paint.

In order to resolve above problems, the same group developed new diode stacks in which Ag_2Te NCs are directly deposited on top of HgTe films [99]. This step leads to a cation exchange process to form a layer of p-doped HgTe/Ag_2Te. At the same time, electron extraction was promoted using a bottom ITO electrode. Figure 1.22a presents the schematic illustration of this structure. Up to now, MWIR photodiodes based on this strategy present the highest detection performances, with responsivity reaching 400 $mA \cdot W^{-1}$ and detectivity above 10^{11} Jones at cryogenic temperatures. 1/f noise typically observed in photoconductive devices

can be fully suppressed in photovoltaic operation. The high sensitivity also enables thermal imaging with this device, as shown in Figure 1.22b. In addition to its success in the MWIR, this strategy was also applied to the SWIR. Similar to their MWIR counterparts, SWIR diodes using Ag_2Te also showed highly competitive performance as a detectivity of 10^{11} Jones at 2.6 µm was reported for a diode working at room temperature [101], comparable to commercial InGaAs technologies.

In parallel with the development of the hole transport layer, much effort was put into improving electron extraction. Notable results include the use of Bi_2Se_3 [102], [103], SnO_2 [104], CdSe [100], and Bi_2S_3 [105]. Adding these layers is electrically beneficial as they help to suppress interfacial loss. By doing so, internal quantum efficiency of more than 90% with a SWIR photodiode has been reported with CdSe [100], while the detectivity of this detector at 200 K reached 9×10^{11} Jones, see Figure 1.22c-e. With Bi_2S_3 [105], a detectivity of beyond 10^{11} Jones at room temperature was recorded.

At the moment, photodiodes are the best devices in terms of photodetection performance. However, the development of the materials also enables many other device concepts to be explored. In the next section, we explore phototransistors, which is the combination of a photoconductive detector and a field-effect transistor.

Phototransistors

The motivation behind the development of phototransistors is the ability to preset the device to a desired electronic state optimal for photodetection. Controlling the doping level of as-synthesis NCs is challenging, particularly for narrow-band gap materials. In phototransistors, the favorable state for detection can be obtained with a gate bias that balances the initial doping of the NC film. The device's dark current can be minimized by setting the Fermi level to the middle of the NC bandgap.

Thermally grown SiO_2 is the most common gate material. Using this strategy, Chen *et al.* demonstrated the use of a HgTe-based phototransistor for CO detection [88]. In their experiment, the presence of the gas is detected through the response of the phototransistor to a laser source, see Figure 1.23a. In addition, it was shown in the same article that, although the dark current can be reduced by tuning the gate bias, the photocurrent also presents a similar behaviour, as shown in Figure 1.23b. The same correlation has been observed in other HgTe NC-based phototransistors [106]–[109]. However, the photocurrent typically exhibits a ‘slower’ decrease compared to the dark current. It is thus beneficial to exploit the offset between the two currents to increase the device’s sensitivity. Indeed, an increase in signal-to-noise ratio up to 2 orders of magnitude has been reported by tuning the gate bias to optimize the operation condition [106], [107].

Beyond the conventional SiO_2, there is currently interest in exploring other gating strategies. Gréboval *el al*. investigated LaF_3, an ionic glass that presents strong transparency in the infrared. The authors showed that using a LaF_3 gate for NC-based phototransistors reduces the required applied bias compared to SiO_2 while offering a faster sweep rate than an electrolyte gate [106].

Figure 1.23: Phototransistor based on HgTe NCs. *a. Room-temperature photoresponse of a HgTe NC-based phototransistor during CO gas sensing measurement. On the right is the setup for gas sensing. b. Photocurrent and dark current of the transistor in part a as functions of the applied gate voltage. From reference [88] c. Schematic of the phototransistor based on ion glass and graphene electrodes. A planar p-n junction can be generated by applying a drain-source bias comparable to the gate bias. From reference [107]. d. Schematic of a ferroelectric-gated phototransistor. e. Current-voltage characteristics of the phototransistor in part d. From reference [110].*

Another interesting gating approach is the generation of planar p-n junction in a single NC film. The first demonstration was reported by Noumbé *et al*. In this article, the authors showed that instead of uniform doping, a p-n junction can be generated when a large drain-source bias is applied between the non-conventional graphene electrodes in their transistors [107], see the illustration in Figure 1.23c. Recently, further improvement in this direction has been made with the use of dual gate [111] and ferroelectric materials [110]. The latter approach is particularly promising as these materials induce gate effect in NCs with their inherent polarization. Therefore, a p-n junction can be formed without continuous bias application. As a result, noise can be strongly reduced for this type of phototransistor.

Investigating phototransistors is essential not only practically but also fundamentally. Information about transport, doping, and their influence on the photoresponse of the material can be revealed by using one single device structure. With the maturity of HgTe NCs, more research could be expected in this fascinating direction.

Beyond single-pixel devices

Infrared technologies are traditionally connected to applications in night vision and thermal imaging. For these applications, the integration of infrared materials into FPAs is presently the best strategy. The array consists of single-pixel elements scanned electrically by circuits integrated with the array, as illustrated in Figure 1.24a. These readout integrated circuits (ROICs) are responsible for reading the detector array and transferring the signal to output taps for imaging.

Figure 1.24: Focal plane arrays for infrared imaging. *a. Process for hybridization of infrared FPA for conventional materials. From reference [2]. b. Illustration for the direct deposition of NC solution of a ROIC. From reference [22]. c. The first multipixel device for SWIR imaging. d. A laser diode beam profile recorded with the array in part c. From reference [69] e. A laser diode beam profile recorded with VGA FPA. From reference [72] f. Passive imaging with FPA functionalized with HgTe NCs. From reference [112].*

The hybridization step is typically performed with flip-chip bonding for conventional infrared semiconductors, such as HgCdTe, InGaAs, and InSb. This technique requires indium bumps deposited either on the ROIC or both on the ROIC and the detector array. The array and the ROIC are then brought into alignment and welded together. However, as the pixel pitch gets smaller (*i.e.*, typically 10-15 µm for MWIR), the alignment process can become challenging, which limits the fabrication yield.

The main advantage of colloidal NCs for FPA integration is solution-processability. They can be directly deposited on the ROICs, as described in Figure 1.24b, which substantially eases the fabrication process and opens up possibilities for smaller pixel design. The first demonstration of NC-functionalized ROIC was reported in 2016 [113], [114]. The device, responsive to the MWIR, exploited active material of HgTe NCs processed with solid-state ligand exchange. For MWIR, thermal imaging is the main target application. NETD, which is the main figure of merit for thermal cameras, was reported to be below 100mK for this first HgTe NC-based FPA.

For SWIR, the first multipixel devices [69] were made with a matrix of detectors directly fabricated on top of a glass substrate, see Figure 1.24c. These detectors were used as infrared

beam profilers, as shown in Figure 1.24d. The improvements in SWIR imaging were later reported by Chu *et al*. and Gréboval *et al.* [112], who employed VGA format ROICs coated with SWIR HgTe films. Figure 1.24e-f, respectively, present an infrared laser beam profile and the first passive imaging of an outside scene taken with these VGA imagers. In order to further enhance the image quality, improving the material quality and deposition process are required.

Element under copyright, unauthorized distribution

Figure 1.25: Recent progress on the development of HgTe NC-based imagers. *a. Schematic illustration of the flat ROIC compatible with NC deposition. On the right, the ROIC is plugged into the camera for imaging. b. SWIR image of a chopper wheel at 170 Hz taken with the ROIC in parts a. From reference [115]. c. Illustration of the working process of trapping-mode photodetectors. d. Comparison of SWIR images of a soldering iron taken with imagers in photoconductive and trapping mode. From reference [116]. e. The configuration of visible pixel and SWIR pixel that are functionalized with perovskite NCs and HgTe NCs. From reference [84].*

Recent results from the collaboration between our group at INSP and New Imaging Technologies include using specially designed flat ROICs, which are more compatible with NC deposition [115]. Figure 1.25a shows the illustration of the flat ROIC coated with a HgTe film. Particularly, this ROIC allows applying a bias voltage between two consecutive pixels, which induces a homogeneous electric field in the NC film. The recent progress in film preparation and the new ROIC configuration leads to a significant enhancement in the image quality compared to the earlier generation of NC-based imagers and an external quantum efficiency reaching 5% when the device is cooled with a Peltier stage. Furthermore, this infrared camera is able to operate full frame with 200 fps and up to 340 fps for a reduced region of interest [115]. An example is given in Figure 1.25b, showing a SWIR image of a chopper wheel at 170 Hz.

Other notable progress in FPA integration involves the introduction of new device architecture for better imaging and multicolor operation [84], [116]. Instead of using a single NC layer, Zhang *et al.* proposed to add one doped HgTe layer on top of an intrinsic one, see Figure 1.25c. This additional layer aims to generate trapping mode, which increases carrier lifetime, and thus, leads to photoconductive gain. In the article, the authors show that the image quality could be strongly improved when operating the imager in trapping mode compared to a photoconductive one (Figure 1.25d). Another interesting concept introduced by the same group is multicolor NC-based imagers [84]. In order to conduct multispectral imaging, the authors employed CMOS-compatible imagers with broad spectral response from the ultraviolet and visible to the SWIR range. These imagers were then functionalized with perovskite NCs (*i.e.,* $CsPbX_3$ with X = Cl, Br, or I) and HgTe NCs for multicolor photodetection, as schematized in Figure 1.25e. Using these devices, images can be taken with different spectral ranges, including the UV, visible and SWIR infrared.

Finally, it is worth emphasizing that cost-effectiveness is an important motivation for the development of NC-based infrared sensors. It has been estimated that the current cost of a NC film on a ROIC is less than €20 with the potential for further reduction with large-scale syntheses [115], while the sensor cost is around €70. To this end, the cost of the active layer based on HgTe NCs becomes negligible compared to the overall camera cost (a SWIR objective costs around €500), which shows the potential and numerous opportunities for the technology's commercialization. However, there remains many problems to be addressed before HgTe NC-based detectors could reach commercial status.

Challenges and objectives of this work

One of the challenges is related to improving the external quantum efficiency of the infrared sensors, currently limited by the trade-off between the absorption depth (≥ 1 µm) and carrier diffusion length (≈ 100-200 nm) in solid HgTe NC films [117]. Besides the improvement on the material side, this issue can be addressed by exploiting light management strategies that enhance NCs-light interaction. Integrating photonic structures into optoelectronic devices has been demonstrated to be an effective approach for improving devices' performances [118]–[121]. Furthermore, light-matter coupling also introduces physical phenomena that could be utilized to generate novel functionalities.

This thesis focuses on the use of optical and plasmonic resonators in HgTe NC-based infrared photodetectors for two main objectives:

(i) Improving the detection performance of the infrared sensors through enhanced light absorption and charge collection with photonic structures.
(ii) Exploring advanced functionalities, particularly the active spectral response shaping of HgTe NC-based infrared sensors.

The experimental chapters will be organized as follows:

Chapter 2 provides an overview of the current status of photonic structures for HgTe NC-based infrared photodetectors. Subsequently, we introduce our optical structure for achieving broadband infrared photodetection.

Chapter 3 focuses on bias reconfigurability and presents our strategy to achieve this functionality in NC-based sensors. The field-dependent hopping transport mechanism will be exploited, in combination with optical resonances generated by our photonic designs.

Finally, in Chapter 4, we show our strategy to optimize the optical design of a photodiode structure. Compared to the commonly used design, the optimized structure significantly enhances NC absorption, leading to a state-of-the-art detection performance in the MWIR for a NC-based photodetector. In addition, by multiplexing an array of plasmonic resonators on the same substrate, we show that the multicolor bias-selectable photoresponse on a single diode stack can be obtained.

Chapter 2: Photonic structure for nanocrystal–based infrared photodetectors

Contents

Related article

- Dang, T. H., Abadie, C., Khalili, A., Gréboval, C., Zhang, H., Prado, Y., Xu, X. Z., Gacemi, D., Descamps-Mandine, A., Ithurria, S., Todorov, Y., Sirtori, C., Vasanelli, A., Lhuillier, E., Broadband Enhancement of Mid-Wave Infrared Absorption in a Multi-Resonant Nanocrystal-Based Device. Adv. Optical Mater. 2022, 10, 2200297.

Material synthesis and device fabrication in this chapter have been performed with the support of all the coauthors from the article. In particular, Yoann Prado (chemical research engineer - INSP) synthesized the HgTe nanocrystals. The imaging and EDX mapping were performed by Armel Descamps-Mandine (Centre de MicroCaractérisation Raimond Castaing, Toulouse). The 2.5 µm laser diode used in the response time measurement was provided by Alexei Baranov (IES laboratory, University of Montpellier).

Optical nanostructures enable the control and manipulation of light at sub-wavelength scales. Integrating these structures into photodetector designs has been demonstrated to improve device speed and sensitivity significantly. In the case of HgTe NC-based photodetectors, using optical resonators is particularly beneficial because of the NC limited carrier transport. In a HgTe NC array, hopping mechanism restricts carrier diffusion length to a few tens of nanometers, several times shorter than the material's absorption depth. This discrepancy leads to a trade-off between optical absorption and charge collection efficiency in NC-based photodetectors. In this chapter, we will present how this short-diffusion-length problem can be overcome using optical nanostructures. The first part of the chapter will introduce state-of-the-art photonic structures for infrared photodetection and fabrication constraints when applying those structures to nanocrystal arrays. The second part will present a plasmonic cavity based on a metal-dielectric-metal (MDM) structure, which generates multiple optical resonances to enhance light-matter interaction in a NC film. Understanding the nature of these resonances allows designing the spectral response of our photodetectors through the resonator's geometrical parameters. In the final part of the chapter, we combine a MWIR NC film with the MDM structure to demonstrate broadband infrared photodetection, which is a subject of great interest for many infrared applications, including sensing, communication, and infrared imaging.

2.1. Introduction

Integrating photonic structures with optoelectronic devices has become increasingly popular thanks to advancements in micro-nanofabrication [122]. Among various emerging applications, plasmon-enhanced photodetection is of particular interest [123]. As shown in the previous chapter, the basic element of a photodetector is a slab of semiconductor connected to electrical contacts. Conventional photodetectors are thus constrained in lateral dimension by diffraction limit and in thickness by the absorption depth of the active material. However, miniaturizing the photodetector dimension below these limits provides many benefits, including increased speed, lower noise, and less power consumption. The photodetector response time is generally set by the carrier transit time or its resistance-capacitance constant (RC constant). Reducing device dimension leads to a shorter transit time for carriers and lower effective device capacitance, which scales proportionally to the device's area. Plasmonic resonators allow confining light efficiently into deep-subwavelength volume, concentrating light in both lateral and vertical dimensions, thus also reducing the material need. The use of plasmonic resonators has been demonstrated not only as an efficient way to improve the performances of photodetectors [119], [124]–[126] but also to introduce new functionalities such as polarization [127], angle, and wavelength selectivity [128]. For HgTe NC-based photodetectors, employing photonic structures to improve detection performance is particularly interesting since the detectors can benefit from substantial optical and electrical gain. This section aims to clarify the last point.

2.1.1. Hopping transport *vs.* material absorption in HgTe nanocrystals

Photoconductivity relies on two main processes: light absorption and charge collection. Most of the incident light onto the active material can be absorbed when the material thickness is

comparable with the material's absorption depth. However, to convert light into an electrical signal, it is crucial that the generated carriers can reach the electrodes, given that charge collection can only be efficient in the range of the carrier diffusion length. In colloidal HgTe NCs, the absorption depth is typically in the order of a few microns, while carrier diffusion lengths are limited to ≈200 nm [117]. This discrepancy results in a large portion of photons not being absorbed by thin NC films (a 200 nm HgTe film absorbs approximately 12% of the incoming light at the exciton wavelength) while building thick, high-quality NC films (≥ 600 nm) can be technically challenging as well as inefficient for charge collection. On the material side, a constant effort has been made to improve carrier transport in colloidal HgTe NCs over recent years [50], [69]. Strengthening intercoupling between nanocrystals through ligand exchange has become a conventional treatment in NC processing for optoelectronic devices.

Another approach to overcome this diffusion length/ absorption depth trade-off is to improve light-matter coupling within the NC films. Plasmonic resonators can confine light within subwavelength layers filled with NCs, enhancing NC absorption. This strategy effectively reduces the absorption depth of the NC film, making it compatible with carrier transport. The spectral response of the NC device is also modified in the presence of optical resonators. Recently, this approach has become a subject of great interest for developing infrared photodetectors based on colloidal HgTe NCs. Before presenting our resonator design, we make a brief state-of-the-art of NC-based infrared photodetectors whose operation is improved by the use of photonic structures for light harvesting.

2.1.2. Photonic structure-enhanced NC-based infrared photodetectors

Several concepts of optical resonators have been explored for HgTe NC-based photodetectors. Ni Zhao and co-workers demonstrated the first example, in which they coupled the longitudinal surface plasmon resonance of gold nanorods with a HgTe absorbing film to obtain improved detectivity for a photodiode working in the NIR [129], see Figure 2.1a-b. In the following work, Yifat *et al.* [130] applied the concept of nano-antenna arrays for a photoconductive MWIR device to obtain a three-fold increase in responsivity for the polarization parallel to the antenna orientation. Tang *et al.* [131] combined plasmonic disks and an optical spacer to push further the performance of a diode stack working in the MWIR. The authors reported an EQE of 45% and a detectivity of 4×10^{11} Jones at 85 K, as presented in Figure 2.1c-d. Chu *et al.* [90] further optimized the use of optical resonators by designing a guided-mode resonator (GMR). In this GMR, the diffraction grating is also employed as electrical contact, significantly reducing the electrode spacing to obtain electrical gain, as shown in Figure 2.1f. The GMR device using SWIR HgTe NCs achieved photocurrent enhancement by three orders of magnitude compared to a reference structure without GMR, see Figure 2.1g. Furthermore, the GMR design offers post-synthesis tunability, enabling the device's spectral response to be designed beyond the synthesized material. As presented in Figure 2.1h, the detection peak of the GMR structure can be controlled by tuning the grating period.

Other photonic structures, such as Fabry-Perot cavity [99], [102], Bragg mirror [132], and metasurface [133] have also been demonstrated to be effective both in terms of absorption enhancement and spectral response shaping. Depending on the quality factor Q of the employed photonic cavity, the fabricated device can show intense, narrow absorption features with strong light confinement (high Q) or broad absorption features due to high losses (low Q).

A structure that obtains broadband absorption through the combination of several high-Q resonances is thus highly desirable. One way to obtain this goal is to use an array of high-Q optical cavities, each concentrating light at a different wavelength [132]. The number of absorption peaks is thus set by the number of constructed cavities. Nevertheless, this approach comes with the price of a laborious fabrication process, considering that having one additional targeted wavelength requires at least one extra fabrication step.

Figure 2.1: NCs coupled with photonic nanostructures for photodetection. *(a, b). Scheme of HgTe NCs/ZnO heterojunction photodiode with gold nanorods embedded within the ZnO layer and the increased detectivity of the structure compared to a reference sample without the nanorods [129]. (c, d). Scheme of a structure combining plasmonic nano-disks with an optical spacer and the increased detectivity of the structure thanks to absorption enhancement [131]. (f, h). Scheme of the GMR coupled to HgTe NCs and the increased responsivity of the detector thanks to the improvement of both optical and electrical properties by the GMR. h. Photocurrent spectra of the GMR photodetector with different grating periods, demonstrating tunability of the photocurrent peak with the grating period [90].*

Another way to obtain strong broadband absorption is to exploit multi-resonant photonic structures, which allow to generate several resonances in the same cavity. In the following section, we will explore the concept of the metal-dielectric-metal nanostructure, which presents remarkable broadband absorption by combining multiple resonances. As we target to apply the optical design for HgTe NC films, fabrication constraints for HgTe NC processing will first be considered. Subsequently, a NC-compatible metal-dielectric-metal (MDM) will be introduced.

2.2. Plasmonic cavities based on metal-dielectric-metal structure

A typical array of MDM cavities is shown in Figure 2.2a. A dielectric slab is embedded between two metallic layers, one is made as a grating to allow coupling light into the cavity. This coupling is controlled through geometrical parameters such as the grating stripe size *s*, the

grating period *p,* and the thickness of the dielectric layer *L*. This type of cavity has been exploited as an efficient means to confine and manipulate light in sub-wavelength dimensions, especially in the microwave [134], [135], MWIR [136] and THz range [137]. Here, we apply this concept for HgTe NCs in the SWIR and MWIR [138].

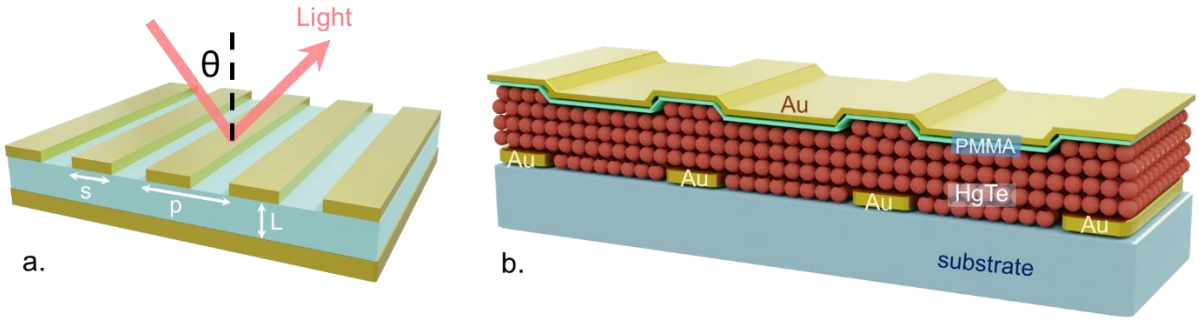

Figure 2.2: Metal-dielectric-metal cavities. *a. Scheme of conventional design for MDM structure. A dielectric layer is sandwiched between two metallic layers, one of which is a grating. Coupling of light into the structure is governed by the grating stripe width* ***s****, the grating period* ***p****, and the dielectric layer thickness* ***L****. b. Scheme of our MDM structure adapted to fabrication constraints of NCs. This design prevents lithography steps after NC deposition. A substrate is required to support the grating and the NC film. The structure is thus illuminated from the substrate side.*

Employing MDM structure for photodetection in this wavelength range is advantageous for various reasons:

- As shown in the following sections, MDM structure generates multiple resonances with sub-wavelength spatial extension in the dielectric layer, which strongly increases light-matter interaction in the dielectric material for enhanced absorption.
- The structure includes metallic layers, which can be utilized as electrodes for efficient photocarrier collection, similar to the case of the GMR structure.
- The possibility of spin-coating the NCs on a gold layer makes the realization of MDM resonators much easier than in the case of epitaxial III-V semiconductors, where wafer-bonding the active region on gold is needed.

However, electromagnetic design needs to take into account the lower refractive index of the NC film compared to III-V semiconductors, which leads to the leakage of optical modes into substrate materials. Fabricating plasmonic resonators usually requires performing optical and electron-beam lithography. These patterning steps are crucial yet require several treatments, including intense UV or e-beam exposure, resist baking (typically from 90 ºC up to 180 ºC), and resist development. These treatments can affect the surface chemistry of the NCs, leading to sintering when NCs are exposed to heat [139] or non-solvents, and modify critical properties of the material, such as carrier mobility, doping, and material bandgap. Therefore, fabrication constraints need to be carefully considered when designing NC-based devices. It is suggested that all lithography steps are conducted before NC deposition, and the fabrication procedure should contain minimal post-deposition processing.

A conventional MDM structure (Figure 2.2a) would require patterning of the grating on top of the dielectric layer. In order to avoid this step on the NC film, we propose a MDM structure

compatible with NCs. In our design, the grating is supported by a substrate. As a result, the layer of HgTe NCs can be deposited after the grating fabrication step, followed by a thin PMMA layer deposition. The structure is completed with a top gold layer. This structure can be illuminated from the substrate side, see Figure 2.2b. In addition to governing optical properties, the grating stripes are also used as interdigitated electrodes when the structure operates as a photoconductive detector. The PMMA is used to prevent possible electrical shorts between two neighboring electrodes through the top gold layer, hence, can be made much thinner than the NC layer. Considering the plane of incidence perpendicular to the stripes, the optical properties of the structure are strongly dependent on polarization parallel (TE or s-polarization) or perpendicular (TM or p-polarization) to the grating stripes. The MDM structure supports three different resonances: *cavity mode* and *surface plasmon* under TM polarization and *Fabry-Perot* under TE polarization. The following sections will present the nature of each resonance and how these resonances can be exploited to design a broadband NC-based photodetector.

2.2.1. Cavity mode resonance under TM polarization

The structure in Figure 2.2b enables electromagnetic confinement in the double-metal region, which behaves as a resonator, supporting cavity modes. In order to understand this confinement, let us first consider a MDM *waveguide* as sketched in Figure 2.3a for a wave propagating in the x-direction [140].

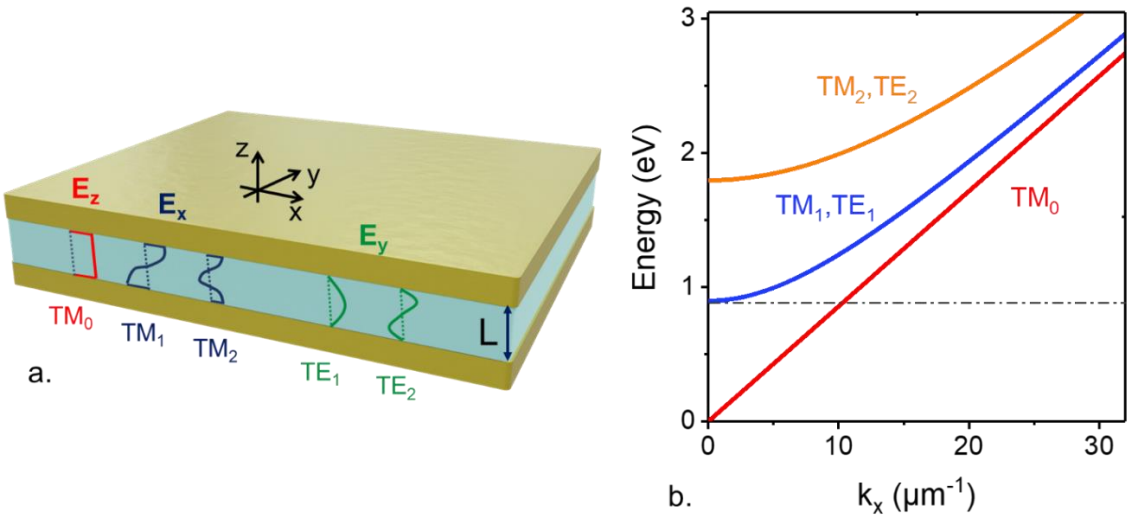

Figure 2.3: Metal-dielectric-metal waveguide. *a. The electric field distribution for the zeroth, first, and second-order TM_m and TE_m modes in a MDM waveguide. b. Calculated energy dispersion relation for the first TM and TE modes, considering a MDM waveguide with perfect metals and a dielectric layer of 300 nm HgTe NCs with a refractive index of 2.3. The dashed line indicates cut-off energy for the TM_1 and TE_1 modes.*

The waveguide supports electromagnetic confinement for both transverse-electric TE wave and transverse-magnetic TM wave. The electric field solutions have the forms

$$E_y \sim \cos(k_z z)\,.\,e^{ik_x x} \text{ for } TE_m \text{ modes}$$

$$E_x \sim \sin(k_z z)\,.\,e^{ik_x x} \text{ for } TM_m \text{ modes}$$

with $k_z = m\pi/L$ since EM waves are confined along the z-axis, and *m = 1,2, ...* The *transverse electric and magnetic* mode, also called TM_0, is another solution that also satisfies boundary conditions, with E_z being the only non-zero electric field component and constant along the z-axis. Figure 2.3a illustrates the electric field distribution of the first TE_m and TM_m modes.

The energy dispersion relations of the confined modes can be obtained by solving Helmholtz equation:

$$E = \frac{\hbar c}{n}\sqrt{k_x^2 + k_y^2 + k_z^2} \text{ with } k_y = 0 \text{ and } k_z = \frac{m\pi}{L} \tag{2.1}$$

where $\hbar$ is the reduced Planck's constant, c is the speed of light, and n is the refractive index of the dielectric material. Figure 2.3b presents the dispersion relations of the modes in a MDM waveguide whose dielectric layer is made of HgTe NCs with *n = 2.3* and *L = 300 nm.* The TM_m and TE_m modes have the same energies for *m ≥ 1* and present cut-off energy

$$E_{cut-off} = \frac{\hbar c m\pi}{nL} \tag{2.2}$$

The TM_0, however, does not show cut-off energy and it is the only mode that can be excited when the excitation energy is lower than the cut-off energy. In this case

$$E \leq E_{cut-off} \quad \text{for} \quad L \leq \frac{\lambda}{2n} \tag{2.3}$$

Because we are interested in light confinement in small volumes, we can choose a dielectric layer thickness satisfying equation (2.3) for the structure in Figure 2.2b. Hence, the double-metal region only supports TM_0 guided mode. In contrast to the double-metal region, the single-metal region supports continuum plane waves. The modal mismatch at the boundary of the two regions causes reflection of the TM_0. The superposition of two counter-propagating guided TM_0 modes leads to standing wave formation when

$$\lambda_K = \frac{2 \cdot n_{eff} \cdot s}{K} \tag{2.4}$$

where λ_K is the resonant wavelength, *K* = 1, 2, 3..., n_{eff} is the effective modal index, and *s* is the grating stripe width. The field map in Figure 2.4 illustrates the case of *K = 1* resonance.

Note that the effective modal index n_{eff} is different from the material refractive index *n* since the phase shift of the TM_0 mode due to the reflection at the boundary between the single and double-metal regions is not an exact multiple of π. The standing wave condition states that the field should recover its phase after a round trip in the double-metal region. Therefore, the value of n_{eff} is actually higher than *n*.

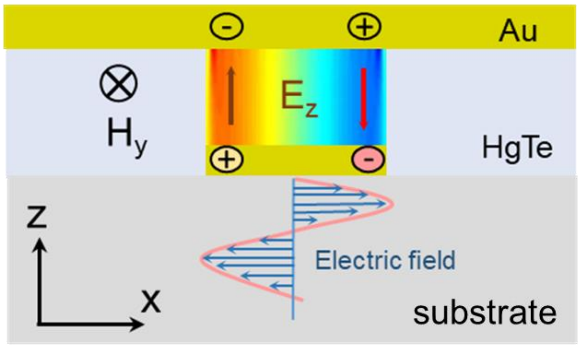

Figure 2.4: TM cavity mode in NC-adapted MDM structure. *Coupling free-space electromagnetic wave with the TM_0 guided mode in MDM cavity through the oscillation of electrons in the grating stripe. The standing wave of E_z electric field component is formed under the double-metal region at the resonant wavelengths $\lambda_K = 2.n_{eff}.s.K^{-1}$. Here, the field map for K = 1 is shown.*

An intuitive description of the coupling of electromagnetic waves from free space into the cavity is also described in Figure 2.4. The incoming wave induces the oscillation of electrons in the grating stripes, and couples to this TM_0 mode in the MDM cavity. At resonant frequencies, a standing wave pattern of the E_z component is formed in the x-direction. The enhanced field is thus mainly confined within the double-metal region. The MDM structure under this configuration produces a localized mode, which differs from delocalized ones with defined dispersion relations, such as guided-mode resonance and surface plasmon. Therefore, the cavity mode is dispersionless (*i.e.*, it possesses a good incident-angle tolerance) [136].

2.2.2. Surface plasmon resonance under TM polarization

The second resonance supported by the MDM structure is related to the surface plasmon polaritons (SPPs), which are the propagating electromagnetic waves bound to both sides of the interface between metal and dielectric materials. Conduction electrons govern the optical response in metals. Collective oscillations of these quasi-free electrons are called plasmons. The plasmons at the metal surface can interact strongly with an electromagnetic wave, resulting in SPPs. In our MDM structure, the interface between the top continuous gold layer and PMMA/HgTe facilitates the propagation of SPPs.

The existence of SPPs can be derived from Maxwell's equation, given the boundary conditions at the metal-dielectric interface. A solution can only be found for TM polarization. Therefore, SPPs do not exist for TE polarization [141]. We focus on the resulting properties of SPPs by considering the interface between a metal of relative permittivity ε_m and a medium with relative permittivity ε_d, as illustrated in Figure 2.5a. The SPP dispersion relation is given by

$$k_x^{SPP} = \frac{E}{\hbar c}\sqrt{\frac{\varepsilon_m \varepsilon_d}{\varepsilon_m + \varepsilon_d}} \tag{2.5}$$

where k_x^{SPP} is the in-plane wavevector of the SPP. Note that ε_m is complex, and the metallic properties imply negative values of $Re(\varepsilon_m)$ within the considered spectral range. Drude model describes metal relative permittivity as

$$\varepsilon_m(E) = 1 - \frac{E_p^2}{E^2 + iE\gamma} \quad \text{with} \quad E_p = \hbar\sqrt{\frac{Ne^2}{m\varepsilon_0}} \tag{2.6}$$

where E_P is the bulk plasma energy, γ represents damping loss, N is the bulk electron density, m is electron mass, and ε_0 is the vacuum permittivity.

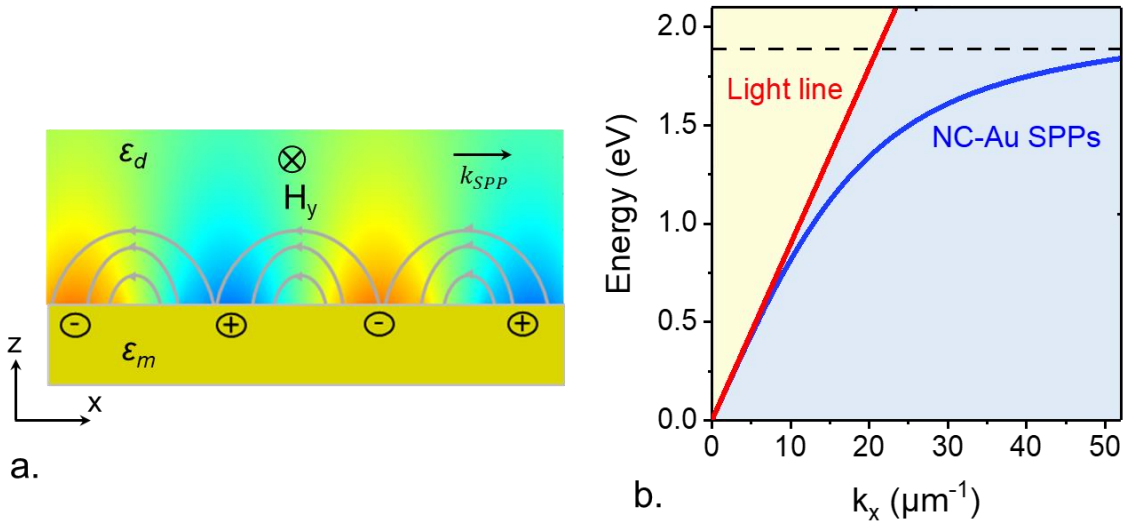

Figure 2.5: SPPs at a metal-dielectric interface. *a. Scheme of an interface with SPPs propagating in the x direction with in-plane wavevector k_x^{SPP}. The SPP wave is TM and bound to the interface through the interaction with the plasmons in the metal. The color map represents E_z component of the electric field. Different colors (orange and blue) correspond to different signs of E_z, described by the arrow direction. b. Dispersion relation of SPPs at the NC-Au interface (blue line). The light line is shown in red. The dashed line is surface plasma energy. The yellow area represents the area for propagating waves. The blue area indicates the area for evanescent waves.*

In Figure 2.5b, we plot relation (2.5) for an interface between a NC film (*i.e.*, $\varepsilon_d \approx 5$) and a gold layer with $\varepsilon_{Au}(E) = 1 - 2.29 \times 10^7/[E(E+i130)]$ with E in *meV*. The light line is the dispersion relation of photons propagating in the same direction as the SPPs in the absence of the gold layer, expressed by the linear relation $E = \hbar k_x c/n$, with n the refractive index of the NC layer. This light line separates propagating waves (yellow area) and evanescent waves (blue area).

When k_x is small, the SPP dispersion curve is very close to the light line. When k_x becomes larger, the SPP energy asymptotically approaches surface plasma energy $E_{SP} = E_p/\sqrt{1+\varepsilon_d}$, indicated by the dashed line in Figure 2.5b. Figure 2.5a shows SPP field intensity decays along the z direction. Decay length δ_{decay} is the characteristic length scale for SPP confinement and is given by

$$\delta_{decay} = \frac{1}{|k_z|} \quad \text{with} \quad k_z = \sqrt{\frac{\varepsilon_d \omega^2}{c^2} - k_x^2} \tag{2.7}$$

Note that SPPs also suffer losses due to the penetration of electric field into the metal. The propagation length L_{decay} is defined as the lateral distance over which SPP electric field intensity decreases by a factor of e. L_{decay} can be calculated as

$$L_{decay} = \frac{1}{2Im(k_x^{SPP})} \tag{2.8}$$

The confinement of SPPs is thus highly effective for enhanced light-matter interaction when the dielectric layer thickness is comparable to δ_{decay}. However, as can be seen in Figure 2.5b, SPP dispersion curve is always below the light line. Photons propagating in the dielectric medium (or air, since $\varepsilon_{air} = 1 < \varepsilon_d$) cannot couple directly to SPPs due to momentum mismatch.

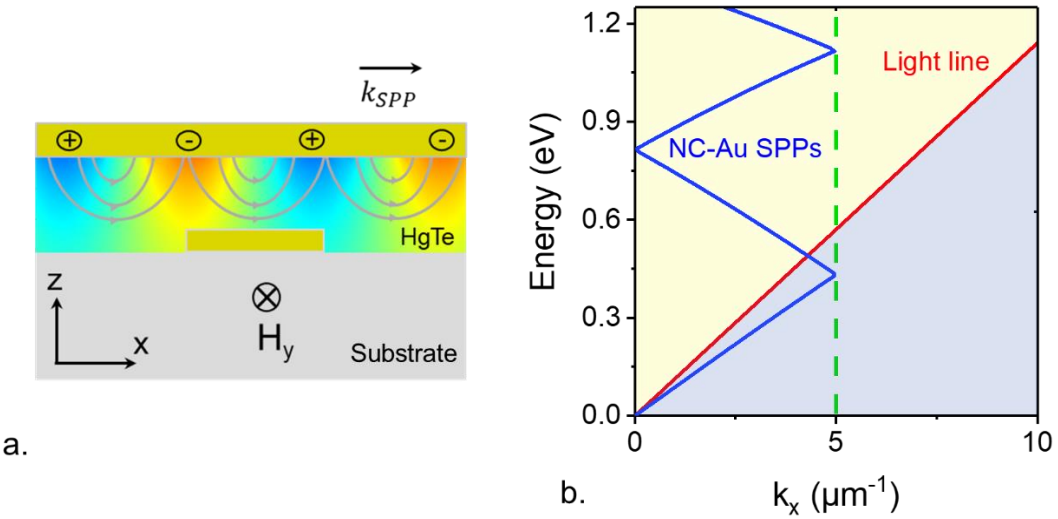

Figure 2.6: Spoof surface plasmon in NC-adapted MDM structure. *a. Scheme of SPPs propagating at the interface between the dielectric layer and top metal layer in our adapted MDM structure described in Figure 2.2b. The grating stripes play the role of scattering centers. When diffraction comes into play, photons propagating in the substrate can couple with the SPP, thanks to the presence of the grating. The color map represents the E_z component of the electric field. Different colors (orange and blue) correspond to different signs of E_z, also described by the arrow direction. b. Dispersion relation of SPPs at the NC-Au interface in a MDM structure (blue line). The light line is shown in red. The green dashed line is the first Brillouin zone boundary. The SPP curve is folded back in the first Brillouin zone and appears above the light line, thus, can couple with light from the substrate side. The yellow area represents the area for propagating waves. The blue area indicates the area for evanescent waves.*

In our MDM structure (see Figure 2.6a), this deficiency of wavevector can be fulfilled thanks to photon diffraction from the periodic shape of the grating. In a simplified picture, grating stripes are scattering centers that give rise to constructive inference under certain values of incident angle θ. The diffracted beam acquires extra momentum of $m\frac{2\pi}{p}\boldsymbol{e_x}$ from the grating and thus can couple to SPPs. Here, m is an integer number, $\boldsymbol{e_x}$ is the unit vector in the direction of the x-axis. Momentum matching requires

$$\boldsymbol{k_x^{in}} + m\frac{2\pi}{p}\boldsymbol{e_x} = \boldsymbol{k_x^{SPP}} \quad \text{or} \quad k_0 \sin\theta + m\frac{2\pi}{p} = k_x^{SPP} \tag{2.9}$$

where $\boldsymbol{k_x^{in}}$ is the in-plane wavevector of the incoming light in the substrate and $\boldsymbol{k_x^{SPP}}$ is the SPP wavevector. Condition (2.9), in combination with $E(\boldsymbol{k_x^{in}}) = E(\boldsymbol{k_x^{SPP}})$, are represented by the folding back of the SPP curve into the first Brillouin zone in the dispersion relation. Coupling of SPPs with light in the substrate medium is allowed when the folded SPP curve is above the light line. The first Brillouin zone limit depends on the grating period as $k_x^{Brillouin} = \pi/p$.

Figure 2.6b shows the SPP dispersion relation similar to that of Figure 2.5b but for an adapted MDM structure with $k_x^{Brillouin} = 5\ \mu m^{-1}$ (*i.e.*, $p = \pi/5\ \mu m$). Note that, here, the line light $E = \hbar k_x c/n$ is plotted for photons propagating in a sapphire substrate (*n = 1.73*), and we focus on the small k_x range where the SPP dispersion relation appears essentially linear (equation 2.5 with $E \ll E_P$). The optical feature of SPPs will be observed in our device, as presented later in this chapter.

2.2.3. Fabry- Perot resonance under TE polarization

In our MDM structure, the single-metal regions between two neighboring grating stripes allow light confinement with a Fabry-Perot cavity nature, as exemplified by the navy-blue dashed boundaries in Figure 2.7a. The electric field, in this case, is localized in the single-metal regions. For TE polarization, E_y is the only non-zero component of the electric field. Light is confined in the horizontal direction (x-axis) due to the presence of the grating, which compels E_y to vanish on the dielectric-metal boundaries. Thus, the resonant wavelength of this Fabry-Perot mode is governed by the opening of the grating slit *o = p–s*. This confinement along the horizontal direction can be understood once again from the modal impedance mismatch between the single-metal and double-metal regions. As mentioned in section 2.2.1, the TE_m modes present cut-off energies. No TE modes below the cut-off energy $\hbar c\pi/nL$ can penetrate the double-metal region. As a result, standing waves of TE_m modes form in single-metal regions.

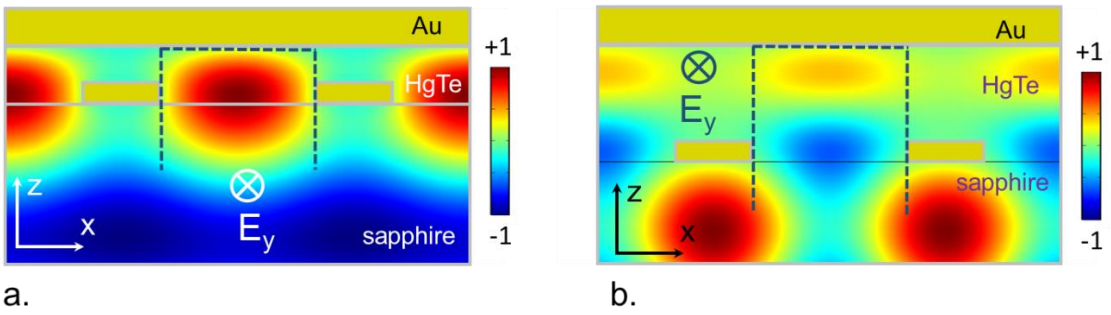

Figure 2.7: TE Fabry-Perot resonance in NC-adapted MDM structure. *a. Fabry-Perot resonance in the horizontal direction. b. Resonance due to the interference in the vertical direction. The presence of the grating and the top gold plane causes E_y to vanish on metal-dielectric boundaries. The color maps show E_y component of the electric field. Different colors (red and blue) correspond to different signs of E_y. The field is confined within the single-metal region indicated by the navy-blue dashed lines.*

It is noted that the interference of the incoming and reflected wave can also give rise to resonances with Fabry-Perot characteristics in the vertical direction, see Figure 2.7b. The field enhancement happens in the single-metal region (indicated with the dashed lines) with the spectral position governed by the NC layer thickness *L*. This resonance can be observed under both TE and TM polarizations. Similarly, the self-interference of the incoming light on the gold grating can also occur. However, the electric field maxima from this interference localize in the sapphire substrate (the red circular spots in Figure 2.7b), thus, not enhancing the NC absorption.

2.3. Broadband NC-based photodetectors

The ability to detect light over a broad spectral range is important for many practical applications, including sensing, communication, and, in particular, infrared imaging. In this section, we present a photodetector based on the structure depicted in Figure 2.2b for broadband photodetection in the SWIR and MWIR. As explained in 2.2, the geometrical parameters of the structure specify electromagnetic field modes coupled with the NC film. In the following, we first perform finite element method simulations to determine the geometrical parameters for the optical design. The fabrication process following the simulated results is then presented, starting with NC synthesis and NC film integration into the optical structure. Finally, we characterize the obtained device as a photoconductive infrared detector.

2.3.1. Electromagnetic design for geometrical parameters

The electromagnetic modeling of our resonator was performed using *COMSOL Multiphysics in 2D, Frequency Domain Interface*. Figure 2.8a shows the scheme of the simulation model. Floquet periodicity is set for boundary conditions at the side edges. A periodic port to generate incoming electromagnetic waves is placed in the substrate layer.

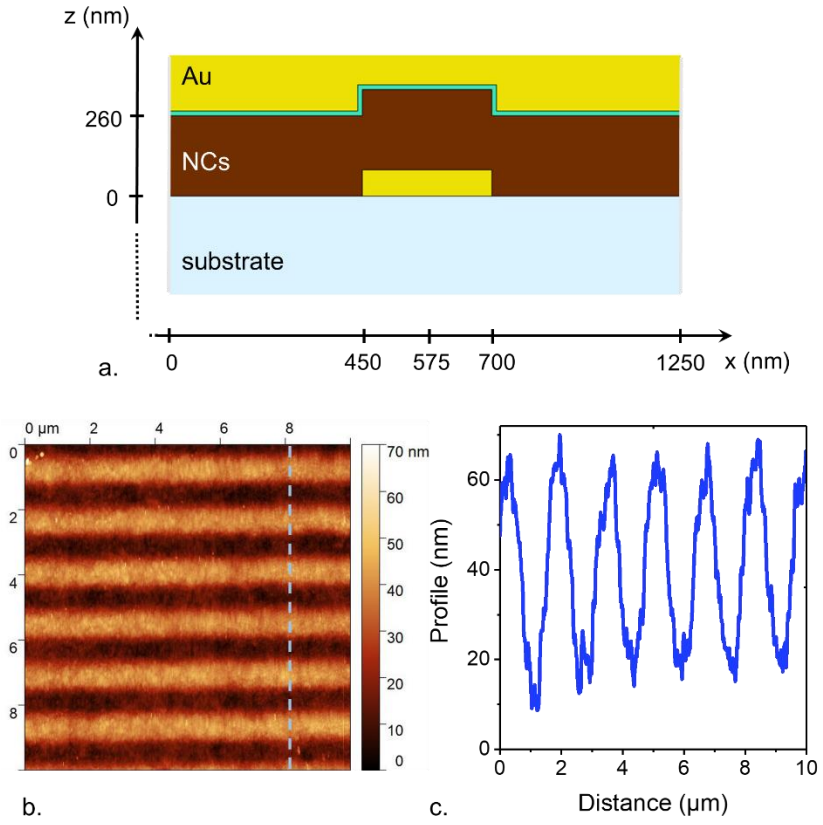

Figure 2.8: Electromagnetic simulation. *a. Schematic of the COMSOL model. b. Atomic force microscope scan of a 300 nm NC film deposited on a 50 nm gold grating. c. Profile of the grating area (gray dashed line in Figure 2.8b) measured by AFM showing a conformal profile of the film. This conformity is considered in our simulation model.*

The dissipated power per unit volume in the metals and nanocrystals can be calculated using the formula $P = -0.5\omega|F|^2 Im(\varepsilon)$, where F is the electric field, ω is the angular frequency of

the incident wave, and $Im(\varepsilon)$ is the imaginary part of the material permittivity [142]. The absorption of one material is calculated by integrating the dissipated power over the volume of the material, then divided by the incident power defined in the pre-defined periodic port. For example, for nanocrystal absorption:

$$Abs_{NC}(\omega) = \frac{P_{NC}(\omega)}{P_{incidence}} = \frac{\iiint 0.5\omega|F|^2 Im(\varepsilon) dV_{NC}}{P_{incidence}} \quad (2.10)$$

The absorption and reflection spectra are obtained by sweeping the frequency in the interested spectral range. NC films are typically deposited using spin coating, which could result in a conformal NC surface when deposited above a grating area. We have deposited a 250 nm HgTe film on top of a 50 nm thick gold grating to examine this effect. AFM scan on the grating area reveals a conformal manner of the NC film, as shown in Figure 2.8b-c. This conformity is also considered in our modeled device geometry.

Sapphire was chosen as the substrate material to provide good transparency up to 6 µm, as we targeted photodetection in the SWIR and MWIR. Furthermore, the refractive index of sapphire ($n_{sapphire} \approx 1.73$) is lower than that of NCs ($n_{HgTe\ NCs} \approx 2.35$) in this spectral range, reducing leakage of the confined electromagnetic field to the substrate side. We then determined the geometrical parameters of the device to generate optical resonances within the NC film: grating stripe width *s*, grating period *p*, and NC film thickness t_{NC} for fabrication.

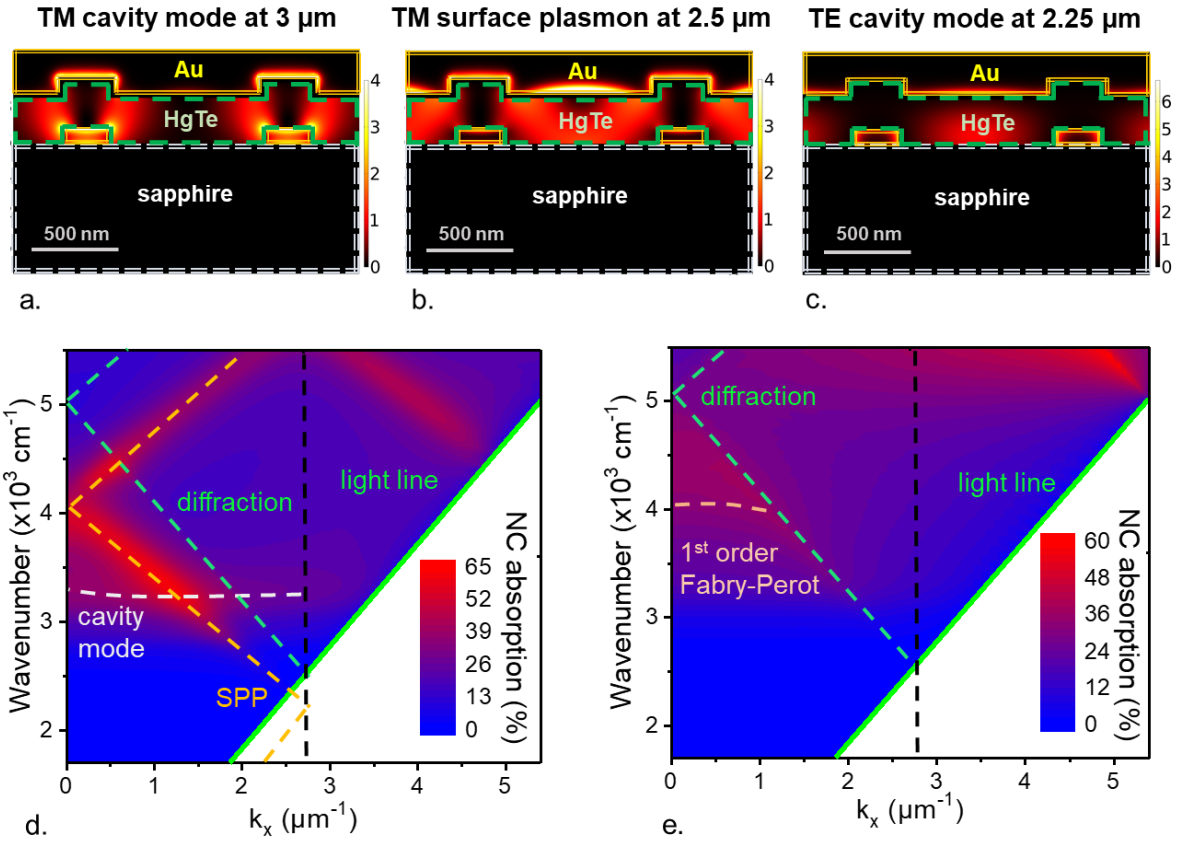

Figure 2.9: Optical properties of the structure from electromagnetic simulations. *a. Absorption map of the device at 3 µm corresponding to the TM cavity mode resonance wavelength. b. Absorption map of the device at 2.5 µm corresponding to the TM surface plasmon mode wavelength. c. Absorption map of the device at 2.25 µm corresponding to the TE Fabry-Perot resonance wavelength. The color scale corresponds to the absorption*

magnitude in arbitrary units. The maps are simulated for illumination at normal incidence. d. (resp. e). NC absorption dispersion map (in color scale) for TM (resp. TE) polarization. The continuous green line is the light line in the sapphire, while the green dashed lines represent its diffracted orders. The yellow dashed line represents the calculated SPP dispersion, together with its diffracted orders. The vertical black line indicates the edge of the first Brillouin zone at $k_x = \pi/p$. The horizontal white dashed lines represent the Fabry-Perot cavity modes.

In order to ensure a high film quality and compatibility with NC carrier transport, the film thickness was chosen to be around 250 nm. On the one hand, high-quality HgTe NC films at this thickness can be reliably obtained by our fabrication method, as presented in the following section. Having a smooth, mirror-like NC film for the optical structure is of particular importance, as it is preferable to prevent optical scattering at the interfaces, thus, reducing optical losses. On the other hand, building a thick film (≥ 500 nm) could lead to crack formation, detrimental to the device's transport and optical properties.

As we targeted a broadband photodetector, grating stripe width *s* and grating period *p* have been chosen to be 250 nm and 1150 nm, respectively. The value of *s* allows light coupling with the TM cavity mode at a resonant wavelength of around 3 µm. This mode concentrates the electric field and enhances NC absorption close to the grating stripes, see Figure 2.9a. Simultaneously, the interface between the top gold layer and the PMMA/NC film supports a surface plasmon mode. The surface plasmon electric field decays in the NC film and intensifies NC absorption over extended areas between two adjacent metals, as shown in Figure 2.9b. To this end, the PMMA thickness has been chosen to be around 10 nm, much smaller than the SPP decay length, to minimize possible optical losses in the PMMA layer. With *p* being 1150 nm, the spectral position of the surface plasmon is set to be around 2.5 µm under normal incidence, broadening the device's absorption.

The dispersive characteristic of the SPP can be recognized in the TM dispersion map in Figure 2.9d. The calculated SPP dispersion following equation (2.5) can be used to reproduce the results of the electromagnetic simulation. However, a slightly lower value of the refractive index of the NC film had to be considered (2.1 instead of 2.35 as in the electromagnetic simulation). This can be attributed to the presence of the PMMA layer.

In TE polarization, light confinement in the single-metal regions between two grating stripes is associated with the Fabry-Perot mode, as presented in Figure 2.9c. The energy of this mode is set to broaden further the device's spectral response with an absorption peak at 2.25 µm. Dispersion maps in Figure 2.9d-e show that both the TM cavity mode and TE Fabry-Perot mode are non-dispersive unless they interfere with the diffraction line at large incident angles. In the TE dispersion map, a second-order Fabry-Perot resonance also appears at higher wavenumbers, around 5500 cm^{-1} (≈ 1.8 µm).

Figure 2.10 compares the absorption of the NC film integrated into the MDM structure with the absorption of a bare NC film with the same thickness at normal incidence. It is clear that the MDM structure enhances NC absorption over a wide spectral range from 2 µm to 4 µm. We thus follow the outcomes of the electromagnetic simulation for device fabrication.

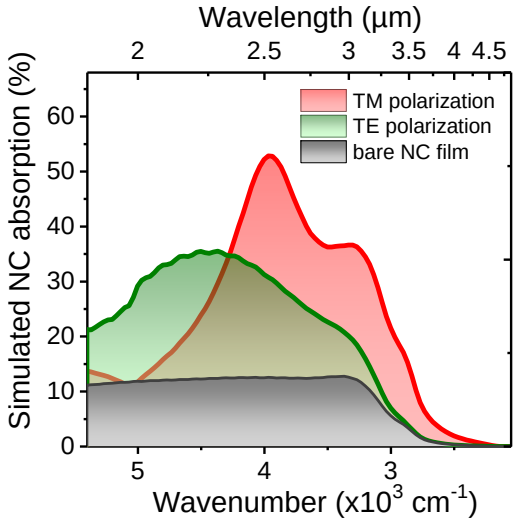

Figure 2.10: Simulated NC absorption at normal incidence. *Absorption of a NC film integrated into our MDM structure and absorption from a bare NC film with the same thickness (250 nm).*

2.3.2. Fabricating NC-based photodetector with MDM structure

Synthesis and pre-processing of the NCs

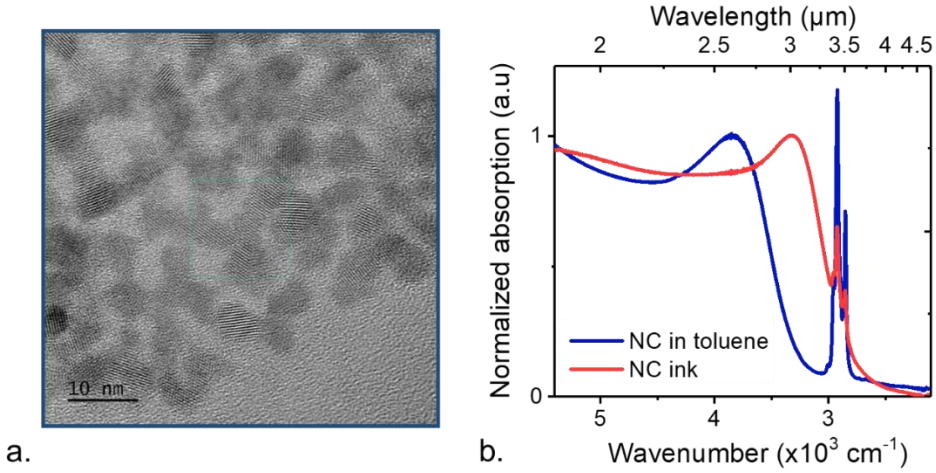

Figure 2.11: Characterization of the synthesized HgTe nanocrystals *a. Transmission electron microscopy image of the HgTe NCs prepared with Keuleyan's procedure [48]. The obtained particles have a size of around 10 nm and a tripod shape. b. Absorption of HgTe NCs before ligand exchange (DDT capped, toluene used as the solvent) and after ligand exchange (ink form, $HgCl_2$-MPOH capped). A shift of the excitonic peak from 2.5 µm to 3 µm can be observed.*

The fabrication process begins with material preparation. The absorbing layer is HgTe NCs, synthesized by Yoann Prado (chemistry research engineer - INSP), using the procedure developed by Keuleyan *et al*. [48]. The obtained NCs have a tripod shape, see Figure 2.11a. The absorption spectrum of the NC solution has been measured using attenuated total reflection (ATR), showing an excitonic peak around 2.5 µm. Liquid phase ligand exchange was performed to replace the initial long capping ligands with the short ones (*i.e.*, a mixture of

$HgCl_2$ and mercaptoethanol) for improving carrier transport. The solution after ligand exchange is called NC ink and will be used for solid film deposition. This step induces a red shift of the excitonic peak and strongly suppresses the C-H bands around 2900 cm^{-1} due to the removal of the free ligands and ligand length reduction, as presented in Figure 2.11b.

Integrating NC film into the plasmonic structure

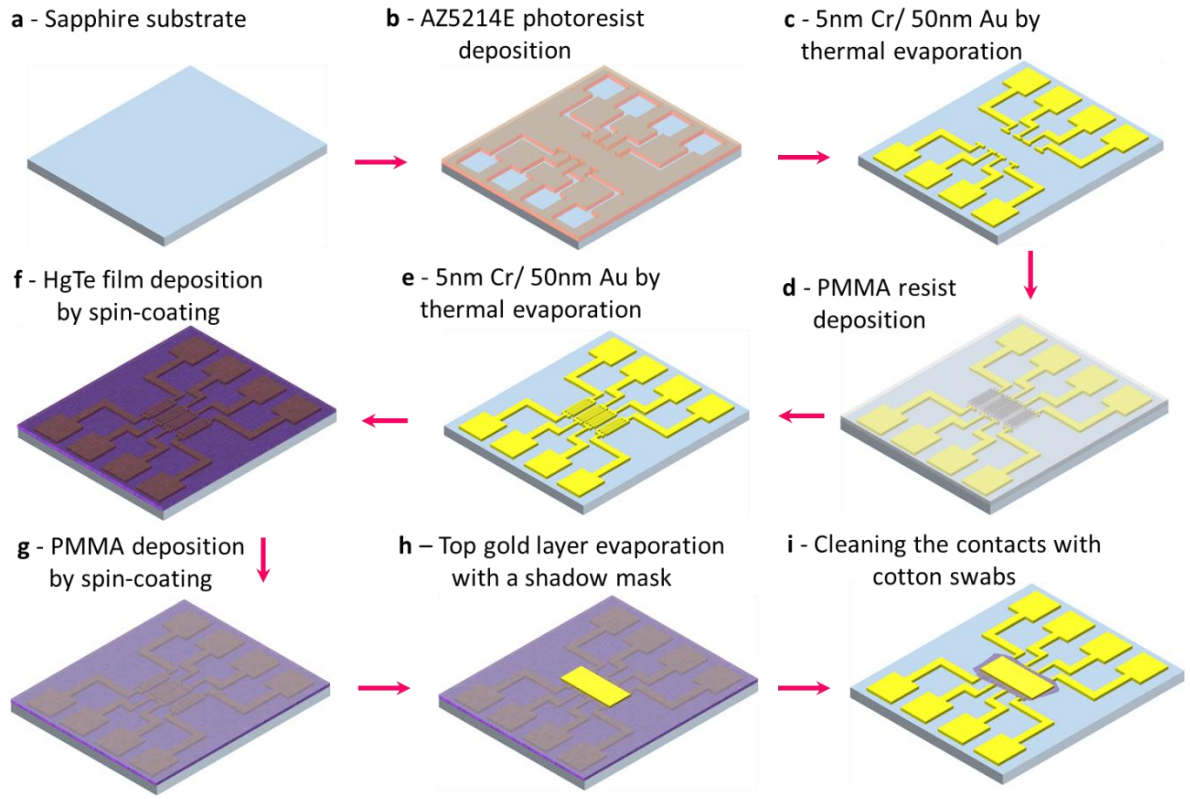

Figure 2.12: Fabrication procedure of the device. *a-c. Optical lithography for the electrical contacts of the device. d-e. Electron beam lithography for the gold gratings. The gratings are connected to the macroscopic contacts as they are also used as interdigitated electrodes. f. (resp. g). NC and PMMA deposition by spin-coating. h. Thermal evaporation of the top gold layer. A shadow mask has been used to deposit gold on the grating area selectively. i. Cotton swabs are used to remove the NC on top of the electrical contacts to ensure a good electrical connection for measurements.*

Figure 2.12 summarizes the fabrication procedure for the device. On a sapphire substrate, electrical contacts and gold grating were fabricated using optical and electron-beam lithography, respectively. The NC film was then deposited on top of the grating using spin-coating. The film thickness can be well-controlled by tuning the NC ink concentration and rotation speed. As mentioned in 2.3.1, we targeted a HgTe film of around 250 nm. Then, a thin layer of PMMA (10-20 nm) is deposited on top of the NC film to ensure electrical isolation between the electrodes and the top gold layer. This PMMA layer is obtained by spin coating a diluted PMMA solution in toluene (20 $mg.mL^{-1}$). Finally, we evaporate the gold through a shadow mask for the top layer. Before device characterization, cotton swabs were used to gently clean the materials (NCs, PMMA) from macroscopic pads to ensure good electrical connections in measurements.

Figure 2.13a provides a cross-sectional image of a fabricated device and confirms the obtained structure is close to the targeted one (depicted in Figure 2.2b). EDX mapping in Figure 2.13b shows the chemical composition of each area, while Figure 2.13c highlights the presence of a thin PMMA layer (*i.e.,* carbon composition) between the NCs and the top gold layer. The TEM slice was prepared using a dual beam SEM/FIB fitted with a micromanipulator for in situ lift-out. The imaging and EDX mapping were performed by Armel Descamps-Mandine (Centre de MicroCaractérisation Raimond Castaing, Toulouse).

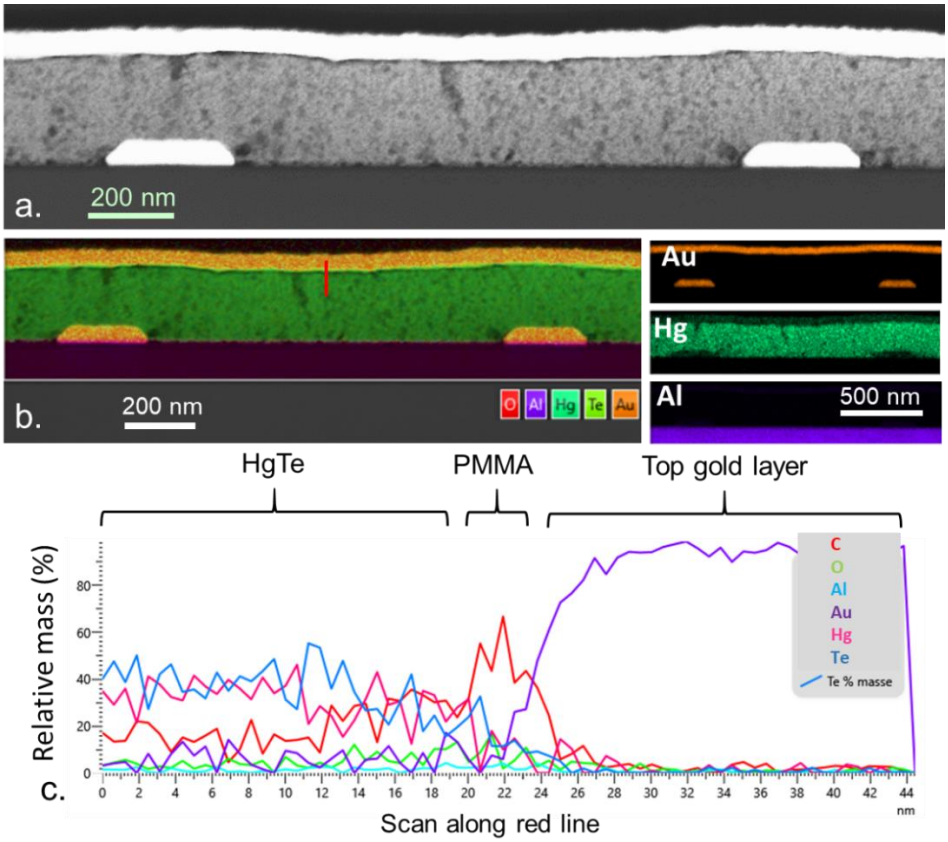

Figure 2.13: NC-based photodetector with MDM structure. *a. TEM image of the fabricated device based on the NC-adapted MDM structure. b. Left panel: EDX mapping of the device side view where the localization of O, Al, Hg, Te, and Au atoms are superimposed. Right panel: maps for the same area of the device only depicting one atom population. c. Relative mass composition for various atoms along the red line in part b. The composition profile highlights an excess C content between the HgTe layer and the top gold mirror, indicating the presence of the PMMA layer.*

Note that the grating also functions as interdigitated electrical contacts for photoconductive operations in our device. In the following parts, the transport is a *planar* electrical transport between two consecutive grating periods. There is no vertical transport between the grating and the top gold layer, thanks to the insulating PMMA layer. However, in some cases, the top layer can be used as a gate electrode for carrier density control.

2.3.3. Device operation as a photoconductive infrared detector

We first measured the device's photocurrent spectra under polarized conditions and compared the spectra with simulated NC absorption. Figure 2.14a shows the photocurrent spectrum of the device under TM polarization, in which a doublet can be observed with a clear overlap of two absorption peaks. The component around 4000 cm^{-1} (2.5 µm) is attributed to the surface plasmon peak, while the redder component at 3100 cm^{-1} (3.2 µm) is associated with the cavity mode and the excitons. Under TE polarization (Figure 2.14b), we observed two main features. The first feature appearing around 3000 cm^{-1} (3.3 µm) is the absorption band edge of the NCs. The second feature at around 4500 cm^{-1} (2.25 µm) corresponds to the Fabry-Perot resonance. Note that the photocurrent spectra are in good agreement with the simulated absorption spectra of the NC film presented as dashed lines. The main notable discrepancy between the photocurrent and the simulated absorption spectra is a small shift at the band edge due to the effect of the temperature. The photocurrent spectra were measured at 80 K, while the NC absorption was calculated using the NC optical index extracted from room temperature measurements [143].

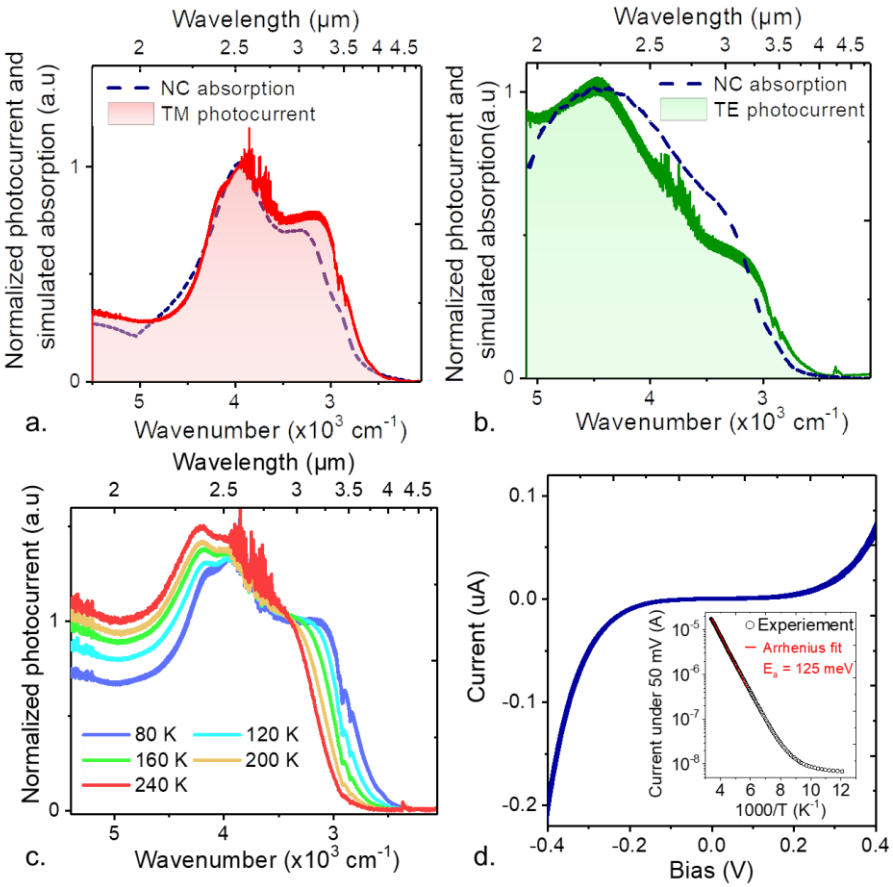

Figure 2.14: Broadband absorption enhancement of the device*. a. (resp b.) Simulated NC absorption and experimental photocurrent spectra of the device under TM (resp. TE) polarization. Photocurrent spectra have been taken at 80 K. c. Experimental unpolarized photocurrent spectra at different temperatures. d. I-V curve under dark condition at 80 K. The inset is current-temperature (I-T) dependence fitted with an Arrhenius law, presenting an activation energy of 125 meV.*

HgTe NC absorption redshifts upon cooling [144], [145], which can be observed in a series of unpolarized photocurrent spectra of the device at different temperatures, as shown in Figure 2.14c. It is noticed that the spectra present slight differences in their shape at different temperatures. The discrepancies are due to a change in the spectral overlap of the material absorption with the cavity resonances. While the material bandgap strongly depends on temperature, the cavity resonance energies barely change since the latter are mainly driven by geometrical factors. Figure 2.14d presents the I-V curve of the device taken under the dark condition at 80 K. The curve appears super linear for large bias voltages greater than 0.2 V. In the linear regime, the current drops as the device temperature decreases. The current-temperature curve can be fitted using Arrhenius law with an estimated activation energy of 125 meV. This activation energy is nearly half the bandgap energy (≈155 meV) as expected for suitable photoconductive materials.

To quantitatively assess the device's photodetection performance, we have realized a series of measurements to determine: (i) the device's responsivity under broadband illumination, (ii) noise current spectral density to determine the device's specific detectivity, and (iii) time response under illumination by a modulated laser.

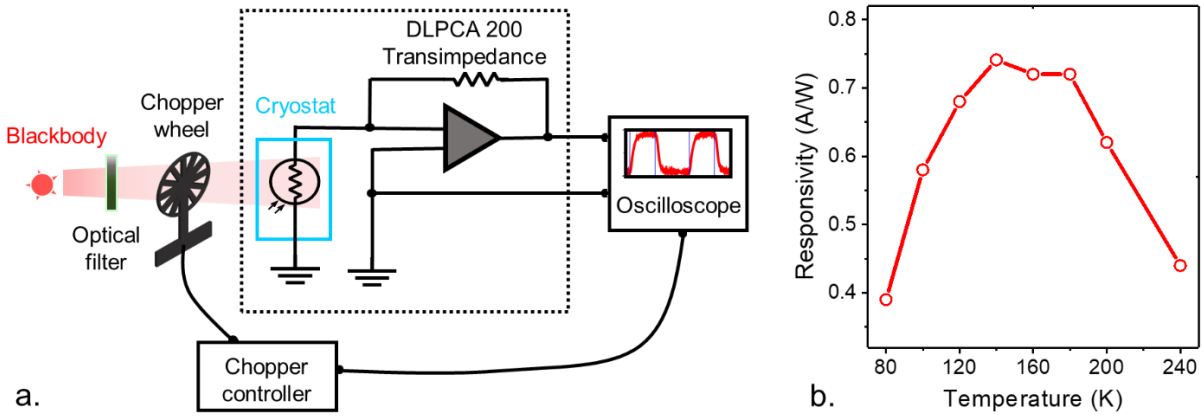

Figure 2.15: Responsivity under broadband illumination. *a. Experimental setup for responsivity measurement under blackbody radiation. b. Measured device's responsivity as a function of temperature. The applied bias was 0.2 V. The device was under illumination of a blackbody at 980ºC.*

Figure 2.15a shows the experimental setup for the responsivity measurement. The device is placed inside the cryostat. A Femto DLPCA 200 amplifier is utilized for biasing the photodetector, acquiring and amplifying the photocurrent signal. The amplified signal is then provided to an oscilloscope. Device responsivity was measured when the device was illuminated by a Blackbody Omega BB-4A set at 980 ºC. The incoming flux is chopped by an optical chopper with a frequency varied from 1 Hz to 1000 Hz. In front of the sample, a Ge window filters out radiation at wavelengths shorter than 1.9 µm. Thus, the incident power to the sample can be computed using the formula:

$$P(W) = \pi A_{det} \cdot \sin^2\left(\frac{\theta}{2}\right) \cdot \int_{1.9\mu m}^{\lambda_{cut-off}} \frac{2hc^2}{\lambda^5} \frac{1}{\exp\left(\frac{hc}{\lambda kT}\right)-1} d\lambda \qquad (2.10)$$

where A_{det} is the area of the photodetector, θ is the field of view, *h* is the Planck constant, *c* is the speed of light, *k* is Boltzmann constant, and *T* is the blackbody temperature equal to 980 ºC. $\lambda_{cut-off}$ is taken from the absorption edge of the material.

The measured device's responsivity as a function of temperature under 0.2 V applied bias is presented in Figure 2.15b. The responsivity ranges from 400 to 700 mA.W^{-1}, depending on the temperature. The responsivity drops below 120 K and above 200 K, which is connected to the decrease in carrier mobility, as will be discussed in the following chapter.

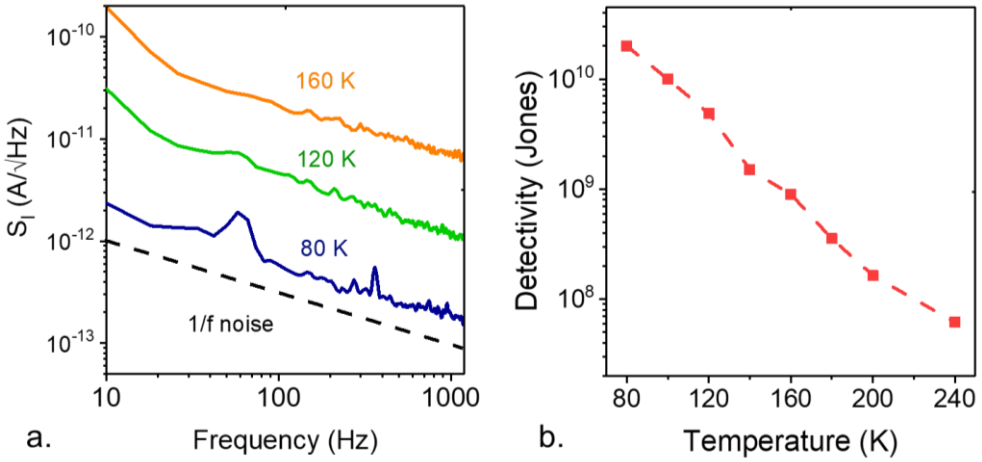

Figure 2.16: Noise and detectivity of the device. *a. Measured noise current density spectra of the device at various temperatures as the applied bias was set at 0.2 V. It is clear that 1/f noise is the dominant noise source. b. Specific detectivity of the device as a function of temperature.*

The ultimate figure of merit for the device's sensitivity is the specific detectivity. To determine the detectivity of our device, noise current spectral density has been measured using an SR780 spectrum analyzer. The device is biased with a Femto DLPCA 200 amplifier. For one measurement, the final noise current density spectrum is obtained after averaging 100 scans. Figure 2.16a presents the noise spectra at different temperatures of the device. 1/f noise appears to be the primary noise source, as expected for a photoconductive NC detector. Detectivity values have been extracted from $D^* = \mathcal{R}\sqrt{A}/S_I$, where $\mathcal{R}$ is the responsivity of the device, A is the device's optical area, and S_I is the measured noise current spectral density. As the device is cooled down, the specific detectivity increases and reaches 2 x 10^{10} Jones at 80 K for our device with light modulated at 1 kHz.

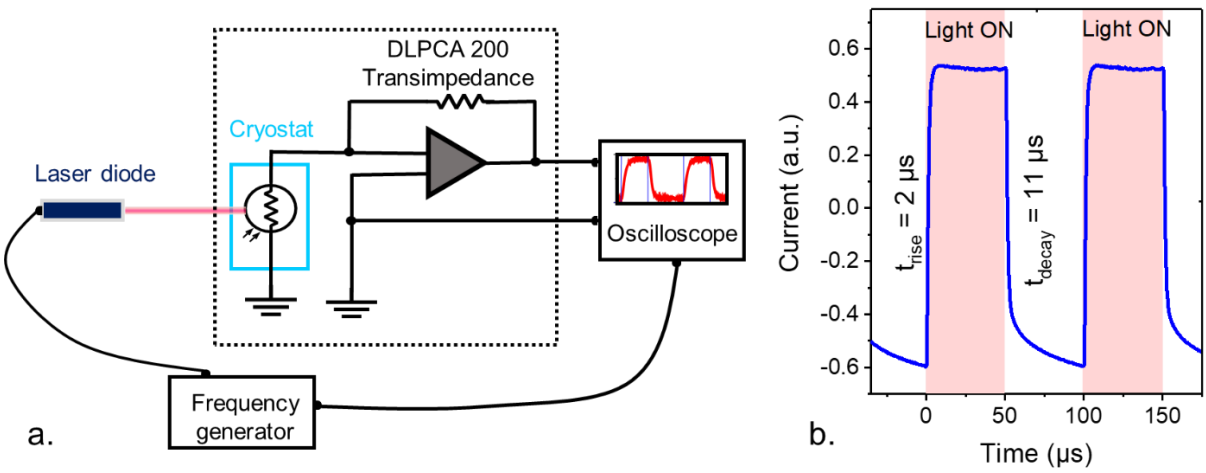

Figure 2.17: Device time response measurement. *a. Experimental setup for response time measurement with a laser diode. b. Current as a function of time under illumination of 2.5 µm*

laser diode modulated at 10 kHz. The applied bias on the device was 0.2 V. Device temperature was 80 K.

Finally, the device's response time has been measured using a setup similar to the responsivity measurement, with the blackbody replaced by a laser diode, as sketched in Figure 2.17a. The laser was provided by Alexei Baranov (IES laboratory, University of Montpellier). The emission wavelength of the laser was 2.5 µm, matching the absorption peak of our photodetector. The device's response time under the illumination of the laser is estimated to be around 11 µs, see Figure 2.17b. Note that this measured response time value is probably setup-limited since our laser can only be modulated with a frequency up to 10 kHz. However, for a device with broadband detection in the SWIR and MWIR, a demonstrated micro-second response time is certainly promising for many practical applications, such as sensing and imaging.

Table 2 compares the performance of our device with state-of-the-art devices based on HgTe NCs presenting designed light-matter coupling. In particular, our device demonstrates one of the highest responsivities for MWIR (4 µm cut-off wavelength) sensing devices thanks to its broadband absorption enhancement. However, its detectivity is surpassed by a vertical geometry photodiode coupled to two resonators [131] since the photodiode structure can operate under 0V bias, thus reducing the dark current. We will discuss specifically a photodiode structure coupled with our MDM structure in Chapter 4.

Table 2: *Figures of merit for HgTe NC infrared sensors with designed light-matter coupling*

Optical design	**Cut-off wavelength**	**Responsivity (A/W)**	**Time response**	**D* (Jones)**	**Operating temperature (K)**
Coupling to gold nanorod structures [129]	1.4 µm	-	0.35 µs	1.4×10^{10}	300
Coupling to nano antennas [130]	4-5 µm	0.19	-	1.52×10^{10}	80
Plasmon & Fabry-Perot for photodiode [131]	4.5-5 µm	1.62	-	4×10^{11}	85
Guided-mode resonator [90]	3 µm	1	<35 µs	10^{10}	200
Fabry-Perot [102]	2.2 µm	0.5	260 ns	7.5×10^{10}	300
Distributed Bragg mirror [132]	2.08 µm	0.22	120 ns	10^{10}	295
Metasurface [133]	1.6 µm	8000	-	1.75×10^{8}	300
Broadband guided-mode resonator [143]	2 µm	0.2	110 ns	2×10^{10}	300

Guided-mode resonator with phototransistor [146]	3 µm	0.15	14 µs	10^{12}	30
This work [138] (broadband MDM structure)	4 µm	0.4	11 µs	$2x10^{10}$	80

2.4. Conclusion

In this first experimental chapter, I have demonstrated that broadband enhancement (over 2500 cm^{-1}, from 2 µm to 4 µm in the electromagnetic spectrum) in light absorption can be obtained from a HgTe NC film integrated into a MDM structure. This simple combination allows building a photodetector benefiting from three photonic modes: a double metal cavity mode, a surface plasmon mode in TM polarization, and a Fabry-Perot mode in TE polarization. The nature of each photonic mode has been presented, which establishes design rules for a broadband infrared photodetector. The obtained device enables sensing in the SWIR and MWIR regions (4 µm cut-off wavelength), with a high responsivity (400 $mA.W^{-1}$), a detectivity above 10^{10} Jones for 80 K operating temperature, and demonstrated micro-second response time.

In the next chapter, I will present how controlling light-matter interaction in a NC-based device can be exploited to generate post-fabrication bias tunability, a domain barely explored for NC photodetectors.

Chapter 3: Bias reconfigurability in nanocrystal–based photodetectors

Contents

Related articles

- Dang, T. H.; Vasanelli, A.; Todorov, Y.; Sirtori, C.; Prado, Y.; Chu, A.; Gréboval, C.; Khalili, A.; Cruguel, H.; Delerue, C.; Vincent, G.; Lhuillier, E. Bias Tunable Spectral Response of Nanocrystal Array in a Plasmonic Cavity. *Nano Lett.* **2021**, *21* (15), 6671–6677.
- Dang, T. H.; Khalili, A.; Abadie, C.; Gréboval, C.; Cavallo, M.; Zhang, H.; Bossavit, E.; Utterback, J. K.; Dandeu, E.; Prado, Y.; Vincent, G.; Ithurria, S.; Todorov, Y.; Sirtori, C.; Vasanelli, A.; Lhuillier, E. Nanocrystal-Based Active Photonics Device through Spatial Design of Light-Matter Coupling. *ACS Photonics* **2022**, *9* (7), 2528–2535.
- Dang, T. H.; Abadie, C.; Chu, A.; Cavallo, M.; Khalili, A.; Dabard, C; Bossavit, E.; Zhang, H; Prado, Y.; Pierucci, D; Utterback, J. K.; Todorov, Y.; Sirtori, C.; Jaeck, J; Vincent, G.; Vasanelli, A.; Fix, B; Lhuillier, E. Bias reconfigurable photoresponse of infrared nanocrystal film integrated into a coupled Fabry-Perot resonator. *ACS Photonics* **2023**, 10 (5), 1601–1607.

Material synthesis and device fabrication in this chapter have been performed with the support of all the coauthors from the articles. In particular, Yoann Prado (chemical research engineer - INSP) synthesized the HgTe nanocrystals. The tight-binding simulations for investigation of quantum-confined Stark effect in HgTe NCs were performed by Christophe Delerue (IEMN – Lille). The coupled resonator structure in section 3.4 has been developed and characterized in collaboration with the ONERA. In particular, Baptiste Fix conducted the scanning near-field imaging measurements.

Reconfigurable response is highly desirable for advanced infrared optoelectronic systems. The ability to actively control the device's optical response is of utmost interest for infrared sensing applications since imaging contrast could be substantially improved by tuning the device's spectral response. Despite the interest, post-fabrication tunability has been a barely explored domain in NC-based infrared devices. Conventional strategies, such as exploiting the quantum confined Stark effect or integrating NCs with MEMS structures, require a large electric field or fabrication techniques incompatible with NC films. In this chapter, we demonstrate the bias-tunable spectral response of NC-based photodetectors by exploiting the interplay between hopping transport and the spatial absorption inhomogeneity induced by optical resonances. Various resonator architectures will be explored. We show that hopping transport, often seen as a limitation for optoelectronic devices, plays a crucial role in designing active photonic devices based on nanocrystals.

3.1. Introduction

The original interest in NCs comes from their size-tunable optical properties associated with quantum confinement. When integrating them into optical resonators, the optical features of NC-based devices can be further controlled through the resonator design, as presented in the previous chapter. In those approaches, spectral tunability is limited to the synthesized materials or to the geometrical parameters of the photonic structures. However, many practical applications can benefit from the capability to actively control (*i.e.*, post-fabrication) the photodetector's spectral response. By tuning the sensitivity of the device with respect to a certain spectral range, spectral response reconfigurability can be combined with advanced color processing algorithms for contrast enhancement in infrared imaging.

In optoelectronics, a common strategy to achieve active spectral modulation is to exploit the quantum-confined Stark effect [147], which induces a spectral shift in the material absorption upon application of an external electric field [148]–[151]. Nevertheless, Stark effect typically requires a large electric field above 100 $kV \cdot cm^{-1}$, equivalent to 0.1 eV energy drop over 10 nm in a semiconductor film. This field leads to strong out-of-equilibrium in narrow-gap systems and difficulties for carrier transport in NC arrays due to electrical breakdowns. In the context of NC films, Stark effect is thus only suitable for tuning the NC's optical features. Recently, other approaches, such as the use of phase-change materials [152], [153] and MEMS structures [154], have been emerging for active photonics thanks to developments in materials science and fabrication methods. While a phase-change material varies its optical properties as a result of phase transitions, MEMS structures allow reconfigurable device geometries, both resulting in modifications of the device's spectral response. However, these approaches are complex to apply to NC-based devices due to their sophisticated fabrication requirements.

For infrared detection, bias reconfigurability obtained from back-to-back photodiode configuration is a common strategy [2]. Figure 3.1a presents this configuration for a back-illuminated structure in which a diode with a longer cut-off wavelength is fabricated on top of a diode with short cut-off wavelength. The short-wave (SW) absorber thus acts as a long-wavelength pass filter for the long-wave (LW) absorber. The operation of these diodes depends on the polarity of the bias voltage applied to the contact. For example, when the LW photodiode is reverse biased, the SW photodiode is forward biased. The photocurrent from

the SW diode is shunted by its low forward-biased impedance, and only the photocurrent from the LW photodiode contributes to the detected signal. Similarly, only the SW photodiode is available when the bias polarity is reversed. For efficient diode operation, band-gap engineering and doping control are critical for the structure design.

Figure 3.1: Bias-reconfigurable structure based on back-to-back diode configuration. *a. Sketch of the back-to-back diode for dual band photodetection. The equivalent electrical circuit is shown on the right. b. Back-to-back diode from multiple layers of NCs in a tandem structure. The spectral response on the diode can be selected by changing bias polarity, as shown by the graph on the right. From reference [103].*

Recently, the back-to-back diode architecture has been realized in a multilayer NC device [103], which demonstrated dual-band photodetection in the SWIR and MWIR, see Figure 3.1b. The diodes are constructed with a vertical stack of ITO/Bi_2Se_3/MWIR HgTe/Ag_2Te/SWIR HgTe/Bi_2Se_3/Au, in which the two HgTe NC layers are the main absorbing layers. However, colloidal fabrication with a large number of layers can be highly challenging due to the incompatibility between formed solid layers and solvents of the next layers, leading to delamination or film dissolution.

This chapter presents an alternative strategy to generate a bias-tunable spectral response in *NC-based infrared photoconductors*. We show that the bias-dependent spectral response can be achieved in the photodetectors by exploiting the interplay between hopping transport and the absorption inhomogeneity induced by optical cavities. The chapter is organized as follows: (i) The first part will present the observation of a spectral shift with bias in our MDM structure and discuss the observed spectral shift's mechanism, which allows us to establish the fundamental requirements for bias tunability in NC-based devices [155]; (ii) the second part will introduce a simple detector design based on our established rules, evidently demonstrating the validity of our assumptions [156]; (iii) in the last part, we present a photodetector design for optimized the bias tunability effect, which ultimately leads to a strong optical band modulation of a photodetector [157].

3.2. Bias-induced shift of the photocurrent spectrum in a plasmonic cavity

3.2.1. Device structure and optical properties

We consider a photodetector with an MDM structure similar to the broadband photodetector presented in the previous chapter. For convenience, we present the front view of the design in Figure 3.2a. Here, we have used HgTe NCs with a faceted spherical shape, developed by Prado *et al*. [49]. Using rounded shape particles could enable better packing in the NC films, which is beneficial for carrier transport. Figure 3.2b presents a TEM image of the synthesized particles with a typical diameter of around 8 to 10 nm. The NC solution shows exciton absorption around 2.4 µm (≈ 4200 cm^{-1}) at room temperature. Before making solid NC film, liquid-phase ligand exchange was conducted to improve the intercoupling between the nanocrystals. Interestingly, this step suppressed the C-H band intensity at around 2900 cm^{-1} without leading to a significant shift in the exciton absorption, as opposed to what is commonly observed in tripod shape HgTe NCs, see Figure 3.2c. Sapphire was again chosen as the substrate material due to its good transparency in the extended SWIR range. The PMMA was used to prevent electrical shorts and as a gate material when the top gold layer acts as a gate electrode. In contrast to the broadband structure, here, we intended to match the TM surface plasmon mode with the exciton absorption resonance.

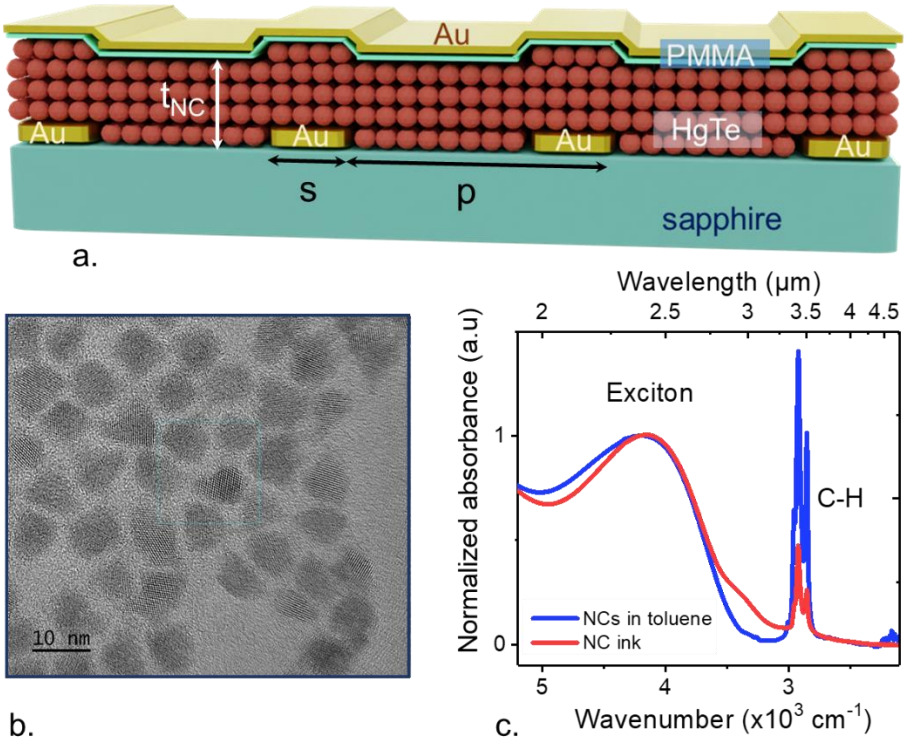

Figure 3.2: HgTe NCs as the active material of the photodetector. *a. Sketch of the plasmonic device with MDM structure. b. TEM image of the faceted spherical HgTe NCs. c. Absorption spectra of the initial NC solution in toluene and the NC ink obtained after liquid phase ligand exchange.*

The choice of the MDM resonator dimensions was guided by COMSOL simulation. The device's geometrical parameters were chosen as follows: a NC film thickness t_{NC} of around 300 nm, a grating stripe width *s* of 500 nm, a grating period *p* of 1350 nm, and a PMMA layer

thickness of around 20 nm, several times thinner than the surface plasmon decay length. Figure 3.3 presents the optical properties of our device by comparing the reflectivity of a NC film deposited on a gold layer (blue symbols) with the reflectivity of the device in TM (top panel) and TE (bottom panel) polarizations, measured at the incidence angle of 15°. The exciton absorption of the NC film can be recognized at around 2.5 μm, which is red-shifted compared to the value measured in the solution due to the change of dielectric environment from the liquid to the solid phase and the carrier wavefunction localization over the thiols. In TM polarization, a second feature appears at 3.1 μm in the tail of the absorption of the NCs. This resonance is associated with the surface plasmon polariton mode. Note that the SPP mode is dispersive, and, at normal incidence, it blueshifts towards the excitonic peak. At 4.5 μm, a weak broad feature appears, which can be associated with the TM cavity mode formed between the top and bottom gold electrodes. In this device, the cavity mode is not resonant with the exciton and thus does not affect the NC absorption (*i.e.,* no impact on the device's spectral response). In TE polarization, the Fabry-Perot resonance results in a broad absorption feature overlapping with the exciton. The simulated reflectivity (red continuous line) is in excellent agreement with the measured one. The electric field maps of the modes are presented in the insets. As discussed later, the inhomogeneous spatial distribution of the modes will play a central role in achieving bias tunability of the photoresponse.

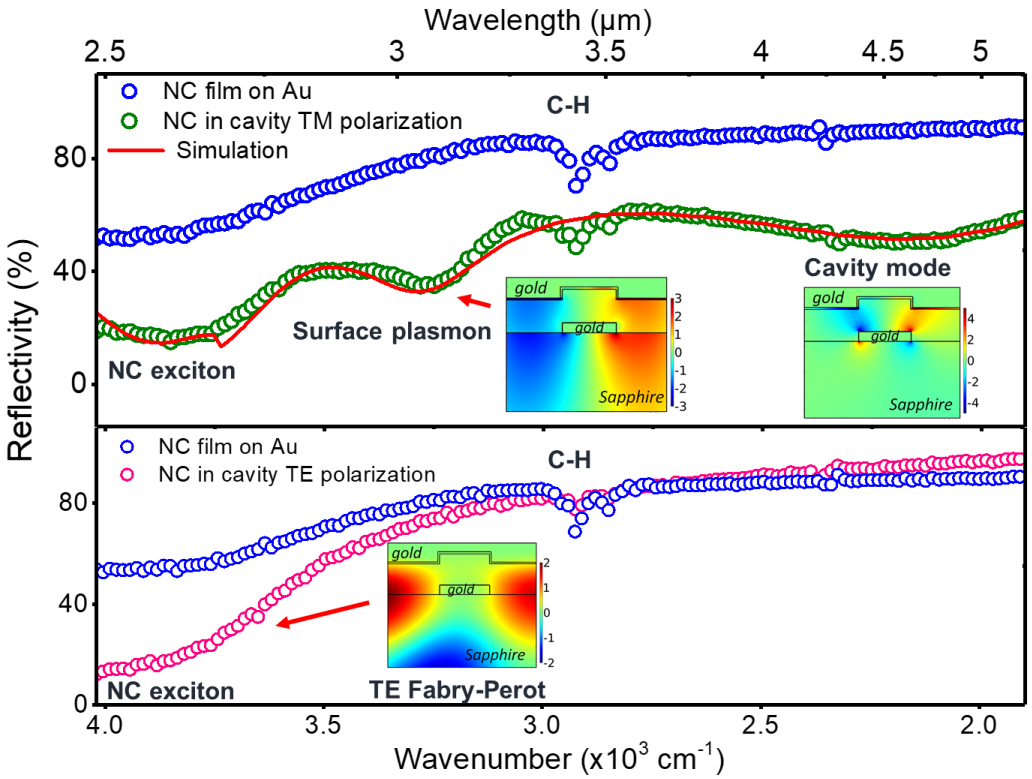

Figure 3.3: Optical properties of the plasmonic device. *Experimental reflectivity spectra measured at room temperature and at 15° incidence angle for a NC film deposited on a gold layer (blue circles), and for our MDM structure with s = 500 nm and p = 1350 nm. The top panel presents the experimental (green circles) and simulated (red line) reflectivity spectrum with TM polarized radiation, the bottom one presents the experimental spectrum under TE polarization. The inset also shows the electric field map associated with the resonance at 3.1 μm (surface plasmon resonance) and 4.5 μm (cavity mode) in TM polarization, and in*

correspondence to the broad feature of the Fabry-Perot resonance observed in TE polarization.

3.2.2. Observation of spectral shift with applied bias

In order to operate the device as a photodetector, we employ the grating stripes as interdigitated electrodes. The generated current thus circulates *in the plane* upon bias application since the presence of the PMMA layer blocks the vertical transport. The planar transport is crucial to observe bias tunability in our device, as shown in the following. Figure 3.4a compares the normalized photocurrent spectra of the plasmonic device with a reference device and with the absorption spectrum of the NC ink. The reference sample was prepared by depositing 150 nm HgTe film on prepatterned array of electrodes separated by 10 µm distance, much larger than the device operation wavelength. Therefore, no optical resonances are expected in the reference device but only a photocurrent peak at the exciton energy. Indeed, the reference device gives a photocurrent spectrum in good agreement with the ink solution absorption. On the contrary, the plasmonic device's spectrum presents a narrow peak at the band edge, demonstrating the effect of the photonic structure. Furthermore, the photocurrent spectra are clearly polarized, as shown in Figure 3.4b.

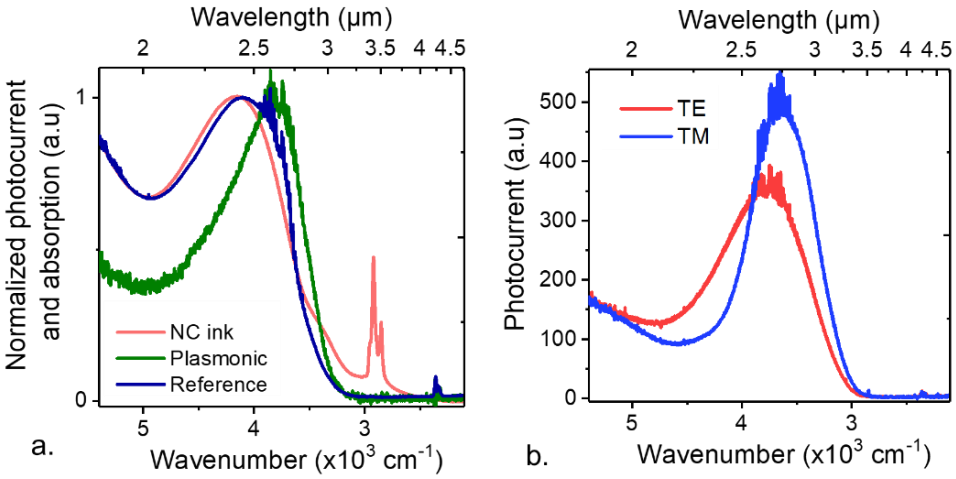

Figure 3.4: Photocurrent spectra of the plasmonic device. *a. Normalized measured photocurrent spectra of the plasmonic device with MDM structure (green) under 0.2 V applied bias at 80 K, the reference device (blue) under 1 V applied bias at 80 K, and absorption spectrum of the NC ink at room temperature. The reference device's photocurrent spectrum follows very well the absorption spectrum of the ink solution, while the MDM structure presents a strong photocurrent peak at the band edge. b. Photocurrent spectra of the MDM structure under TE and TM polarizations at 80 K.*

Noticeably, when the applied bias is varied, we observe a spectral shift in the photocurrent spectrum of the plasmonic device, which was not observed in the reference device even under much higher bias voltages (*i.e.,* comparable induced electrostatic field), see Figure 3.5a and c. Note that the spectral response in Figure 3.5a was measured with devices prepared with the same geometrical parameters but with a different batch of NCs, thus the exciton peak is slightly shifted compared with that of the spectra in Figure 3.4a. However, we consistently observed the spectral shift with bias in all fabricated devices.

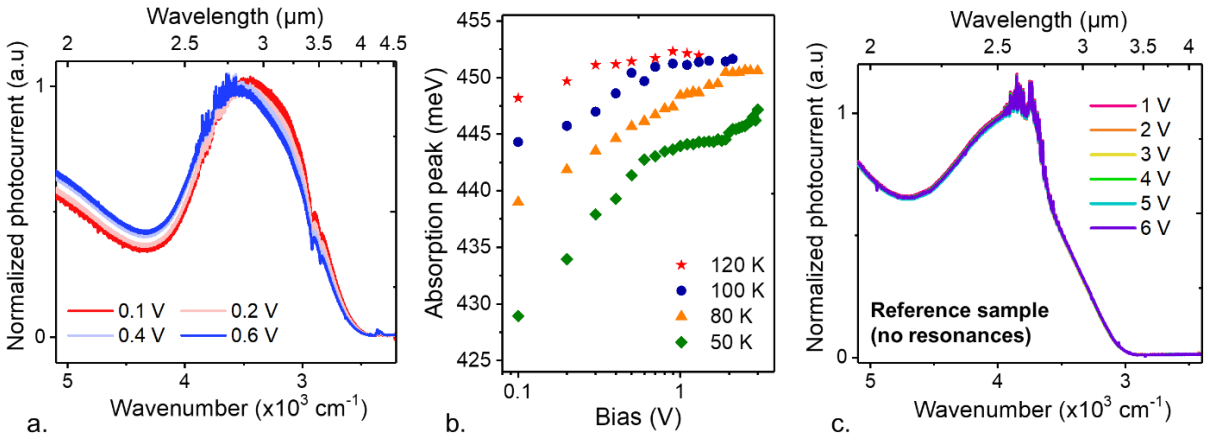

Figure 3.5: Bias-tunable spectral shift. *a. Photocurrent spectra with unpolarized light under various applied bias voltages for the plasmonic device, measured at 50 K. b. Energy of the photocurrent peak as a function of the applied bias at different operating temperatures. c. Photocurrent spectra for unpolarized light at various applied bias voltages for the reference device, measured at 80 K.*

The shift with bias is present in both TM and TE polarizations, see Figure 3.6, and is fully reversible when bias is suppressed. Furthermore, a blue shift is observed for both bias polarities when the applied bias increases in magnitude. It was also noted that a *stronger shift* with bias could be observed *at low temperatures*, as a 15 meV blue shift can be generated when the applied bias is tuned from 0.1 V to 3 V at 50 K, see Figure 3.5b. This blue shift is somehow counterintuitive because applying an electric field on size-confined semiconductors usually leads to a redshift as the electron and hole wavefunctions “leak” into the potential barriers. We thus look into possible mechanisms for the phenomenon.

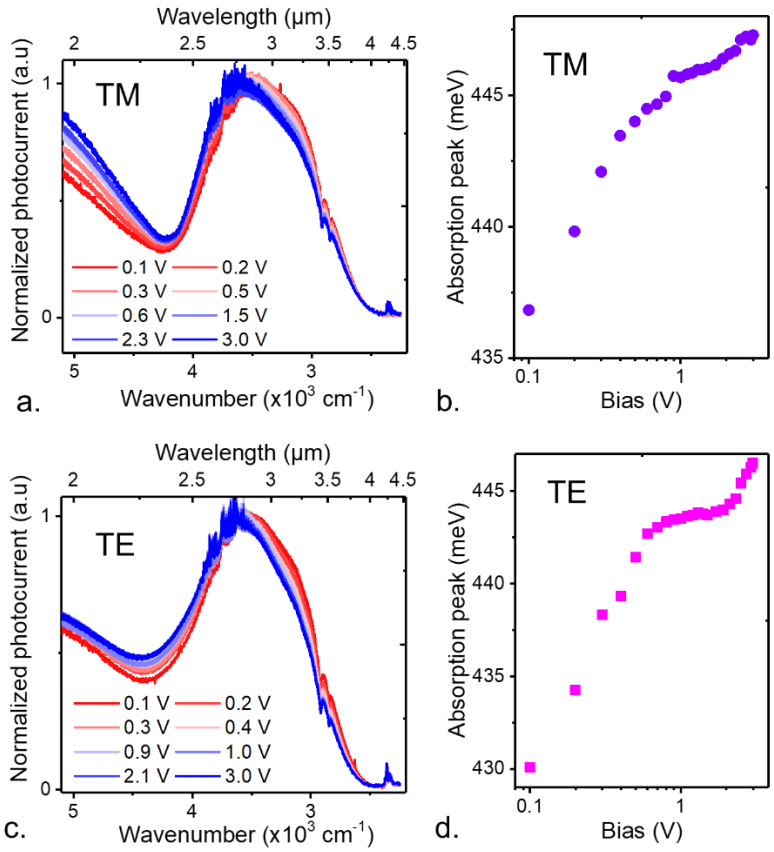

Figure 3.6: Effect of polarization on the spectral shift*. a. (resp. c.) Photocurrent spectra of the plasmonic device for TM (resp. TE) polarization under various applied bias voltages, at 50 K. b. (resp. d.) Energy of the photocurrent peak as a function of the applied bias for TM (resp. TE) polarization.*

3.2.3. Discussion on possible physical origins of the spectral shift

As mentioned in previous sections, a shift induced by applied bias is typically related to Stark effect in quantum-confined materials. We examined this hypothesis with tight-binding simulations [158], [159], considering a spherical shape for HgTe particles with a diameter of 6.4 nm under a uniform electric field. The simulations were performed by Christophe Delerue (IEMN, Université de Lille) and predicted a 6 cm^{-1} (less than 1 meV) redshift of the ground energy transition under 100 $kV{\cdot}cm^{-1}$ external electric field, see Figure 3.7. In contrast, we observed a shift of opposite sign of more than 15 meV under 40 $kV{\cdot}cm^{-1}$ (3 V over 0.85 µm electrode spacing) in our device at 50 K. Furthermore, if the Stark effect were at play, we should have observed a spectral shift in the reference device, as opposed to what was shown in Figure 3.5c. We can conclude that the observed shift is not induced by an effect of the electric field on the electronic states of the NCs.

The next possible cause of the spectral shift is Joule effect. As a bias is applied, the current flowing within the device may generate heat. HgTe NCs present an inverted temperature dependence of the bandgap, leading to a blueshift of the bandgap upon heating, as presented in Figure 3.8a. To quantify this effect, we performed a series of photocurrent spectra at various temperatures and found a 120 $\mu eV{\cdot}K^{-1}$ value for dEg/dT for NCs at this size, see Figure 3.8b.

Hence, the 15 meV observed shift would correspond to an increase of 120 K in temperature, which is improbable to be induced by the negligible Joule dissipated power ($RI^2 \approx$ a few nW under 1 V bias $\ll$ several mWs cooling power of the cryocooler at 80 K) in our device at low temperatures. Moreover, this heating should be more critical when the device resistance is reduced (*i.e.,* at higher temperatures). In contrast, in our device, the opposite trend is observed (*i.e.,* a more noticeable shift as temperature decreases). Therefore, we ruled out Joule heating as the spectral shift's origin.

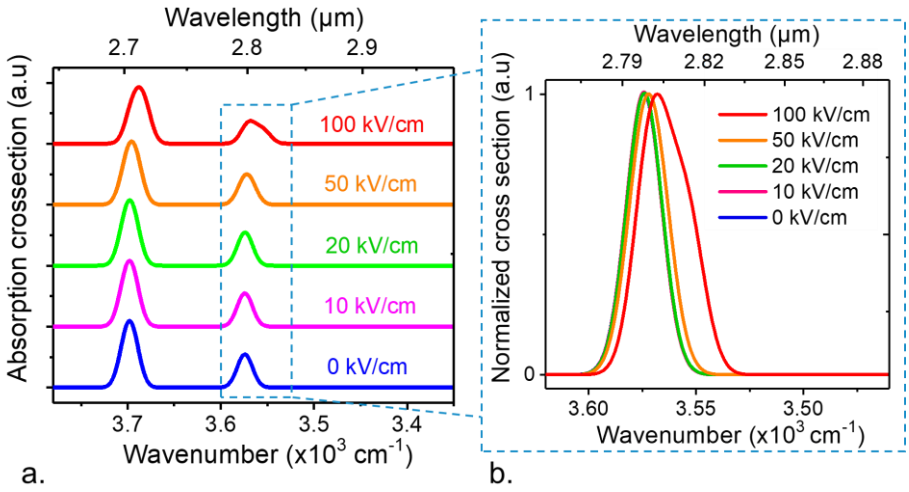

Figure 3.7: Tight binding simulation under static electric field. *a. Absorption cross-section of HgTe NCs under different applied electric field. The spectra show a clear red-shift trend when a stronger electric field is applied. Under a large field (>100 kV.cm^{-1}), the two states in the ground transition start to split, and two distinct contributions can be seen. b. Normalized absorption cross-section of the 1st exciton transition. Stark effect on such confined HgTe NCs leads to a conventional redshift of the spectrum and is thus not responsible for the observed blueshift of our device. The simulations have been performed by C. Delerue (IEMN, Lille).*

We then investigate if the spectral shift can be induced by a variation of the carrier density with the electric field. For this, we use the PMMA layer as a gate dielectric to apply a large electric field to the NC layer. No shift is observed while the magnitude of the gate-induced electric field (1 V over 20 nm of PMMA) corresponds to 500 kV·cm^{-1}, which is one order of magnitude larger than the drain-source electric field applied to generate the shift, see Figure 3.8c. As a consequence, the observed shift cannot be induced by a variation in the carrier density.

It should be also pointed out that even devices with smaller electrode spacing, with ≈50 nm separation between the electrodes [91], and consequently with even larger applied electric fields, do not present such a bias dependence of the photocurrent spectrum. Therefore, it is suggested that the device architecture, generating a specific coupling between the exciton and the optical modes of the plasmonic structure, is at the origin of this spectral response tunability. We thus discuss this light-matter coupling in the following section.

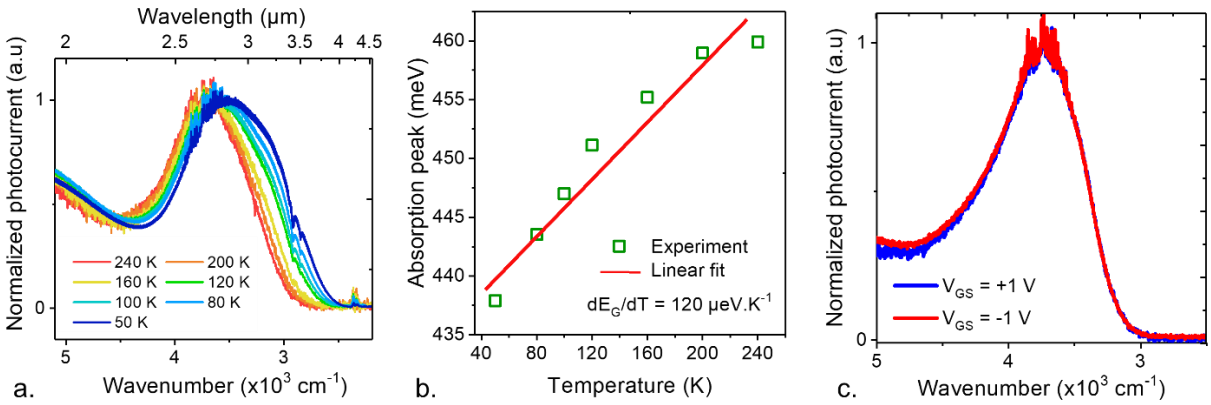

***Figure 3.8: Impact of temperature and carrier density on the photocurrent spectrum**. a. Unpolarized photocurrent spectra of the cavity device at various temperatures, with 0.3 V applied bias. b. Energy of the first exciton as a function of the temperature. A linear fit with a 120 µeV·K^{-1} slope is also shown. c. Photocurrent spectra for non-polarized light for two different gate bias voltages.*

3.2.4. Interplay between the transport and absorption inhomogeneity

The mechanism governing bias reconfigurability can be revealed by looking into the light absorption of the device and the carrier transport properties of the NCs. In the following, we begin with the field-dependence transport in HgTe NCs before showing how this property is important to generate bias-tunability when combined with the specific NC absorption in a plasmonic device.

Field-dependent transport in HgTe NC films

Concerning carrier transport, NCs present peculiar transport properties resulting from the hopping mechanism. The diffusion lengths of the carriers are typically far below the device size. As a result, charge collection is more efficient in the vicinity of the electrodes. However, it has also been proposed that hopping conduction is a bias-dependent process, in which the carrier mobilities and, thus, the diffusion lengths depend on the external electrostatic field [160]–[162]. In particular, Nenashev *et al.*, considering a hopping system with Miller-Abraham transition rates and Gaussian disorder model, show that the mobility of hopping carriers can be strongly increased in the presence of applied electric field [163]. Recently, Xing *et al.* suggested that an external electric field can enhance carrier mobility as a result of the shortened effective path lengths across the NC film [164]. In order to probe the carrier transport under applied bias, we built on a Si/SiO_2 substrate a field-effect transistor whose conductive channel comprises a 150 nm HgTe NC film. Here, the gate insulator is a 300 nm SiO_2 layer with a capacitance per unit area of 11 nF·cm^{-2}. A scheme of the FET device is shown in Figure 3.9a.

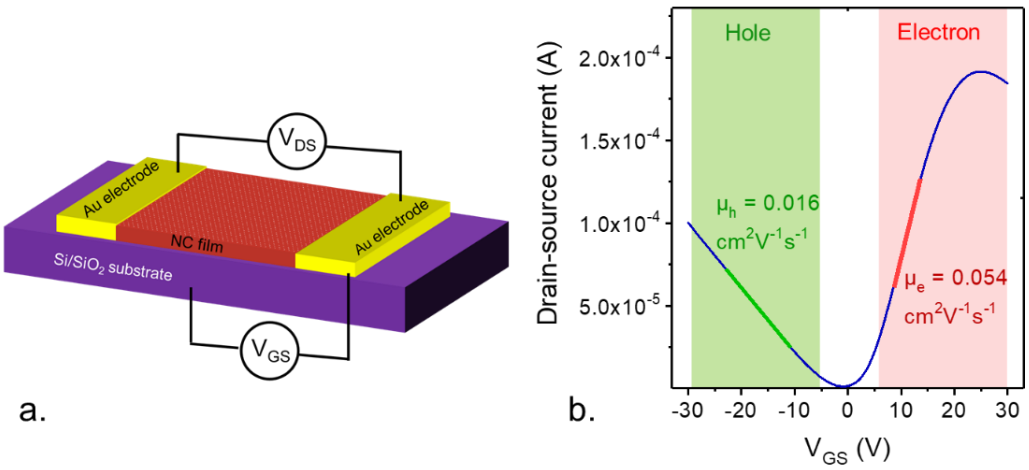

Figure 3.9: HgTe NC field-effect transistor. *a. FET device on Si/SiO₂ substrate to probe carrier transport. b. FET transfer curve as a function of gate potential V_{GS} when a bias V_{DS} = 2 V is applied between the drain and source electrodes, at 120 K. Linear regions for hole and electron transports are highlighted by the green and red lines, respectively.*

We operate the FET in the linear regime, which allows field-effect carrier mobilities to be extracted from the linear regions of the transfer curve, see Figure 3.9b. For a source-drain voltage V_{DS} negligible with respect to the gate voltage V_{GS}, the mobility is calculated as:

$$\mu = \frac{L}{W \cdot C_i \cdot V_{DS}} \times \frac{\partial I_{DS}}{\partial V_{GS}} \tag{3.1}$$

where L is the channel length, W is the channel width, C_i is the gate insulator capacitance per unit area (11 nF.cm^{-2}), I_{DS} is the drain-source current [74]. This formula is applied to extract the electron and hole mobilities for different values of the source – drain voltage at different temperatures.

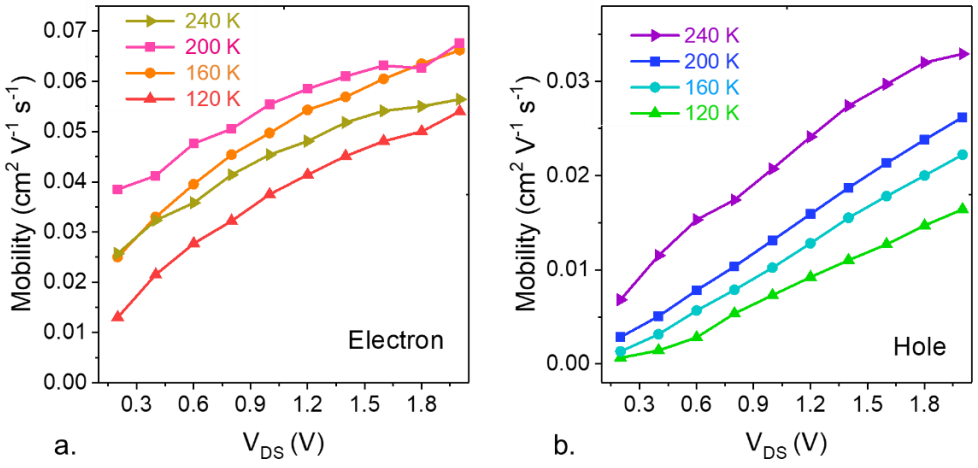

Figure 3.10: Carrier mobilities in HgTe NCs as a function of the applied bias. *a. (resp b.) Extracted electron (resp. hole) mobility as a function of drain-source bias (V_{DS}) at various temperatures. As the applied bias increases, we observe an increase in carrier mobilities.*

We observe an increase in both electron and hole mobilities under increased applied source-drain bias. Notably, at 120 K, electron mobility presents a 4-fold increase from 0.013 cm^2 V^{-1} s^{-1} to 0.054 cm^2 V^{-1} s^{-1} when the drain-source bias increases from 0.2 V to 2 V. On the same bias voltage range, hole mobility shows an even more significant, 26-fold, increase, from

6.2×10^{-4} cm^2 V^{-1} s^{-1} to 0.016 cm^2 V^{-1} s^{-1}, see Figure 3.10. Furthermore, it is also worth noting from Figure 3.10 that the increase in carrier mobilities with bias voltage is more significant at low temperatures. This is due to the fact that at low temperatures, thermal effect does not provide sufficient energy to support the carrier transport.

The bias-dependence of mobility was observed from 120 K to 240 K. This increase of carrier mobility under applied electric field is rather significant, and it can be related to an increase in the carrier diffusion length, L_D. Indeed, $L_D=(D.\tau)^{1/2}$ with D the diffusion coefficient and τ the carrier lifetime. Einstein's electrical mobility equation links the diffusion coefficient and the carrier mobility μ through $D=\mu k_B T/e$, with k_B the Boltzmann constant, e the elementary charge, and T the temperature. This leads to $L_D=(D.\tau)^{1/2}=(\mu k_B T/(e.\tau))^{1/2}$. Assuming that the carrier lifetime τ remains mostly unaffected by electric field application, the 4 and 26-fold increases in mobility with bias correspond to 2 and 5-fold increases in the carrier diffusion lengths for electrons and holes, respectively. In our plasmonic device, the applied bias induces electrostatic field in the planar direction. The carrier diffusion lengths are thus expected to extend horizontally as the applied bias increases.

Absorption inhomogeneity in the NC film and the origin of the spectral shift

We then analyzed the device absorption maps at the optical resonances. Figure 3.11a and c show the simulated absorption maps at the surface plasmon resonance under TM polarization and the Fabry-Perot resonance under TE polarization, respectively. In both cases, the maps appear to be strongly inhomogeneous. In particular, the NC absorption is greatly enhanced between, rather than above, the grating stripes. Furthermore, the normalized NC absorption spectra in Figure 3.11c and d show that the areas between the stripes (indicated as Region 1 in Figure 3.11a and b) present a maximum of the NC absorption blue-shifted compared to those above the stripes (indicated as Region 2 in Figure 3.11a and b).

As discussed in the previous section, increasing the applied bias between the electrodes leads to an increase in the carrier diffusion lengths in the planar direction. Photocarriers generated in Region 1 can thus reach the electrodes more efficiently as the bias voltage increases. Hence, the weight from the absorption occurring in Region 1 becomes more important for increased voltages, leading to the observed blueshift of the photoresponse. We then attribute the bias-induced spectral shift to the interplay between the field-dependent hopping transport in HgTe NCs and the inhomogeneous absorption induced by the plasmonic cavity.

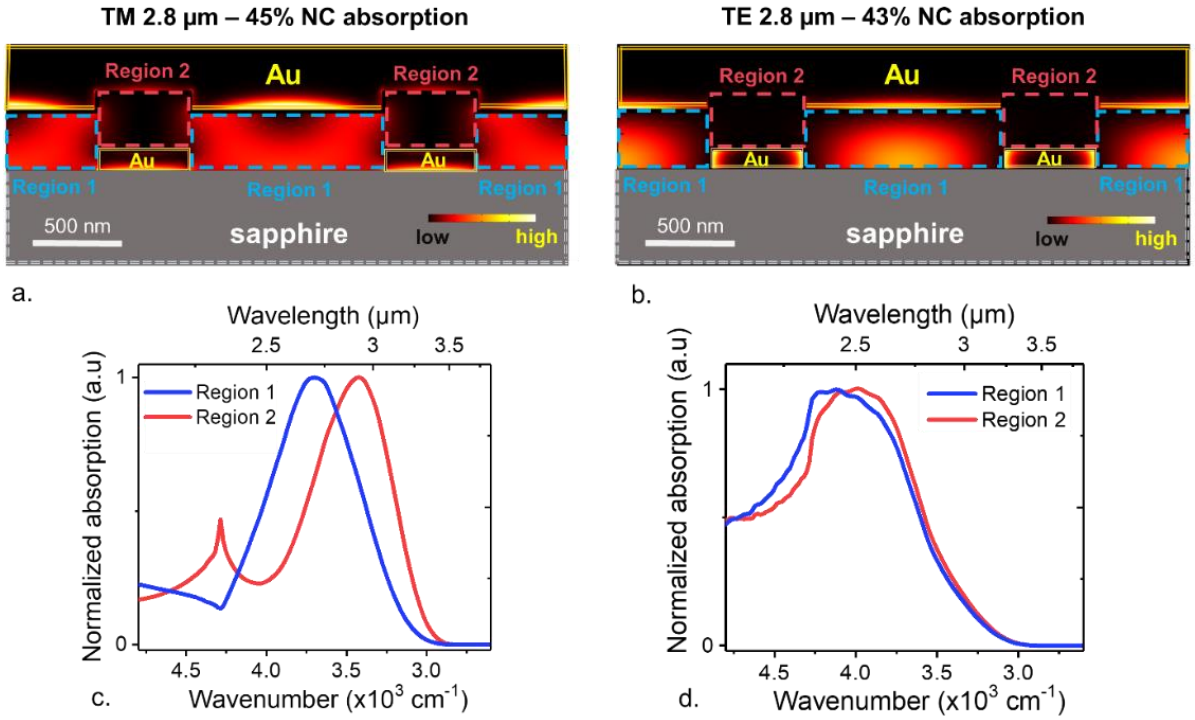

Figure 3.11: Absorption maps at the resonant wavelengths*. a (resp. b). Simulated absorption map for the SPP (resp. Fabry-Perot) resonance under TM polarization (resp. TE polarization). For the NC film, we define two zones: Region 1 is between two neighboring grating stripes, Region 2 is above the metallic stripes. The absorption map is strongly inhomogeneous as the absorption is mainly enhanced in Region 1. c (resp. d). Simulated normalized NC absorption spectra in Region 1 and 2 defined on part a (resp. b). The absorption in Region 1 is slightly blue-shifted compared to the absorption in Region 2.*

To illustrate the effect for the case of the surface plasmon resonance, we have plotted the maps of the product between the position-dependent NC absorption *Abs(r)* (Figure 3.11a) and a Gaussian term $exp(-r^2/(2L_D^2))$, with *r* the distance from the different positions in the NC film to the electrodes. The Gaussian term is proportional to the collection efficiency in a diffusive model. $Abs(r) \times exp(-r^2/(2L_D^2))$ maps thus represent the contribution from the different positions in the NC film to the overall photocurrent signal. We plot the maps with L_D = 20 nm, 50 nm, 100 nm, and 200 nm at the surface plasmon resonance in Figure 3.12a-d. As L_D increases, we see an apparent increase in the signal from the areas between the electrodes (Region 1). Furthermore, we can plot the spectral response of the device, by integrating the product $Abs(r,\lambda) \times exp(-r^2/(2L_D^2))$ over the NC film for each wavelength of interest. A blueshift of the spectral response with increasing diffusion length, corresponding to experimentally increasing the applied bias voltage, is observed for both polarizations, as shown in Figure 3.12e-f. Thus, using simple assumptions, our model nicely depicts the spectral shift resulting from the field-dependent transport in the NC array.

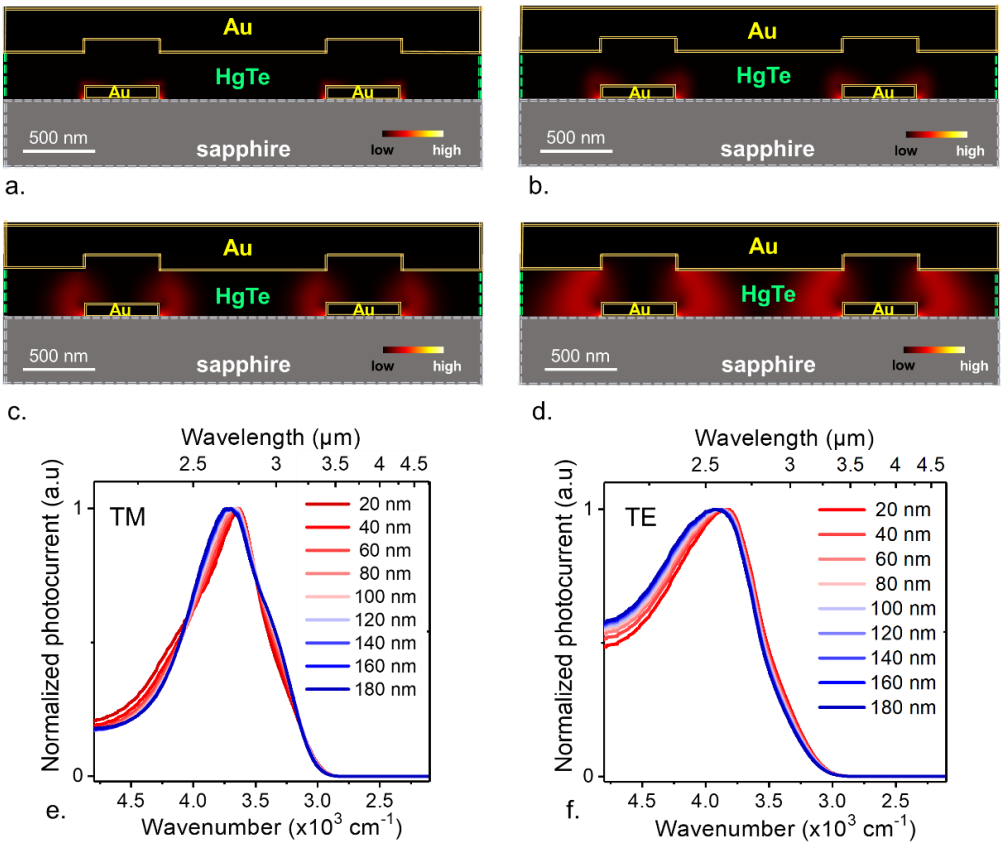

Figure 3.12: Illustration for the origin of the bias-induced shift. *a-d. Absorption maps at the SPP resonance normalized by a Gaussian term exp(-r^2/2L_D^2), with r the distance to the electrode while L_D is set equal to 20 nm, 50 nm, 100 nm, and 200 nm for a, b, c, and d, respectively. As L_D increases, the contribution of the region between the electrodes becomes more important. e (resp. f). Normalized calculated photoresponse for various L_D values for TM polarization (resp. TE polarization). In both cases, we observe a blueshift in the modeled photoresponse.*

Overall, two requirements should be met to obtain reconfigurable photoresponse in NC-based photodetectors: (*i*) the photonic structure needs to generate an inhomogeneous NC absorption within the device, (*ii*) the charge collection needs to be electric field dependent. The last condition is an inherent property of hopping conduction. Understanding the mechanism leading to the spectral shift allows us to engineer novel NC-based devices with a controlled bias-selectable spectral response. In the following sections, we present two devices, in which on-demand electromagnetic maps and charge collection through hopping have been exploited to provide novel functionalities through bias-dependent photoresponse.

3.3. Spatial design of the absorption map

The previous section shows that the field-dependent transport is an interesting property of HgTe NCs, which can be employed to generate bias-tunable photoresponse in NC-based photodetectors. However, the bias-induced spectral shift in the previous design was very limited, as the shift remains considerably smaller compared with the linewidth of the exciton absorption. In this section, we demonstrate a grating architecture with significant improvement in the spectral control of the resonances. The bias modulation, as shown later, is related to

two resonances located in the SWIR and MWIR ranges. Thus, the reconfigurable response will be demonstrated between two optical bands. The section begins with introducing the material and optical design of the photodetectors, followed by the demonstration of bias-reconfigurability. In the last section, we will show some photodetection characterization of the device at different applied bias voltages.

3.3.1. Spectral design of the resonances with a metallic grating

The geometry of our detector is depicted in Figure 3.13a. Despite being a simple geometry, a grating coupled to a NC film offers several degrees of freedom for the design of the light-matter coupling (*i.e.,* the grating period *p*, the electrode size *s*, and the film thickness t_{NC}). As we target photodetection in the SWIR and MWIR, HgTe NCs with spherical shape and cut-off absorption wavelength of around 3.5 µm at room temperature were synthesized, see Figure 3.13b. As usual, liquid phase transfer was performed to exchange the initial long capping ligands for hybrid passivation combining short thiols and ions. Smooth, conductive NC films were then obtained by spin-coating.

We also prepared a reference sample with a 150 nm photoconductive film of this material on prefabricated electrodes (10 µm electrode spacing, with no generated optical resonances in the considered range). Figure 3.13c shows the photocurrent spectra measured on the reference sample at 80 K under various applied bias voltages. Apart from the redshift compared to the initial absorption spectrum owing to the ligand exchange process and the temperature effect, the reference device presents no bias-tunable photoresponse.

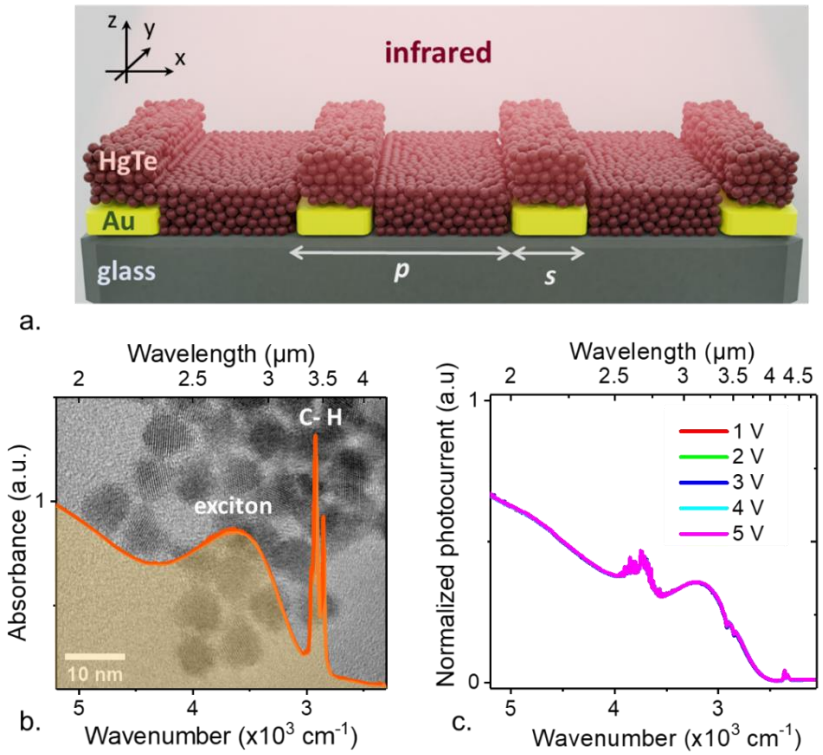

Figure 3.13: Design of the infrared sensor and HgTe NCs for the absorbing layer. *a. Illustration of the HgTe NC infrared detector with grating geometry on a glass substrate. Optical properties of the device are defined by the grating period p and stripe size s. b. Room-temperature absorption spectrum of the HgTe NCs in solution. The background is a high-*

resolution transmission electron microscopy image of those HgTe NCs. c. Photocurrent spectra of the reference interdigitated device, with 10 µm spacing between the electrodes. The spectra, obtained at different applied voltages, are almost identical.

For the resonator device, we intend to use the interdigitates electrodes also as grating stripes, allowing a inhomogeneous NC absorption. Therefore, the objective of optical design is to introduce two electromagnetic modes. The first mode is located in the vicinity of the electrodes in order for photogenerated carriers to be collected under low applied electric fields. The second mode is located away from the electrodes to generate photocarriers that will only be collected under higher electric fields. We obtain this objective by exploiting two resonances under TE polarization: a guided-mode resonance and a Fabry-Perot resonance.

Fabry – Perot resonance under TE polarization

A Fabry-Perot mode can be generated by taking advantage of the impedance mismatch between the areas in the openings between the electrodes and those on the top of the gold. The Fabry-Perot resonance, spatially located between the electrodes, can be generated as long as the gold and NC film thicknesses are well-chosen, see Figure 3.14a. The resonance wavelength of this mode is driven by the opening size $o = p\text{-}s = 2 \cdot n_{eff} \cdot \lambda_{FP}$, where n_{eff} is the effective index of the mode, p is the grating period, and s is the electrode size. By choosing o= 1 µm, we set the Fabry - Perot resonance to match the NC exciton, with a peak around 3.2 µm at low temperature, see Figure 3.14c. The TE dispersion map of the device confirms the nature of this Fabry-Perot resonance with a dispersionless feature around 3100 cm^{-1}, resonant with the exciton peak, as shown in Figure 3.14d. We then design the mode near the electrodes by exploring optical resonances depending on the other geometrical parameters.

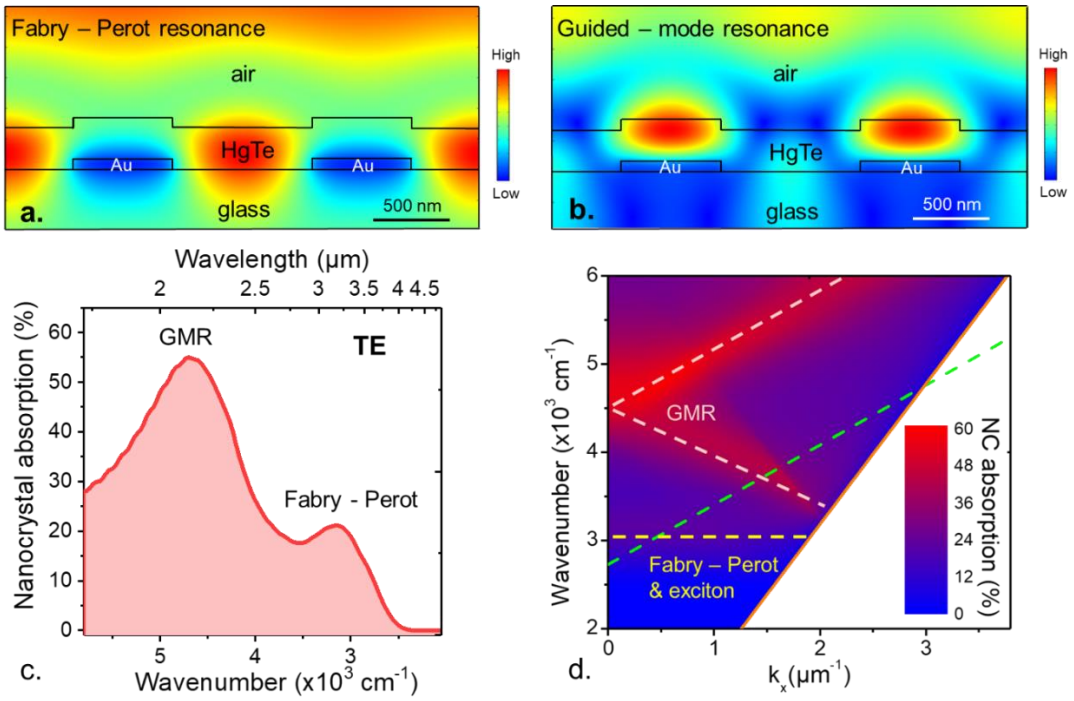

Figure 3.14: Simulated optical properties of the device under TE polarization. *a. Electric field map $|E|$ of the Fabry-Perot resonance under normal incidence. The strong field is concentrated in between the gold stripes. b. Electric field map $|E|$ of the guided-mode*

resonance under normal incidence. The strong field is concentrated on top of the gold stripes. c-d. Simulated NC absorption spectrum under normal incidence in TE polarization and dispersion map of the device with p = 1650 nm, s = 650 nm and t_{NC} = 260 nm. The Fabry – Perot resonance is indicated by the yellow dashed line. The diffraction order limit for m = 1 in equation 3.2 is indicated by the green dashed line. The GMR is indicated by the pink dashed line. The light line for light propagating in air is indicated by the orange continuous line.

Guided – mode resonance under TE polarization

Thanks to the presence of the grating, the diffraction orders of the incoming light can be coupled with a waveguide mode. This mode is mainly confined in the NC film thanks to its greater refractive index ($n_{NC} \approx 2.35$) compared to that of air ($n_{air} = 1$) and of the substrate material ($n_{glass} \approx 1.5$). This is referred to as a guided-mode resonance (GMR) [90], [146].

More importantly, at normal incidence, the GMR focuses light on the NCs above the grating stripes, spatially separated from the Fabry-Perot resonance, see Figure 3.14b. As it relates to a diffraction phenomenon, the GMR absorption peak strongly depends on the grating period *p* and the NC film thickness t_{NC}, as shown in Figure 3.15. Here, we have set *p = 1650 nm* and t_{NC} *= 260 nm* such that the GMR peak is around 2.2 µm under normal incidence, see Figure 3.14c.

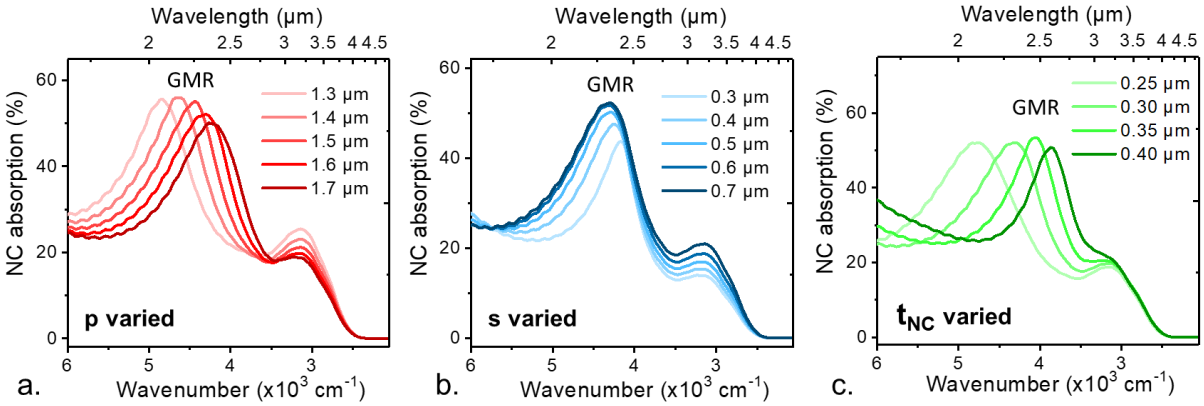

Figure 3.15: Impact of the grating geometrical parameters on the GMR. *a. Simulated absorption spectra under TE polarized radiation for fixed stripe size s = 650 nm and NC film thickness t_{NC} = 260 nm with different grating period p values. b. Simulated absorption spectra under TE polarized radiation for fixed period p = 1650 nm and NC film thickness t_{NC} = 260 nm with different stripe size s values. c. Simulated absorption spectra under TE polarized radiation for fixed stripe size s= 650 nm, and period p = 1650 nm with different NC film thickness t_{NC}.*

The GMR resonance is identified from the following considerations. Considering a TE polarized wave incident on the structure depicted in Figure 3.13a, the wavevector *k* of the light in the NC film satisfies:

$$k^2 = {k_x}^2 + {k_z}^2 = {n_{NC}}^2 {k_o}^2$$

where k_o is the wavevector in air, n_{NC} is the refractive index of the NC film. Note that $k_y = 0$ as we are considering TE polarization. Diffraction orders appear in the NC film as

$$k_z \geq 0 \Rightarrow n_{NC} k_o \geq k_x$$

The grating coupling condition states that

$$k_x{}^{(m)} = k_x \pm m\frac{2\pi}{p}$$

where *m* is an integer number, p is the grating period. So, the limit for this order to appear is equivalent to

$$n_{NC}k_o = k_x{}^{(m)} \quad (3.2)$$

Replacing $E = \hbar c k_0$ into equation 3.2 allows us to plot the limit for diffracted orders to appear in the dispersion map. Figure 3.14d shows the limit for *m = 1* (green dashed line) in our structure. Furthermore, the slope of GMR must follow the slope of diffracted lines, as is the case here. The dependence of the observed absorption feature on the incidence angle and the existence of diffracted orders in the NC film confirm that the feature we are looking at is associated with a GMR.

With the two modes designed to be separated spectrally and spatially (Figure 3.14a-c), we expect to see bias reconfigurability when the device is illuminated under TE polarization. We next discuss the infrared resonances under TM polarization.

Resonances under TM polarization

The dispersion map of our device under TM polarization in Figure 3.16a indicates that there are different resonances spectrally overlapping with the NC exciton. The spectra confirm the presence of several resonances since not obvious changes can be observed in the absorption peaks when the geometrical parameters of the grating are varied, as presented in Figure 3.16b-c. We did not identify all the resonances under TM polarization and focus on the spatial distribution of NC absorption.

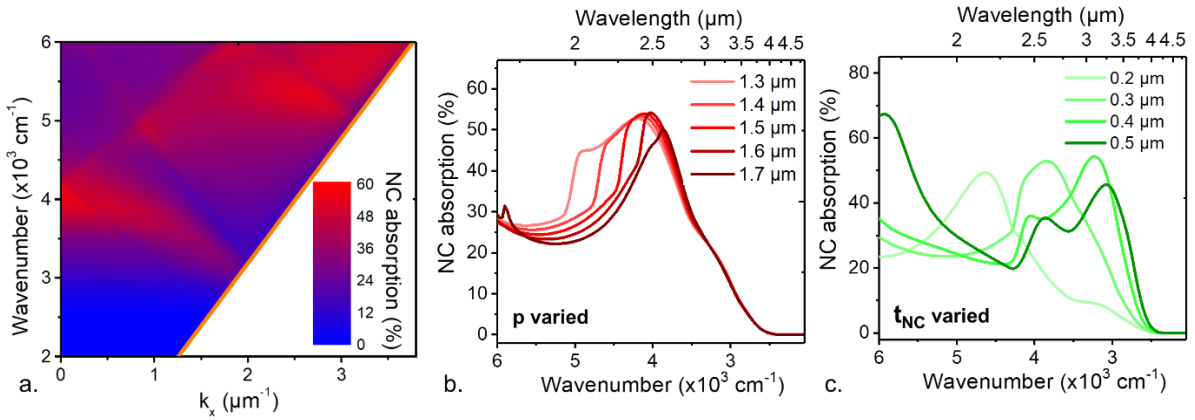

Figure 3.16: Optical properties of the device under TM polarization. *a. Dispersion map of the device with p = 1650 nm, s = 650 nm, and t_{NC} = 260 nm in TM polarization. The light line is indicated by the orange continuous line. b. Simulated absorption spectra under TM polarized radiation for fixed stripe size s = 650 nm and NC film thickness t_{NC} = 260 nm with different grating period p values. c. Simulated absorption spectra under TM polarized radiation for fixed stripe size s= 650 and period p = 1650 nm with different NC film thickness t_{NC}.*

Figure 3.17a shows the electric field map at 4000 cm^{-1} under normal incidence in TM polarization. The resonances strongly enhance the electromagnetic field and absorption of the NC film above the electrodes. Expectedly, the simulated absorption of the NCs between the grating stripes is much lower than that of NCs above the stripes, see Figure 3.17b. Therefore, a negligible voltage dependence is anticipated for the device photoresponse under TM polarization.

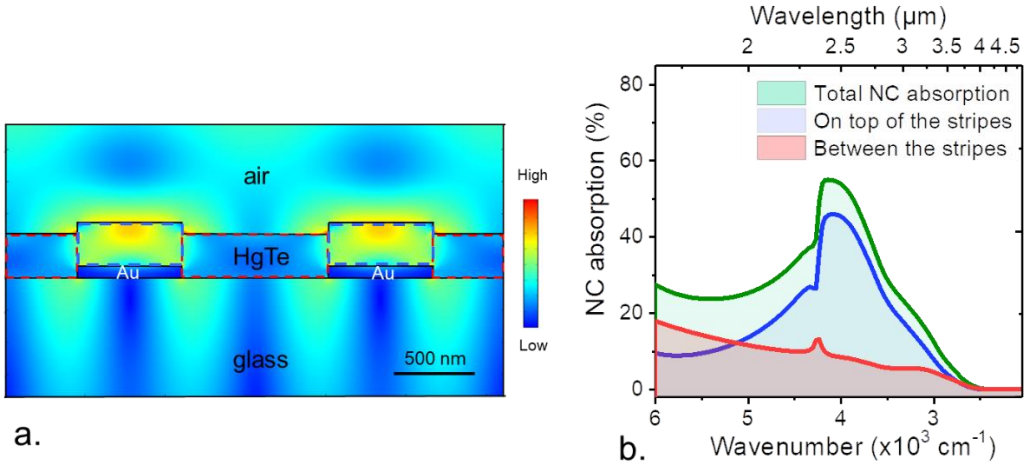

Figure 3.17: Electric field map and NC absorption spectra at the resonance wavelength under TM polarization. *a. Simulated electric field map at 4000 cm^{-1} (=2.5 μm) under normal incidence in TM polarization. b. Total NC absorption spectrum and NC absorption spectra in the different areas highlighted with dashed boxes in part a. The figure shows that at resonant wavelength 2.5 μm, absorption by NC mainly occurs above the stripes.*

3.3.2. Device characterization

Bias-modulated photoresponse

With the optical properties of the device established, we then conducted photocurrent measurements to examine the bias dependence of the fabricated device. Figure 3.18 shows the photocurrent spectra of the device as a function of various bias voltages at 80 K for TE and TM polarizations. The photocurrent spectra under TE polarization, as predicted, present two features associated with the GMR and Fabry-Perot resonances, in very good agreement with the simulated NC absorption in the device (Figure 3.14c). Furthermore, a notable photoresponse tunability with applied bias can be observed in Figure 3.18a.

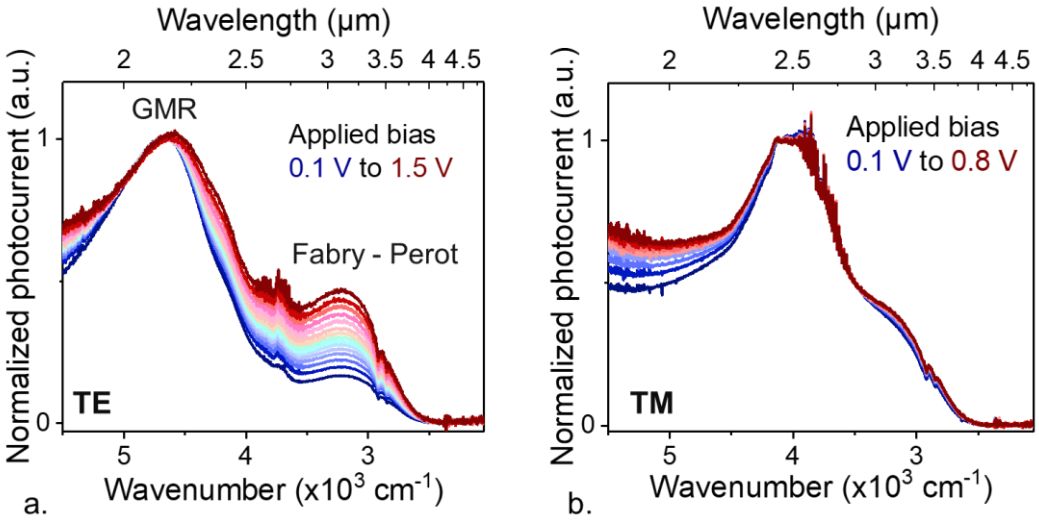

Figure 3.18: Bias tunability of the grating resonator. *a. Normalized photocurrent spectra of the device in TE polarization under various applied biases from 0.1 V to 1.5 V (step of 0.1 V), at 80 K. b. Normalized photocurrent spectra of the device in TE polarization under various applied biases from 0.1 V to 0.8 V (step of 0.1 V), at 80 K.*

In contrast, no significant change in the photocurrent spectrum was observed when the incident light is TM polarized, see Figure 3.18b.

The amplitude of the TE Fabry-Perot resonance grows as the applied bias increases with respect to the GMR resonance, as it can be seen in the photocurrent spectra normalized to the GMR peak. Note that this spectral modulation is fully reversible (*i.e.,* the Fabry-Perot peak decreases when the applied bias decreases) and is not dependent on the bias polarity. Here, Stark effect can be excluded as a possible mechanism to explain the origin of this bias reconfigurability since we observed no bias tunability in the reference device (Figure 3.13c). Moreover, Stark effect will affect both polarizations in the same way.

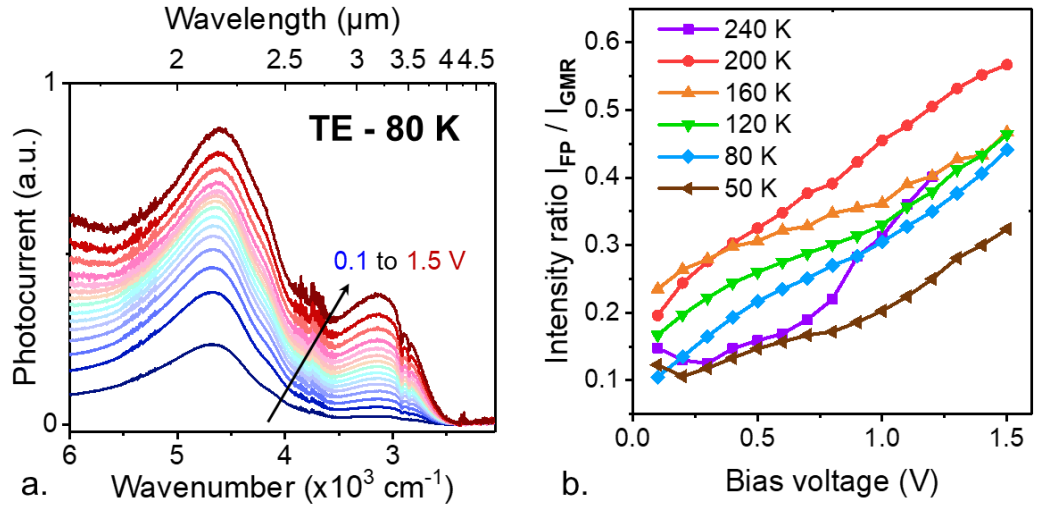

Figure 3.19: Photocurrent spectra under TE polarization at 80K and bias modulation at various temperatures. *a. Photocurrent spectra (non-normalized) of the device in TE polarization under various applied biases from 0.1 V to 1.5 V (step of 0.1 V), at 80 K. b. Intensity ratio between the Fabry-Perot resonance and the GMR in TE polarization as a function of applied bias at various temperatures.*

The bias dependence of the spectral response in our device under TE polarization was observed in a wide range of temperatures, from 50 K to 240 K, see Figure 3.19b, while the TM photocurrent spectrum remained almost unchanged. It should be noted that the intensity ratio of the two TE resonances increases when the photocurrent signal from both resonances also increases with the applied bias, see Figure 3.19a. We attribute this modulation to different degrees of overlap between the electromagnetic resonances and the induced electrostatic field. Since the grating is used as interdigitated electrodes, the in-plane electrostatic field component dominates. A greater field strength is established in the slits between neighboring electrodes than above the electrodes, as illustrated in Figure 3.20. Under low electric fields, charge collection mainly occurs near the electrodes, which favors the spectral weight of the nearby resonance, evidenced by a stronger spectral weight of the GMR in Figure 3.18a. When a large electric field is applied, charge collection from areas between the electrodes becomes more efficient. The spectral weight associated with the TE Fabry-Perot resonance, spatially localized away from the electrodes, increases. The drastic change in intensity ratio also raises a crucial point to NC-based infrared sensors' design rules, which have mainly focused on enhancing material absorption using optical resonators. It shows that spatially designing the resonances well aligned with the applied electrostatic field is also essential for efficient charge extraction, meaning that the optical modes can be effectively exploited. However, it is noteworthy that, although the Fabry-Perot resonance field (Figure 3.14a) fits better with the electrostatic field map (Figure 3.20a) than the GMR (Figure 3.14a), photocurrent is higher at GMR resonance because of its stronger field enhancement.

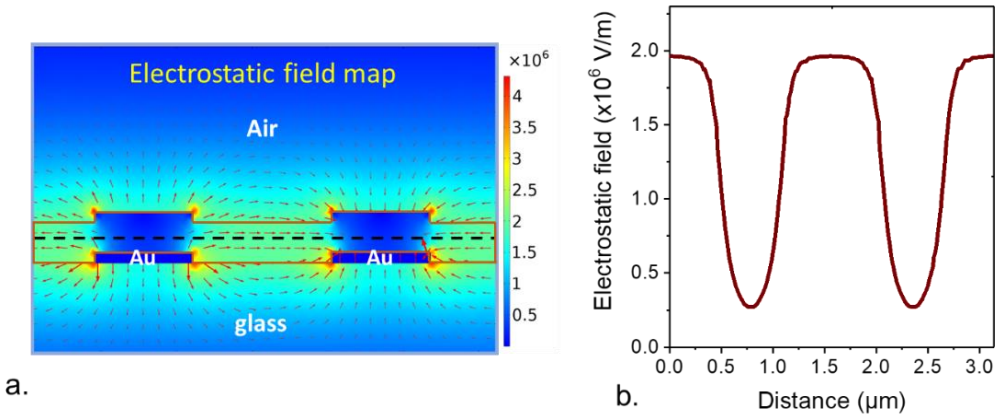

Figure 3.20: Electrostatic field map. *a. Simulated electrostatic field map when a bias voltage is applied between two neighboring electrodes. The color map indicates the magnitude of the electrostatic field. The red arrows indicate the direction of the electrostatic field. NC film is highlighted with the brown boundary. In the figure, electric potential of the electrodes on the left and right are set to +1V and -1V, respectively. The electrical conductivity of air, NC film and glass substrate are set to 10^{-14} S/m, 5 x 10^{-4} S/m and 10^{-12} S/m, respectively. b. Magnitude of the electric field along the dark dashed line in part a. This figure shows that the electrostatic field is mainly located in the area between the electrodes.*

Photodetection performance

The photodetection performance of the device was then characterized. First, the photocurrent signal was quantified with responsivity measurements. Under broadband radiation (blackbody at 980 ºC), the device's responsivity appears to depend strongly on the temperature. The

measured responsivity of the device reaches a maximum of ≈ 110 mA·W^{-1} at around 160 K to 180 K when a bias of 0.1 V is applied, see Figure 3.21a. Noticeably, we observe a significant decrease in responsivity when the temperature is higher than 200 K for a series of devices fabricated using the same material. This decrease can be attributed to the electron mobility drop above 200 K, previously shown in Figure 3.10a.

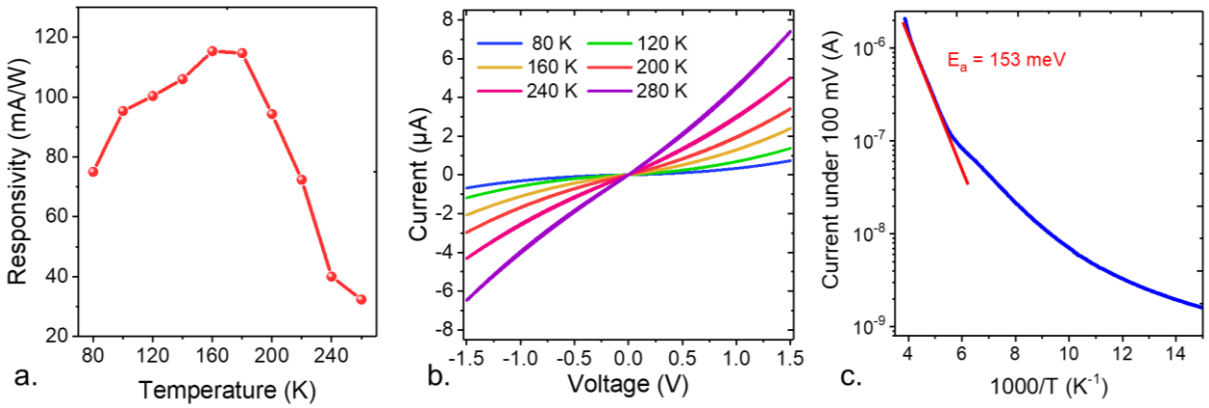

Figure 3.21: Responsivity and dark current of the device at different temperatures. *a. Responsivity of the device under broadband illumination (blackbody at 980 ºC) as a function of the temperature when biased with 0.1 V. b. I-V curves at various temperatures of the device. c. Dark current as a function of temperature of the device under 0.1V bias. Activation energy of the material is estimated to be around 153 meV using Arrhenius' fit.*

We then examined the dependence of the dark current on temperature. The I-V curve under the dark condition is linear at 280 K and appears more super-linear at low temperatures, as presented in Figure 3.21b. The dark current decreases monotonically with decreasing temperature. In addition, an Arrhenius fit for the current-temperature dependence gives an estimated activation energy of around 153 meV. This value is close to half of the material band-edge energy (≈180 meV), which is an expected characteristic for intrinsic semiconductors. Note that we do not rule out the existence of carrier doing in our sample, but the transport is dominated by their intrinsic properties. A high activation energy is advantageous for photodetection at low temperatures since the dark current can be drastically reduced upon cooling.

The device operation at cryogenic temperature was then characterized. A typical transient response of the device to 1.2 ns laser pulses using a 1.57 μm laser source is shown in Figure 3.22a, where a quick increase in the photocurrent is followed by a slower drop to the dark current values. The whole rise and decay process were estimated to be around 130 ns. Responsivity grows as a result of increased applied bias, as shown in Figure 3.22c, from 70 mA·W^{-1} to 320 mA·W^{-1} when the bias changes from 0.1 V to 1.5 V. However, current noise density also rises as the bias increases, see Figure 3.22b. The detectivity (at 1 kHz) of the device peaks at 7x10^{10} Jones for 0.2 V applied bias before steadily lowering while maintaining a value of more than 10^{9} Jones up to 1.5 V. Overall, our device, while can be straightforward for the fabrication process thanks to the basic geometry design, presents a fast response time while retaining a highly competitive detectivity in low-temperature operation.

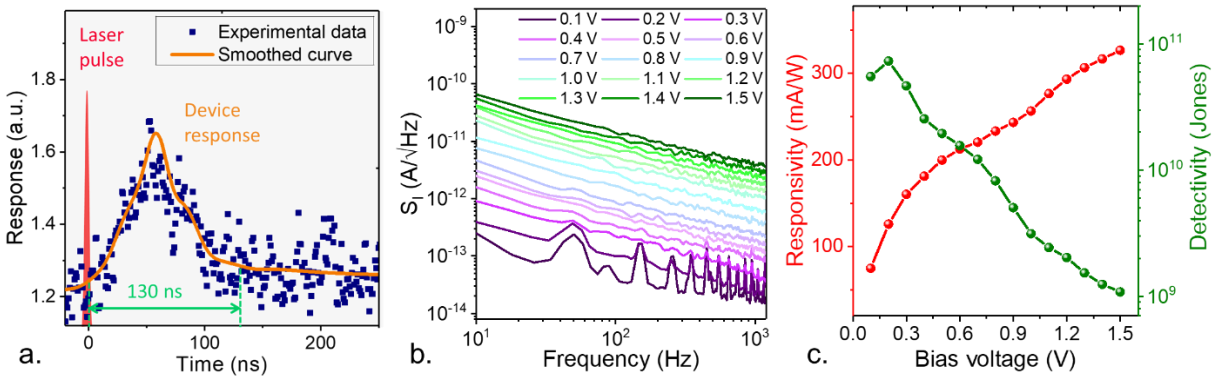

Figure 3.22: Photodetection performance of the device at 80 K. *a. Photoresponse of the device when illuminated with 1.2 ns laser pulses (λ = 1.57 µm), at 80 K. b. Noise measurement at different applied bias voltages at 80 K. c. Responsivity of the device under broadband illumination (blackbody at 980 ºC) and detectivity (at 1 kHz) of the device as a function of the applied bias, at 80 K.*

The grating device shows the importance of an optimized structure to further exploit the field-dependent transport for bias reconfigurability in NC-based photodetectors. Now that the key elements for bias tunability are well identified, in the following section another optical design will be proposed to further enhance the bias modulation effect.

3.4. Tuning spectral response with controlled charge collection

The work presented in this section was a collaborative effort between the ONERA, INSP and LPENS. The resonator structure has been developed at the ONERA by Baptiste Fix and Audrey Chu. The optical simulations were carried out with the help of Claire Abadie. Baptiste Fix also designed the scanning near-field optical microscopy experiment and conducted the field imaging measurements. I was involved in the photodetector fabrication and characterizations, in collaboration with Audrey Chu and Claire Abadie.

As revealed in the previous sections, the field-dependent transport is an interesting property of HgTe NCs. This section focuses on exploiting this property to generate bias-reconfigurability with a new resonator design, sketched in Figure 3.23a. The key feature of this resonator structure lies in a two-pattern periodic grating, in which the symmetry breaking in each period induces two spatially and spectrally distinct resonances. Furthermore, using the grating as interdigitated electrodes leads to different electrostatic fields generated in the large and small grooves upon applying bias. The photocarriers from the two grooves, associated with two different optical resonances, are collected differently when the applied bias varies. This effect displays in the photocurrent spectrum under different bias voltages, that is, bias reconfigurability. We begin this section by introducing the optical design of the structure and presenting the structure's optical properties simulated with COMSOL software. Afterward, measurements using infrared scanning near-field optical microscopy will be presented to support the simulated results. Finally, we will show strongly enhanced bias tunability obtained with the new design.

3.4.1. Optical design of the coupled resonators induced by symmetry breaking

We generate an inhomogeneous absorption map by introducing two optical cavities in one structure. Our two-pattern periodic grating has been inspired by the coupled Fabry-Perot resonator [165], which has been first proposed by ONERA group. The structure, sketched in Figure 3.23a, was fabricated on a Si/SiO_2 substrate. Optical elements include a SWIR-absorbing HgTe NC layer (Figure 3.23b), a gold grating layer on top of the Al_2O_3 optical spacer, and a backside gold mirror. The grating design contains, within one period, two grooves of different sizes. To generate a resonance that matches the NC band-edge, we select a 1 µm period for the grating, and the openings are 200 nm and 400 nm for the small and large grooves of the structure in Figure 3.23a, respectively. Each groove confines the electromagnetic field at a different wavelength in TM polarization.

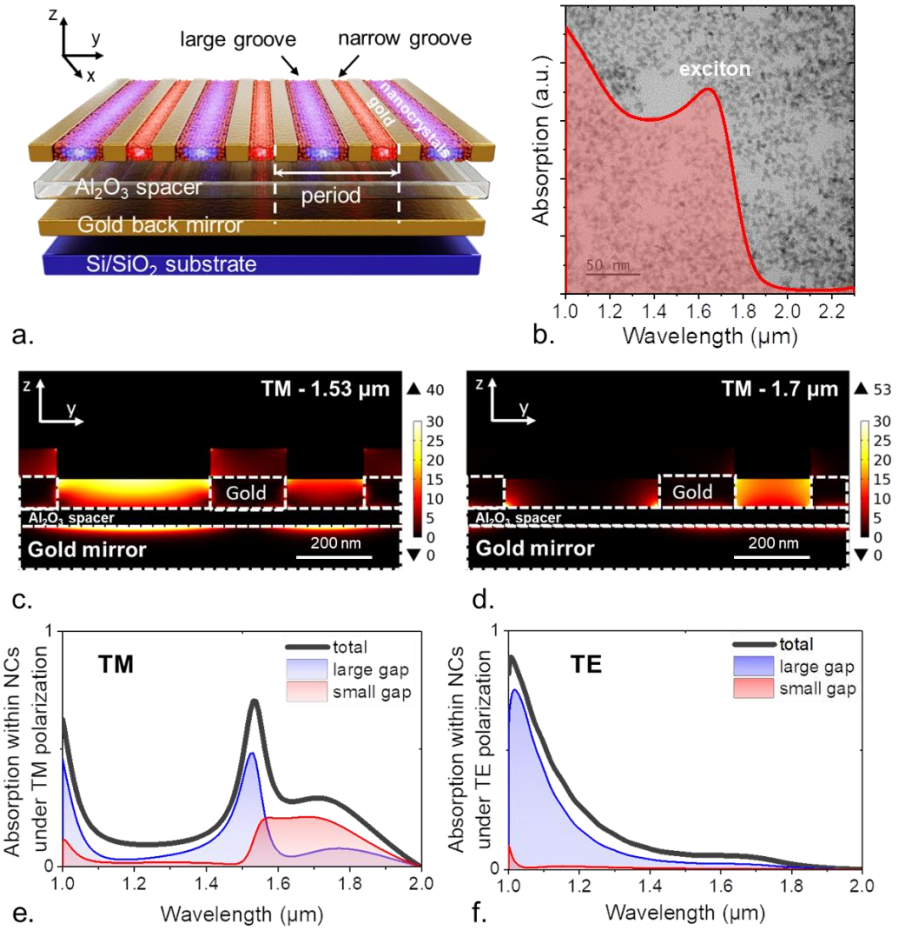

Figure 3.23: Optical properties of the coupled resonators. *a. Scheme of our resonator. b. Absorption spectra of the HgTe NCs used as infrared light absorbers and TEM images of the nanoparticles. c (resp. d). Simulated absorption spectra within the NCs for the structure depicted in a. The absorption spectra for NCs in the large and small grooves are also plotted. e (resp. f). Absorption map at 1.53 µm and 1.7 µm (corresponding to the two absorption peaks) under TM polarization.*

Figure 3.23 c-d present the absorption maps at the 1.53 µm and 1.7 µm under TM polarization, corresponding to absorption peaks of the large and small grooves, respectively. Note that, even though Figure 3.23a shows NCs only within the grooves, in practice, spin coating deposition leads to the formation of a quasi-conformal film with NCs both in the grooves and

on top of the grating. We thus account in the simulation for the presence of the NC film also on top of the electrodes. Due to the presence of the grating, the optical properties of the structure are strongly dependent on the polarization of the incident light. Under TE polarization, the structure presents a single absorption peak centered at around 1 μm, see Figure 3.23f. However, the absorption at the NC band edge is relatively weak. On the other hand, strong absorption around the NC exciton resonance is obtained under TM polarization at around 1.53 μm, as shown in Figure 3.23e. Beyond the strong absorption, the asymmetric structure allows the direct design of a bicolor structure where the two modes are spatially disjoint. The design thus naturally satisfies the condition of an inhomogeneous absorption map. We next follow the optical design to fabricate the photodetector.

3.4.1. Device fabrication

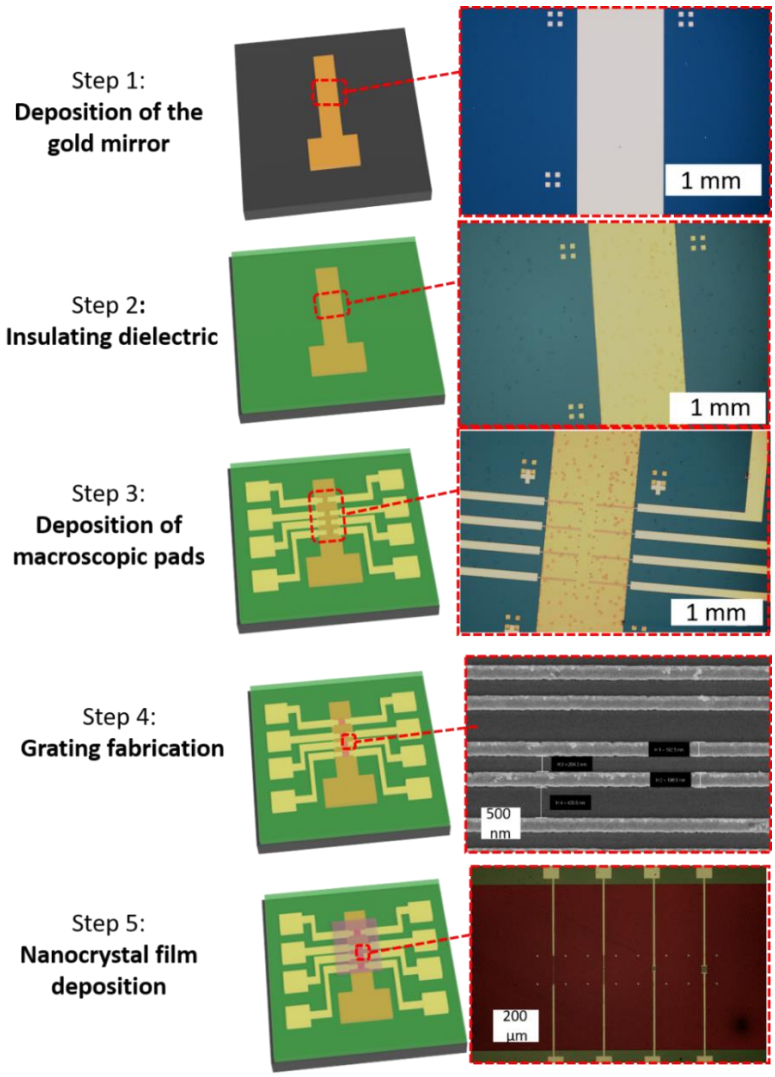

Figure 3.24: Fabrication process for the coupled resonators.

The five-stage fabrication process to obtain the coupled resonator structure is described in Figure 3.24. On a Si substrate, a backside gold mirror with a thickness of 80 nm was first prepared with thermal evaporation. Atomic layer deposition (ALD) was then performed to achieve a 40 nm Al_2O_3 optical spacer. The electrical contacts and the grating were

subsequently fabricated with optical and electron beam lithography. The contact pad and gold grating thicknesses are both 50 nm. Finally, 80 nm of HgTe NC film was deposited on top of the grating using spin-coating. Here, the HgTe film can be much thinner than typical photoconductive NC films (200-300 nm) thanks to the strong absorption of the optical structure.

3.4.2. Infrared scanning near-field optical microscopy measurements

In order to verify the optical simulations, we have compared our simulated results with infrared scanning near-field optical microscopy (SNOM) measurements. The measurements were performed by Baptiste Fix and Claire Abadie at the ONERA using a SNOM imaging set up from Neaspec GmbH, which allows obtaining the electromagnetic field maps at the sample surface. The scattering-type scanning near-field optical microscope is based on a tapping mode atomic force microscope. A 1.55 µm DFB pro TOPTICA laser with a linearly polarized beam was focused on an AFM tip, creating a strong near-field nano-focus at its apex, as presented in Figure 3.26a. While the illuminated tip scans the sample surface, near-field optical properties of the sample modify the tip-scattering light. The amplitude and phase of the tip-scattered light contain information about the sample's optical properties. In the measurements, there is a 60° incidence angle between the laser beam and the normal to the sample surface. The scattered light is measured by an InGaAs detector.

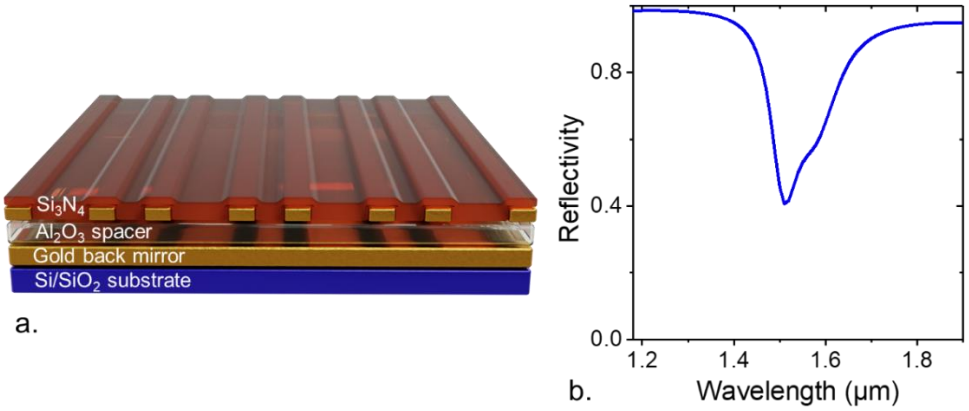

Figure 3.25: SNOM sample with NC film replaced by Si_3N_4. *a. Coupled resonator structure with HgTe NCs replaced by a layer of 140 nm Si_3N_4. b. Simulated reflectivity spectrum of the structure with Si_3N_4 layer under 60º incidence angle.*

Experimentally, conducting the SNOM measurement on a grating structure coated with NCs is challenging since the NC film appears too soft for the scans. Thus, we have replaced the NCs with a hard, dielectric thin film of Si_3N_4 whose refractive index ($n_{Si3N4} \approx 2$) is close to the one of the NC film ($n_{NC} \approx 2.35$) [143], as presented in Figure 3.25a. The Si_3N_4 layer was deposited using PECVD Corial D250 and has a thickness of 140 nm. Under 60º incidence angle, the main resonance of the structure matches the laser wavelength ($\lambda = 1.55\ \mu m$) of the SNOM setup, see Figure 3.25b. As mentioned in the previous section, the simulation predicts that (*i*) the signal is polarized, with a TM polarization much more intense than the TE one, and (*ii*) under TM polarization, the signal at the main resonance is mainly localized within the large gap, as predicted by the simulations and shown in Figure 3.23.

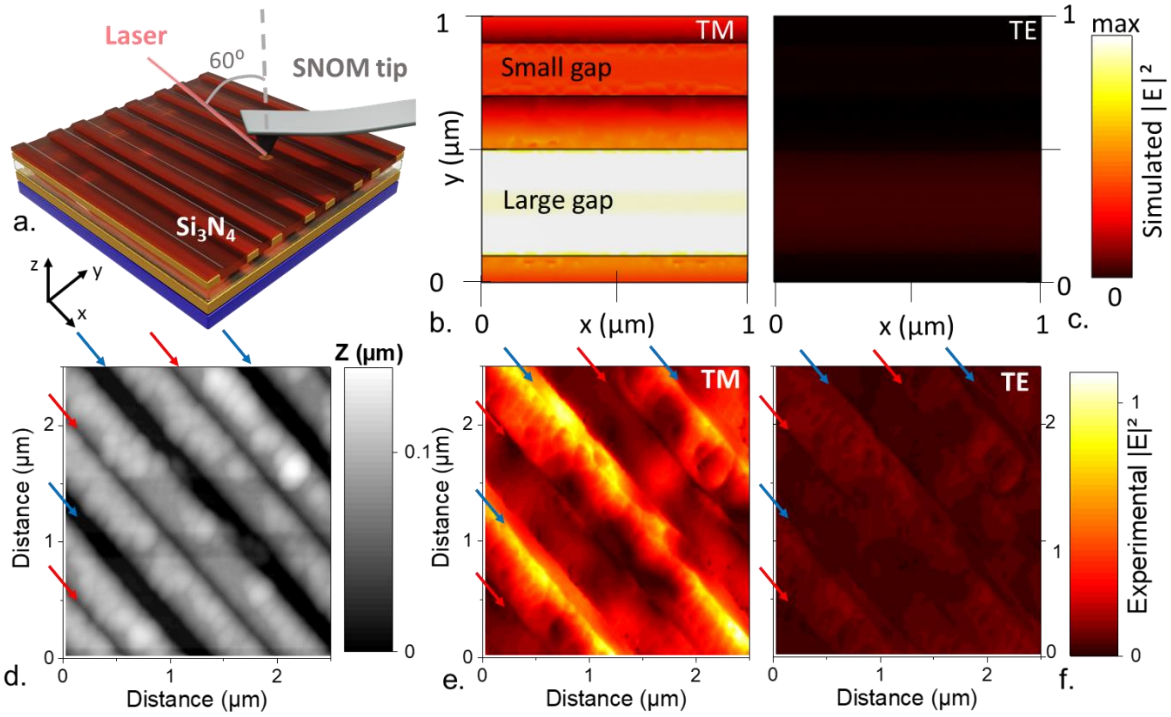

Figure 3.26: Infrared near-field microscopy characterization of coupled Fabry-Perot structure. *a. Schematic of the SNOM measurements on a coupled Fabry-Perot structure in which the NC layer is replaced by a thin Si_3N_4 film. The laser comes with a 60° incidence angle. Simulated electric field map $|E|^2$ at 1.55 µm in TM (b.) and TE (c.) polarization. d. Topography map of the coupled Fabry-Perot structure. Blue and red arrows highlight, respectively, the large and small grooves. Experimental electric field map $|E|^2$ at 1.53 µm in TM (e.) and TE (f.) polarization, obtained from the SNOM measurements.*

The top-view simulated electric field maps, accounting for the 60° incident angle, are shown in Figure 3.26b-c. The topography map (Figure 3.26d) shows a periodic structure presenting both large (highlighted with blue arrows) and narrow grooves (highlighted with red arrows). The experimental maps of the electric field are given in Figure 3.26e-f for TM and TE polarization, respectively. As expected, the magnitude of the field is much weaker for TE polarization. Comparing Figure 3.26d and e, we can correlate the maximum field magnitude under TM polarization with large grooves. The SNOM measurement thus confirms the validity of our simulations: the two grooves generate two spatially and spectrally distinguishable resonances. In the following, we will focus on the photoconductive properties of the NC-based structure and investigate how they are affected by the presence of these two resonances.

3.4.3. Defining the charge collection area for bias reconfigurability

As the structure's unit cell is not symmetric, the active electrical area of the device can be determined by the way the grating stripes are connected to form electrodes. We consider two different configurations: the "tuning fork" configuration (Figure 3.27a), where two consecutive stripes are electrodes with the same sign, and the 'interdigitated" configuration (Figure 3.27b), in which two consecutive stripes are electrodes with opposite signs.

In the “tuning fork” configuration, we focus on the “large tuning fork” structures, where the large grooves separate two electrodes of the same sign, thus screening the applied electrostatic field generated over the grooves. Therefore, only the small grooves are activated under bias application, corresponding to the absorption map under illumination in Figure 3.23c. We thus expect the photoresponse to follow NC absorption in the small groove (red spectra in Figure 3.23e-f).

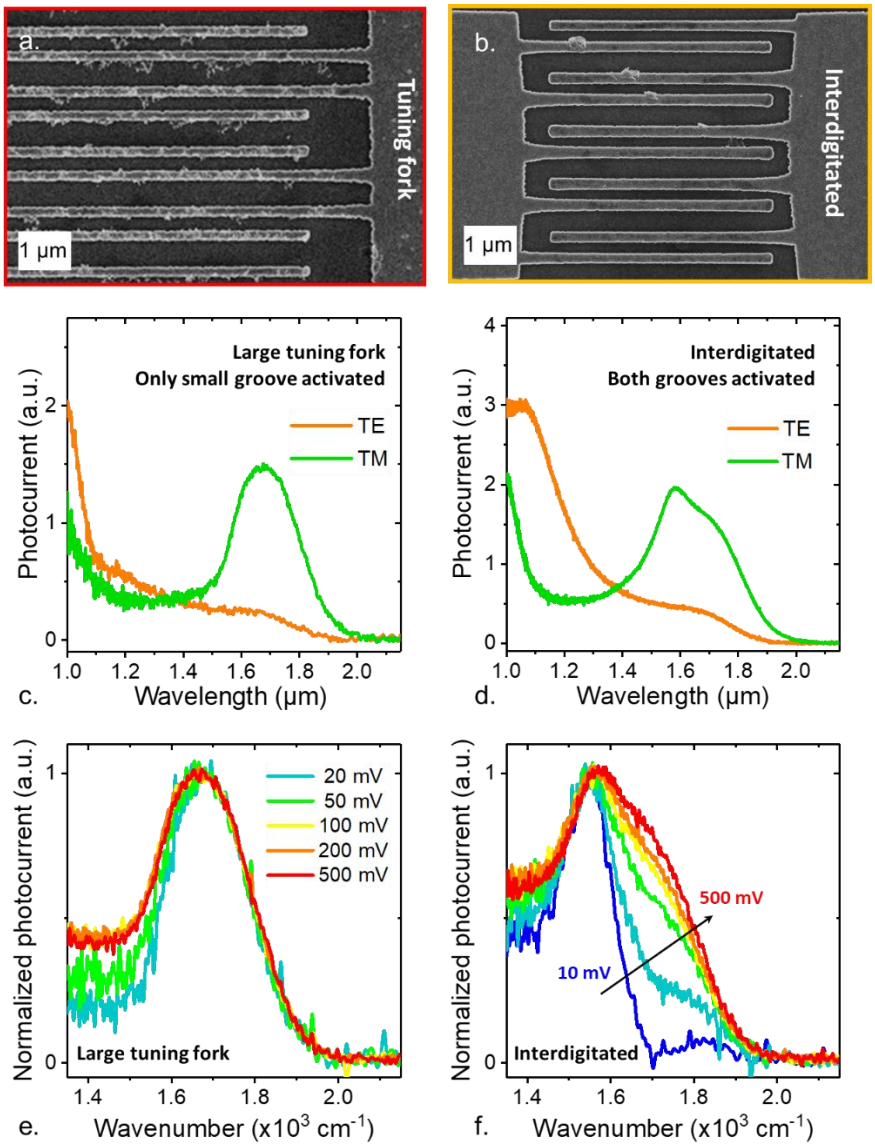

Figure 3.27: Different configurations to form electrodes. *a (resp. b). Scanning electron microscopy image of the structure with tuning fork (resp. interdigitated) configuration. c (resp.d). Photocurrent spectra of the “large tuning fork” (resp. interdigitated) device measured at 250 K with applied bias of 500 mV. e (resp.f). Unpolarized photocurrent spectra of the “large tuning fork” (resp. interdigitated) device measured at 250 K with various applied bias voltages.*

On the other hand, the interdigitated configuration allows the electrostatic field to be applied over both the large and narrow grooves. Therefore, a photoresponse with spectral features from both gaps is expected. Indeed, the experimental photocurrent spectra of the “large tuning fork” and the interdigitated configurations, presented in Figure 3.27c-d, show a good agreement with the simulated absorption spectra in Figure 3.23e-f. In particular, the “large

tuning fork" photocurrent spectrum under TM polarization depicts a single resonant peak, while the interdigitated configuration shows a broad absorption with a narrow peak (at 1.6 μm) next to a less intense feature (at 1.7 μm) around the NC band edge.

Furthermore, the photoresponse of the interdigitated device presents a significant bias tunability, as the intensity of the second feature is strongly dependent on the applied bias, see Figure 3.27f. Noticeably, the feature around 1.7 μm can be switched ON and OFF as the applied bias varies from 10 mV to 500 mV. On the contrary, bias dependence appears negligible for the "tuning fork" device, as shown in Figure 3.27e. The bias dependence of interdigitated device can be explained as follows: since the absorption is stronger in the larger groove, the photocurrent from the large groove prevails at low electric fields. When the bias is increased, the electrostatic field in the narrow groove becomes more important due to its smaller size, and charges generated in the narrow groove are more efficiently collected thanks to the NC field-dependent transport. Here, the increase of the applied bias effectively changes the active area of the photodetector as a result of the broken symmetry of the periodic pattern. The second feature that contributes to the photocurrent spectrum at high bias voltages thus can be attributed to the NC absorption from the narrow groove. Therefore, the bias-tunable response is substantial and can be observed up to 250 K in our structure.

In this section, we have demonstrated a new strategy to design a bias-reconfigurable photodetector based on HgTe NCs and a two-pattern periodic structure. Optically, the structure generates different resonances that are spatially and spectrally separated. At the same time, the applying bias voltage induces different electrostatic fields on areas where the resonances localize. Thanks to the field-dependent transport of the NCs, the tuning electrostatic field leads to a change in the photodetector's active area, which modifies the device's photocurrent spectrum upon increasing applied bias. Compared to the devices in the previous sections, the observed bias-reconfigurable photoresponse of the new design is more significant, with the full suppression of one resonance at low bias voltages. Furthermore, the bias tunability has been observable up to 250 K, readily attainable without cryogenic cooling systems.

3.5. Conclusion

This chapter presents an approach to bias reconfigurability in NC-based photodetectors. Here, we have exploited the bias dependence of carrier mobilities in HgTe nanocrystal films. This peculiar property and an inhomogeneous absorption in NC-based devices are then pointed out as critical ingredients for bias-reconfigurable photoresponse.

We further demonstrate this point by fabricating different device architectures, demonstrating tunable photoresponses from a spectral shift to bias-modulated optical bands. We show that bias-dependent photoresponse can be obtained by combining a single film of NCs with properly designed optical structures. Understanding the effect's mechanism lays the groundwork for further studies of active photonic systems based on nanocrystals.

Chapter 4: Highly sensitive MWIR NC-based photodiodes with bias-selectable spectral response

Contents

Related article

- Dang, T. H.; Cavallo, M.; Khalili, A.; Dabard, C.; Bossavit, E.; Zhang, H.; Ledos, N.; Prado, Y.; Lafosse, X.; Abadie, C.; Gacemi, D.; Ithurria, S.; Vincent, G.; Todorov, Y.; Sirtori, C.; Vasanelli, A.; Lhuillier, E. Multiresonant Grating to replace Transparent Conductive Oxide Electrode for Bias Selected Filtering of Infrared Photoresponse. *Nano Lett.* **2023**, 23 (18), 8539 – 8546.

Material synthesis and device fabrication in this chapter have been performed with the support of all the coauthors from the article. In particular, Yoann Prado (chemical research engineer – INSP) and Adrien Khalili (PhD student – INSP) provided the nanocrystals. Xavier Lafosse (C2N, Palaiseau) performed ITO coating on sapphire substrate. Djamal Gacemi (research engineer – LPENS) designed and assisted in the rectification measurements.

Boosting the performance of photodetectors requires optimizing the devices' optical and electrical properties. Much progress in material development has recently been made, allowing for obtaining highly sensitive MWIR HgTe NC-based photovoltaic devices. These detectors present several advantages over their photoconductive counterparts; of particular interest is the lower dark current thanks to the 0 V bias operation. However, on the optical side, the typical design using transparent conductive oxide layers for the device's electrodes is suboptimal. The issue arises from the significant optical losses of the electrodes in the MWIR range. Alternative designs for electrodes of mid-wave infrared devices are thus actively sought. This chapter presents a photodiode based on a carefully designed metallic grating as an electrode. The grating generates a multi-resonant photonic structure over the diode stack, allowing strong broadband absorption. The obtained device achieves the highest performances reported so far for a MWIR nanocrystal-based detector, with detectivity of $7x10^{11}$ jones at 80 K for 5 µm cut-off wavelength and sub 100 ns time response. Furthermore, we demonstrate that combining different gratings with a single diode stack can generate multicolor bias reconfigurable response and develop new functionalities such as band rejection and current bi-directionality.

4.1. Introduction

Photovoltaic devices typically rely on a vertical geometry, which concerns the bottom electrode design and the choice of the substrate in case of back illumination. In the visible range, transparent conductive oxides (TCOs) are traditionally employed as electrical contact thanks to their good conductivity and high optical transmission. Nevertheless, these materials present significant optical losses moving towards longer wavelengths, as exemplified in Figure 4.1. When designing devices in the near-infrared, a trade-off between electrical conductivity and optical losses in TCOs must be considered [166]. Indeed, while lowering the electrode thickness reduces the contact absorption, it also leads to an increased contact resistance, which prevents large current injection and fast operation of the device. In the MWIR, the high losses of TCO contact become even more problematic considering the limited transmission of substrate materials in this spectral range.

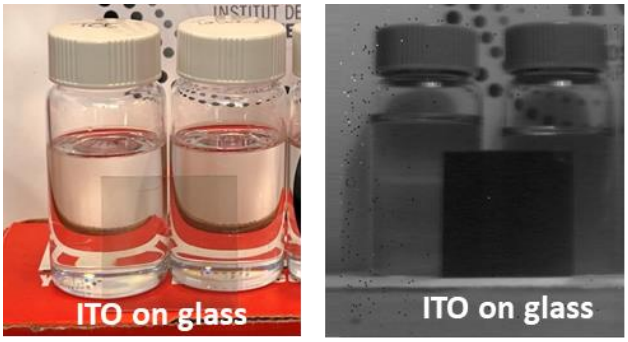

Figure 4.1: Transmission of ITO in the visible and SWIR range. *Visible image on the left shows good transmission of an ITO-coated glass slide. On the right in the SWIR image, while the glass vials still present good transmission, the glass slide coated with ITO shows strong absorption.*

On the contrary, metals behave as nearly perfect conductors at low-frequency (*i.e.,* at frequencies much smaller than their plasma frequency) since only a minor fraction of the electromagnetic wave can penetrate the metals. Optical losses of metallic structures are thus significantly reduced in the infrared. Furthermore, appropriate patterning of metallic surfaces can result in resonators, as discussed in previous chapters, which enable strong light confinement [123] and extraordinary optical transmission [167]–[170] while offering excellent electrical conductivity for optoelectronic engineering. Therefore, using metal structures [171]–[173] for transparent electrodes is of great promise to improve the performance of photodiodes working in the MWIR range.

This chapter focuses on the possibility of using metallic grating structures to replace the conventional TCO contact layer in NC-based MWIR photodiodes. In the first part, we introduce our metallic grating design aiming to generate multiple resonances in the NC absorbing film of a diode stack, leading to broadband enhancement of the device's absorption. We show that the detectors using metallic electrodes present superior performance compared with a photodiode stack using the conventional indium tin oxide (ITO) contact layer. The second part of the chapter presents the use of these gratings as a strategy to achieve multicolor bias-selectable photoresponse. So far, multicolor response in NC-based photodetectors is mainly achieved by associating devices sensitive to different optical bands [76], [103], [132], [174]. On the other hand, stacking two photodiodes [103], [175] on top of each other is a common strategy for reconfigurable photodetection, as presented in Chapter 3. However, multilayer fabrication with colloidal materials is highly complicated. Here, we show that by employing plasmonic resonators, a *multicolor reconfigurable response* can be obtained from *a single diode stack*, tremendously simplifying the fabrication process required by conventional approaches. Advanced functionalities, such as optical band selection and narrow-band rejection, will be demonstrated. This chapter highlights the novel capabilities offered by plasmonic resonators to NC-based systems beyond pushing the devices' performances.

4.2. Metallic structure to replace TCO layer in MWIR photodiode

Besides using TCOs as electrode materials, the most common strategy to design a partly transparent electrode is using a metallic grid [176]–[180]. In this case, the electrode transmission is mainly set by the metal filling factor. On the one hand, the filling factor has to be low to render the electrode transmission as high as possible. On the other hand, a low filling factor not only presents a higher sheet resistance but also lengthens the collection pathways of the photogenerated charges, which is strongly detrimental in the case of low-mobility materials such as NCs. A combination of a metallic grid/pad and a thin TCO layer [131], [181] has also been used as an approach to combine transparency and conductivity or to tune the work function of the TCO layer [143]. In this section, we explore the design of resonant metallic structures offering an alternative to TCO as a transparent electrode in the infrared.

4.2.1. Optical loss in the TCO contact of NC-based photodiodes

At present, MWIR NC-based diodes are typically based on the HgTe/Ag_2Te stack introduced by Ackerman *et al.* in 2018 [99]. In such diodes, the mid-wave infrared absorption relies on HgTe NCs, while Ag_2Te NCs play the role of hole extractors. The bottom contact of the diode

is commonly made of ITO thanks to its work function ($\Phi_{ITO} = 4.7\ eV$) which is well-suited for electron extraction from HgTe ($\Phi_{HgTe} = 4.6 \pm 0.1\ eV$), see Figure 4.2a. On the bottom side of the device, a sapphire substrate can be used when targeted detection wavelengths are less than 6 µm. This design has become a common platform for HgTe NC-based photovoltaic devices in recent years [100], [101], [103]–[105], [131].

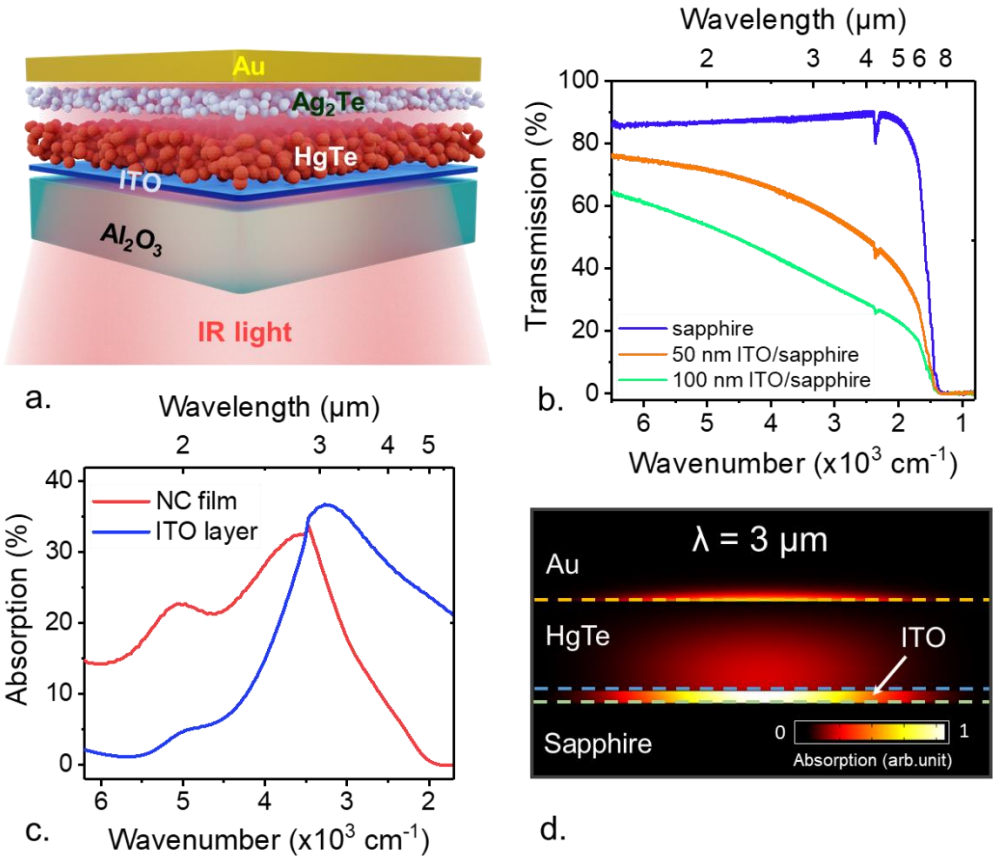

***Figure 4.2: HgTe NC-based photodiode using a transparent conductive oxide as the electrode**. a. Schematic of a photodiode based on sapphire/ITO/HgTe/Ag_2Te/Au stack. b. Measured transmission spectra for a pristine sapphire substrate and for a substrate coated with ITO layer with two different thicknesses. c. Simulated absorption spectra of the NC film and of the ITO layer used as a contact in the photodiode. d. Absorption map (at 3 µm) for the diode stack depicted in part a.*

Although widely used, the ITO bottom contact in MWIR devices exhibits a major issue: it presents a strong absorption of electromagnetic waves above 2 µm. Notably, the transmission of a 50 nm thin ITO layer on a sapphire substrate is only 40 % at 5 µm, detrimental to the photodiode's efficiency, as shown in Figure 4.2b. This issue is evident in the simulated absorption spectra of a typical diode stack (*i.e.,* 350 nm thickness of NC stack, 50 nm ITO contact layer), which shows that most of the light absorption occurs in the ITO layer, see Figure 4.2c-d. As a result, the incoming light transforms into ohmic losses rather than photocurrent signals. It is thus necessary to find an alternative design for the bottom contact that reduces the optical loss while maintaining a good electrical connection. The following section presents our approach to addressing this problem with metallic grating.

4.2.2. Overcome optical loss in the mid infrared with metallic structures

In order to improve the NC film's absorption, we design a structure in which the ITO layer is replaced by a gold grating, depicted in Figure 4.3a. Here, we target to enhance the NC absorption in the 3-5 µm spectral range, where ITO presents significant optical losses. The new diode architecture resembles the MDM structure presented in Chapter 2, thus inheriting all the optical advantages from a plasmonic resonator. The generated resonances, as a result, include the Fabry-Perot resonance under TE polarization and surface plasmon polariton and cavity mode under TM polarization. Note that the measurements with the broadband detectors presented in Chapter 2 have shown that surface plasmon resonance leads to the photocurrent peak with strongest enhancement. Therefore, we optimize the grating mainly by following NC absorption under TM polarization. Once again, the optical design was performed with COMSOL software.

Optical properties of the metallic structure

Under TM polarization, the cavity mode's resonant wavelength matches the exciton absorption at 4.1 µm when the grating stripe width *s* is set at 350 nm. The TM surface plasmon and TE Fabry-Perot wavelengths are then controlled through the grating period *p*. Figure 4.3b-c show the NC absorption spectra for different values of *p* from 1200 nm to 1800 nm under TM and TE polarization, respectively. Under TM polarization, two features are visible, associated with the cavity mode at 4.1 µm, and the SPP. The latter can be recognized by the pronounced peak that shifts with different grating periods. In order to match the SPP wavelength with the exciton absorption, the grating period is set to be around 1800 nm.

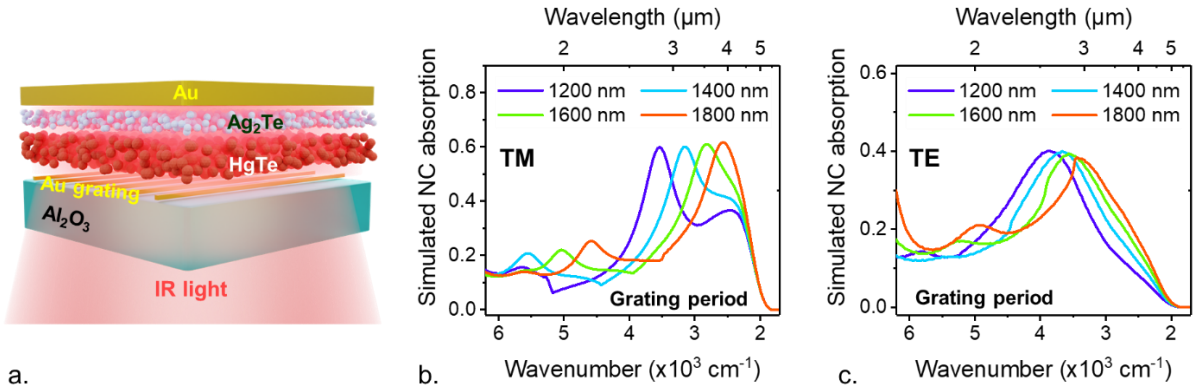

Figure 4.3: Resonant 1D grating used as a transparent conductive electrode. *a. Schematic of a photodiode based on sapphire/1D Au grating/HgTe/Ag_2Te/Au stack. b. (resp c.) Simulated NC absorption spectra for the diode depicted in part a for various values of the grating period p in TM (resp TE) polarization. The grating stripes s = 350 nm and the NC thickness t_{NC} = 350 nm.*

Under TE polarization, a similar behavior can be seen for the Fabry-Perot resonance. This resonance depends on the opening *o* = *p*-*s*, thus shifts towards longer wavelengths as *p* increases. At *p* = 1800 nm, the resonance does not match the exciton absorption and appears slightly blue-shifted, see Figure 4.3c. Consequently, it contributes to the broadening of the overall absorption spectrum.

Regarding the diode stack thickness, hopping transport in NC films limits the carrier mobilities in HgTe, and thus a thick NC film (≥ 500 nm) is not favorable for the photogenerated carrier collection. On the other hand, too thin NC film could result in poor light absorption. We thus optimize the diode stack thickness to maximize the overall device absorption in the NC film, considering that a reasonable film thickness for efficient charge transport is usually below 500 nm. Figure 4.4a-b show the simulated NC absorption spectra for the grating (s = 350 nm, p = 1800 nm) under TM polarization and the ITO device with unpolarized light, for different thicknesses of the NC layer. The basic design guideline for ITO-based diodes is that the thicker the NC film the higher the absorption. This is not the case for the grating structure. Indeed, we identify an optimum thickness for the absorbing layer coupled to the grating corresponding to t_{NC} = 350 nm. Thus, another advantage of the metallic structure is the possibility of using a NC layer with lower thickness to reach the same absorptivity. This results in a reduced material consumption and improved transport.

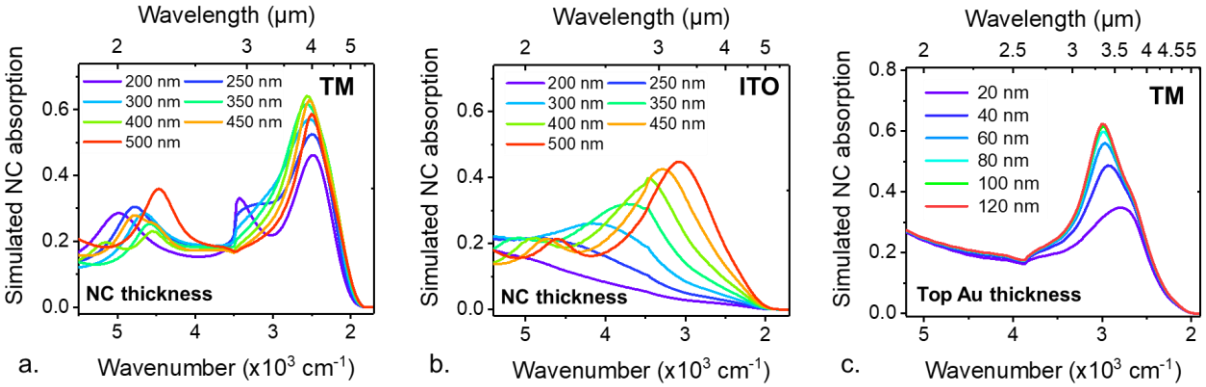

***Figure 4.4: Impact of NC film thickness and top Au layer thickness on NC absorption**. a. Simulated NC absorption spectra for the diode depicted in Figure 4.3a for various values of the NC thickness t_{NC} in TM polarization. The grating stripes s = 350 nm and the grating period p = 1800 nm. b. Simulated NC absorption spectra for the diode with ITO bottom layer (depicted in Figure 4.2a) for various values of the NC thickness. c. Simulated NC absorption spectra for the diode depicted in Figure 4.3a for various values of the top gold layer thickness in TM polarization. The grating stripes s = 350 nm, the period p = 1800 nm, and the NC thickness t_{NC} = 350 nm.*

Beyond the grating geometrical parameters, it is also worth mentioning that the choice of the top gold layer thickness is also important. Usually, such metallic back reflector thickness is designed to match the metal's skin depth. Indeed, Figure 4.4c shows that a top metallic layer with a thickness below 80 nm can be optically leaky and leads to reduced NC absorption. Therefore, our structure was chosen with a top gold layer thickness t_{Au} of at least 80 nm. The optimized structures were fabricated with geometrical parameters s = 350 nm, p = 1800 nm, t_{NC} = 350 nm, and t_{Au} = 80 nm.

Device fabrication

We follow the outcomes of the simulation for the fabrication of the diode stack. For the absorbing layer, HgTe NCs have been grown by Yoann Prado (chemical research engineer - INSP) using the procedure developed by Keuleyan *et al*. [48]. The grown particles display an exciton peak at around 3.5 μm, as shown in Figure 4.5a. The cut-off wavelength will later be

redshifted upon ligand exchange and cooling. Unlike the SWIR NCs with the tripod shape, the obtained MWIR particle shape is the tetrahedron, see Figure 4.5b.

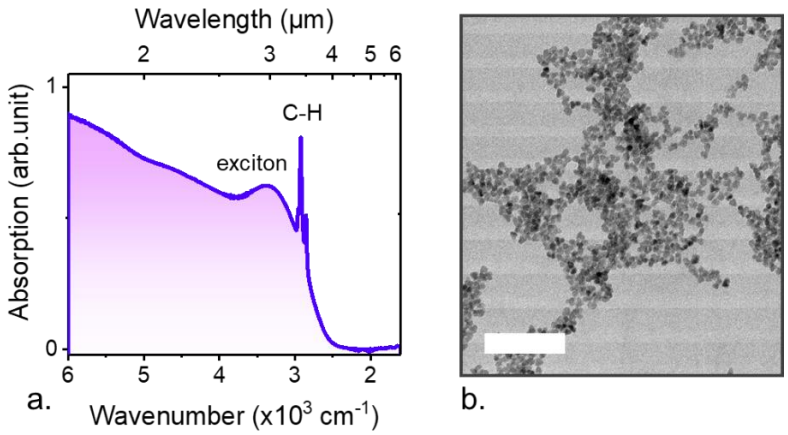

Figure 4.5: HgTe NCs used in the diode stack*. a. Absorption spectrum of the HgTe NC solution after synthesis. b. TEM image of the HgTe NCs with MWIR absorption. Scale bar is 100 nm long.*

The Ag_2Te particles were synthesized by Adrien Khalili (Ph.D student - OCN team, INSP), following the procedure in reference [104]. Briefly, $AgNO_3$ is mixed with oleylamine and oleic acid in a three-neck flask. The flask is degassed and later filled with nitrogen before TOP/Te is added for the reaction under controlled atmospheric and temperature conditions. The synthesis results in a crude solution of Ag_2Te that can be stored in a freezer at -20ºC. Before use, the crude solution is cleaned and dispersed in hexane/octane for device fabrication.

In order to have a consistent comparison of performances between the two structures depicted in Figure 4.2a and Figure 4.3b, we built on the same sapphire substrate the diodes with the ITO contact layer and grating structures. The fabrication process is described in Figure 4.6.

The sapphire substrate was first coated with 50 nm of ITO by sputtering (Figure 4.6a). This sputtering step has been conducted by Xavier Lafosse at the C2N, Palaiseau. Afterward, optical lithography was performed to obtain a mask on the ITO layer. The substrate was then dipped in HCl to etch away the uncovered ITO. The remaining resist was removed by acetone, leaving the ITO with an area of 100 µm x 100 µm on sapphire (Figure 4.6b). The macroscopic contact pads were obtained with another optical lithography step and thermal evaporation of 5 nm Cr/ 50 nm Au layers (Figure 4.6c). Then, electron-beam lithography was conducted for the gratings (Figure 4.6d), followed by the deposition of the diode stack layers (Figure 4.6e). The diode is formed when Ag_2Te is deposited on a solid film of HgTe. The deposition is conducted by gently casting cleaned Ag_2Te solution (in hexane/octane) on the solid HgTe film, followed by a few drops of $HgCl_2$ (10 mM in methanol) for the cation exchange process. The film is then rinsed in IPA for 10 seconds before drying. This Ag_2Te/ $HgCl_2$/ IPA treatment is repeated another time, resulting in a 50 nm increase in thickness compared to the initial HgTe film. The deposition is finalized by dipping the film in acetonitrile (ACN) with EDT (1% in volume) for 30 seconds, followed by the last cleaning step of ACN dipping for 30 seconds. Finally, a complete device is obtained after the evaporation of the top electrode through a shadow mask (Figure 4.6f).

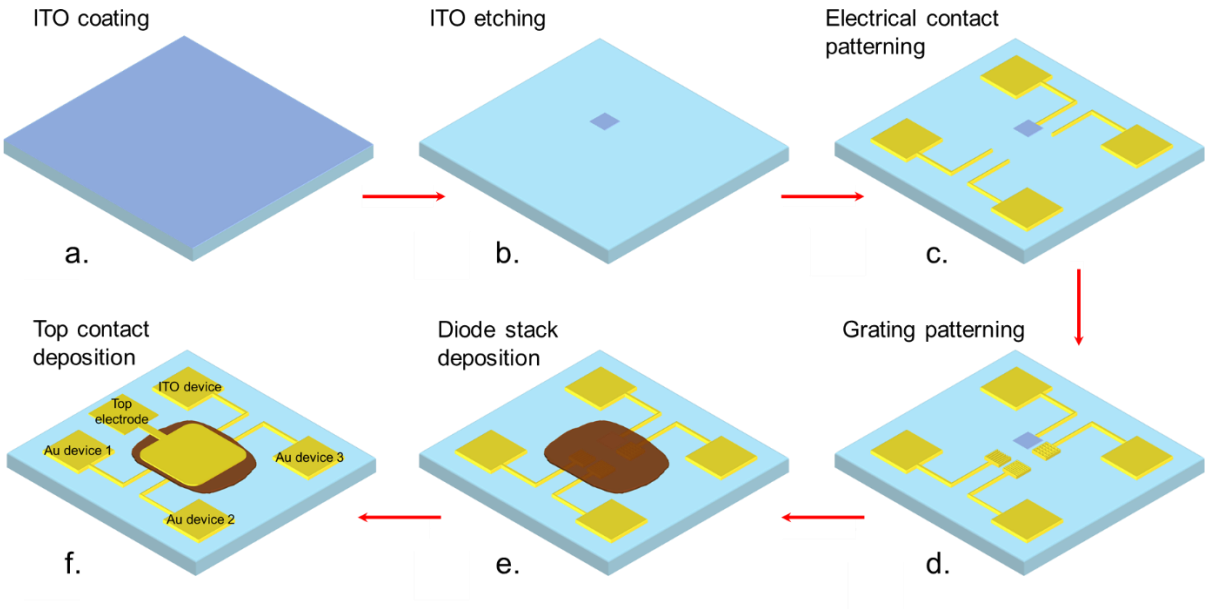

Figure 4.6: Fabrication process for the photodiodes. *a. Sapphire substrate coated with sputtered ITO layer. b. ITO area on the sapphire substrate after HCl etching form the electrode with area of 100 µm x 100 µm. c. Macroscopic contact pads fabricated with optical lithography. d. Gold grating structures fabricated with electron-beam lithography. e. Deposition of the HgTe/Ag_2Te stack. f. Deposition of the top gold contact though a shadow mask.*

Note that the fabrication process allows for obtaining several devices *on the same chip*. These devices share a common diode stack of HgTe/Ag_2Te, while the bottom contacts can be defined differently by electron beam lithography. We thus eliminate sample-to-sample variation due to different NC film processing. The ITO-based device can then be used as a benchmark when evaluating the performances of other metallic devices. In the following section, we first present the impact of the metallic gratings on the diodes' optical and electrical properties before comparing the performances of grating-based devices' and the reference ITO-based one.

4.2.3. Device characterization

Impact of the grating on optical properties of the diodes

The impact of the metallic grating on the optical properties of the photodiodes is shown in Figure 4.7a-b. The photocurrent spectra for a series of diodes with different grating periods agree exceptionally well with our simulated NC absorption spectra in Figure 4.3b-c. In particular, the grating with a period of 1800 nm shows a clear resonance in the range from 3 µm to 5 µm under TM polarization. However, under TE polarization, the resonance obtained with this period is observed below 2 µm, far from the exciton wavelength.

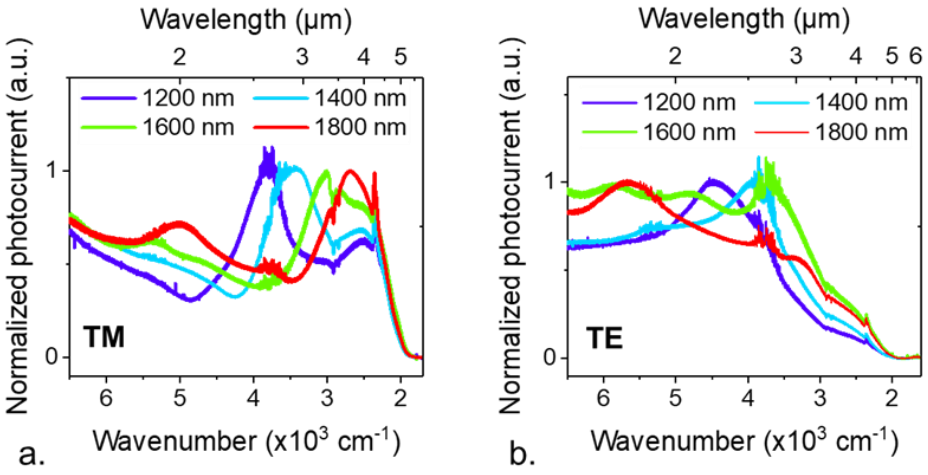

Figure 4.7: Resonant metal structure for MWIR photodiode. *a. (resp. b.) Photocurrent spectra for the grating device with various values of the grating period in TM (resp. TE) polarization.*

In order to maximize the absorption amplitude at resonance for both polarizations, we switch the 1D grating to a 2D grid with a square lattice, as shown in Figure 4.8a. Figure 4.8b compares quantitatively the photocurrent signal under unpolarized illumination between a 2D grid, a grating, and an ITO device based on the same HgTe/Ag_2Te diode stack. The benefit of the 2D grid over the 1D grating and the ITO layer is the selective increase in the device's absorption close to the material's band edge. At shorter wavelengths, the photocurrent from the 2D grid is reduced compared to the 1D grating. This decrease can be explained by the enhanced reflection of the 2D structure in this spectral range since the 2D design also increases the metal filling factor. When comparing the grid to the ITO device, we can see that the photocurrent spectrum of the 2D grid device is significantly higher. Furthermore, the ITO device presents no resonances. The increased photocurrent signal of the 1D grating and 2D grid devices comes from the improved NC absorption and reduced contact resistance. The latter will be discussed in the next paragraph.

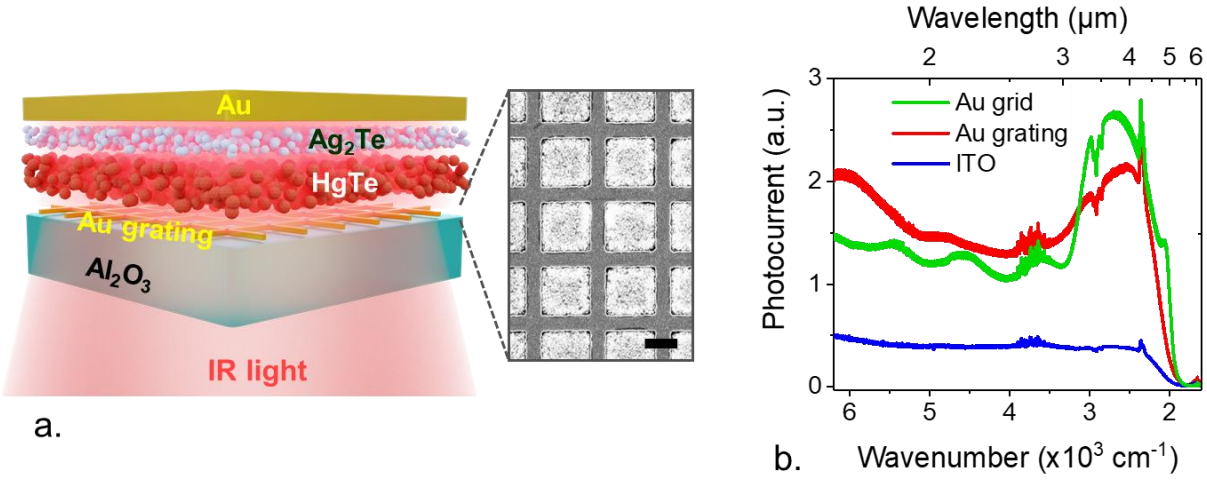

Figure 4.8: From 1D grating to 2D grid for the bottom contact. *a. Schematic of a photodiode based on sapphire/2D Au grid/HgTe/Ag_2Te/Au stack. On the right panel, we show an SEM image of a fabricated 2D gold grid on a sapphire substrate. The scale bar is 1 μm. b. Photocurrent spectra of the diodes with the bottom electrodes made of ITO, 1D grating, and 2D grid.*

Impact of the grating on electrical properties of the diodes

With the established optical and electrical properties, we next perform measurements to quantitatively compare the detection performances of the gold-based and ITO-based devices. Choosing gold to replace ITO raises concerns regarding the gold work function (Φ_{Au}= 5.1 eV), which might diminish the rectification behavior of the diode stack. It is thus critical to check that diode behavior is maintained for photovoltaic operation. The IV curves of the 2D grid device at various temperatures are shown in Figure 4.9a. Indeed, the IV curves present a strong rectifying behavior at low temperatures. Compared with the ITO device, the current density in the Au grid device is higher under both dark and illumination conditions at all temperatures, as shown in Figure 4.9c-d. Particularly, the open-circuit voltage of the 2D grid device appears to be comparable with the ITO-based device under the same illumination condition, see Figure 4.9b. These results show that the photovoltaic operation of the diode stack is well preserved when replacing the ITO bottom contact with the gold structures.

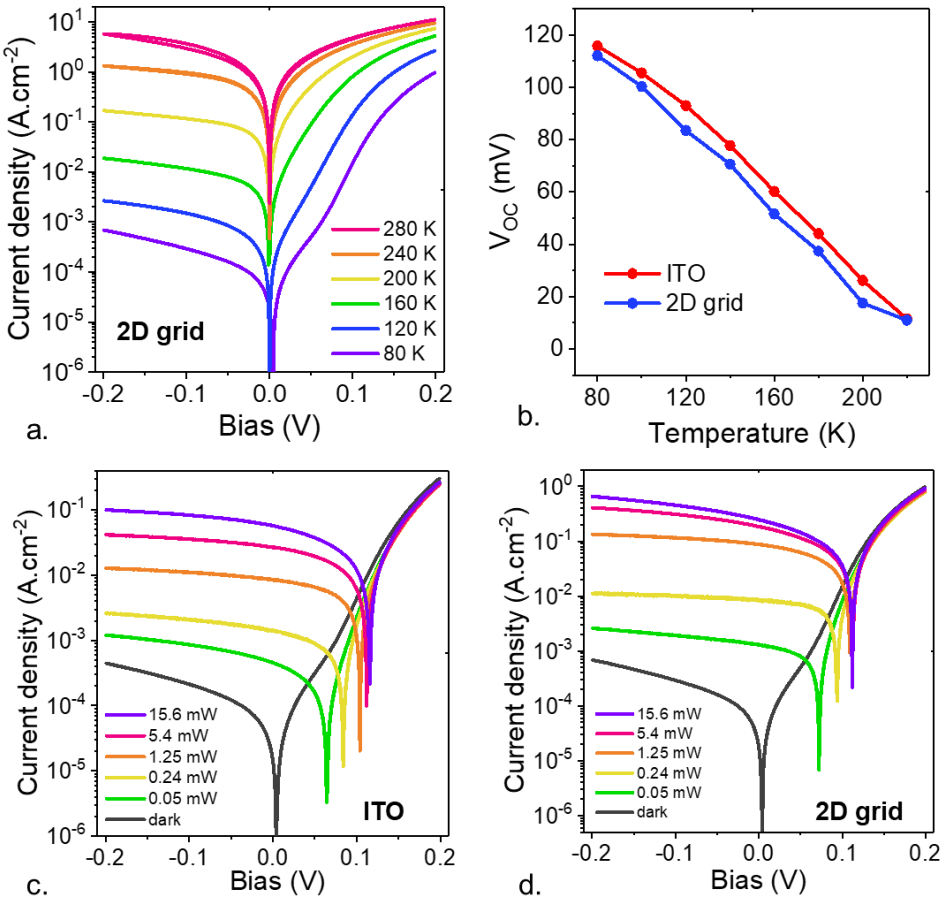

Figure 4.9: Rectifying behavior of the diodes. *a. I-V curves of the 2D grid device under dark condition at various temperatures. b. Open-circuit voltage under quantum cascade laser illumination (λ ≈ 4.4 μm - 15.6 mW nominal laser power) of the ITO and the 2D grid device at various temperatures. c. I-V curves in dark condition and under illumination (λ=4.4 μm - 15.6 mW nominal laser power) measured at 80 K for the ITO device. d. I-V curves in dark condition and under illumination (λ = 4.4 μm - 15.6 mW nominal laser power) measured at 80 K for the 2D grid device.*

Photodetection performance

The benefits of the optical structures exhibit clearly in the devices' responsivity. The maximum responsivity of the 2D grid device measured with a blackbody at 600 ºC reaches 2.9 $A.W^{-1}$ for temperatures around 120 K. This value is very high, as it is very close to the responsivity of a 4 µm device with 100 % external efficiency, calculated to be 3.2 $A.W^{-1}$. Figure 4.10a shows that, at all temperatures, the responsivity of the 2D grid device is slightly higher than the 1D grating device and significantly exceeds the responsivity of the ITO device. However, all devices present a strong decrease in responsivity at temperatures above 150 K. This decrease can be attributed to a decreased carrier lifetime caused by higher concentration of thermal carriers [182].

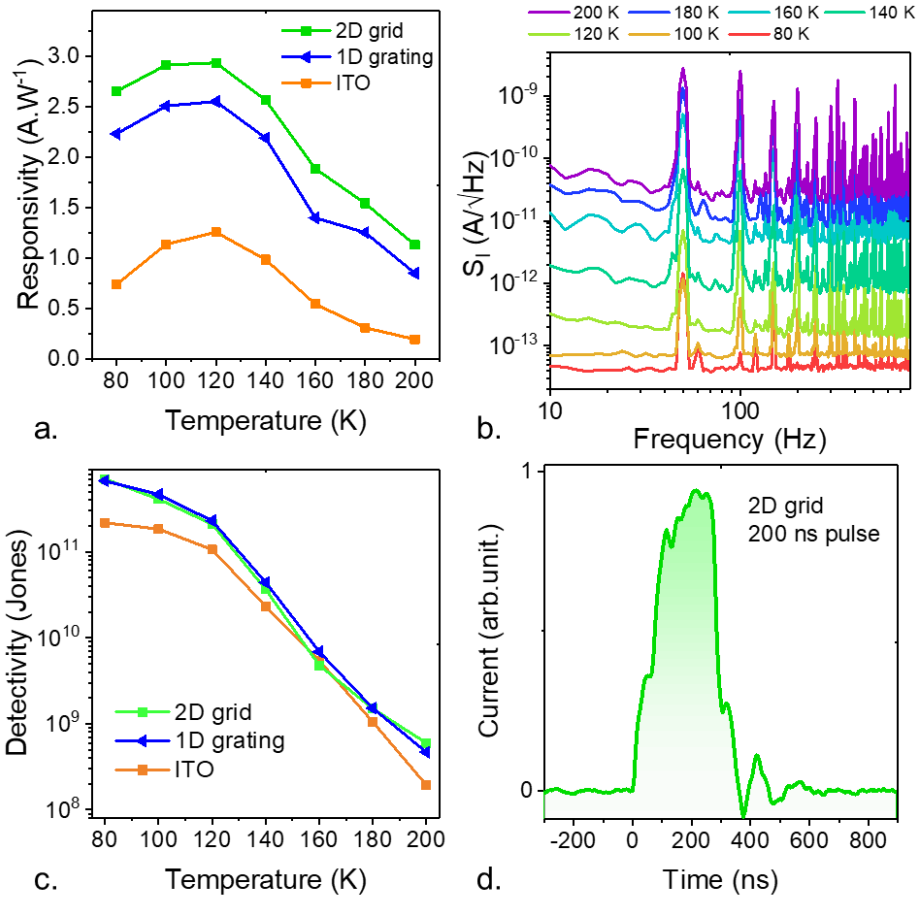

Figure 4.10: Photodetection performances of the diodes. *a. Responsivity (in front of a 600°C blackbody source) as a function of the temperature for a diode in which the bottom electrode is made of ITO film, 1D grating, and 2D grid. b. Noise current spectral density for 2D grid device measured at various temperatures. c. Specific detectivity (at 1 kHz) as a function of the temperature for a diode in which the bottom electrode is made of ITO film, 1D grating, and 2D grid. d. Photocurrent as a function of the time in response to a 200 ns long pulse of light emitted by a 4.4 µm quantum cascade laser.*

Note that the polarization independence introduced by the grid should have increased the responsivity by a factor of two compared to that of the grating. However, one should also consider the increased reflectivity of the grid and the increased metal losses due to the higher filling factor. On the one hand, the reflection for out-of-resonance wavelengths increases due to higher metal coverage. On the other hand, NC absorption resulting from the surface

plasmon resonance in the 2D grid is not exactly double that of the 1D grating because the additional metal stripes limit the spatial overlap of the mode with the NCs.

We next assess the noise current density of the devices. As opposed to photoconductive operation, the photovoltaic operation allows the elimination of 1/f noise. For the 2D grid device, white noise prevails at cryogenic temperatures, see Figure 4.10b. The specific detectivity of this diode, calculated by $D = R\sqrt{A}/S_I$, reaches 7x10^{11} Jones at 80 K, a three-fold increase compared to the device with the ITO electrode, as presented in Figure 4.10c. Interestingly, the 1D grating device also presents a detectivity comparable with that of the 2D grid, which can be attributed to the lower dark current (*i.e.*, lower device's noise current density) thanks to the reduced device's electrical area (1D grating geometry vs. 2D grid geometry).

We determine the device's response time with $T_{90\text{-}10\%}$, which refers to the interval in which the measured signal changes from 90 to 10% of the full span (*e.g.* the time taken for a 10 V signal to decrease from 9 V to 1 V). The response to a pulse of light emitted by a quantum cascade laser resonant with the particle band edge is around 80 ns (Figure 4.10d) for the 2D grid device (with a device's area of 100x100 µm^2). This value is close to the laser's rise time limit. Thus, we also have used microwave rectification technique [183] to determine the device bandwidth, as it is a characterization technique only exploiting dark operation of the device. The measurements were realized with the help of Djamal Gacemi (research engineer – LPENS).

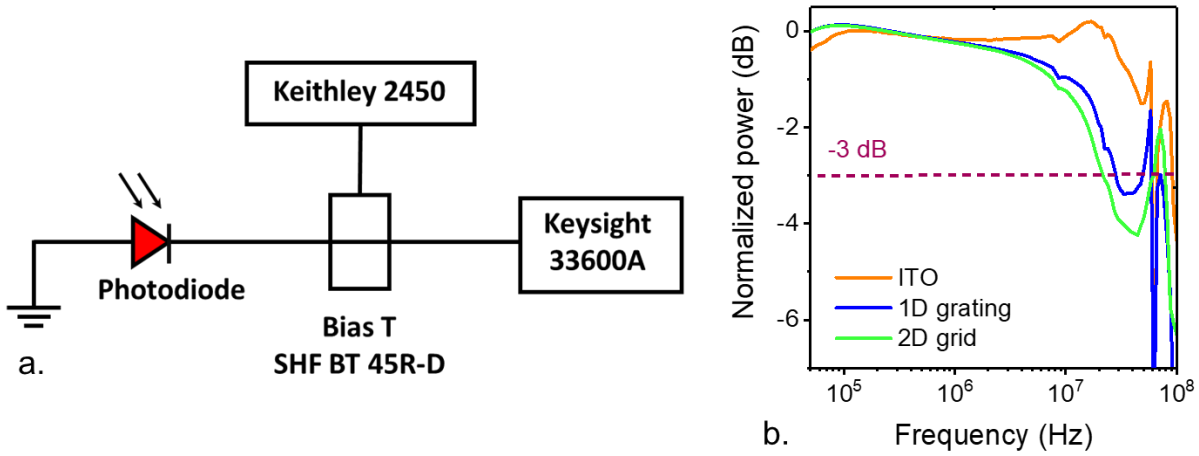

Figure 4.11: Rectification measurement. *a. Schematic of the rectification measurement with a photodiode connected to both DC and AC sources. DC bias is applied by the Keithley through the bias T. The AC power is supplied by the Keysight waveform generator. b. Electrical power as a function of the signal frequency for the diode with ITO contact, 1D grating and 2D grid as electrodes.*

The rectification measurement is based on the inherent nonlinear I-V characteristic of the diodes. The second derivative d^2I/dV^2 of the IV curve depends on the AC frequency with a relationship reflecting the transport behavior and the device's architecture [183]. The experimental setup for the measurement is shown in Figure 4.11a. The DC bias is applied through a SHF BT 45R-D bias-T using Keithley 2450 Source Meter. The AC power is provided by a Keysight 33600A Waveform Generator with a frequency up to 120 MHz. The -3dB bandwidth of the 2D grid device measured by rectification is found to be around 20 MHz, corresponding to a rise time of t_{rise}=0.35/f_{3dB}≈18 ns, comparable to the result obtained with the optical measurement, see Figure 4.11b. This result suggests that the device's dynamics are

mainly determined by the capacitance of the diode. As a result, a faster response could be attainable by optimizing the device's architecture.

Table 3 summarizes the detection figures of merit of state-of-the-art mid-wave infrared-operated NC-based devices. The performance of our 2D grid device is currently among the most sensitive and fastest MWIR photodetectors reported based on colloidal NCs for 80 K operation.

Table 3: *Performances of light sensors operating in the MWIR based on NCs. (PC: photoconductive, PD: photodiode, * set-up limited)*

Absorbing material	**Operating mode**	**Responsivity** (A.W^{-1})	**Response time**	**Detectivity** (Jones)	**Operating temperature** (K)	**Ref.**
			Intraband			
HgSe	PC	5 x 10^{-4}		8.5 x 10^{8}	80	[184]
HgSe	PC	0.7	8.75 ms	10^{8}	300	[185]
HgSe	PD	5 x 10^{-3}	200 ns	2 x 10^{9}	80	[176]
HgSe	PC	77 x 10^{-3}	1 µs	1.7 x 10^{9}	80	[186]
HgSe	PC	0.145	2.1 s	-	300	[187]
Ag_2Se	PD	19 x 10^{-3}	-	7.8 x 10^{6}	300	[188]
Ag_2Se	PC	13.3 x 10^{-3}	-	3 x 10^{5}	300	[189]
Ag_2Se	PC	8 x 10^{-6}	≈10s	-	300	[190]
Ag_2Se	PC	350 x 10^{-6}	-	-	90	[191]
			Interband			
HgTe	PC	0.25	-	2 x 10^{9}	130	[57]
HgTe	PD	1.3	1 µs	3.3 x 10^{11}	85	[99]
HgTe	PD	1.62	-	4 x 10^{11}	85	[131]
HgTe	PD	0.4	2.5 µs*	3 x 10^{10}	85	[103]
HgTe	PD	2.7	-	2.7 x 10^{11}	80	[192]
HgTe	PC	0.7	11 µs*	2 x 10^{10}	80	[138]
HgTe	PD	2.65	80 ns	7 x 10^{11}	80	**This work**

Other metals for the bottom electrodes

Using gold for both top and bottom electrodes might not be optimal for carrier extraction of a diode stack. In this direction, improvement can be made by exploring other low-work function metals which provide better band alignment for the diode operation. During device optimization, we have also explored the possibilities of using aluminum (Φ_{Al}= 4.08 eV) and silver (Φ_{Ag}= 4.25 – 5.1 eV) to alternate gold (Φ_{Au}= 5.1 eV) for the bottom metallic grating. However, each of these metals presents its issues.

In devices with bottom aluminum electrodes, although rectifying behavior of the diode can be observed, optical resonances appear to be lacking in the photocurrent spectrum, see Figure 4.12a. This lack of resonances can be attributed to oxidation, which partly transforms aluminum into alumina (Al_2O_3) during the device processing, ultimately leading to the

diminishment of the optical resonances [193], [194]. Further investigation and optimization are thus necessary for the future use of aluminum as a plasmonic material in HgTe NC-based devices.

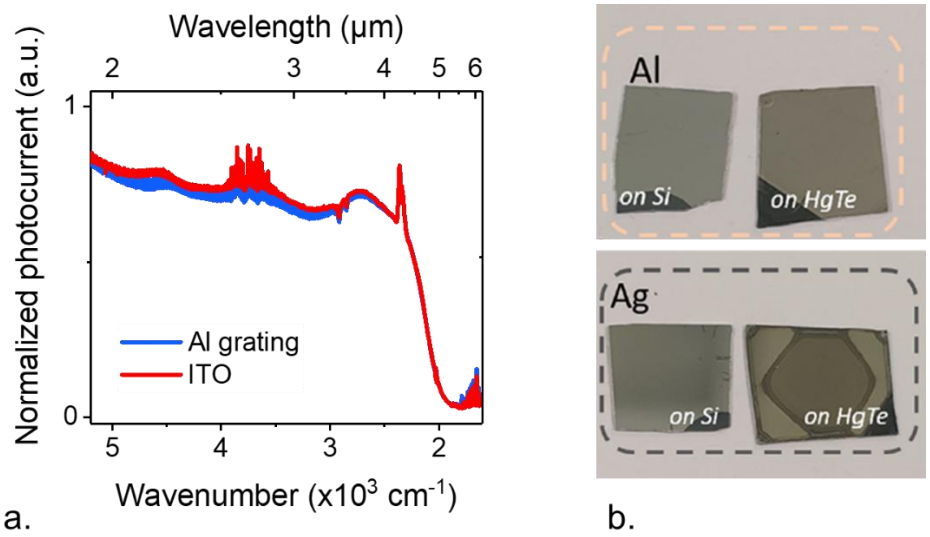

Figure 4.12: Al and Ag as alternative materials for the bottom electrode. *a. Normalized photocurrent spectra of diodes with ITO bottom electrode and Al grating electrode (s = 350 nm, p = 1800 nm, and t_{NC} = 350 nm). b. Top: image of Al films on a Si substrate and a HgTe film. Bottom: image of Ag films on a Si substrate and a HgTe film. While the Al film does not present any visible change, the Ag film on HgTe displays a clear dark color and a lack of metallic shine. From reference [195].*

Compared to aluminum, silver is more robust toward oxidation. However, when a silver film is in contact with HgTe, a clear change in color of the silver surface can be noticed, indicating possible chemical reactions between the silver layer and the HgTe film. A comparison between aluminum and silver films deposited on different materials is shown in Figure 4.12b. The color change of silver can be explained by the cation exchange process, which transforms Ag into Ag_2Te while releasing Hg to form an amalgam [195]. This process is detrimental as it alters silver's optical and plasmonic properties. Chemical instability is thus the main drawback when using silver in HgTe-based optoelectronic devices. To this end, the use of gold is justified thanks to its excellent optical behaviors for a plasmonic material, good electrical conductivity, and chemical stability.

4.3. Multiplexing the photodiodes for bias-selectable detection band

In the previous section, we demonstrated that Au grids and gratings could replace TCO in a MWIR diode stack advantageously. This section shows that the resonant electrodes open new possibilities for obtaining novel device functionalities from a bias-reconfigurable response. For this purpose, multiple gratings with different periods have been fabricated on the same chip, as sketched in Figure 4.13a. Instead of operating the diodes in a vertical geometry, we apply bias between two planar electrodes connected to the gratings. As shown in the previous section, the grating period determines the diode spectral response (Figure 4.7a-b). Figure 4.13b describes the formation of back-to-back diodes. Here, the diodes are built from a single

diode stack, which is less demanding in terms of fabrication compared to the conventional tandem configuration [103], [175].

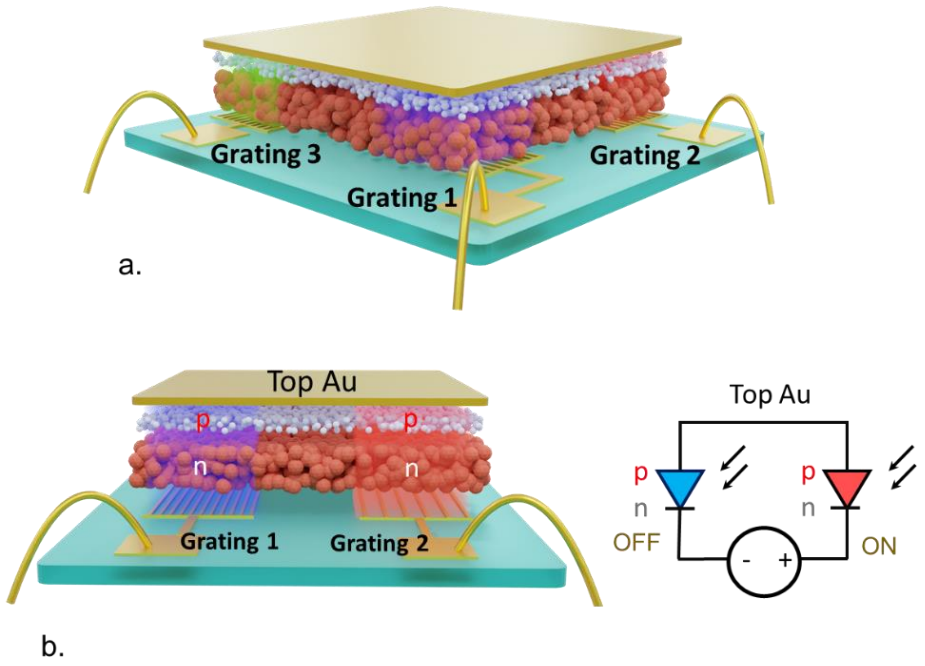

Figure 4.13: Back-to-back diode configuration based on a single diode stack. *a. Schematic of an array of back-to-back diodes in which the periods of the bottom electrodes are varied. b. Schematic of two gratings connected to the same stack and the illustrated circuit diagram. In the circuit, the diode on the left is in forward bias and does not respond to light. The diode on the right, on the other hand, is in reverse bias, and thus, is photoresponsive.*

In contrast to the vertical geometry in which the grating is connected as one electrode and the top contact as the second electrode, back-to-back diodes are formed with two gratings connected in series. The gratings are on the *n*-side, and the top gold layer is associated with the *p*-side. Depending on the applied bias voltage sign, one diode operates in forward mode (not photoresponsive) while the other is in reverse-bias operation (photoresponsive), as illustrated by the simplified circuit diagram in Figure 4.13b. This operation is enabled by the fact that the distance between the gratings within the plane (>100 µm) makes the planar transport very inefficient compared to the vertical transport, which only occurs over 500 nm.

Here, multiple operation modes can be generated by properly coupling diodes associated with different gratings. Figure 4.14 presents the spectra resulting from pairing different gratings, and each initially presents a distinct response, as shown in Figure 4.7a for vertical geometry. Figure 4.14a shows an example when two gratings with p_1 = 1400 nm and p_2 = 1800 nm are coupled. The photocurrent spectrum under photovoltaic mode (*i.e.,* 0V applied bias voltage), presented by the red curve, changes its sign according to the illumination wavelength. As a result, it is possible to use the photocurrent sign as spectral information since the current sign is directly connected to the spectral range where the associated grating presents a resonance. Thus, phase detection can provide spectral information of the illuminating light.

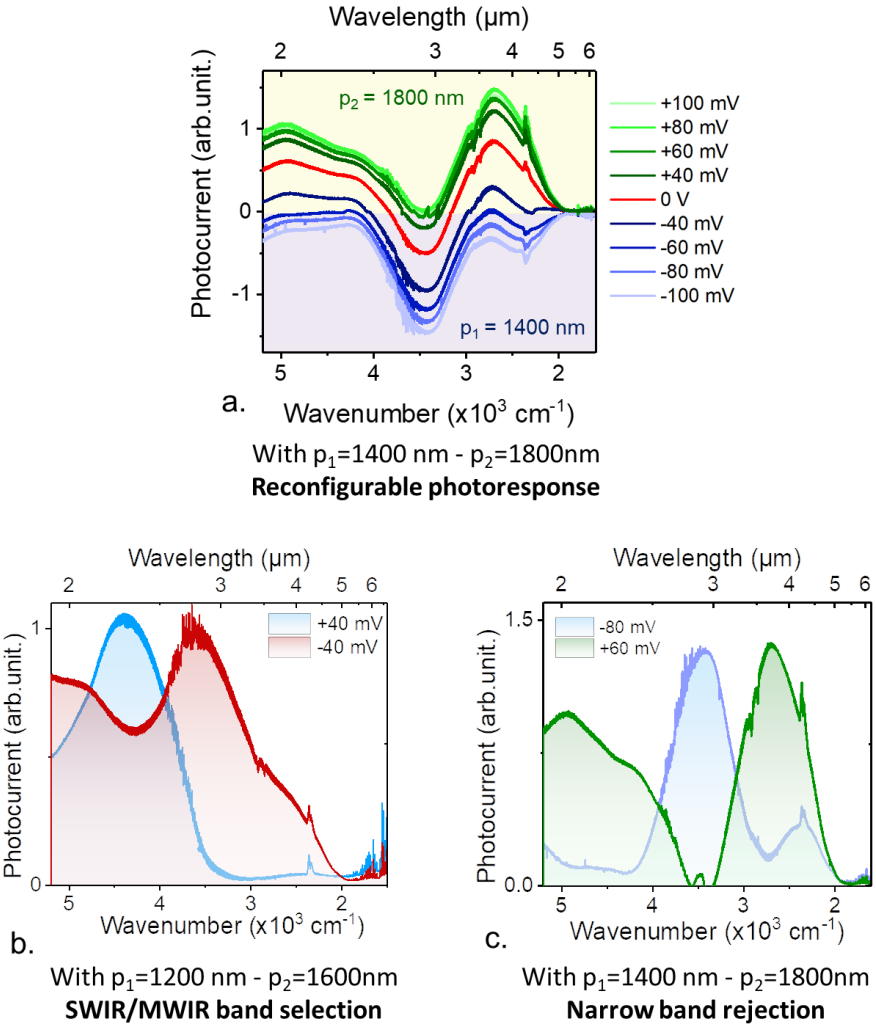

Figure 4.14: Bias-selectable optical band of back-to-back diodes. *a. Photocurrent spectra, under various positive and negative biases, in case 1400 nm and 1800 nm period gratings are coupled. By tuning the applied bias, the spectral response of the device can be modulated. In the figure, positive biases correspond to the case when diode p_2 is activated. b. Absolute value of photocurrent spectra under +/- 40 mV in the case where 1200 and 1600 nm gratings are selected. With bias, the MWIR response can be switched ON and OFF. c. Absolute value of photocurrent spectra, under positive and negative bias, in the case where 1400 and 1800 nm gratings are selected. With bias, the response of a narrow band can be turned ON and OFF.*

The back-to-back configuration can also be used for bias-selectable spectral response by changing the applied bias. Figure 4.14a also presents a series of spectra generated at different applied bias voltages. The spectrum associated with resonances from p_1 = 1400 nm and p_2 = 1800 nm can be promoted/demoted depending on the sign and magnitude of the applied bias voltage. This bias-dependent response allows optical band selection.

One example of this application is presented in Figure 4.14b. Switching bias between two coupled gratings with periods of 1200 nm and 1600 nm makes it possible to switch the response from broadband MWIR/SWIR to SWIR-only (Figure 4.14b). When the currents flowing in the two diodes are equal in intensity, the device's overall response becomes null

since they are opposite in sign. A single device allowing band switching can be practically useful for remote temperature monitoring and contrast enhancement in IR imaging [2].

Using plasmonic resonators also enables narrow spectral band rejection. So far, this functionality has not been reported in NC-based photodetectors. In Figure 4.14c, we show that the spectral response at 3 µm can be turned OFF while MWIR detection remains strong (the green curve) by applying proper bias voltages. A typical countermeasure strategy to prevent infrared imaging is blurring the sensor using a high-power laser. Here, with the capacity to turn off the response over a selected band, we can prevent possible saturation of the detector and continue imaging even if the detector has been spotted.

Note that even narrower band rejection can be obtained if the exploited resonances are optimized in terms of quality factor. The idea of back-to-back diodes with coupled resonators, in fact, can be applied to any type of resonator as long as the bottom electrodes define the spectral response of the fabricated device. The concept of coupling resonators for back-to-back diodes based on a single p-n junction is general and not limited to a specific optical design.

4.4. Conclusion

In this chapter, we introduce an approach to replace the transparent conductive electrodes for NC-based MWIR detectors. We demonstrate that a careful design of metallic grating can minimize optical loss while enhancing the effective absorption in the active semiconductor layer. Here, we propose a strategy combining three resonances from a single metallic grating. The polarization dependence of the grating structure can then be lifted using a 2D grid design. The obtained device presents outstanding performances with responsivity up to 2.65 $A.W^{-1}$ for a device with 5 µm cut-off wavelength and operate at 80 K. Detectivity at cryogenic temperature reaches $7x10^{11}$ jones, while the diode response time under mid-wave infrared excitation is below 100 ns.

We also demonstrate that different metallic gratings can be combined with a single diode stack to form multicolor and reconfigurable photodiodes. The concept of back-to-back diodes based on a single diode stack coupling with different resonators enables spectral filtering. Compared to existing strategies, our approach allows obtaining devices far easier to fabricate while offering new functionalities, such as band rejection, which can be used against countermeasure applications.

Conclusion and perspectives

This work is devoted to the realization of infrared sensors combining HgTe colloidal nanocrystals and plasmonic structures. The main idea behind this research work is the possibility of improving the performances of these sensors by confining the infrared radiation into distances comparable with the carrier diffusion length in nanocrystal films. Several plasmonic architectures have been explored in this work, resulting in several new functionality such as bias reconfigurability, wavelength tuning and band rejection.

After an introduction on infrared detection and state of the art of HgTe nanocrystal-based devices, in Chapter 2, we present a broadband infrared detector obtained by integrating a HgTe film into an array of metal-dielectric-metal cavities. The device presents broadband enhancement (from 2 µm to 4 µm) in light absorption thanks to three generated optical resonances. Design rules have been established based on the nature of each resonance. In terms of detection performance, the broadband detector enables sensing in the SWIR and MWIR regions (4 µm cut-off wavelength), with a high responsivity of 700 $mA.W^{-1}$, a detectivity above 10^{10} Jones for 80 K operating temperature, and demonstrated micro-second response time.

Chapter 3 focuses on bias-tunable photoresponse with nanocrystal-based infrared sensors. In this chapter, voltage-dependent carrier mobilities in solid nanocrystal films have been exploited. We combine this peculiar property with inhomogeneous absorption induced by optical modes generated by optical structures to demonstrate bias-tunable photoresponse in nanocrystal-based photodetectors. The tunability has been presented from a spectral shift to bias-modulated optical bands. We show that hopping transport can play a crucial role in designing active photonic devices based on nanocrystals.

Finally, in Chapter 4, we investigate the coupling of a nanocrystal-photodiode for mid-wave infrared sensing. We introduce an approach to advantageously replace the transparent conductive electrodes with a metallic structure operating both as a contact and as a resonator, minimizing the optical loss and enhancing the absorption of the active nanocrystal layer. The obtained device presents outstanding performances with a detectivity reaching $7x10^{11}$ jones at cryogenic temperature, among the most sensitive MWIR NC-based infrared sensors reported so far. Furthermore, we also demonstrate that different metallic gratings can be combined with a single diode stack to form multicolor and reconfigurable photodiodes. Many advanced functionalities have also been demonstrated, particularly narrow-band rejection, which was presented for the first time in infrared detectors based on nanocrystals.

A perspective related to the study in Chapter 4 is the optimization of the diode structure by replacing gold grating with other plasmonic materials better suited for electron extraction. In this direction, dielectric materials with low optical losses can be explored.

A perspective for light-matter coupling study in nanocrystal-based infrared sensors will be the integration of the optical structures onto focal plane arrays. The introduction of photonic structures to nanocrystal-based infrared sensors has been demonstrated to be highly beneficial. We thus expect this approach to have the same impact on the efficiency of the current nanocrystal-based FPA imagers.

To this end, designing efficient resonant structures at the scale of a single pixel is necessary. Some preliminary results have been obtained with the coupled resonators presented in

Chapter 3, showing that the antenna effect can be expected when the resonator array area is reduced [157]. The device's effective optical area (*i.e.,* related to the responsivity) can become larger than its electrical area (*i.e.,* related to electrical noise), thus improving signal to noise ratio, and ultimately, detection performance of the device.

Finally, on a more fundamental side, the improvement of the synthesis of nanocrystals in the longwave infrared could allow their coupling with resonators with reduced ohmic losses with respect to those measured in this work. In this case, it could be possible to reach the strong light-matter coupling regime. Several works have shown a modified carrier transport in the presence of a strong coupling with a cavity mode [196], which is particularly beneficial in materials where transport is dominated by hopping mechanisms.

List of publications

First author articles

1. Dang, T. H.; Vasanelli, A.; Todorov, Y.; Sirtori, C.; Prado, Y.; Chu, A.; Gréboval, C.; Khalili, A.; Cruguel, H.; Delerue, C.; Vincent, G.; Lhuillier, E. Bias Tunable Spectral Response of Nanocrystal Array in a Plasmonic Cavity. *Nano Lett.* **2021**, *21*, 6671–6677.
2. Dang, T. H.; Abadie, C.; Khalili, A.; Gréboval, C.; Zhang, H.; Prado, Y.; Xu, X. Z.; Gacemi, D.; Descamps-Mandine, A.; Ithurria, S.; Todorov, Y.; Sirtori, C.; Vasanelli, A.; Lhuillier, E., Broadband Enhancement of Mid-Wave Infrared Absorption in a Multi-Resonant Nanocrystal-Based Device. *Adv. Optical Mater.* ***2022***, 10, 2200297.
3. Dang, T. H.; Khalili, A.; Abadie, C.; Gréboval, C.; Cavallo, M.; Zhang, H.; Bossavit, E.; Utterback, J. K.; Dandeu, E.; Prado, Y.; Vincent, G.; Ithurria, S.; Todorov, Y.; Sirtori, C.; Vasanelli, A.; Lhuillier, E. Nanocrystal-Based Active Photonics Device through Spatial Design of Light-Matter Coupling. *ACS Photonics* **2022**, *9*, 2528–2535.
4. Dang, T. H.; Abadie, C.; Chu, A.; Cavallo, M.; Khalili, A.; Dabard, C; Bossavit, E.; Zhang, H; Prado, Y.; Pierucci, D; Utterback, J. K.; Todorov, Y.; Sirtori, C.; Jaeck, J; Vincent, G.; Vasanelli, A.; Fix, B; Lhuillier, E. Bias reconfigurable photoresponse of infrared nanocrystal film integrated into a coupled Fabry-Perot resonator. *ACS Photonics* **2023**, 10, 1601–1607.
5. Dang, T. H.; Cavallo, M.; Khalili, A.; Dabard, C.; Bossavit, E.; Zhang, H.; Ledos, N.; Prado, Y.; Lafosse, X.; Abadie, C.; Gacemi, D.; Ithurria, S.; Vincent, G.; Todorov, Y.; Sirtori, C.; Vasanelli, A.; Lhuillier, E. Multiresonant Grating to replace Transparent Conductive Oxide Electrode for Bias Selected Filtering of Infrared Photoresponse. *Nano Lett*. **2023**, 23, 8539 – 8546.

Other articles

6. Cavallo, M.; Bossavit, E.; Matzen, S.; Maroutian, T.; Alchaar, R.; Dang, T. H.; Khalili, A.; Dabard, C.; Zhang, H.; Prado, Y.; Abadie, C.; Utterback, J. K.; Dayen, J. F.; Silly, M. G.; Dudin, P.; Avila, J.; Lhuillier, E.; Pierucci, D. Coupling Ferroelectric to Colloidal Nanocrystals as a Generic Strategy to Engineer the Carrier Density Landscape. *Adv. Funct. Mater.* **2023**, 2300846.
7. Pierini, S.; Abadie, C.; Dang, T. H.; Khalili, A.; Zhang, H.; Cavallo, M.; Prado, Y.; Gallas, B.; Ithurria, S.; Sauvage, S.; Dayen, J. F.; Vincent, G.; Lhuillier, E. Lithium-Ion Glass Gating of HgTe Nanocrystal Film with Designed Light-Matter Coupling. *Materials* **2023**, *16*.
8. Khalili, A.; Cavallo, M.; Dang, T. H.; Dabard, C.; Zhang, H.; Bossavit, E.; Abadie, C.; Prado, Y.; Xu, X. Z.; Ithurria, S.; Vincent, G.; Coinon, C.; Desplanque, L.; Lhuillier, E. Mid-Wave Infrared Sensitized InGaAs Using Intraband Transition in Doped Colloidal II–VI Nanocrystals. *J. Chem. Phys.* **2023**, *158*, 094702.
9. Zhang, H.; Guilloux, V.; Bossavit, E.; Fu, N.; Dabard, C.; Cavallo, M.; Dang, T. H.; Khalili, A.; Abadie, C.; Alchaar, R.; Gréboval, C.; Xu, X. Z.; Utterback, J. K.; Pierucci, D.; Ithurria,

S.; Climente, J. I.; Barisien, T.; Lhuillier, E. Visible and Infrared Nanocrystal-Based Light Modulator with CMOS Compatible Bias Operation. *ACS Photonics* **2023**, *10*, 430–436.

10. Cavallo, M.; Bossavit, E.; Zhang, H.; Dabard, C.; Dang, T. H.; Khalili, A.; Abadie, C.; Alchaar, R.; Mastrippolito, D.; Prado, Y.; Becerra, L.; Rosticher, M.; Silly, M. G.; Utterback, J. K.; Ithurria, S.; Avila, J.; Pierucci, D.; Lhuillier, E. Mapping the Energy Landscape from a Nanocrystal-Based Field Effect Transistor under Operation Using Nanobeam Photoemission Spectroscopy. *Nano Lett.* **2023**, *23*, 1363–1370.
11. Cavallo, M.; Alchaar, R.; Bossavit, E.; Zhang, H.; Dang, T. H.; Khalili, A.; Prado, Y.; Silly, M. G.; Utterback, J. K.; Ithurria, S.; Dudin, P.; Avila, J.; Pierucci, D.; Lhuillier, E. Inside a Nanocrystal-Based Photodiode Using Photoemission Microscopy. *Nanoscale* **2023**, *15*, 9440–9448.
12. Zhang, H.; Alchaar, R.; Prado, Y.; Khalili, A.; Gréboval, C.; Cavallo, M.; Bossavit, E.; Dabard, C.; Dang, T. H.; Abadie, C.; Methivier, C.; Darson, D.; Parahyba, V.; Potet, P.; Ramade, J.; Silly, M. G.; Utterback, J. K.; Pierucci, D.; Ithurria, S.; Lhuillier, E. Material Perspective on HgTe Nanocrystal-Based Short-Wave Infrared Focal Plane Arrays. *Chem. Mater.* **2022**, *34*, 10964–10972.
13. Abadie, C.; Paggi, L.; Fabas, A.; Khalili, A.; Dang, T. H.; Dabard, C.; Cavallo, M.; Alchaar, R.; Zhang, H.; Prado, Y.; Bardou, N.; Dupuis, C.; Xu, X. Z.; Ithurria, S.; Pierucci, D.; Utterback, J. K.; Fix, B.; Vincent, G.; Bouchon, P.; Lhuillier, E. Helmholtz Resonator Applied to Nanocrystal-Based Infrared Sensing. *Nano Lett.* **2022**, *22*, 8779–8785.
14. Rastogi, P.; Izquierdo, E.; Gréboval, C.; Cavallo, M.; Chu, A.; Dang, T. H.; Khalili, A.; Abadie, C.; Alchaar, R.; Pierini, S.; Cruguel, H.; Witkowski, N.; Utterback, J. K.; Brule, T.; Xu, X. Z.; Hollander, P.; Ouerghi, A.; Gallas, B.; Silly, M. G.; Lhuillier, E. Extended Short-Wave Photodiode Based on CdSe/HgTe/Ag2Te Stack with High Internal Efficiency. *J. Phys. Chem. C* **2022**, *126*, 13720–13728.
15. Pierini, S.; Capitani, F.; Scimeca, M.; Kozlov, S.; Pierucci, D.; Alchaar, R.; Abadie, C.; Khalili, A.; Cavallo, M.; Dang, T. H.; Zhang, H.; Bossavit, E.; Gréboval, C.; Avila, J.; Baptiste, B.; Klotz, S.; Sahu, A.; Feuillet-Palma, C.; Xu, X. Z.; Ouerghi, A.; Ithurria, S.; Utterback, J. K.; Sauvage, S.; Lhuillier, E. Vanishing Confinement Regime in Terahertz HgTe Nanocrystals Studied under Extreme Conditions of Temperature and Pressure. *J. Phys. Chem. Lett.* **2022**, *13*, 6919–6926.
16. Gréboval, C.; Izquierdo, E.; Abadie, C.; Khalili, A.; Cavallo, M.; Chu, A.; Dang, T. H.; Zhang, H.; Lafosse, X.; Rosticher, M.; Xu, X. Z.; Descamps-Mandine, A.; Ouerghi, A.; Silly, M. G.; Ithurria, S.; Lhuillier, E. HgTe Nanocrystal-Based Photodiode for Extended Short-Wave Infrared Sensing with Optimized Electron Extraction and Injection. *ACS Appl. Nano Mater.* **2022**, *5*, 8602–8611.
17. Khalili, A.; Weis, M.; Mizrahi, S. G.; Chu, A.; Dang, T. H.; Abadie, C.; Gréboval, C.; Dabard, C.; Prado, Y.; Xu, X. Z.; Péronne, E.; Livache, C.; Ithurria, S.; Patriarche, G.; Ramade, J.; Vincent, G.; Boschetto, D.; Lhuillier, E. Guided-Mode Resonator Coupled with Nanocrystal Intraband Absorption. *ACS Photonics* **2022**, *9*, 985–993.
18. Bossavit, E.; Qu, J.; Abadie, C.; Dabard, C.; Dang, T. H; Izquierdo, E.; Khalili, A.; Gréboval, C.; Chu, A.; Pierini, S.; Cavallo, M.; Prado, Y.; Parahyba, V.; Xu, X. Z.; Decamps-Mandine, A.; Silly, M.; Ithurria, S.; Lhuillier, E. Optimized Infrared LED and Its

Use in an All-HgTe Nanocrystal-Based Active Imaging Setup. *Adv. Opt. Mater.* **2022**, *10*, 2101755.

19. Khalili, A.; Abadie, C.; Dang, T. H.; Chu, A.; Izquierdo, E.; Dabard, C.; Gréboval, C.; Cavallo, M.; Zhang, H.; Pierini, S.; Prado, Y.; Xu, X. Z.; Ithurria, S.; Vincent, G.; Coinon, C.; Desplanque, L.; Lhuillier, E. Colloidal II–VI—Epitaxial III–V Heterostructure: A Strategy to Expand InGaAs Spectral Response. *Appl. Phys. Lett.* **2022**, *120*, 051101.
20. Chehaibou, B.; Izquierdo, E.; Chu, A.; Abadie, C.; Cavallo, M.; Khalili, A.; Dang, T. H.; Gréboval, C.; Xu, X. Z.; Ithurria, S.; Vincent, G.; Gallas, B.; Mugny, G.; Arnaud, A.; Lhuillier, E.; Delerue, C. The Complex Optical Index of PbS Nanocrystal Thin Films and Their Use for Short Wave Infrared Sensor Design. *Nanoscale* **2022**, *14*, 2711–2721.
21. Dabard, C.; Planelles, J.; Po, H.; Izquierdo, E.; Makke, L.; Gréboval, C.; Moghaddam, N.; Khalili, A.; Dang, T. H.; Chu, A.; Pierini, S.; Abadie, C.; Cavallo, M.; Bossavit, E.; Xu, X. Z.; Hollander, P.; Silly, M.; Lhuillier, E.; Climente, J. I.; Ithurria, S. Optimized Cation Exchange for Mercury Chalcogenide 2D Nanoplatelets and Its Application for Alloys. *Chem. Mater.* **2021**, *33, 9252–9261*.
22. Gréboval, C.; Dabard, C.; Konstantinov, N.; Cavallo, M.; Chee, S.-S.; Chu, A.; Dang, T. H.; Khalili, A.; Izquierdo, E.; Prado, Y.; Majjad, H.; Xu, X. Z.; Dayen, J.-F.; Lhuillier, E. Split-Gate Photodiode Based on Graphene/HgTe Heterostructures with a Few Nanosecond Photoresponse. *ACS Appl. Electron. Mater.* **2021**, *3*, 4681–4688.
23. Chee, S.-S.; Gréboval, C.; Magalhaes, D. V.; Ramade, J.; Chu, A.; Qu, J.; Rastogi, P.; Khalili, A.; Dang, T. H.; Dabard, C.; Prado, Y.; Patriarche, G.; Chaste, J.; Rosticher, M.; Bals, S.; Delerue, C.; Lhuillier, E. Correlating Structure and Detection Properties in HgTe Nanocrystal Films. *Nano Lett.* **2021**, *21*, 4145–4151.
24. Rastogi, P.; Chu, A.; Dang, T. H.; Prado, Y.; Gréboval, C.; Qu, J.; Dabard, C.; Khalili, A.; Dandeu, E.; Fix, B.; Xu, X. Z.; Ithurria, S.; Vincent, G.; Gallas, B.; Lhuillier, E. Complex Optical Index of HgTe Nanocrystal Infrared Thin Films and Its Use for Short Wave Infrared Photodiode Design. *Adv. Opt. Mater.* **2021**, *9*, 2002066.
25. Gréboval, C.; Noumbé, U. N.; Chu, A.; Prado, Y.; Khalili, A.; Dabard, C.; Dang, T. H.; Colis, S.; Chaste, J.; Ouerghi, A.; Dayen, J.-F.; Lhuillier, E. Gate Tunable Vertical Geometry Phototransistor Based on Infrared HgTe Nanocrystals. *Appl. Phys. Lett.* **2020**, *117*, 251104.
26. Gréboval, C.; Rastogi, P.; Qu, J.; Chu, A.; Ramade, J.; Khalili, A.; Dabard, C.; Dang, T. H.; Cruguel, H.; Ouerghi, A.; Witkowski, N.; Silly, M. G.; Lhuillier, E. Time-Resolved Photoemission to Unveil Electronic Coupling between Absorbing and Transport Layers in a Quantum Dot-Based Solar Cell. *J. Phys. Chem. C* **2020**, *124*, 23400–23409.

Book chapters

1. Lhuillier, E.; Dang, T. H.; Cavallo, M.; Abadie, C.; Khalili, A.; Peterson, J. C.; Gréboval, C. Infrared Sensing Using Mercury Chalcogenide Nanocrystals. In *Handbook of II-VI Semiconductor-Based Sensors and Radiation Detectors: Volume 2, Photodetectors*; Springer International Publishing: Cham, **2023**; 155–181.

2. Lhuillier, E.; Dang, T. H.; Cavallo, M.; Abadie, C.; Khalili, A.; Gréboval, C. Electronic Structure of Mercury Chalcogenides Nanocrystals. In *Handbook of II-VI Semiconductor-Based Sensors and Radiation Detectors: Volume 1, Materials and Technology*; Springer International Publishing: Cham, **2023**; 133–156.

Conferences

1. Dang, T. H.; Vasanelli, A.; Todorov, Y.; Sirtori, C.; Lhuillier, E. Gate tunable colloidal nanocrystal-based infrared sensor. *GDR NanoTeraMIR*. **2021**.
2. Dang, T. H.; Vasanelli, A.; Todorov, Y.; Sirtori, C.; Prado, Y.; Delerue, C.; Lhuillier, E. Towards nanocrystal-based active nanophotonic device. *NanoGe Fall meeting*. **2021**.
3. Dang, T. H.; Vasanelli, A.; Todorov, Y.; Sirtori, C.; Prado, Y.; Delerue, C.; Lhuillier, E. Towards nanocrystal-based active nanophotonic device. *NanoGe Spring meeting*. **2022**.
4. Dang, T. H.; Khalili, A.; Gréboval, C.; Chu, A.; Prado, Y.; Sirtori, C.; Vasanelli, A.; Lhuillier, E. Towards nanocrystal-based active photonic devices. *Gordon Research Conference*. **2022** (poster presentation).
5. Dang, T. H.; Chu, A.; Abadie, C.; Prado, Y.; Fix, B; Vincent, G.; Sirtori, C.; Vasanelli, A.; Lhuillier, E. Active photonics with hopping transport for IR detection. *GDR NanoTeraMIR*. **2023**.
6. Dang, T. H.; Chu, A.; Abadie, C.; Prado, Y.; Fix, B; Vincent, G.; Sirtori, C.; Vasanelli, A.; Lhuillier, E. Active photonics with hopping transport for IR detection. *Infrared and Terahertz quantum workshop*. **2023**.

Bibliography

[1] E. Rosencher and B. Vinter, *Optoelectronics*. Cambridge University Press, **2002**.

[2] A. Rogalski, 'Infrared detectors: status and trends', *Prog. Quantum Electron.*, 27, 59–210, **2003**, doi: 10.1016/S0079-6727(02)00024-1.

[3] A. W. Van Herwaarden and P. M. Sarro, 'Thermal sensors based on the seebeck effect', *Sens. Actuators*, 10, 321–346, **1986**, doi: 10.1016/0250-6874(86)80053-1.

[4] R W Whatmore, 'Pyroelectric devices and materials', *Rep. Prog. Phys.*, 49, 1335, **1986**, doi: 10.1088/0034-4885/49/12/002.

[5] P. Richards, 'Bolometers for infrared and millimeter waves', *J. Appl. Phys.*, 76, 1–24, **1994**.

[6] A. Rogalski, 'HgCdTe infrared detector material: history, status and outlook', *Rep. Prog. Phys.*, 68, 2267, **2005**, doi: 10.1088/0034-4885/68/10/R01.

[7] S. R. Jost, V. F. Meikleham, and T. H. Myers, 'InSb: A Key Material for IR Detector Applications', *MRS Online Proc. Libr.*, 90, 429, **1986**, doi: 10.1557/PROC-90-429.

[8] J. Kaniewski and J. Piotrowski, 'InGaAs for infrared photodetectors. Physics and technology', *Opto-Electron. Rev.*, 12, 139–148, **2004**.

[9] B. F. Levine, K. K. Choi, C. G. Bethea, J. Walker, and R. J. Malik, 'New 10 μm infrared detector using intersubband absorption in resonant tunneling GaAlAs superlattices', *Appl. Phys. Lett.*, 50, 1092–1094, **1987**, doi: 10.1063/1.97928.

[10] L. Gendron, M. Carras, A. Huynh, V. Ortiz, C. Koeniguer, and V. Berger, 'Quantum cascade photodetector', *Appl. Phys. Lett.*, 85, 2824–2826, **2004**, doi: 10.1063/1.1781731.

[11] T. Ueda, S. Komiyama, Z. An, N. Nagai, and K. Hirakawa, 'Temperature dependence of the performance of charge-sensitive infrared phototransistors', *J. Appl. Phys.*, 105, 064517, **2009**, doi: 10.1063/1.3087579.

[12] T. W. Case, 'Notes on the change of resistance of certain substances in light', *Phys. Rev.*, 9, 305, **1917**.

[13] S. F. Johnston, *A history of light and colour measurement: science in the shadows*. CRC Press, **2015**.

[14] R. Cashman, 'Film-type infrared photoconductors', *Proc. IRE*, 47, 1471–1475, **1959**.

[15] W. D. Lawson, S. Nielsen, E. H. Putley, and A. S. Young, 'Preparation and properties of HgTe and mixed crystals of HgTe-CdTe', *J. Phys. Chem. Solids*, 9, 325–329, **1959**, doi: 10.1016/0022-3697(59)90110-6.

[16] J. B. Johnson, 'Thermal agitation of electricity in conductors', *Phys. Rev.*, 32, 97, **1928**.

[17] H. Liu, E. Lhuillier, and P. Guyot-Sionnest, '1/f noise in semiconductor and metal nanocrystal solids', *J. Appl. Phys.*, 115, 154309, **2014**, doi: 10.1063/1.4871682.

[18] M. Long *et al.*, 'Room temperature high-detectivity mid-infrared photodetectors based on black arsenic phosphorus', *Sci. Adv.*, 3, e1700589, **2017**, doi: 10.1126/sciadv.1700589.

[19] Q. Guo *et al.*, 'Black Phosphorus Mid-Infrared Photodetectors with High Gain', *Nano Lett.*, 16, 4648–4655, **2016**, doi: 10.1021/acs.nanolett.6b01977.

[20] I. Omkaram, Y. K. Hong, and S. Kim, 'Transition metal dichalcogenide photodetectors', *Two-Dimens. Mater. Photodetector*, **2018**.

[21] X. Guan *et al.*, 'Recent progress in short-to long-wave infrared photodetection using 2D materials and heterostructures', *Adv. Opt. Mater.*, 9, 2001708, **2021**.

[22] C. Gréboval, A. Chu, N. Goubet, C. Livache, S. Ithurria, and E. Lhuillier, 'Mercury Chalcogenide Quantum Dots: Material Perspective for Device Integration', *Chem. Rev.*, 121, 3627–3700, **2021**, doi: 10.1021/acs.chemrev.0c01120.

[23] P. Guyot-Sionnest, M. M. Ackerman, and X. Tang, 'Colloidal quantum dots for infrared detection beyond silicon', *J. Chem. Phys.*, 151, 060901, **2019**, doi: 10.1063/1.5115501.

[24] S. A. McDonald *et al.*, 'Solution-processed PbS quantum dot infrared photodetectors and photovoltaics', *Nat. Mater.*, 4, 138–142, **2005**, doi: 10.1038/nmat1299.

[25] G. Konstantatos *et al.*, 'Ultrasensitive solution-cast quantum dot photodetectors', *Nature*, 442, 180–183, **2006**, doi: 10.1038/nature04855.

[26] L. Brus, 'Electronic wave functions in semiconductor clusters: experiment and theory', *J. Phys. Chem.*, 90, 2555–2560, **1986**, doi: 10.1021/j100403a003.

[27] Y.-M. Niquet, G. Allan, C. Delerue, and M. Lannoo, 'Quantum confinement in germanium nanocrystals', *Appl. Phys. Lett.*, 77, 1182–1184, **2000**.

[28] B. Delley and E. Steigmeier, 'Quantum confinement in Si nanocrystals', *Phys. Rev. B*, 47, 1397, **1993**.

[29] J. Butkus *et al.*, 'The evolution of quantum confinement in CsPbBr3 perovskite nanocrystals', *Chem. Mater.*, 29, 3644–3652, **2017**.

[30] V. I. Klimov, *Nanocrystal quantum dots*. CRC press, **2017**.

[31] A. W. H. Mau *et al.*, 'Hydrogen photoproduction by Nafion/cadmium sulfide/platinum films in water/sulfide ion solutions', *J. Am. Chem. Soc.*, 106, 6537–6542, **1984**, doi: 10.1021/ja00334a014.

[32] Y. M. Tricot, A. Emeren, and J. H. Fendler, 'In situ generation of catalyst-coated cadmium sulfide particles in polymerized and unpolymerized surfactant vesicles and their utilization for efficient visible-light-induced hydrogen production', *J. Phys. Chem.*, 89, 4721–4726, **1985**, doi: 10.1021/j100268a015.

[33] M. Grätzel and J. Moser, 'Multielectron storage and hydrogen generation with colloidal semiconductors', *Proc. Natl. Acad. Sci.*, 80, 3129–3132, **1983**, doi: 10.1073/pnas.80.10.3129.

[34] A. Henglein, 'Photochemistry of colloidal cadmium sulfide. 2. Effects of adsorbed methyl viologen and of colloidal platinum', *J. Phys. Chem.*, 86, 2291–2293, **1982**, doi: 10.1021/j100210a010.

[35] A. Fojtik, H. Weller, U. Koch, and A. Henglein, 'Photo-Chemistry of Colloidal Metal Sulfides 8. Photo-Physics of Extremely Small CdS Particles: Q-State CdS and Magic Agglomeration Numbers', *Berichte Bunsenges. Für Phys. Chem.*, 88, 969–977, **1984**, doi: 10.1002/bbpc.19840881010.

[36] U. Koch, A. Fojtik, H. Weller, and A. Henglein, 'Photochemistry of semiconductor colloids. Preparation of extremely small ZnO particles, fluorescence phenomena and size quantization effects', *Chem. Phys. Lett.*, 122, 507–510, **1985**, doi: 10.1016/0009-2614(85)87255-9.

[37] C. B. Murray, D. J. Norris, and M. G. Bawendi, 'Synthesis and characterization of nearly monodisperse CdE (E = sulfur, selenium, tellurium) semiconductor nanocrystallites', *J. Am. Chem. Soc.*, 115, 8706–8715, **1993**, doi: 10.1021/ja00072a025.

[38] D. V. Talapin, S. K. Poznyak, N. P. Gaponik, A. L. Rogach, and A. Eychmüller, 'Synthesis of surface-modified colloidal semiconductor nanocrystals and study of photoinduced charge separation and transport in nanocrystal-polymer composites', *Phys. E Low-Dimens. Syst. Nanostructures*, 14, 237–241, **2002**, doi: 10.1016/S1386-9477(02)00391-0.

[39] A. Rogach *et al.*, 'Colloidally Prepared HgTe Nanocrystals with Strong Room-Temperature Infrared Luminescence', *Adv. Mater.*, 11, 552–555, **1999**, doi: 10.1002/(SICI)1521-4095(199905)11:7<552::AID-ADMA552>3.0.CO;2-Q.

[40] H. Kim *et al.*, 'Photocurrent mechanism in a hybrid system of 1-thioglycerol-capped HgTe nanoparticles', *Appl. Phys. Lett.*, 83, 4619–4621, **2003**, doi: 10.1063/1.1631052.

[41] H. Kim *et al.*, 'Optoelectronic characteristics of close-packed HgTe nanoparticles in the infrared range', *Solid State Commun.*, 137, 315–319, **2006**, doi: 10.1016/j.ssc.2005.11.037.

[42] N. A. Cade and P. M. Lee, 'Self consistent energy band structures for HgTe and CdTe', *Solid State Commun.*, 56, 637–641, **1985**, doi: 10.1016/0038-1098(85)90974-3.

[43] P. Sengupta, T. Kubis, Y. Tan, M. Povolotskyi, and G. Klimeck, 'Design principles for HgTe based topological insulator devices', *J. Appl. Phys.*, 114, 043702, **2013**, doi: 10.1063/1.4813877.

[44] E. Izquierdo, A. Robin, S. Keuleyan, N. Lequeux, E. Lhuillier, and S. Ithurria, 'Strongly Confined HgTe 2D Nanoplatelets as Narrow Near-Infrared Emitters', *J. Am. Chem. Soc.*, 138, 10496–10501, **2016**, doi: 10.1021/jacs.6b04429.

[45] N. Goubet *et al.*, 'Terahertz HgTe Nanocrystals: Beyond Confinement', *J. Am. Chem. Soc.*, 140, 5033–5036, **2018**, doi: 10.1021/jacs.8b02039.

[46] M. T. Harrison, S. V. Kershaw, M. G. Burt, A. Rogach, A. Eychmüller, and H. Weller, 'Investigation of factors affecting the photoluminescence of colloidally-prepared HgTe nanocrystals', *J. Mater. Chem.*, 9, 2721–2722, **1999**, doi: 10.1039/A907224A.

[47] M. V. Kovalenko *et al.*, 'Colloidal HgTe Nanocrystals with Widely Tunable Narrow Band Gap Energies: From Telecommunications to Molecular Vibrations', *J. Am. Chem. Soc.*, 128, 3516–3517, **2006**, doi: 10.1021/ja058440j.

[48] S. Keuleyan, E. Lhuillier, and P. Guyot-Sionnest, 'Synthesis of Colloidal HgTe Quantum Dots for Narrow Mid-IR Emission and Detection', *J. Am. Chem. Soc.*, 133, 16422–16424, **2011**, doi: 10.1021/ja2079509.

[49] Y. Prado *et al.*, 'Seeded Growth of HgTe Nanocrystals for Shape Control and Their Use in Narrow Infrared Electroluminescence', *Chem. Mater.*, 33, 2054–2061, **2021**, doi: 10.1021/acs.chemmater.0c04526.

[50] X. Lan *et al.*, 'Quantum dot solids showing state-resolved band-like transport', *Nat. Mater.*, 19, 323–329, **2020**, doi: 10.1038/s41563-019-0582-2.

[51] H. Zhang and P. Guyot-Sionnest, 'Shape-Controlled HgTe Colloidal Quantum Dots and Reduced Spin–Orbit Splitting in the Tetrahedral Shape', *J. Phys. Chem. Lett.*, 11, 6860–6866, **2020**, doi: 10.1021/acs.jpclett.0c01550.

[52] N. Goubet *et al.*, 'Wave-Function Engineering in HgSe/HgTe Colloidal Heterostructures To Enhance Mid-infrared Photoconductive Properties', *Nano Lett.*, 18, 4590–4597, **2018**, doi: 10.1021/acs.nanolett.8b01861.

[53] G. Shen and P. Guyot-Sionnest, 'HgTe/CdTe and HgSe/CdX (X = S, Se, and Te) Core/Shell Mid-Infrared Quantum Dots', *Chem. Mater.*, 31, 286–293, **2019**, doi: 10.1021/acs.chemmater.8b04727.

[54] M. H. Hudson *et al.*, 'Conduction Band Fine Structure in Colloidal HgTe Quantum Dots', *ACS Nano*, 12, 9397–9404, **2018**, doi: 10.1021/acsnano.8b04539.

[55] M. Chen *et al.*, 'High Carrier Mobility in HgTe Quantum Dot Solids Improves Mid-IR Photodetectors', *ACS Photonics*, 6, 2358–2365, **2019**, doi: 10.1021/acsphotonics.9b01050.

[56] P. Guyot-Sionnest, 'Electrical Transport in Colloidal Quantum Dot Films', *J. Phys. Chem. Lett.*, 3, 1169–1175, **2012**, doi: 10.1021/jz300048y.

[57] S. Keuleyan, E. Lhuillier, V. Brajuskovic, and P. Guyot-Sionnest, 'Mid-infrared HgTe colloidal quantum dot photodetectors', *Nat. Photonics*, 5, 489–493, **2011**, doi: 10.1038/nphoton.2011.142.

[58] H. Kim, K. Cho, D.-W. Kim, H.-R. Lee, and S. Kim, 'Bottom- and top-gate field-effect thin-film transistors with p channels of sintered HgTe nanocrystals', *Appl. Phys. Lett.*, 89, 173107, **2006**, doi: 10.1063/1.2364153.

[59] J. Kim *et al.*, 'High electron mobility of β-HgS colloidal quantum dots with doubly occupied quantum states', *RSC Adv.*, 7, 38166–38170, **2017**, doi: 10.1039/C7RA07193K.

[60] E. Lhuillier, S. Keuleyan, P. Zolotavin, and P. Guyot-Sionnest, 'Mid-Infrared HgTe/As2S3 Field Effect Transistors and Photodetectors', *Adv. Mater.*, 25, 137–141, **2013**, doi: 10.1002/adma.201203012.

[61] D. Yu, C. Wang, and P. Guyot-Sionnest, 'n-Type Conducting CdSe Nanocrystal Solids', *Science*, 300, 1277–1280, **2003**, doi: 10.1126/science.1084424.

[62] D. A. R. Barkhouse, A. G. Pattantyus-Abraham, L. Levina, and E. H. Sargent, 'Thiols Passivate Recombination Centers in Colloidal Quantum Dots Leading to Enhanced Photovoltaic Device Efficiency', *ACS Nano*, 2, 2356–2362, **2008**, doi: 10.1021/nn800471c.

[63] J. M. Luther, M. Law, Q. Song, C. L. Perkins, M. C. Beard, and A. J. Nozik, 'Structural, Optical, and Electrical Properties of Self-Assembled Films of PbSe Nanocrystals Treated with 1,2-Ethanedithiol', *ACS Nano*, 2, 271–280, **2008**, doi: 10.1021/nn7003348.

[64] M. V. Kovalenko, M. Scheele, and D. V. Talapin, 'Colloidal Nanocrystals with Molecular Metal Chalcogenide Surface Ligands', *Science*, 324, 1417–1420, **2009**, doi: 10.1126/science.1170524.

[65] A. Nag, M. V. Kovalenko, J.-S. Lee, W. Liu, B. Spokoyny, and D. V. Talapin, 'Metal-free Inorganic Ligands for Colloidal Nanocrystals: S2–, HS–, Se2–, HSe–, Te2–, HTe–, TeS32–, OH–, and NH2– as Surface Ligands', *J. Am. Chem. Soc.*, 133, 10612–10620, **2011**, doi: 10.1021/ja2029415.

[66] Z. Ning, H. Dong, Q. Zhang, O. Voznyy, and E. H. Sargent, 'Solar Cells Based on Inks of n-Type Colloidal Quantum Dots', *ACS Nano*, 8, 10321–10327, **2014**, doi: 10.1021/nn503569p.

[67] D. M. Balazs *et al.*, 'Counterion-Mediated Ligand Exchange for PbS Colloidal Quantum Dot Superlattices', *ACS Nano*, 9, 11951–11959, **2015**, doi: 10.1021/acsnano.5b04547.

[68] A. Fischer *et al.*, 'Directly Deposited Quantum Dot Solids Using a Colloidally Stable Nanoparticle Ink', *Adv. Mater.*, 25, 5742–5749, **2013**, doi: 10.1002/adma.201302147.

[69] B. Martinez *et al.*, 'HgTe Nanocrystal Inks for Extended Short-Wave Infrared Detection', *Adv. Opt. Mater.*, 7, 1900348, **2019**, doi: 10.1002/adom.201900348.

[70] J. Yang *et al.*, 'Ligand-Engineered HgTe Colloidal Quantum Dot Solids for Infrared Photodetectors', *Nano Lett.*, 22, 3465–3472, **2022**, doi: 10.1021/acs.nanolett.2c00950.

[71] P. R. Brown *et al.*, 'Energy Level Modification in Lead Sulfide Quantum Dot Thin Films through Ligand Exchange', *ACS Nano*, 8, 5863–5872, **2014**, doi: 10.1021/nn500897c.

[72] A. Chu *et al.*, 'HgTe Nanocrystals for SWIR Detection and Their Integration up to the Focal Plane Array', *ACS Appl. Mater. Interfaces*, 11, 33116–33123, **2019**, doi: 10.1021/acsami.9b09954.

[73] C. R. Kagan and C. B. Murray, 'Charge transport in strongly coupled quantum dot solids', *Nat. Nanotechnol.*, 10, 1013–1026, **2015**, doi: 10.1038/nnano.2015.247.

[74] D. A. Neamen, *Semiconductor Physics and Devices Basic Principles*. Tata McGraw Hill Publishing, **1992**.

[75] S. H. Kim *et al.*, 'Electrolyte-Gated Transistors for Organic and Printed Electronics', *Adv. Mater.*, 25, 1822–1846, **2013**, doi: 10.1002/adma.201202790.

[76] E. Lhuillier, A. Robin, S. Ithurria, H. Aubin, and B. Dubertret, 'Electrolyte-Gated Colloidal Nanoplatelets-Based Phototransistor and Its Use for Bicolor Detection', *Nano Lett.*, 14, 2715–2719, **2014**, doi: 10.1021/nl5006383.

[77] E. Lhuillier *et al.*, 'Electrolyte-Gated Field Effect Transistor to Probe the Surface Defects and Morphology in Films of Thick CdSe Colloidal Nanoplatelets', *ACS Nano*, 8, 3813–3820, **2014**, doi: 10.1021/nn500538n.

[78] H. Seong, K. Cho, and S. Kim, 'Photocurrent characteristics of solution-processed HgTe nanoparticle thin films under the illumination of 1.3 μm wavelength light', *Semicond. Sci. Technol.*, 23, 075011, **2008**.

[79] M. Böberl, M. V. Kovalenko, S. Gamerith, E. J. W. List, and W. Heiss, 'Inkjet-Printed Nanocrystal Photodetectors Operating up to 3 μm Wavelengths', *Adv. Mater.*, 19, 3574–3578, **2007**, doi: 10.1002/adma.200700111.

[80] J. Tang *et al.*, 'Colloidal-quantum-dot photovoltaics using atomic-ligand passivation', *Nat. Mater.*, 10, 765–771, **2011**, doi: 10.1038/nmat3118.

[81] A. H. Ip *et al.*, 'Hybrid passivated colloidal quantum dot solids', *Nat. Nanotechnol.*, 7, 577–582, **2012**, doi: 10.1038/nnano.2012.127.

[82] X. Tang, X. Tang, and K. W. C. Lai, 'Scalable Fabrication of Infrared Detectors with Multispectral Photoresponse Based on Patterned Colloidal Quantum Dot Films', *ACS Photonics*, 3, 2396–2404, **2016**, doi: 10.1021/acsphotonics.6b00620.

[83] X. Tang, M. Chen, M. M. Ackerman, C. Melnychuk, and P. Guyot-Sionnest, 'Direct Imprinting of Quasi-3D Nanophotonic Structures into Colloidal Quantum-Dot Devices', *Adv. Mater.*, 32, 1906590, **2020**, doi: 10.1002/adma.201906590.

[84] S. Zhang *et al.*, 'Direct Optical Lithography Enabled Multispectral Colloidal Quantum-Dot Imagers from Ultraviolet to Short-Wave Infrared', *ACS Nano*, 16, 18822–18829, **2022**, doi: 10.1021/acsnano.2c07586.

[85] E. Lhuillier, S. Keuleyan, P. Rekemeyer, and P. Guyot-Sionnest, 'Thermal properties of mid-infrared colloidal quantum dot detectors', *J. Appl. Phys.*, 110, 033110, **2011**, doi: 10.1063/1.3619857.

[86] A. Jagtap *et al.*, 'Short Wave Infrared Devices Based on HgTe Nanocrystals with Air Stable Performances', *J. Phys. Chem. C*, 122, 14979–14985, **2018**, doi: 10.1021/acs.jpcc.8b03276.

[87] M. Chen *et al.*, 'Fast, Air-Stable Infrared Photodetectors based on Spray-Deposited Aqueous HgTe Quantum Dots', *Adv. Funct. Mater.*, 24, 53–59, **2014**, doi: 10.1002/adfm.201301006.

[88] M. Chen *et al.*, 'Mercury Telluride Quantum Dot Based Phototransistor Enabling High-Sensitivity Room-Temperature Photodetection at 2000 nm', *ACS Nano*, 11, 5614–5622, **2017**, doi: 10.1021/acsnano.7b00972.

[89] M. E. Cryer and J. E. Halpert, '300 nm Spectral Resolution in the Mid-Infrared with Robust, High Responsivity Flexible Colloidal Quantum Dot Devices at Room

Temperature', *ACS Photonics*, 5, 3009–3015, **2018**, doi: 10.1021/acsphotonics.8b00738.

[90] A. Chu *et al.*, 'Near Unity Absorption in Nanocrystal Based Short Wave Infrared Photodetectors Using Guided Mode Resonators', *ACS Photonics*, 6, 2553–2561, **2019**, doi: 10.1021/acsphotonics.9b01015.

[91] A. Chu *et al.*, 'Infrared photoconduction at the diffusion length limit in HgTe nanocrystal arrays', *Nat. Commun.*, 12, 1794, **2021**, doi: 10.1038/s41467-021-21959-x.

[92] C. Abadie *et al.*, 'Helmholtz Resonator Applied to Nanocrystal-Based Infrared Sensing', *Nano Lett.*, 22, 8779–8785, **2022**, doi: 10.1021/acs.nanolett.2c02769.

[93] C. Livache *et al.*, 'Band Edge Dynamics and Multiexciton Generation in Narrow Band Gap HgTe Nanocrystals', *ACS Appl. Mater. Interfaces*, 10, 11880–11887, **2018**, doi: 10.1021/acsami.8b00153.

[94] S. H. Im, H. Kim, S. W. Kim, S.-W. Kim, and S. I. Seok, 'Efficient HgTe colloidal quantum dot-sensitized near-infrared photovoltaic cells', *Nanoscale*, 4, 1581–1584, **2012**, doi: 10.1039/C2NR11722C.

[95] P. Guyot-Sionnest and J. A. Roberts, 'Background limited mid-infrared photodetection with photovoltaic HgTe colloidal quantum dots', *Appl. Phys. Lett.*, 107, 253104, **2015**, doi: 10.1063/1.4938135.

[96] S. Günes *et al.*, 'Hybrid Solar Cells Using HgTe Nanocrystals and Nanoporous TiO2 Electrodes', *Adv. Funct. Mater.*, 16, 1095–1099, **2006**, doi: 10.1002/adfm.200500638.

[97] M. Nam, S. Kim, S. Kim, S. Jeong, S.-W. Kim, and K. Lee, 'Near-infrared-sensitive bulk heterojunction solar cells using nanostructured hybrid composites of HgTe quantum dots and a low-bandgap polymer', *Sol. Energy Mater. Sol. Cells*, 126, 163–169, **2014**, doi: 10.1016/j.solmat.2014.03.027.

[98] M. Grätzel, 'Dye-sensitized solar cells', *J. Photochem. Photobiol. C Photochem. Rev.*, 4, 145–153, **2003**.

[99] M. M. Ackerman, X. Tang, and P. Guyot-Sionnest, 'Fast and Sensitive Colloidal Quantum Dot Mid-Wave Infrared Photodetectors', *ACS Nano*, 12, 7264–7271, **2018**, doi: 10.1021/acsnano.8b03425.

[100] P. Rastogi *et al.*, 'Extended Short-Wave Photodiode Based on CdSe/HgTe/Ag2Te Stack with High Internal Efficiency', *J. Phys. Chem. C*, 126, 13720–13728, **2022**, doi: 10.1021/acs.jpcc.2c02044.

[101] M. M. Ackerman, M. Chen, and P. Guyot-Sionnest, 'HgTe colloidal quantum dot photodiodes for extended short-wave infrared detection', *Appl. Phys. Lett.*, 116, 083502, **2020**, doi: 10.1063/1.5143252.

[102] X. Tang, M. M. Ackerman, G. Shen, and P. Guyot-Sionnest, 'Towards Infrared Electronic Eyes: Flexible Colloidal Quantum Dot Photovoltaic Detectors Enhanced by Resonant Cavity', *Small*, 15, 804920, **2019**, doi: 10.1002/smll.201804920.

[103] X. Tang, M. M. Ackerman, M. Chen, and P. Guyot-Sionnest, 'Dual-band infrared imaging using stacked colloidal quantum dot photodiodes', *Nat. Photonics*, 13, 277–282, **2019**, doi: 10.1038/s41566-019-0362-1.

[104] C. Gréboval *et al.*, 'HgTe Nanocrystal-Based Photodiode for Extended Short-Wave Infrared Sensing with Optimized Electron Extraction and Injection', *ACS Appl. Nano Mater.*, 5, 8602–8611, **2022**, doi: 10.1021/acsanm.2c02103.

[105] J. Yang *et al.*, 'Bi2S3 Electron Transport Layer Incorporation for High-Performance Heterostructure HgTe Colloidal Quantum Dot Infrared Photodetectors', *ACS Photonics*, **2023**, doi: 10.1021/acsphotonics.2c01145.

[106] C. Gréboval *et al.*, 'Field-Effect Transistor and Photo-Transistor of Narrow-Band-Gap Nanocrystal Arrays Using Ionic Glasses', *Nano Lett.*, 19, 3981–3986, **2019**, doi: 10.1021/acs.nanolett.9b01305.

[107] U. N. Noumbé *et al.*, 'Reconfigurable 2D/0D p–n Graphene/HgTe Nanocrystal Heterostructure for Infrared Detection', *ACS Nano*, 14, 4567–4576, **2020**, doi: 10.1021/acsnano.0c00103.

[108] Y. Dong *et al.*, 'Solution Processed Hybrid Polymer: HgTe Quantum Dot Phototransistor with High Sensitivity and Fast Infrared Response up to 2400 nm at Room Temperature', *Adv. Sci.*, 7, 2000068, **2020**, doi: 10.1002/advs.202000068.

[109] C. Livache *et al.*, 'Charge Dynamics and Optolectronic Properties in HgTe Colloidal Quantum Wells', *Nano Lett.*, 17, 4067–4074, **2017**, doi: 10.1021/acs.nanolett.7b00683.

[110] M. Cavallo *et al.*, 'Coupling Ferroelectric to colloidal Nanocrystals as a Generic Strategy to Engineer the Carrier Density Landscape', *Adv. Funct. Mater.*, 2300846, **2023**, doi: 10.1002/adfm.202300846.

[111] S.-S. Chee *et al.*, 'Correlating Structure and Detection Properties in HgTe Nanocrystal Films', *Nano Lett.*, 21, 4145–4151, **2021**, doi: 10.1021/acs.nanolett.0c04346.

[112] C. Greboval *et al.*, 'Infrared narrow band gap nanocrystals: recent progresses relative to imaging and active detection', *ArXiv Prepr. ArXiv200111554*, **2020**.

[113] C. Buurma, R. E. Pimpinella, A. J. Ciani, J. S. Feldman, C. H. Grein, and P. Guyot-Sionnest, 'MWIR imaging with low cost colloidal quantum dot films', presented at the Optical Sensing, Imaging, and Photon Counting: Nanostructured Devices and Applications 2016, SPIE, **2016**, 993303.

[114] A. J. Ciani, R. E. Pimpinella, C. H. Grein, and P. Guyot-Sionnest, 'Colloidal quantum dots for low-cost MWIR imaging', presented at the Infrared Technology and Applications XLII, SPIE, **2016**, 333–341.

[115] C. Gréboval *et al.*, 'Photoconductive focal plane array based on HgTe quantum dots for fast and cost-effective short-wave infrared imaging', *Nanoscale*, 14, 9359–9368, **2022**, doi: 10.1039/D2NR01313D.

[116] S. Zhang *et al.*, 'Wafer-Scale Fabrication of CMOS-Compatible Trapping-Mode Infrared Imagers with Colloidal Quantum Dots', *ACS Photonics*, 10, 673–682, **2023**, doi: 10.1021/acsphotonics.2c01699.

[117] J. C. Peterson and P. Guyot-Sionnest, 'Room-Temperature 15% Efficient Mid-Infrared HgTe Colloidal Quantum Dot Photodiodes', *ACS Appl. Mater. Interfaces*, 15, 19163–19169, **2023**, doi: 10.1021/acsami.3c00487.

[118] M. Kwon *et al.*, 'Surface-plasmon-enhanced light-emitting diodes', *Adv. Mater.*, 20, 1253–1257, **2008**.

[119] D. Palaferri *et al.*, 'Room-temperature nine-μm-wavelength photodetectors and GHz-frequency heterodyne receivers', *Nature*, 556, 85–88, **2018**, doi: 10.1038/nature25790.

[120] W. Li, Z. J. Coppens, L. V. Besteiro, W. Wang, A. O. Govorov, and J. Valentine, 'Circularly polarized light detection with hot electrons in chiral plasmonic metamaterials', *Nat. Commun.*, 6, 8379, **2015**.

[121] J. J. Wierer Jr, A. David, and M. M. Megens, 'III-nitride photonic-crystal light-emitting diodes with high extraction efficiency', *Nat. Photonics*, 3, 163–169, **2009**.

[122] L. Novotny and N. van Hulst, 'Antennas for light', *Nat. Photonics*, 5, 83–90, **2011**, doi: 10.1038/nphoton.2010.237.

[123] J. A. Schuller, E. S. Barnard, W. Cai, Y. C. Jun, J. S. White, and M. L. Brongersma, 'Plasmonics for extreme light concentration and manipulation', *Nat. Mater.*, 9, 193–204, **2010**, doi: 10.1038/nmat2630.

[124] S. E. Schwarz and B. T. Ulrich, 'Antenna-coupled infrared detectors', *J. Appl. Phys.*, 48, 1870–1873, **1977**, doi: 10.1063/1.323940.

[125] L. Cao, J.-S. Park, P. Fan, B. Clemens, and M. L. Brongersma, 'Resonant Germanium Nanoantenna Photodetectors', *Nano Lett.*, 10, 1229–1233, **2010**, doi: 10.1021/nl9037278.

[126] D. Palaferri *et al.*, 'Patch antenna terahertz photodetectors', *Appl. Phys. Lett.*, 106, 61102, **2015**, doi: 10.1063/1.4918983.

[127] L. Tang *et al.*, 'Nanometre-scale germanium photodetector enhanced by a near-infrared dipole antenna', *Nat. Photonics*, 2, 226–229, **2008**, doi: 10.1038/nphoton.2008.30.

[128] E. Laux, C. Genet, T. Skauli, and T. W. Ebbesen, 'Plasmonic photon sorters for spectral and polarimetric imaging', *Nat. Photonics*, 2, 161–164, **2008**, doi: 10.1038/nphoton.2008.1.

[129] M. Chen *et al.*, 'Photocurrent Enhancement of HgTe Quantum Dot Photodiodes by Plasmonic Gold Nanorod Structures', *ACS Nano*, 8, 8208–8216, **2014**, doi: 10.1021/nn502510u.

[130] Y. Yifat, M. Ackerman, and P. Guyot-Sionnest, 'Mid-IR colloidal quantum dot detectors enhanced by optical nano-antennas', *Appl. Phys. Lett.*, 110, 041106, **2017**, doi: 10.1063/1.4975058.

[131] X. Tang, M. M. Ackerman, and P. Guyot-Sionnest, 'Thermal Imaging with Plasmon Resonance Enhanced HgTe Colloidal Quantum Dot Photovoltaic Devices', *ACS Nano*, 12, 7362–7370, **2018**, doi: 10.1021/acsnano.8b03871.

[132] X. Tang, M. M. Ackerman, and P. Guyot-Sionnest, 'Acquisition of Hyperspectral Data with Colloidal Quantum Dots', *Laser Photonics Rev.*, 13, 1900165, **2019**, doi: 10.1002/lpor.201900165.

[133] N. Đorđević *et al.*, 'Metasurface Colloidal Quantum Dot Photodetectors', *ACS Photonics*, 9, 482–492, **2022**, doi: 10.1021/acsphotonics.1c01204.

[134] A. P. Hibbins, J. R. Sambles, C. R. Lawrence, and J. R. Brown, 'Squeezing Millimeter Waves into Microns', *Phys. Rev. Lett.*, 92, 143904, **2004**, doi: 10.1103/PhysRevLett.92.143904.

[135] M. J. Lockyear, A. P. Hibbins, J. R. Sambles, P. A. Hobson, and C. R. Lawrence, 'Thin resonant structures for angle and polarization independent microwave absorption', *Appl. Phys. Lett.*, 94, 041913, **2009**, doi: 10.1063/1.3059568.

[136] P. Jouy, Y. Todorov, A. Vasanelli, R. Colombelli, I. Sagnes, and C. Sirtori, 'Coupling of a surface plasmon with localized subwavelength microcavity modes', *Appl. Phys. Lett.*, 98, 021105, **2011**, doi: 10.1063/1.3536504.

[137] Y. Todorov *et al.*, 'Optical properties of metal-dielectric-metal microcavities in the THz frequency range', *Opt. Express*, 18, 13886–13907, **2010**, doi: 10.1364/OE.18.013886.

[138] T. H. Dang *et al.*, 'Broadband Enhancement of Mid-Wave Infrared Absorption in a Multi-Resonant Nanocrystal-Based Device', *Adv. Opt. Mater.*, 10, 2200297, **2022**, doi: 10.1002/adom.202200297.

[139] H. Zhang *et al.*, 'Material Perspective on HgTe Nanocrystal-Based Short-Wave Infrared Focal Plane Arrays', *Chem. Mater.*, 34, 10964–10972, **2022**, doi: 10.1021/acs.chemmater.2c02955.

[140] M. J. Adams, *An Introduction to Optical Waveguides*. in Wiley-Interscience publication. Wiley, **1981**.

[141] S. A. Maier, 'Surface Plasmon Polaritons at Metal / Insulator Interfaces', in *Plasmonics: Fundamentals and Applications*, S. A. Maier, Ed., New York, NY: Springer US, **2007**, 21–37. doi: 10.1007/0-387-37825-1_2.

[142] H. A. Haus and J. R. Melcher, *Electromagnetic Fields and Energy*. Prentice Hall, **1989**.

[143] P. Rastogi *et al.*, 'Complex Optical Index of HgTe Nanocrystal Infrared Thin Films and Its Use for Short Wave Infrared Photodiode Design', *Adv. Opt. Mater.*, 9, 2002066, **2021**, doi: 10.1002/adom.202002066.

[144] E. Lhuillier, S. Keuleyan, and P. Guyot-Sionnest, 'Optical properties of HgTe colloidal quantum dots', *Nanotechnology*, 23, 175705, **2012**, doi: 10.1088/0957-4484/23/17/175705.

[145] N. Moghaddam *et al.*, 'The Strong Confinement Regime in HgTe Two-Dimensional Nanoplatelets', *J. Phys. Chem. C*, 124, 23460–23468, **2020**, doi: 10.1021/acs.jpcc.0c07533.

[146] C. Gréboval *et al.*, 'Ferroelectric Gating of Narrow Band-Gap Nanocrystal Arrays with Enhanced Light–Matter Coupling', *ACS Photonics*, 8, 259–268, **2021**, doi: 10.1021/acsphotonics.0c01464.

[147] D. A. B. Miller *et al.*, 'Band-Edge Electroabsorption in Quantum Well Structures: The Quantum-Confined Stark Effect', *Phys. Rev. Lett.*, 53, 2173–2176, **1984**, doi: 10.1103/PhysRevLett.53.2173.

[148] S. A. Empedocles and M. G. Bawendi, 'Quantum-Confined Stark Effect in Single CdSe Nanocrystallite Quantum Dots', *Science*, 278, **1997**, doi: 10.1126/science.278.5346.2114.

[149] R. Scott *et al.*, 'Time-Resolved Stark Spectroscopy in CdSe Nanoplatelets: Exciton Binding Energy, Polarizability, and Field-Dependent Radiative Rates', *Nano Lett.*, 16, 6576–6583, **2016**, doi: 10.1021/acs.nanolett.6b03244.

[150] E. J. D. Klem, L. Levina, and E. H. Sargent, 'PbS quantum dot electroabsorption modulation across the extended communications band 1200–1700nm', *Appl. Phys. Lett.*, 87, 053101, **2005**, doi: 10.1063/1.2001737.

[151] G. Walters *et al.*, 'The quantum-confined Stark effect in layered hybrid perovskites mediated by orientational polarizability of confined dipoles', *Nat. Commun.*, 9, 4214, **2018**, doi: 10.1038/s41467-018-06746-5.

[152] A. V. Pogrebnyakov *et al.*, 'Reconfigurable near-IR metasurface based on Ge2Sb2Te5 phase-change material', *Opt. Mater. Express*, 8, 2264–2275, **2018**, doi: 10.1364/OME.8.002264.

[153] X. Shi, C. Chen, S. Liu, and G. Li, 'Nonvolatile, Reconfigurable and Narrowband Mid-Infrared Filter Based on Surface Lattice Resonance in Phase-Change Ge2Sb2Te5', *Nanomaterials*, 10, **2020**, doi: 10.3390/nano10122530.

[154] T. Stark *et al.*, 'MEMS Tunable Mid-Infrared Plasmonic Spectrometer', *ACS Photonics*, 3, 14–19, **2016**, doi: 10.1021/acsphotonics.5b00290.

[155] T. H. Dang *et al.*, 'Bias Tunable Spectral Response of Nanocrystal Array in a Plasmonic Cavity', *Nano Lett.*, 21, 6671–6677, **2021**, doi: 10.1021/acs.nanolett.1c02193.

[156] T. H. Dang *et al.*, 'Nanocrystal-Based Active Photonics Device through Spatial Design of Light-Matter Coupling', *ACS Photonics*, 9, 2528–2535, **2022**, doi: 10.1021/acsphotonics.2c00738.

[157] T. H. Dang *et al.*, 'Bias Reconfigurable Photoresponse of an Infrared Nanocrystal Film Integrated into a Coupled Fabry-Perot Resonator', *ACS Photonics*, 10, 1601–1607, **2023**, doi: 10.1021/acsphotonics.3c00214.

[158] G. Allan and C. Delerue, 'Tight-binding calculations of the optical properties of HgTe nanocrystals', *Phys. Rev. B*, 86, 165437, **2012**, doi: 10.1103/PhysRevB.86.165437.

[159] S. E. Keuleyan, P. Guyot-Sionnest, C. Delerue, and G. Allan, 'Mercury Telluride Colloidal Quantum Dots: Electronic Structure, Size-Dependent Spectra, and Photocurrent Detection up to 12 μm', *ACS Nano*, 8, 8676–8682, **2014**, doi: 10.1021/nn503805h.

[160] A. V. Nenashev, F. Jansson, S. D. Baranovskii, R. Österbacka, A. V. Dvurechenskii, and F. Gebhard, 'Effect of electric field on diffusion in disordered materials. I. One-

dimensional hopping transport', *Phys. Rev. B*, 81, 115203, **2010**, doi: 10.1103/PhysRevB.81.115203.

[161] A. V. Nenashev, F. Jansson, S. D. Baranovskii, R. Österbacka, A. V. Dvurechenskii, and F. Gebhard, 'Effect of electric field on diffusion in disordered materials. II. Two- and three-dimensional hopping transport', *Phys. Rev. B*, 81, 115204, **2010**, doi: 10.1103/PhysRevB.81.115204.

[162] R. Richert, L. Pautmeier, and H. Bässler, 'Diffusion and drift of charge carriers in a random potential: Deviation from Einstein's law', *Phys. Rev. Lett.*, 63, 547–550, **1989**, doi: 10.1103/PhysRevLett.63.547.

[163] A. V. Nenashev, J. O. Oelerich, A. V. Dvurechenskii, F. Gebhard, and S. D. Baranovskii, 'Fundamental characteristic length scale for the field dependence of hopping charge transport in disordered organic semiconductors', *Phys. Rev. B*, 96, 035204, **2017**, doi: 10.1103/PhysRevB.96.035204.

[164] Y. Xing, N. Yazdani, W. M. M. Lin, M. Yarema, R. Zahn, and V. Wood, 'Effect of Positional Disorders on Charge Transport in Nanocrystal Quantum Dot Thin Films', *ACS Appl. Electron. Mater.*, 4, 631–642, **2022**, doi: 10.1021/acsaelm.1c01011.

[165] B. Fix, J. Jaeck, P. Bouchon, S. Héron, B. Vest, and R. Haïdar, 'High-quality-factor double Fabry–Perot plasmonic nanoresonator', *Opt. Lett.*, 42, 5062–5065, **2017**, doi: 10.1364/OL.42.005062.

[166] R. A. Maniyara *et al.*, 'Highly transparent and conductive ITO substrates for near infrared applications', *APL Mater.*, 9, 021121, **2021**, doi: 10.1063/5.0040864.

[167] H. Liu and P. Lalanne, 'Microscopic theory of the extraordinary optical transmission', *Nature*, 452, 728–731, **2008**, doi: 10.1038/nature06762.

[168] S. G. Rodrigo, F. de León-Pérez, and L. Martín-Moreno, 'Extraordinary Optical Transmission: Fundamentals and Applications', *Proc. IEEE*, 104, 2288–2306, **2016**, doi: 10.1109/JPROC.2016.2580664.

[169] R. Gordon, D. Sinton, K. L. Kavanagh, and A. G. Brolo, 'A New Generation of Sensors Based on Extraordinary Optical Transmission', *Acc. Chem. Res.*, 41, 1049–1057, **2008**, doi: 10.1021/ar800074d.

[170] T. W. Ebbesen, H. J. Lezec, H. F. Ghaemi, T. Thio, and P. A. Wolff, 'Extraordinary optical transmission through sub-wavelength hole arrays', *Nature*, 391, 667–669, **1998**, doi: 10.1038/35570.

[171] J. Tong, F. Suo, J. Ma, L. Y. M. Tobing, L. Qian, and D. H. Zhang, 'Surface plasmon enhanced infrared photodetection', *Opto-Electron. Adv.*, 2, 180026, **2018**, doi: 10.29026/oea.2019.180026.

[172] N. Yan, Y. Qiu, X. He, X. Tang, Q. Hao, and M. Chen, 'Plasmonic Enhanced Nanocrystal Infrared Photodetectors', *Materials*, 16, **2023**, doi: 10.3390/ma16083216.

[173] M. Chen, L. Lu, H. Yu, C. Li, and N. Zhao, 'Integration of Colloidal Quantum Dots with Photonic Structures for Optoelectronic and Optical Devices', *Adv. Sci.*, 8, 2101560, **2021**, doi: 10.1002/advs.202101560.

[174] X. Tang, X. Tang, and K. W. C. Lai, 'Scalable Fabrication of Infrared Detectors with Multispectral Photoresponse Based on Patterned Colloidal Quantum Dot Films', *ACS Photonics*, 3, 2396–2404, **2016**, doi: 10.1021/acsphotonics.6b00620.

[175] S. Zhang *et al.*, 'Single-/fused-band dual-mode mid-infrared imaging with colloidal quantum-dot triple-junctions', *Photonics Res.*, 10, 1987–1995, **2022**, doi: 10.1364/PRJ.458351.

[176] C. Livache *et al.*, 'A colloidal quantum dot infrared photodetector and its use for intraband detection', *Nat. Commun.*, 10, 2125, **2019**, doi: 10.1038/s41467-019-10170-8.

[177] Y. Galagan *et al.*, 'Current Collecting Grids for ITO-Free Solar Cells', *Adv. Energy Mater.*, 2, 103–110, **2012**, doi: 10.1002/aenm.201100552.

[178] J. W. Lim *et al.*, 'Effect of geometric lattice design on optical/electrical properties of transparent silver grid for organic solar cells', *Opt. Express*, 22, 26891–26899, **2014**, doi: 10.1364/OE.22.026891.

[179] Y. Choi *et al.*, 'Interdigitated front contact crystalline silicon solar cell', *Sol. Energy*, 100, 94–101, **2014**, doi: 10.1016/j.solener.2013.12.007.

[180] D. K. Gupta, M. Langelaar, M. Barink, and F. van Keulen, 'Optimizing front metallization patterns: Efficiency with aesthetics in free-form solar cells', *Renew. Energy*, 86, 1332–1339, **2016**, doi: 10.1016/j.renene.2015.09.071.

[181] Q. Le-Van, X. Le Roux, A. Aassime, and A. Degiron, 'Electrically driven optical metamaterials', *Nat. Commun.*, 7, 12017, **2016**, doi: 10.1038/ncomms12017.

[182] J. C. Peterson and P. Guyot-Sionnest, 'Room-Temperature 15% Efficient Mid-Infrared HgTe Colloidal Quantum Dot Photodiodes', *ACS Appl. Mater. Interfaces*, 15, 19163–19169, **2023**, doi: 10.1021/acsami.3c00487.

[183] H. C. Liu, Jianmeng Li, M. Buchanan, and Z. R. Wasilewski, 'High-frequency quantum-well infrared photodetectors measured by microwave-rectification technique', *IEEE J. Quantum Electron.*, 32, 1024–1028, **1996**, doi: 10.1109/3.502380.

[184] Z. Deng, K. S. Jeong, and P. Guyot-Sionnest, 'Colloidal Quantum Dots Intraband Photodetectors', *ACS Nano*, 8, 11707–11714, **2014**, doi: 10.1021/nn505092a.

[185] E. Lhuillier *et al.*, 'Infrared Photodetection Based on Colloidal Quantum-Dot Films with High Mobility and Optical Absorption up to THz', *Nano Lett.*, 16, 1282–1286, **2016**, doi: 10.1021/acs.nanolett.5b04616.

[186] M. Chen, Q. Hao, Y. Luo, and X. Tang, 'Mid-Infrared Intraband Photodetector via High Carrier Mobility HgSe Colloidal Quantum Dots', *ACS Nano*, 16, 11027–11035, **2022**, doi: 10.1021/acsnano.2c03631.

[187] X. Tang, G. fu Wu, and K. W. C. Lai, 'Plasmon resonance enhanced colloidal HgSe quantum dot filterless narrowband photodetectors for mid-wave infrared', *J. Mater. Chem. C*, 5, 362–369, **2017**, doi: 10.1039/C6TC04248A.

[188] S. B. Hafiz, M. M. Al Mahfuz, S. Lee, and D.-K. Ko, 'Midwavelength Infrared p–n Heterojunction Diodes Based on Intraband Colloidal Quantum Dots', *ACS Appl. Mater. Interfaces*, 13, 49043–49049, **2021**, doi: 10.1021/acsami.1c14749.

[189] S. B. Hafiz, M. M. Al Mahfuz, and D.-K. Ko, 'Vertically Stacked Intraband Quantum Dot Devices for Mid-Wavelength Infrared Photodetection', *ACS Appl. Mater. Interfaces*, 13, 937–943, **2021**, doi: 10.1021/acsami.0c19450.

[190] J. Qu *et al.*, 'Intraband Mid-Infrared Transitions in Ag2Se Nanocrystals: Potential and Limitations for Hg-Free Low-Cost Photodetection', *J. Phys. Chem. C*, 122, 18161–18167, **2018**, doi: 10.1021/acs.jpcc.8b05699.

[191] S. B. Hafiz, M. R. Scimeca, P. Zhao, I. J. Paredes, A. Sahu, and D.-K. Ko, 'Silver Selenide Colloidal Quantum Dots for Mid-Wavelength Infrared Photodetection', *ACS Appl. Nano Mater.*, 2, 1631–1636, **2019**, doi: 10.1021/acsanm.9b00069.

[192] X. Xue, M. Chen, Y. Luo, T. Qin, X. Tang, and Q. Hao, 'High-operating-temperature mid-infrared photodetectors via quantum dot gradient homojunction', *Light Sci. Appl.*, 12, 2, **2023**, doi: 10.1038/s41377-022-01014-0.

[193] M. W. Knight, N. S. King, L. Liu, H. O. Everitt, P. Nordlander, and N. J. Halas, 'Aluminum for Plasmonics', *ACS Nano*, 8, 834–840, **2014**, doi: 10.1021/nn405495q.

[194] 0A Rai, K. Park, L. Zhou, and M. Zachariah, 'Understanding the mechanism of aluminium nanoparticle oxidation', *Combust. Theory Model.*, 10, 843–859, **2006**.

[195] R. Alchaar *et al.*, 'On the Suitable Choice of Metal for HgTe Nanocrystal-Based Photodiode: To Amalgam or Not to Amalgam', *J. Phys. Chem. C*, **2023**, doi: 10.1021/acs.jpcc.3c01603.

[196] E. Orgiu *et al.*, 'Conductivity in organic semiconductors hybridized with the vacuum field', *Nat. Mater.*, 14, 1123–1129, **2015**, doi: 10.1038/nmat4392.

PhD thesis
Tung Huu Dang

27 September 2023

Light manipulation for enhanced photodetection performance and novel functionalities in colloidal nanocrystal-based infrared sensing devices

Abstract: This thesis focuses on the use of optical nanostructures in nanocrystal-based infrared photodetectors. Integrating optical structures into photodetectors has been demonstrated to improve the devices' speed and sensitivity. In the case of nanocrystal-based photodetectors, using optical resonators is particularly beneficial. Indeed, because of the hopping mechanism, carrier diffusion lengths in a nanocrystal array are several times shorter than the material's absorption depth. This limited transport leads to a trade-off for the thickness of nanocrystal films between optical absorption and charge collection efficiency in photodetectors. Optical nanostructures enable the manipulation of light at subwavelength scales. They can thus be exploited to focus light on ultrathin nanocrystal films compatible with carrier transport. In addition to the enhanced performance of the sensing devices, we also show that advanced functionalities can be generated by coupling nanocrystals with optical structures. Such functionalities result from the bias-reconfigurable photoresponse of the devices. We show that hopping transport, often seen as a limitation for optoelectronic devices, is a crucial ingredient for bias reconfigurability and the design of active photoconductive nanocrystal devices. Lastly, a combination of a photodiode structure and plasmonic resonators will be presented. The obtained device is among the most sensitive and fastest mid-wave infrared photodetectors reported so far based on colloidal nanocrystals operating at cryogenic temperature. Furthermore, we demonstrate that combining our plasmonic structures with a single diode stack can generate a multicolor bias reconfigurable response and introduce new functionalities such as band rejection and current bi-directionality.

Keywords: infrared, colloidal nanocrystals, HgTe, photonic structures, active photonics, reconfigurable response.

Résumé de la thèse

Découvert il y a plus de 200 ans, le rayonnement infrarouge est devenu l'une des parties du spectre électromagnétique les plus utilisées pour les applications. Initialement motivée par les applications militaires stratégiques, la détection infrarouge peut désormais trouver de nombreuses applications civiles, notamment à des fins industrielles, scientifiques, commerciales et médicales. L'importance de l'infrarouge pour les applications a conduit au développement de diverses technologies de détection. Cependant, la détection infrarouge haute performance repose principalement sur les semi-conducteurs III-V et II-VI épitaxiés, qui nécessitent des outils de fabrication couteux.

Ces dernières années ont vu l'émergence de nanoparticules colloïdales en optoélectronique infrarouge. Les nanocristaux colloïdaux, ou boîtes quantiques colloïdales, sont des particules semi-conductrices fabriquées en solution dont les dimensions sont nanométriques. Dans un semi-conducteur massif, les bandes de valence et de conduction sont séparées par un intervalle d'énergie fixe, appelé « bande interdite », qui détermine les propriétés optiques et électroniques du matériau. La situation des nanocristaux colloïdaux est différente puisque la taille des particules est comparable à la longueur d'onde de de Broglie des électrons et des trous, ce qui permet d'observer l'effet de confinement quantique. Par conséquent, la bande interdite des nanocristaux colloïdaux peut être contrôlée en fonction de la taille des particules.

De plus, ces nanocristaux sont fabriqués par des méthodes chimiques, permettant ainsi la production en grande quantité des matériaux et la possibilité de traitement en solution pour la fabrication de dispositifs. Ainsi, les nanocristaux colloïdaux constituent une plateforme très prometteuse pour le développement de dispositifs de détection infrarouge rentables et performants. Les premières démonstrations de capteurs infrarouges basés sur des matériaux colloïdaux ont déjà montré un grand potentiel de détection rapide et sensible.

Grâce aux progrès récents dans le développement des matériaux, les matériaux colloïdaux sont désormais prêts à être intégrés dans des architectures de dispositifs avancées. Ce travail de thèse se concentre sur les nanocristaux de tellulure de mercure (HgTe) et leur potentiel pour les applications de détection infrarouge. Comme le HgTe massif est un semi-conducteur sans bande interdite, le seuil d'absorption des NC colloïdaux de HgTe est déterminé par le confinement et peut varier entre 1.5 eV pour la forme colloïdale la plus confinée à pratiquement zéro. Cette propriété est le premier aspect fondamental pour motiver le développement de ce matériau.

Dans ce travail, nous présentons l'utilisation de structures photoniques pour la manipulation de la lumière dans des capteurs infrarouges à base de nanocristaux. Les principaux objectifs de ces travaux comprennent : (*i*) l'amélioration des performances de détection du dispositif et en particulier de l'absorption et (*ii*) le contrôle électrique de la réponse spectrale grâce au couplage lumière-nanocristal. Alors que le premier objectif constitue le défi ultime pour les systèmes de détection, le deuxième objectif est largement inexploré dans le domaine des capteurs infrarouges à base de nanocristaux. Néanmoins, la capacité de contrôler activement la réponse optique du dispositif présente un grand intérêt pour les applications de détection infrarouge, car le contraste de l'imagerie pourrait être considérablement amélioré en ajustant la réponse spectrale du dispositif.

Ce manuscrit présente les différentes architectures et dispositifs dessinés, fabriqués et caractérisés pendant ma thèse. Il est divisé en quatre chapitres, dont les résultats principaux sont résumés ici.

Le **chapitre 1** passe en revue la progression historique de la technologie de détection infrarouge et l'état actuel du domaine. Plus précisément, la physique sous-jacente et les principes de fonctionnement des photodétecteurs infrarouges quantiques sont décrits. De plus, les figures de mérite pour évaluer et comparer les performances des différentes technologies de détection infrarouge seront présentées.

Le **chapitre 2** donne un aperçu de l'état de l'art actuel des structures photoniques pour les photodétecteurs infrarouges à base de nanocristaux. Les nanostructures optiques permettent le contrôle et la manipulation de la lumière à des échelles inférieures à la longueur d'onde. Il a été démontré que l'intégration de ces structures dans la conception de photodétecteurs améliore considérablement la vitesse et la sensibilité du dispositif. Dans le cas des photodétecteurs à base de nanocristaux de HgTe, l'utilisation de résonateurs optiques est particulièrement bénéfique en raison du transport à courte distance résultant du caractère polycristallin du film. En effet, dans un réseau de nanocristaux de HgTe, le mécanisme de « hopping » limite la longueur de diffusion des porteurs à quelques dizaines de nanomètres, une longueur significativement plus courte que la profondeur d'absorption du matériau. Cette décorrélation entre les longueurs caractéristiques de l'absorption et du transport conduit à un compromis entre l'absorption optique et l'efficacité de la collecte de charges dans les photodétecteurs à base de nanocristaux. Dans ce chapitre, nous présentons comment la courte longueur de diffusion peut être surmontée à l'aide de nanostructures optiques. La première partie du chapitre présente les structures photoniques à l'état de l'art pour la photodétection infrarouge et les contraintes de fabrication lors de l'application de ces structures aux réseaux de nanocristaux. La deuxième partie présente une cavité plasmonique basée sur une structure métal-diélectrique-métal, qui génère de multiples résonances optiques pour améliorer l'interaction lumière-matière dans un film de nanocristaux. Comprendre la nature de ces résonances permet de concevoir la réponse spectrale de nos photodétecteurs à travers les paramètres géométriques du résonateur. Dans la dernière partie du chapitre, nous combinons un film de nanocristaux absorbant dans l'infrarouge moyen avec la structure métal-diélectrique-métal pour démontrer un photodétecteur infrarouge à large bande, qui constitue un sujet de grand intérêt pour de nombreuses applications infrarouges, notamment la détection, la communication et l'imagerie. Le dispositif présente une amélioration de l'absorption sur une large bande spectrale (de 2 µm à 4 µm) grâce à trois résonances optiques générées : le mode cavité, le plasmon polariton de surface et la résonance Fabry-Perot. Des règles de conception ont été établies en fonction de la nature de chaque résonance. En termes de performances de détection, le détecteur à large bande permet une détection dans les régions infrarouges SWIR et MWIR, avec une responsivité de 700 $mA.W^{-1}$, une détectivité supérieure à 10^{10} Jones à 80 K et un temps de réponse de l'ordre de la microseconde.

Le **chapitre 3** se concentre sur la reconfigurabilité de la réponse via l'application de tension et présente notre stratégie pour obtenir cette fonctionnalité dans les capteurs infrarouges à base de nanocristaux. Une réponse reconfigurable est hautement souhaitable pour les systèmes optoélectroniques infrarouges avancés. En effet, la capacité de contrôler activement la réponse optique du dispositif est de grand intérêt pour les applications de détection infrarouge, car le contraste de l'imagerie pourrait être considérablement amélioré en ajustant la réponse spectrale du dispositif. Malgré cet intérêt, l'accordabilité post-fabrication reste un domaine à peine

exploré dans les dispositifs infrarouges à base de nanocristaux. Les stratégies conventionnelles, telles que l'exploitation de l'effet Stark confiné ou l'intégration de nanocristaux avec des structures MEMS, nécessitent un champ électrique important ou des techniques de fabrication incompatibles avec les films de nanocristaux. Dans ce chapitre, nous démontrons des photodétecteurs à base de nanocristaux avec une réponse spectrale dépendant du voltage appliqué. Ce dispositif exploite l'interaction entre le transport par hopping et l'inhomogénéité d'absorption spatiale induite par les résonances optiques. Nous montrons que le transport par hopping, souvent considéré comme une limitation pour les dispositifs optoélectroniques, joue un rôle crucial dans la conception de dispositifs photoniques actifs basés sur des nanocristaux. Cette approche ouvre la voie à une photonique active basée sur des nanocristaux colloïdaux.

Enfin, au **chapitre 4**, nous montrons notre stratégie pour optimiser la conception optique d'une photodiode. Augmenter les performances des photodétecteurs nécessite d'optimiser les propriétés optiques et électriques des dispositifs. De nombreux progrès ont été récemment réalisés dans le développement de matériaux, permettant d'obtenir des dispositifs photovoltaïques très sensibles dans le moyen infrarouge à base de nanocristaux de HgTe. Ces détecteurs présentent plusieurs avantages par rapport à leurs homologues photoconducteurs. Le courant d'obscurité plus faible grâce au fonctionnement photovoltaïque est particulièrement intéressant. Cependant, la conception reposant sur des couches d'oxyde transparent conducteur (TCO) pour au moins l'une des électrodes n'est pas optimale du point de vue optique. Le problème vient des importantes pertes optiques du TCO dans l'infrarouge moyen. Des solutions alternatives pour les électrodes dans le moyen infrarouge sont donc activement recherchées. Ce chapitre présente une photodiode basée sur un réseau métallique jouant à la fois le rôle d'électrode et de structure optique. Par rapport à la conception couramment utilisée dans laquelle des oxydes transparents conducteurs (ITO, FTO...) sont utilisés comme électrodes, notre structure optimisée permet une amélioration significative de l'absorption des nanocristaux, conduisant à des performances de détection record dans l'infrarouge moyen pour un photodétecteur à base de nanocristaux. L'utilisation d'un réseau métallique permet de générer une structure photonique multi-résonante, permettant une intense absorption large bande. Le dispositif obtenu atteint les performances les plus élevées reportées jusqu'à présent pour un détecteur à base de nanocristaux infrarouges dans le MWIR fonctionnant à des températures cryogéniques, avec une détectivité de $7x10^{11}$ Jones à 80 K pour une longueur d'onde de coupure de 5.5 µm et un temps de réponse inférieur à 100 ns. De plus, nous démontrons que la combinaison de différents réseaux avec un seul empilement de diodes peut générer une réponse multicolore reconfigurable en polarisation. Cette propriété peut être utilisée pour développer de nouvelles fonctionnalités telles que la réjection de bande et la bidirectionnalité du courant.

En résumé, ce travail est consacré à la réalisation de capteurs infrarouges combinant nanocristaux colloïdaux de HgTe et structures photoniques. L'idée principale de ce projet est la possibilité d'améliorer les performances de ces capteurs en confinant le rayonnement infrarouge à des distances comparables à la longueur de diffusion des porteurs dans les films de nanocristaux. Diverses structures optiques et photoniques ont été explorées, aboutissant à plusieurs nouvelles fonctionnalités, telles que la reconfigurabilité avec le voltage, l'accordabilité en longueur d'onde et la réjection de bande.

Ce travail ouvre plusieurs perspectives, à la fois dans la physique fondamentale et dans les technologies de détection infrarouge. La première perspective qui nous semble intéressante est l'intégration des structures optiques pour implémenter des matrices dans des imageurs

infrarouges. L'amélioration des performances observée au niveau du composant isolé pourrait ainsi avoir un impact sur la conception des imageurs. Pour cette application, il est nécessaire de concevoir des structures photoniques à l'échelle d'un pixel. Les résultats préliminaires présentés dans cette thèse montrent que cela est possible. Du point de vue de la physique fondamentale, il nous semble intéressant d'explorer le régime de couplage fort entre un mode du résonateur optique et l'exciton du nanocristal, et les éventuelles conséquences de ce régime sur le transport de charge.

List of removed figures

Figure 1.26: Colloidal synthesis of nanocrystals. *a. Photo of a typical setup for colloidal synthesis. b. Absorbance spectra of CdSe NCs with different sizes. From reference [37]. c. Emission from CdSe colloidal NCs of different sizes in solution when illuminated with UV light (©Nexdot). d. Transmission electron microscope (TEM) images of CdSe CQD. The inset presents a high-resolution TEM image of a single CdSe dot with an observable crystalline structure. From reference [38].*

Figure 1.27: *Bulk band structure of CdTe (a) and HgTe (b). The ordering of the conduction and valence bands near the band gap at the Γ point in HgTe is opposite to the one in CdTe. In HgTe, the hole state is above the electron state. From reference [43].*

Figure 1.28: HgTe NCs obtained from Keuleyan's procedure. *a. TEM image of HgTe NCs having PL peak around 2500 cm^{-1}. The scale bar is 20 nm. b. Normalized absorbance spectra of HgTe NCs solutions. c. Photocurrent spectra of HgTe NC films with different NC sizes. From reference [48].*

Figure 1.29: Liquid phase ligand exchange. *a. Long ligands capping NCs are replaced by shorter ones in the liquid phase. The NCs capped with long ligands in a nonpolar solvent are mixed with a polar solvent containing short ionic ligands. b. Infrared absorption spectra of as-synthesized HgTe NCs and the NC ink obtained from ligand exchange process. The NCs have a cut-off wavelength of around 2.5 µm. The initial solvent is toluene. Ligand exchange reduces the C-H absorption and gives rise to the O-H bond from the short ligands (MPOH). From reference [69].*

Figure 1.30: Impact of various ligands on electronic states in SWIR HgTe NCs. *Relative energies of the ground states of valence and conduction band, and Fermi energy in HgTe NCs with 1.7 µm cut-off wavelength with different capping ligands. From reference [72].*

Figure 1.31: Early developed-photoconductive-detectors based on colloidal HgTe NCs. *a. The first reported detecting device using organic-capped HgTe NCs. b. I-V characteristics of the device in part under dark and illumination conditions. From reference [41]. c. Schematic and I-V characteristics of the first HgTe NC-based detector with vertical structure. From reference [78]. d. Top view of the interdigitated contacts with ink-jet printed stripes of colloidal HgTe NCs. e. Normalized photocurrent spectra of the device in part d with two different sizes of NCs. HgTePD2:4nm and HgTePD3: 6 nm. From reference [79].*

Figure 1.32: Interdigitated electrodes and HgTe films prepared with novel methods. *a. Optical microscope image of gold interdigitated electrodes fabricated on a Si substrate. b. False-color SEM image of patterned HgTe film made with PMMA-assisted transfer. From reference [82]. c. Cross-sectional SEM image of original/imprinted HgTe NC film. The scale bar is 100 nm. From reference [83]. d. Optical microscope image of NC patterns prepared with direct optical lithography. The scale bars are 100 µm. From reference [84].*

Figure 1.33: HgTe NC-based photodiodes of first generations. *a. Schematic illustration of the solar cell-like device structure using NIR HgTe NC absorber. b. Band energy diagram for the device in part a. c. Absorption spectrum and TEM image (in the inset) of the NCs. From*

reference [94]. d. Schematic of the first MWIR diode. e. Photocurrent spectra of some diodes in part d. f. Current-voltage characteristic of a MWIR diode. The black curve is the dark I-V with the thermal shield closed. The blue curve is measured with the shield open, implying the detector reaches BLIP regime. The red curve is measured under blackbody illumination. From reference [95].

Figure 1.34: Recent advancements in MWIR and SWIR photodiodes. *a. Schematic of the first MWIR diode based on HgTe/Ag_2Te stack. b. Thermal imaging capture with a MWIR diode with structure in part a. From reference [99]. c. Schematic of SWIR with CdSe electron transport layer. d. SEM cross-sectional image of the stack. d. Detectivity as a function of temperature for the diode in parts c and d. From reference [100].*

Figure 1.35: Phototransistor based on HgTe NCs. *a. Room-temperature photoresponse of a HgTe NC-based phototransistor during CO gas sensing measurement. On the right is the setup for gas sensing. b. Photocurrent and dark current of the transistor in part a as functions of the applied gate voltage. From reference [88] c. Schematic of the phototransistor based on ion glass and graphene electrodes. A planar p-n junction can be generated by applying a drain-source bias comparable to the gate bias. From reference [107]. d. Schematic of a ferroelectric-gated phototransistor. e. Current-voltage characteristics of the phototransistor in part d. From reference [110].*

Figure 1.36: Focal plane arrays for infrared imaging. a. Process for hybridization of infrared FPA for conventional materials. From reference [2]. b. Illustration for the direct deposition of NC solution of a ROIC. From reference [22]. c. The first multipixel device for SWIR imaging. d. A laser diode beam profile recorded with the array in part c. From reference [69] e. A laser diode beam profile recorded with VGA FPA. From reference [72] f. Passive imaging with FPA functionalized with HgTe NCs. From reference [112]

Figure 1.37: Recent progress on the development of HgTe NC-based imagers. a. Schematic illustration of the flat ROIC compatible with NC deposition. On the right, the ROIC is plugged into the camera for imaging. b. SWIR image of a chopper wheel at 170 Hz taken with the ROIC in parts a. From reference [115]. c. Illustration of the working process of trapping-mode photodetectors. d. Comparison of SWIR images of a soldering iron taken with imagers in photoconductive and trapping mode. From reference [116]. e. The configuration of visible pixel and SWIR pixel that are functionalized with perovskite NCs and HgTe NCs. From reference [84].

Figure 2.18: NCs coupled with photonic nanostructures for photodetection. *(a, b). Scheme of HgTe NCs/ZnO heterojunction photodiode with gold nanorods embedded within the ZnO layer and the increased detectivity of the structure compared to a reference sample without the nanorods [129]. (c, d). Scheme of a structure combining plasmonic nano-disks with an optical spacer and the increased detectivity of the structure thanks to absorption enhancement [131]. (f, h). Scheme of the GMR coupled to HgTe NCs and the increased responsivity of the detector thanks to the improvement of both optical and electrical properties by the GMR. h. Photocurrent spectra of the GMR photodetector with different grating periods, demonstrating tunability of the photocurrent peak with the grating period [90].*

Figure 3.28: Bias-reconfigurable structure based on back-to-back diode configuration. a. Sketch of the back-to-back diode for dual band photodetection. The equivalent electrical circuit is shown on the right. b. Back-to-back diode from multiple layers

of NCs in a tandem structure. The spectral response on the diode can be selected by changing bias polarity, as shown by the graph on the right. From reference [103]